High-resolution diffusion imaging of the hippocampus

by

Kevin Grant Solar

A thesis submitted in partial fulfillment of the requirements for the degree of

Doctor of Philosophy

Department of Biomedical Engineering

University of Alberta

Abstract

The human hippocampus is difficult to image given its small size, location, shape, and complex internal architecture. Structural magnetic resonance imaging (MRI) has shown that typical age-related hippocampal volume changes vary along its anterior–posterior axis. Diffusion tensor imaging (DTI) provides complementary microstructural metrics, but there are few hippocampus DTI studies investigating typical age-related changes and all are limited by low spatial resolution. Structural MRI has also demonstrated smaller hippocampal volumes in individuals with prenatal alcohol exposure (PAE), which animal models suggest may result from microstructural changes due to cell loss and altered myelination; however, there are no PAE hippocampus DTI studies. Moreover, there are complex intra-hippocampal pathways with crossing fibers that DTI cannot resolve, hence there are few *in vivo* hippocampus DTI tractography studies and a more sophisticated approach is necessary and would be valuable for examining neurological/psychiatric disorders. Constrained spherical deconvolution (CSD) can disentangle complex fibers, however the only hippocampal CSD study used a low b value and low spatial resolution.

Chapter 4 uses high spatial resolution 1 mm isotropic DTI of 153 healthy volunteers aged 5–74 years to investigate hippocampus diffusion and volume trajectories (whole-structure/head/body/tail) and memory correlations. Manually traced (on mean diffusion-weighted images, DWI) hippocampal volumes demonstrated age-related changes that varied across the head/body/tail. Fractional anisotropy (FA) and mean/axial/radial diffusivities (MD/AD/RD) yielded peaks or minima, respectively, at ~30–35 years across the hippocampus. Memory and FA and/or volume correlations were significant in younger volunteers (5–17 years), but not 18–49 or 50–74 year-olds. MD significantly correlated with memory in 18–49 year-olds, but not at other

ages. Chapter 4 demonstrated regionally-specific age effects and cognitive correlations along the hippocampus anterior–posterior axis from 5-74 years. These findings form the basis of comparison to numerous neurological or psychiatric disorders.

Chapter 5 comprises the first application of hippocampus DTI in PAE. Using the 1 mm isotropic DTI from Chapter 4, T1-weighted images, and cognitive testing, 36 healthy controls (8-24 years) and 19 participants with PAE (8-23 years) were studied. Whole-hippocampus volumes were 18% smaller in PAE than in controls on manually traced DTI, but automated T1-weighted image segmentations did not show group differences. Manual subregion DTI segmentation revealed reduced body/tail but not head volumes. There were no hippocampal diffusion metric group differences. Age and volume correlations were not significant in either group, whereas negative correlations between age and whole-hippocampus MD/AD/RD, and head/body (but not tail) MD/AD/RD were significant in both groups. In controls, seven positive linear correlations were found between hippocampal volume and episodic and working memory (left) and working memory and processing speed (right). In PAE, left tail MD positively correlated with executive functioning, and right head MD negatively correlated with episodic memory. Chapter 5 demonstrated hippocampal volume reductions and altered relationships with memory that suggest disrupted hippocampal development in PAE.

Chapter 6 uses a multi-shell (64 b500s; 64 b2000s) version of the 1 mm isotropic diffusion protocol in Chapters 4/5. This qualitative pilot study included: 40 cross-sectional (scanned once) volunteers aged 5-90 years to demonstrate the feasibility of CSD tractography in comparison to DTI tractography across the lifespan, and six longitudinal (scanned twice) volunteers aged 23-40 years to demonstrate replicability. DTI ellipsoid maps and streamlines and CSD fiber orientation distribution function maps and streamlines demonstrated consistent anatomically-plausible fiber

orientation patterns corresponding to polysynaptic and direct hippocampal pathways from 5-90 years and across the longitudinal data. CSD provided additional information in the form of anatomically-plausible crossing fibers that DTI could not resolve due to model limitations; the greatest portion of crossing fibers was in the hippocampal head. High spatial resolution diffusion data enables both DTI and CSD-based intrahippocampal tractography to provide anatomically-plausible results, but only CSD can resolve crossing fiber regions. Chapter 6 suggests that high spatial resolution diffusion tractography with DTI or CSD could be applied to study neurological and psychiatric disorders to identify potentially missing streamlines or differences in quantitative tract-based metrics that may relate to memory and other cognitive deficits.

Altogether, this thesis demonstrates the applicability of clinically-relevant 1 mm isotropic hippocampus diffusion MRI protocols. These 3T MRI acquisitions allowed for novel studies of the hippocampus in humans across the typical life span (Chapters 4/6) and with PAE (Chapter 5).

Preface

This thesis is an original work by Kevin Grant Solar. All research projects for which this thesis was a part received ethics approval from the University of Alberta Research Ethics Board. All subjects were scanned at the Peter S. Allen MRI Research Centre in the University of Alberta Hospital and written informed consent was obtained from all controls and individuals with prenatal alcohol exposure (PAE) included here. The three research chapters of this dissertation contain unique contributions to the international MRI research community.

Chapter 4 of this thesis has been published as Solar, K.G., Treit, S., Beaulieu, C. (2021) High resolution diffusion tensor imaging of the hippocampus across the lifespan (Hippocampus, doi: https://doi.org/10.1002/hipo.23388). Data for this chapter were acquired in a Siemens Prisma 3.0 T MRI system (n = 153) using a high-resolution diffusion MRI acquisition for the hippocampus that was recently published by the Beaulieu Lab Group (Treit et al., 2018). Volunteer recruitment was accomplished by advertising at community venues (e.g., recreation centers) in Edmonton, AB, and participants were screened for self-reported history of brain injury or neurological/psychiatric disorders. Cognitive testing and image acquisition was performed by 7 members of the Beaulieu Lab Group (Emily Stolz, Graham Little, Julia Rickard, Kevin Solar, Pascal Tetreault, Prayash Katlariwala, and Sarah Treit). I was responsible for the literature review, image processing, manual segmentation, qualitative and quantitative image analyses, data interpretation, creation of tables and figures, and writing of the text. My co-authors, Drs. Christian Beaulieu and Sarah Treit helped with data interpretation, figure/table/text edits and response-to-reviewer documents.

Chapter 5 of this thesis has been published as Solar, K.G., Treit, S., Beaulieu, C. (2022) High-resolution diffusion tensor imaging identifies hippocampal volume loss without diffusion changes in individuals with prenatal alcohol exposure (Alcoholism: Clinical and Experimental

Research, doi: https://doi.org/10.1111/acer.14857). Data for this chapter were acquired on the same Siemens Prisma 3.0T MRI system using the same recently published high-resolution diffusion MRI acquisition for the hippocampus (Treit et al., 2018). The healthy control group included 36 volunteers and the prenatal alcohol exposure (PAE) group included 19 volunteers. Controls were enrolled, scanned, and cognitively tested as part of a larger normative study on brain development as described for Chapter 4. Volunteers in the PAE group were recruited through advertising and word of mouth, had confirmed prenatal alcohol exposure, and had been previously assessed in one of several fetal alcohol spectrum disorders (FASD) clinics in Alberta. Image acquisition and cognitive testing of individuals in the PAE group was completed by Dr. Sarah Treit, and Dr. Graham Little assisted in cognitive testing. The volunteers in the PAE group were scanned and cognitively tested in same manner as described for the controls for Chapter 4. I was responsible for the literature review, image processing, manual segmentation, qualitative and quantitative image analyses, data interpretation, creation of tables and figures, and writing of the text. My co-authors, Drs. Christian Beaulieu and Sarah Treit helped with data interpretation, figure/table/text edits and response-to-reviewer documents.

Chapter 6 is an original contribution to this thesis and has not been published elsewhere. Data for this chapter were acquired on the same Siemens Prisma 3.0T MRI system using an advanced iteration of the recently published high-resolution diffusion MRI acquisition for the hippocampus (Treit et al., 2018) as part of a large normative study that included 390 healthy volunteers (Treit et al., 2022). The 1 mm isotropic diffusion MRI protocol used in Chapters 4 and 5 was based on a single-shell acquisition with 10 averages of 10 directions at b 500 s/mm^2 (Treit et al., 2018). The multi-shell 1 mm isotropic diffusion MRI protocol used in Chapter 6 was based on the single-shell acquisition but it and additional shell, one shell of 64 directions at b 500 s/mm^2

and a second shell of 64 directions at b 2000 s/mm^2. Chapter 6 was based on a subsample (n = 40) with the same sex and age composition as the full sample (n = 390). I was responsible for the development of the multi-shell protocol. I ran multi-shell diffusion imaging tests on phantoms (e.g., kerosene), then moved to volunteers to test various combinations of shells (i.e., 2 or 3 shells) and b values (i.e., the lower shell was tested with b values of 500 and 750, the higher shell was tested with b values of 1500, 2000, 2500 s/mm^2). I was responsible for the literature review, image processing, manual segmentation, qualitative and quantitative image analyses, data interpretation, creation of tables and figures, and writing of the text.

Dedication

To my family. Keep smiling.

In further detail, I dedicate this thesis to the ones I love. Thank you to my family and best friend Emil for your unwavering support throughout all my schoolin'. Thank you to my mom and dad who encourage me to pursue my passions and enjoy life and support me through all my trials and tribulations. Thank you to my sister Justine for putting up with me and allowing me to scan and immortalize her brain for this dissertation. Thank you to my Baba and Dido who were renowned educators and enjoyers of life. Thank you to my Granny and Papa who came to this country to start a family and built a business that has continued over half a century. Thank you to my sweet Leia hound, and Birch and Oaky and MC; life is better with dogs. You all carry and inspire me everyday. Lastly, I am forever grateful for my beautiful, wise, and wonderful wife Diana who I met out West in the City of Champions when I arrived for my PhD. During unprecedented times in 2020, we married at our family's cottage on Nutimik Lake in the Whiteshell, Manitoba, and the next summer we welcomed the first member of our family, MC, our sour Spaniel boy out of the Rocky Mountain Foothills of Alberta. *La vida es buena contigo.*

“Forward. Not backward.”

— Mom

“No matter how aggravating something may be I have found that when people (judges or clients) have given me what I felt was an unreasonably hard time, those are the situations that I have learned more from and have made me better in my profession.”

— Dad

“Hmm.”

— My wife, Diana

“Science is like a blabbermouth who ruins the movie by telling you how it ends.”

— Flanders

“Others ask, "What if?" We ask, "Why if?"”

— Futurama

“Don't walk around the down and out. Lend a helping hand instead of doubt. And the kindness that you show every day, will help someone along their way. You got to try a little kindness. Yes, show a little kindness. Just shine your light for everyone to see. And if you try a little kindness, then you'll overlook the blindness, of narrow-minded people on the narrow-minded streets.”

— Glen Campbell

Acknowledgements

This work was funded by the Canadian Institutes of Health Research (CIHR), the Natural Sciences and Engineering Research Council of Canada (NSERC), the University of Alberta, and the University of Alberta Graduate Students' Association in cohort with the Myer Horowitz Fund. I want to give thanks especially to NSERC for the 3-year CGS-D that paid most of my salary. I am thankful to Maisie Goh for always looking out for us graduate students and coming shopping with us to Costco for spring BBQs. Thanks to Carol Hartle and Dr. Alan Wilman for their valuable support throughout the program. Thank you to Peter Seres for helping me develop the AB300 hippocampus protocol and to better understand MRI in general. Thank you to Dr. Sarah Treit for assisting me in segmentation, data interpretation, and manuscript preparation as my co-author. Thanks to my lab mates who guided me early on, including Drs. Graham Little and Pascal Tetrault. Thank you to my examining committee members, including Drs. Ali Khan (external, Western University), Donald Gross, Nikolai Malykhin, and Trevor Steve. Finally, thank you to my supervisor Dr. Christian Beaulieu, the black belt, for bringing me in and sharing his research ideas, feedback, and funding throughout my PhD, and for helping me grow into the scientist I am today.

I also want to thank the City of Champions, Edmonton, AB, and its River Valley for a fabulous place to call home while working on my PhD.

Table of Contents

List of Tables

List of Figures

List of Symbols and Abbreviations

γ: Gyromagnetic ratio

δ: Duration of the diffusion gradients

$\lambda_{1,2,3}$: Diffusion ellipsoid eigenvalues

τ: Gradient time

ω: Larmor frequency

2D: Two dimensional

3D: Three dimensional

AD: Axial diffusivity

ADC: Apparent diffusion coefficient

ADNI: Alzheimer's Disease Neuroimaging Initiative

BW: Bandwidth

CA: Cornu ammonis

CNS: Central nervous system

CSD: Constrained spherical deconvolution

CSF: Cerebrospinal fluid

D: Diffusion coefficient

DG: Dentate gyrus

DTI: Diffusion tensor imaging

DWI: Diffusion weighted image

EADC: European Alzheimer's Disease Consortium

EPI: Echo-Planar Imaging

FA: Fractional anisotropy

FDR-BH: Benjamini-Hochberg False Discovery Rate

FID: Free induction decay

fODF: Fiber orientation distribution function

FOV: Field of view

G: Gradient strength

GM: Grey matter

GRAPPA: GeneRalized Autocalibrating Partially Parallel Acquisitions

HARDI: High Angular Resolution Diffusion Imaging

Harp: Harmonized Hippocampal Protocol

M: Magnetization vector

MD: Mean diffusivity

MPRAGE: Magnetization Prepared RApid Gradient Echo

MRI: Magnetic resonance imaging

NDI: Neurite density index

NMR: Nuclear magnetic resonance

NODDI: Neurite Orientation Dispersion and Density Imaging

ODI: Orientation dispersion index

RD: Radial diffusivity

RF: Radiofrequency

ROI: Region of interest

SLM: Stratum lacunosum moleculare

SNR: Signal to noise ratio

SS-EPI: Single-shot EPI

TE: Echo time

TR: Repetition time

WM: White matter

Introduction

The human brain undergoes changes that begin in prenatal development and continue throughout the lifespan. The hippocampus is a deep grey matter (GM) brain structure that is critical for memory and learning, and it has unique cellular properties as the only brain region to undergo continued neurogenesis into late adulthood. Magnetic resonance imaging (MRI) studies are useful in elucidating both normal and abnormal developmental and aging changes in the hippocampus, and concurrent cognitive exams help link such brain changes to cognitive changes. In prenatal alcohol exposure (PAE), hippocampal atrophy is one of the most reported brain structure volume losses. However, the hippocampus is difficult to image given its small size, location, shape, and complex internal architecture. Consequently, the majority of healthy and all of PAE hippocampal MRI studies focus on macrostructure (volumetrics and shape), be it the whole structure or subfields including the two laminae that make up the hippocampus, the dentate gyrus (DG) and cornu ammonis (CA). A complementary imaging method to structural MRI is diffusion tensor imaging (DTI). Ex vivo DTI at ultra-high spatial resolution provides exceptional images of internal hippocampus architecture, measurements indicative of microstructure, as well as intra-hippocampal memory pathway identification using diffusion tractography. In vivo DTI at lower spatial resolution has revealed age-related changes in hippocampal diffusion measurements and correlations with memory performance. However, DTI is limited by its inability to depict crossing or tightly curving fibers which have been demonstrated ex vivo in the hippocampus.

The aim of this thesis is to characterize the healthy hippocampus across the lifespan using 1 mm isotropic high spatial resolution DTI (Chapter 4) and a more advanced diffusion MRI method called constrained spherical deconvolution (CSD) – a technique that is capable of resolving complex fiber orientations (Chapter 6). This thesis also applied the same high spatial resolution

DTI protocol to examine the hippocampus in prenatal alcohol exposure (PAE) in children to young adults. This dissertation includes an introduction to the healthy human brain with a focus on the hippocampus (Chapter 1), MRI with a focus on diffusion-weighted imaging (DWI) (Chapter 2), and the effects of PAE on the human brain (Chapter 3). In Chapter 4, I examine cross-sectional age changes and relationships to cognitive performance for hippocampal volume and microstructure in a healthy cohort (aged 5-74 years). In Chapter 5, I examine group differences and cross-sectional age changes in hippocampal volume and microstructure, and the relationship to cognitive performance in PAE. In Chapter 6, I examine cross-sectional changes and provide proof of concept that CSD is superior to DTI for examining intra-hippocampal memory pathways. Following these research chapters, there is a brief discussion (Chapter 7) on the impact of the thesis findings, their limitations, and the future directions.

1. Healthy Human Brain Structure and Function

1.1. Macrostructural Anatomy and Function

The human brain is an astounding example of complex, organic structure and function that exists merely in the form of a ~3 lb mass composed of 70-80% water (an important property for MRI). Three principal anatomical divisions of the human brain include the forebrain (made up of the cerebrum and diencephalon), midbrain and hindbrain (made up of the medulla, pons, and cerebellum). In turn, the cerebrum is made up of 2 cerebral hemispheres (left, right), each of which consists of cortical grey matter (GM), interconnecting white matter (WM) pathways (within and between hemispheres; the corpus collosum being the main interhemispheric bundle) (Figure 1.1a, b, c), and deep grey matter regions including the hippocampus (Figure 1.1c, f, g). The cerebral hemispheres are further divided into the frontal, parietal, temporal and occipital lobes by the main sulci/fissures, including the central sulcus, Sylvian fissure, parieto-occipital sulcus, and the

preoccipital notch (Figure Figure 1.2: Anatomy of a typical neuron.1.1d). The diencephalon consists of the thalamus and hypothalamus. The cerebellum or "little brain" is split by the primary fissure into anterior and posterior lobes (Figure 1.1d). The midbrain, pons and medulla are also collectively referred to as the brain stem (Figure 1.1d).

In terms of function, the frontal, parietal, temporal and occipital lobes are each involved in a variety of processes. The frontal lobes are involved in a variety of high-level functions including planning, attention and decision making, as well as motor movement, and speech production (only in left frontal lobe, Broca's area). The parietal lobes are responsible for processing sensory information, including pressure, pain, temperature, and touch. The temporal lobe contains the memory centre of the brain, the hippocampus, and is generally involved in processes of memory, emotion, and auditory processing (e.g., the left hemisphere contains Wernicke's area which is vital for speech comprehension). The occipital lobe is critical for visual processing. The brainstem and cerebellum work together to regulate body functions (e.g., respiration, blood pressure) and movements (e.g., eyes and limbs). However, despite the anatomical localization of some principal functions such as visual and auditory processing, most complex processes such as memory processing and emotional regulation rely on the input from and communication between multiple areas.

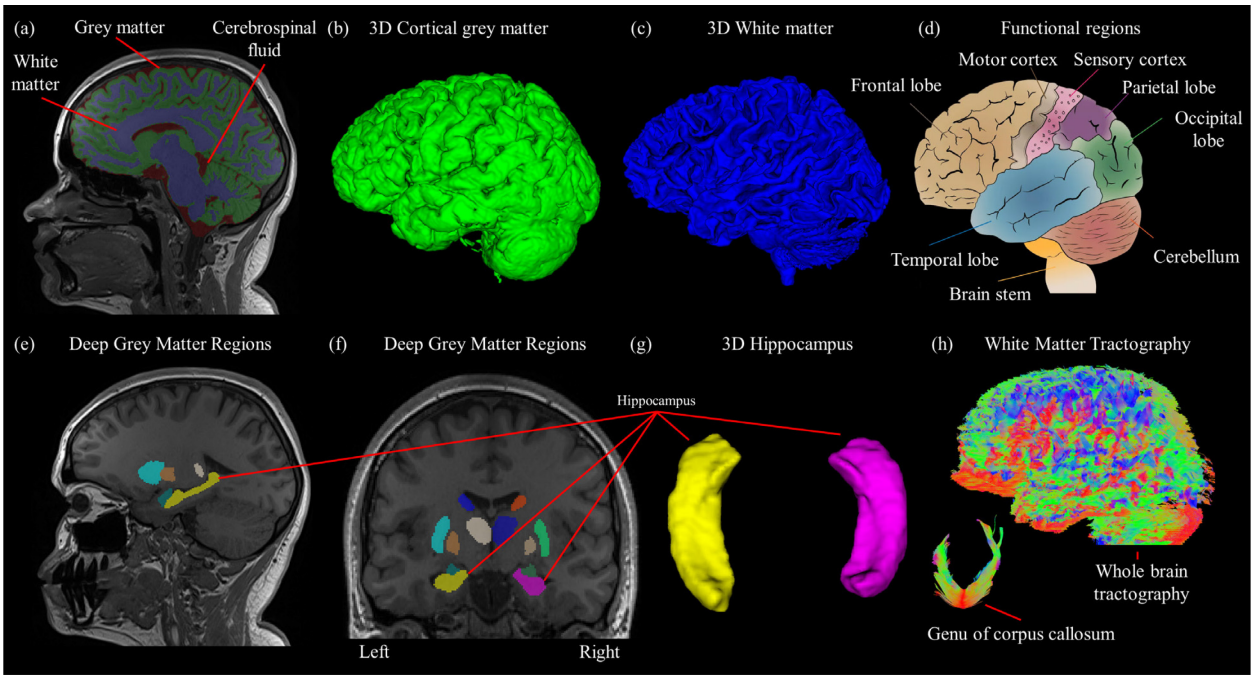

Figure 1.1: Macrostructural organization of the human brain. (a) Sagittal T1-weighted image featuring white matter (WM), grey matter (GM) and cerebrospinal fluid (CSF). (b) 3D rendering of cortical GM. (c) 3D rendering of WM. (d) Basic functional divisions of the brain. (e) Sagittal T1-weighted image featuring deep GM regions. (f) Coronal T1-weighted image featuring deep grey matter regions. (g) 3D rendered bilateral hippocampus. (h) WM diffusion tractography. (a-c, e-h) Data is from a healthy 24-year-old female. (d) Adapted from Wikimedia Commons (public domain).

1.2. Microstructural Anatomy and Function

The brain is made up of ~40-130 billion neurons at a ~1:1 ratio with glial cells to form anatomically and functionally distinct regions that work together (von Bartheld et al., 2016). Neurons are the computational and communicative units of the brain that are responsible for sending and receiving chemical/electrical signals (synaptic transmission) by conducting nerve impulses. Glial cells play numerous, critical supporting roles for the neurons, including immunological responses and metabolic functions (microglia); maintenance of water and ion homeostasis and of the blood brain barrier (astrocytes); and the insulation of axons for quick and efficient nerve impulse transduction (oligodendrocytes) (Jäkel & Dimou, 2017). Generally, neurons are post-mitotic cells, meaning they cannot divide to generate new neurons. There are

exceptions which are still being debated, for example, the dentate gyrus of the hippocampus has shown neurogenesis that persists into adulthood (Lee & Thuret, 2018). Conversely, glial cells throughout the brain are capable of reproduction (e.g., in response to damage) (Jäkel & Dimou, 2017).

The basic neuron, starting from the receiving end, moving in the direction of a nervous impulse, consists of electrical impulse receiving dendrites that extend from the cell body or soma, from which an axon also extends and branches into axon terminals to synapse with the next cell via soma or dendrites (Figure 1.2: Anatomy of a typical neuron.). The structure of the axon is primarily composed of microtubules, neurofilaments and microfilaments, wrapped up with an axonal plasma membrane and surrounded with axonal cytoplasm. Most neurons in the human brain are insulated by a lipid-rich, hydrophobic myelin sheath provided and maintained by oligodendrocytes (Figure 1.2: Anatomy of a typical neuron.). The purpose of this insulation is to speed up signal transduction by forcing the outgoing signal to jump along the open spaces in the myelin sheath; these spaces are called nodes of Ranvier (Figure 1.2: Anatomy of a typical neuron.). There are a variety of neuronal sub-types that differ based on their structure (e.g., pyramidal, Purkinje). The GM of the brain is largely made up of the neuronal soma, dendrites, and glia, leading to a grey appearance (Figure 1.1, 1.2). There are 2 distinct forms of GM, (i) cortical GM which encapsulates the periphery of the brain's surface (Figure 1.1a, b), and (ii) subcortical or deep GM regions that are structurally and functionally distinct from surrounding regions (e.g., hippocampus) (Figure 1.1e-g). The WM of the brain is mainly composed of the myelinated neuronal axons (as well as glia) which leads to the white appearance (Figure 1.1, 1.2).

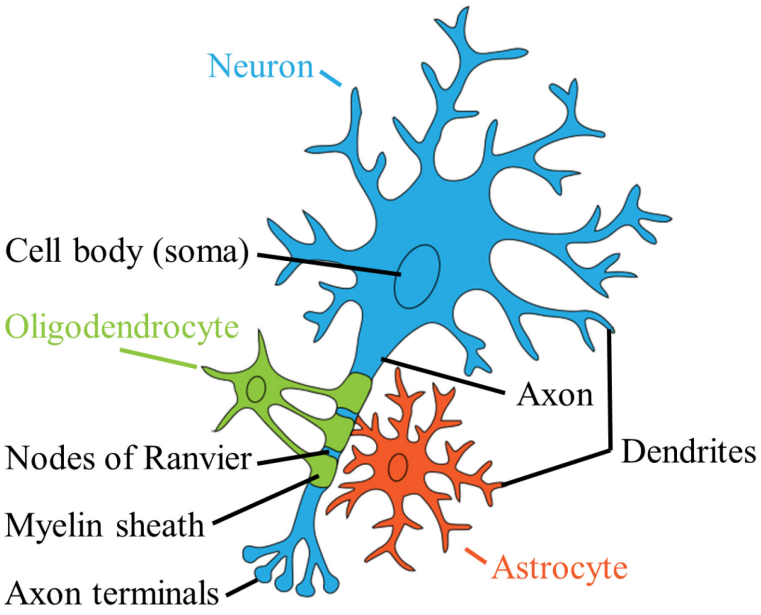

Figure 1.2: Anatomy of a typical neuron. Anatomy of a typical neuron (blue) with glial cells (oligodendrocyte, green; astrocyte, orange). Adapted from Wikimedia Commons (public domain).

1.3 The Hippocampus

The hippocampus is a small (~4 - 4.5 cm in length and ~0.5-2 cm in width along the long anterior-posterior axis; ~ 1300 - 3500 mm^3 in volume) bilateral structure located in the temporal lobes (Duvernoy et al., 2013). At the macroscopic scale, it is C-shaped like its namesake, the seahorse (genus Hippocampus). It can be divided into 3 simple parts along its anterior-posterior axis: the head, body, and tail. It is a bi-laminate structure composed of 2 U-shaped laminae that interlock into one another along the long axis in the anterior-posterior direction; these include the cornu ammonis (CA) and the dentate gyrus (DG). The C-shaped curvature of the hippocampus is so that especially the head and partly the tail turn inwards toward the medial direction, relative to the body. This curvature is exemplified by the observation that the relative position of the CA and DG laminae are the same as viewed from a coronal section at the body as in the sagittal sections of the head and tail (Figure 1.3g). The CA is made up of 6 layers, mainly the alveus, and the stratum oriens, pyramidale, radiatum, lacunosum and molecular (Figure 1.3h). The alveus is made up of axons projecting from the somata of the hippocampus and serves as the central efferent

hippocampal pathway. The stratum oriens is difficult to define as it blends with pyramidale, but it does contain scarce basket cells. The stratum pyramidale is composed of pyramidal neurons and comprises the key component of the CA; the axons of the pyramidal neurons mainly project to the septal nuclei, but some also turn back to synapse with other pyramidal neurons and are called Schaffer collaterals. The stratum radiatum is largely composed of parallel apical dendrites from pyramidal somata. The stratum lacunosum is generally comprised of numerous axonal fasciculi that come from the Perforant pathway and Schaffer collaterals. The stratum moleculare is made up of scarce interneurons. The CA can also be divided into 4 subfields based on the heterogeneity of the pyramidal somata across the stratum pyramidale. CA1 is composed of triangular pyramidal somata. CA2 is composed of densely packed ovoid pyramidal somata. CA3 is composed of nonmyelinated fibers called mossy fibers with ovoid pyramidal somata less densely packed than in CA2; CA3 is also the curve of CA where it interlocks with the DG. CA4 is composed of large and mossy fibers with large ovoid pyramidal somata that are less densely packed than CA2 and CA3; CA4 is located in the concavity of the DG. The DG is made up of 3 distinct layers: the stratum granulosum (consists of granular somata, round and densely packed, with mossy fibers that project to CA3/4) and moleculare (contains perforant pathway, septal and commissural fibers), along with the polymorphic layer (consists of granular axons and connects stratum granular to CA4). Additionally, the surface of the hippocampus is not smooth, instead, there are protruding digitations on the head and tail formed by folds of the DG and CA, and relatively smaller dentations on the body formed by protrusions of the DG (Figure 1.3d, f).

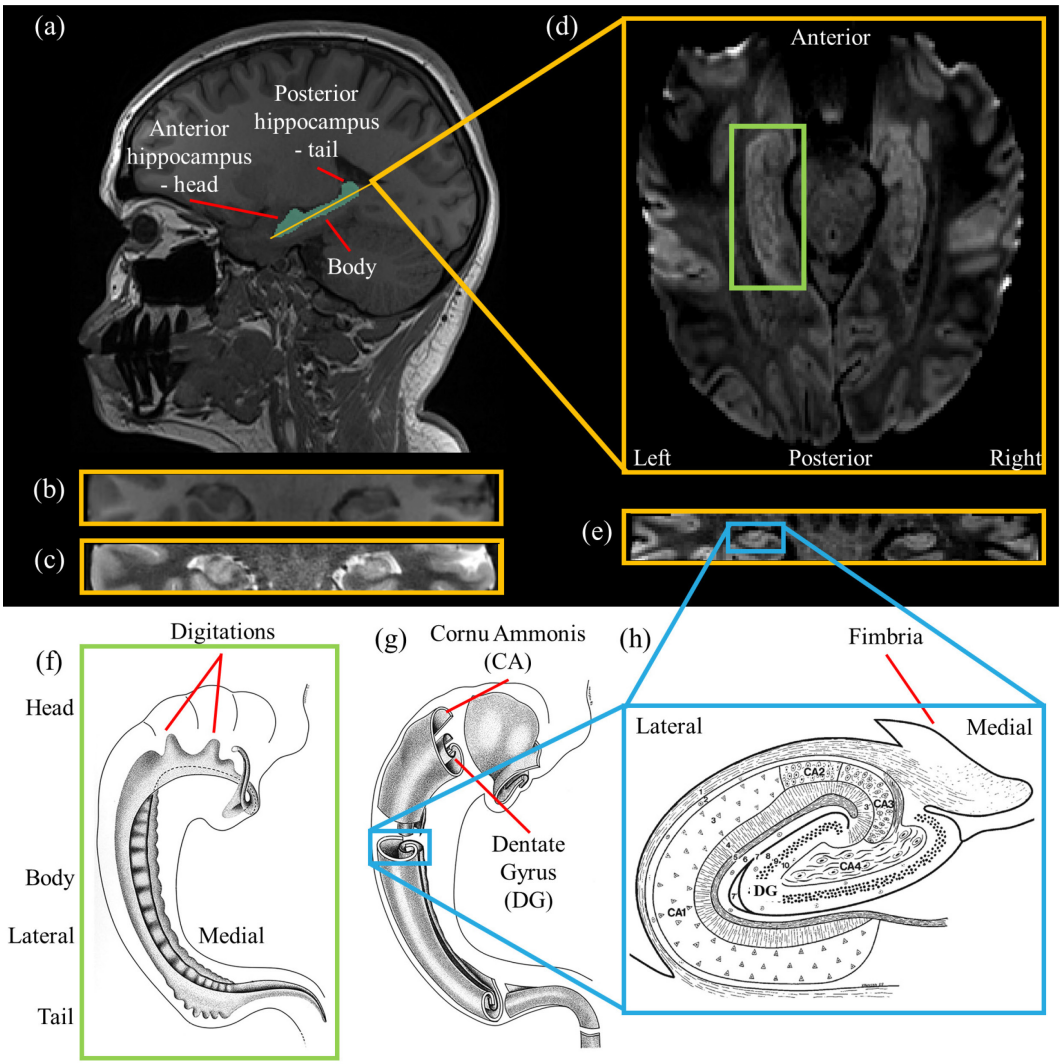

Figure 1.3: Typical hippocampus anatomy. (a) Sagittal view of the hippocampus (green) on a T1-weighted image. Coronal view through the hippocampus body on (b) T1-weighted and (c) T2-weighted images. (d) Axial-oblique view on the (as indicated on (a) by the yellow line along the anterior-posterior (A-P) hippocampus axis) mean diffusion weighted image (DWI) featuring the longest A-P view of the hippocampus. (e) Coronal view through the hippocampus body on mean DWI. (f) Surface of the dentate gyrus (DG) along the A-P axis, featuring head digitations. (g) The bilaminate hippocampus structure, featuring the interlocking U-shaped cornu ammounis (CA) and DG. (h) Coronal view through the hippocampus body, featuring the 6 CA layers: (1) alveus; (2) stratum oriens; (3) stratum pyramidale; (3`) stratum lucidum, (4) stratum radiatum; (5) stratum lacunosum; (6) stratum moleculare), (7) the vestigial hippocampal sulcus (and (7`) a residual cavity), and the 3 layers of the DG (8) stratum moleculare, (9) stratum granulosum, (10) polymorphic layer. (h) This diagram also shows CA subfields 1-4 which are defined by the heterogeneous composure of the stratum pyramidale; the fimbria is also featured on the medial aspect. (a-e) Data from a healthy 24-year-old female. (f-h) Reprinted/adapted by permission from Springer Nature Customer Service Centre GmbH: Springer Nature by Henri Duvernoy, Françoise Cattin, Pierre-Yves Risold 2013.

The hippocampus is considered a deep GM structure, but it has white matter features including the alveus and fimbria which connect the hippocampus with other subcortical and cortical regions of the brain (Figure 1.4). There are 2 main intra-hippocampal pathways: the polysynaptic and direct pathways (Figure 1.4). The polysynaptic pathway is a sequence of neuronal connections that involves the majority of hippocampal regions (Figure 1.3a; the direct pathway uses a subset of these segments, Figure 1.3c): it begins at the entorhinal area wherefrom the perforant pathway reaches the DG, from which glutaminergic mossy fibers connect to CA3 and CA4, from which Schaeffer collaterals connect to CA1 and other axons project to the alveus and then the fimbria as the efferent path to other regions of the brain outside of the hippocampus formation. Additionally, the CA1 collaterals reach the subiculum, and then to the alveus and fimbria (Duvernoy et al., 2013).

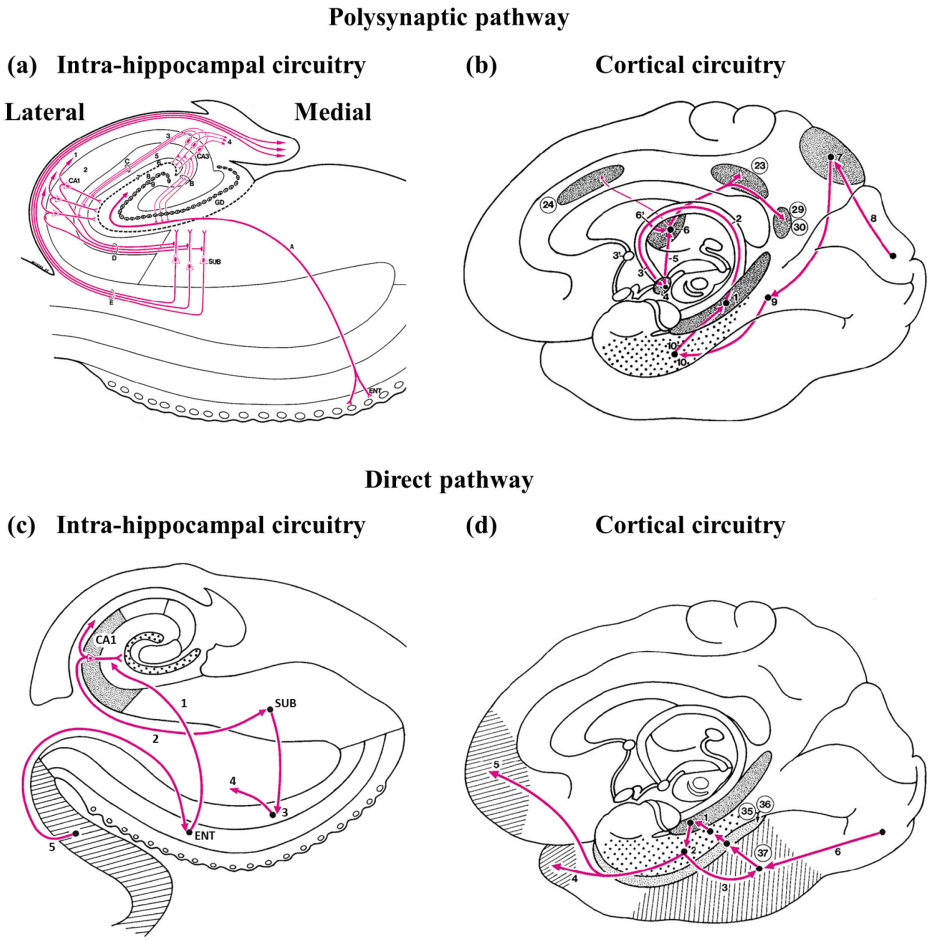

Figure 1.4: Intra-hippocampal memory pathway anatomy. Polysynaptic pathway (a) intra-hippocampal circuitry and (b) cortical circuitry. (a) Polysynaptic intra-hippocampal pathway starts from the entorhinal cortex (ENT) via the Perforant pathway (A) which perforates the subiculum (SUB) and enters the dentate gyrus (DG), followed by the next link (B) to cornu ammonus (CA) 3, which then connects (C) back to the subiculum from which the final link (E) projects to the alveus, then the fimbria, both of which lay on the superior surface of the hippocampus and contain connections that exit the polysynaptic pathway by turning to the anterior-posterior direction and running along the (b, 2) anterior-posterior axis into the fornix. Direct pathway (c) intra-hippocampal circuitry and (d) cortical circuitry. (c) The first segment of the direct pathway projects from the entorhinal cortex, into the hippocampus to synapse with CA1 pyramidal neurons which project back to the subiculum and away from the hippocampus back toward the entorhinal cortex. (a, b, c, d) Reprinted/adapted by permission from Springer Nature Customer Service Centre: The human hippocampus by Henri Duvernoy, Françoise Cattin, Pierre-Yves Risold 2013.

The human hippocampus and its critical role in memory became a hot topic of research after seminal Patient H.M. underwent bilateral hippocampal resection to combat severe epileptic seizures which resulted in global amnesia (Scoville and Milner, 1957). Following the surgical

procedure, H.M. experienced severe memory deficits, including both anterograde and retrograde amnesia. Anterograde amnesia involves the incapability to form new memories, and retrograde amnesia involves the failure to remember/recall. Interestingly, retrograde amnesia generally demonstrates a temporal gradient, wherein the case of H.M., he could not remember information from ~11 years preceding the surgery, but he could remember information past 11 years. The study of H.M. exemplified the importance of the hippocampus - in fact, H.M. was the subject of 5 decades of research (Squire & Wixted, 2011), and blazed the trail for the path that ultimately led to the hippocampal investigative work presented in this thesis. Since this discovery, studies have shown that the hippocampus is involved in multiple aspects of memory, including visual and auditory aspects of working and episodic memory (Baddeley et al., 2011; Burgess et al., 2002; Lisman et al., 2017; Postle, 2016), and there is a growing body of evidence that suggests that hippocampus is involved in a breadth of other cognitive processes including executive functioning, attention, social behaviour, spatial navigation, and language use (Lisman et al., 2017; Rubin et al., 2014).

1.3.1 MRI Studies of the Hippocampus

The location, shape, small size, and complex internal architecture of the hippocampus makes it challenging to image *in vivo*. MRI examinations of the hippocampus have been largely based on macrostructural measurements (i.e., shape, volume) of the whole-hippocampus. These studies generally agree on right-larger-than-left asymmetry (Malykhin et al., 2008; Nobis et al., 2019; Pedraza et al., 2004; Voineskos et al., 2015; Wellington et al., 2013) and nonlinear changes with age (Malykhin et al., 2017; Narvacan et al., 2017; Walhovd et al., 2005; Yang et al., 2013), but report mixed findings for sex differences (Malykhin et al., 2017; Narvacan et al., 2017; Nobis et al., 2019; Wellington et al., 2013).

Beyond the whole-hippocampus structure, the head, body and tail along the anterior-posterior (A-P) axis demonstrate varying macrostructural changes throughout development (Daugherty et al., 2017; Lin et al., 2013; Riggins et al., 2015, 2018) and aging (Chen et al., 2009; Gordon et al., 2013; Malykhin et al., 2008, 2017; Nordin et al., 2018). The digitations of the hippocampal head as qualitatively assessed on MRI have shown inter-subject variation across healthy subjects (Piccirilli et al., 2020), and reductions in numbers in Alzheimer's disease (Adler et al., 2018) and temporal lobe epilepsy (Henry et al., 2011; Oppenheim et al., 1998); however, age-related changes in numbers of digitations have not been investigated. Brain-cognition relationships also differ along the A-P axis in development (De Master et al., 2014; Riggins et al., 2015, 2018; Schlichting et al., 2017) and aging (Chen et al., 2009; Hackert et al., 2002; Nordin et al., 2018).

DTI – an MRI method that will be explained in Chapter 2 – at ultra-high resolution in *ex vivo* samples has revealed exceptional images of internal hippocampal architecture and DTI metrics that are indicative of the microstructure (Coras et al., 2014; Shepherd et al., 2007). At lower resolution, *in vivo* DTI reveals microstructural abnormalities in the whole-hippocampus as inferred from DTI metrics in epilepsy (Kimiwada et al., 2006; Yokoi et al., 2019), preterm children (Duerden et al., 2016), and Alzheimer's disease (Fellgiebel & Yakushev, 2011; Hong et al., 2013; Mak et al., 2017). Brain-cognitive relationships are also evident with hippocampus DTI metrics. Memory performance is correlated to whole hippocampus DTI changes in development (Callow et al., 2020; Fjell et al., 2019), aging (Carlesimo et al., 2010; Den Heijer et al., 2012), and across the lifespan with tighter relationships in older participants (Langnes et al., 2020). In terms of age-related hippocampus DTI metric changes, mean diffusivity (MD) shows reductions with age in development (Callow et al., 2020; Fjell et al., 2019; Mah et al., 2017), likewise with radial

diffusivity (RD) (Mah et al., 2017), and FA is higher with older age (Fjell et al., 2019; Mah et al., 2017). In aging, the opposite pattern in DTI metrics is apparent, wherein higher MD and lower fractional anisotropy (FA) is associated with older age (Anblagan et al., 2018; Carlesimo et al., 2010; Den Heijer et al., 2012; Pereira et al., 2014; Venkatesh et al., 2020). Prior to the current work, there was only a single investigation that had examined hippocampal DTI (MD only) across the lifespan (4-93 years of age). The authors reported longitudinal reductions of anterior hippocampus MD from childhood until ~50 years, after which MD increased into the 90s, while posterior hippocampus MD did not change during childhood to adolescence, but increased at older ages (Langnes et al., 2020). The aforementioned hippocampal DTI studies all were limited by the use of low spatial resolution acquisitions with voxel volumes that ranged from 5-25 mm^3, and the majority used 2x2x2 = 8 mm^3 (Table 1.1; there were only 9 total DTI studies that focus on the healthy hippocampal changes, with only 3 at a spatial resolution below 8 mm^3 voxels, but still none acquired voxels lower than 5 mm^3). Although this low-resolution DTI is sufficient and typical for whole-brain acquisitions, it does not allow for accurate representation of hippocampal subregions and causes greater partial volume errors in diffusion quantification. With low-resolution DTI, hippocampal segmentation undoubtedly relies on co-registration to higher resolution anatomical images (e.g., T1 or T2) - a process that is confounded by co-registration errors. Our lab has demonstrated that high spatial resolution (1 mm^3 voxel volume) DTI of the hippocampus is achievable at 3T by only imaging a partial-brain slab with twenty 1 mm axial-oblique slices, aligned along the long axis of the hippocampus. This acquisition can be made in 5.5 minutes (Treit et al., 2018). This protocol yields mean diffusion-weighted images (DWI) with excellent contrast and visualization of the external hippocampal surface and internal architecture, enabling direct segmentation (i.e., without co-registration to T1/T2). This protocol has revealed subfield specific

hippocampal diffusion abnormalities and correlations with verbal memory in epilepsy (Treit et al., 2019), but it has not yet been applied to study healthy neurodevelopment or aging. Chapter 4 comprises the first published application of this high-resolution DTI as applied across the healthy lifespan from 5-74 years.

Table 1.1: Diffusion tensor imaging studies of the healthy hippocampus.

	DTI Resolution (mm^3)	Age range (years)	Sample size	Age-related ΔDiffusion	Memory x DTI correlations
Development					
Callow et al., 2020	2.2x2.2x3.5 = 17 mm^3	4-8	93	↓MD	Yes
Fjell et al., 2019	2x2x2 = 8 mm^3	4-25	650	↑FA, ↓MD	Yes
Mah et el., 2017	2.2x2.2x2.2 = 11 mm^3	8-13	27	↑FA, ↓MD, ↓RD	Did not test
Aging					
Anblagan et al., 2018	2x2x1.3 = 5 mm^3	73-76	1124	↓FA, ↑MD	Tested, non-significant
Carlesimo et al., 2010	1.8x1.8x1.8 = 6 mm^3	20-80	76	↓FA, ↑MD	Yes
Den Heijer et al., 2012	2.2x3.3x3.5 = 25 mm^3	≥55	892	↓FA, ↑MD	Yes
Pereira et al., 2014	2x2x2 = 8 mm^3	50-75	50	↓FA, ↑MD	Did not test
Venkatesh et al., 2020	1.7x1.7x1.7 = 5 mm^3	20-38	49	↓FA, ↑MD	Did not test
Lifespan					
Langnes et al., 2020	2x2x2 = 8 mm^3	4-93	1790	↓MD in dev; ↑MD in aging	Yes

Beyond standard ROI analyses, DTI is commonly used to map major WM tracts of the human brain using diffusion tractography which can be used to virtually identify and quantify WM microstructure (Basser et al., 2000). Diffusion tractography of typical WM has revealed developmental increases of FA and decreases of MD that are regionally-dependent and non-linear

from childhood into adolescence and early adulthood, indicative of increased myelination, axonal packing density, and fiber orientation coherence (see review: Lebel, Treit, & Beaulieu, 2019). Regionally-varying peak FA and minimum MD values of WM tracts have been observed from ~20-40 years (Lebel et al., 2012), with regionally-varying declines of FA and increases of MD observed as indicators of decreased axonal density and fiber loss in typical aging (see review: Zhang et al., 2022). The critical role of the hippocampus in learning and memory processes relies on complex intra-hippocampal circuitry, namely two circuits, the polysynaptic pathway and the direct pathway (Figure 1.4). These pathways involve tightly packed and curvaceous fibers within the small bi-laminate structure of the hippocampus. Despite the importance of intra-hippocampal connections, there are few DTI studies that utilize tractography to identify these tracts (Meyer et al., 2017; Zeineh et al., 2012). *Ex vivo* DTI at ultra-high spatial resolution has been used to perform tractography of typical intra-hippocampal fibers, and it has revealed streamlines that form sections of these pathways, including the perforant path (Colon-Perez et al., 2015; Coras et al., 2014) and alveus (Coras et al., 2014) as part of the polysynaptic pathway; it also identified altered intra-hippocampal connectivity in temporal lobe epilepsy (TLE) relative to healthy controls (Coras et al., 2014), hence suggesting the potential clinical significance of performing intra-hippocampal diffusion tractography. *In vivo* DTI at lower spatial resolutions has been variably applied to conduct intra-hippocampal tractography. The earliest *in vivo* study was published as a pilot study (6 healthy adults, no ages given) that explored hippocampal subfield inter-connectivity (Zeineh et al., 2012). The authors tracked anatomically plausible segments of the polysynaptic and direct pathways. Although they used better than average (e.g., 2x2x2 = 8 mm^3) spatial resolution with 1.7 x 1.7 x 1.7 mm^3 = 4.9 mm^3 voxels, this voxel size is still too large to accurately track fibers within the hippocampus structure that ranges only ~2-4.5 cm^3 in size, and their whole-brain DTI

protocol required ~1 hour of scanning time which negates use in the clinic (Zeineh et al., 2012). On the other hand, the investigation by Meyer et al did not identify any particular anatomically plausible intra-hippocampal tracts, although the anterior-posterior streamlines that they featured in a healthy group of adults (mean age = 48 years) and in a "medication overuse headache" patient group (mean age = 47 years) may include alveus and/or fimbria (Meyer et al., 2017). The lack of tract identification by Meyer et al is likely related to the low spatial resolution of the DTI data used for tractography (2 x 2 x 2 = 8 mm^3 - Meyer et al., 2017), also not suitable for tractography of intra-hippocampal connections.

The existence of so few in vivo intra-hippocampal DTI tractography papers (2 total: Zeineh *et al.*, 2012; Meyer *et al.*, 2017) is most likely related to the fact that the diffusion tensor model can only resolve a single fiber orientation within a given voxel and cannot resolve regions with multiple fiber orientations (e.g., crossing or kissing fibers) (Alexander et al., 2007; Jones et al., 2013; Soares et al., 2013). This DTI limitation cannot be ignored when considering tractography within the hippocampus because intra-hippocampal pathways exhibit tightly packed axons with complex organization (e.g., crossing, curving) within the bi-laminate structure of the hippocampus (Beaujoin et al., 2018; Colon-Perez et al., 2015; Duvernoy et al., 2013; Shepherd et al., 2007), and it is expanded upon in the next chapter on MRI. There are higher order approaches beyond DTI for analyzing diffusion MRI data which rely on high angular resolution diffusion imaging (HARDI). HARDI data typically acquires at least ~64 directions (64 DWIs) at a b value of ~1500-4500 s/mm^2, whereas DTI acquisitions normally acquire ~32 directions (32 DWIs) at a b value of ~1000 s/mm^2 (Descoteaux, 2015). HARDI data is often acquired with multiple b values, referred to as multi-shell, whereas DTI is often done with a single shell. CSD is a non-parametric HARDI approach that can estimate multiple fiber orientations within a given voxel (Tournier et

al., 2004, 2012). There is one study that utilized CSD to perform diffusion tractography within the hippocampus within healthy adults aged 19-33 years to examine relationships between intra-hippocampal pathways and learning performance, however the data was not well-suited for CSD as it was acquired at a lower than recommended b value of 1000 s/mm^2, (Tournier et al., 2008, from the team that developed the CSD approach, recommends a minimum b value of 2000 s/mm^2 to resolve crossing fibers) nor was it appropriate for intra-hippocampal tractography due to low spatial resolution of 2 x 2 x 2 = 8 mm^3 (Schlichting et al., 2021). Nonetheless, the authors reported a significant positive linear relationship between CA3-CA1 streamline count and exception learning performance (Schlichting et al., 2021), however streamline count should be interpreted with caution (Calamante, 2019; Jones et al., 2013). Diffusion MRI of the hippocampus at high spatial resolution (1 mm isotropic voxels with no interslice gap) and high angular resolution with high b values (2 diffusion-weighted shells, 64 directions at 2000 s/mm^2, 64 directions at 500 s/mm^2, and 20 non-DWIs) (Treit et al., 2022) is feasible at 3T with 20 1 mm axial-oblique slices aligned to the anterior-posterior hippocampal axis, and can be acquired in a clinically-applicable time of 7:50 min (Treit et al., 2022). The technical aspects of diffusion MRI are explained in Chapter 2.

1.3.2. MRI Segmentation of the Hippocampus

For all diffusion data in this thesis, the hippocampus was manually traced on the mean DWIs. The whole hippocampus structure was segmented with general guidance by boundaries provided in the European Alzheimer's Disease Consortium (EADC) and Alzheimer's Disease Neuroimaging Initiative (ADNI) Harmonized Protocol (HarP) (Boccardi, Bocchetta, Apostolova, et al., 2015; Frisoni et al., 2015). The EADC ADNI HarP includes the fimbria/alveus and subiculum in the whole-hippocampus structure, but the subiculum was excluded in this thesis

because it is distinct from the hippocampus proper (CA and DG) as transitional cortex medial of CA1 that connects the hippocampus to the rest of the temporal lobe cortex (Duvernoy et al., 2013). Moreover, the subiculum is characterized by a large pyramidal cell layer that is less densely packed than the pyramidal layer of CA1 (O'mara, 2005) which constitutes a microstructural difference that could affect DTI parameters which are a main focus of this thesis. This microstructural difference also aided in visual differentiation and exclusion of the subiculum in manual segmentation of the hippocampus with reference to morphology described in (Duvernoy et al., 2013). The alveus and fimbria were included because they are the major conduits for afferent and efferent hippocampal connections. The alveus is a thin layer of WM that covers the ventricular surface of the hippocampus and bundles into the fimbria towards the tail of the hippocampus before separating from the hippocampus as the crus and column of the fornix (Figure 1.4).

Segmentation boundaries and landmarks for the whole-hippocampus described for T1-weighted images in the EADC-ADNI HarP were interpreted for the 1 mm isotropic mean DWIs utilized in this thesis and are described below. In the EADC-ADNI HarP, most of the tracing is performed in the coronal plane with reference to the axial and sagittal planes. The images referred to in EADC-ADNI HarP are not aligned to the anterior-posterior hippocampal axis like the diffusion images acquired for this thesis. The anterior-posterior alignment allows for excellent holistic visualization of the hippocampal structure in the axial-oblique plane wherein the entire classic seahorse shape can be visualized by choosing a slice in the middle (inferior-superior) of the structure that shows a long axial-posterior slice through the hippocampus (e.g., Figure 1.5a, slices 11/12; 1.5b, slices 11/12; 1.5c, slices 8/9). Traditional hippocampal segmentation is performed mainly in the coronal plane with reference to axial and sagittal planes, whereas the segmentation procedure in this thesis relied on axial-oblique slices with reference to coronal and

sagittal planes. The key advantage of the axial-oblique anterior-posterior hippocampal axis aligned images is that the entire hippocampus can be visualized across less than 20 1 mm axial-oblique slices, typically ~10 slices (e.g., Figure 1.5a, 5-year-old male, 12 slices; 1.5b, 28-year-old female, 10 slices; 1.5c, 90-year-old male, 9 slices). Visualization of the hippocampal structure along its anterior-posterior axis allows for greater reliance on overall morphology (as guided by Duvernoy et al., 2013) because the entire structure and its boundaries are easily observed in the known seahorse (genus Hippocampus) shape across only ~10 axial-oblique slices instead of ~50 coronal slices at 1 mm isotropic. This holistic axial-oblique view represents a unique and major advantage for manual hippocampal segmentation.

On the mean DWIs used for segmentation in this thesis, the tracing procedure began by identifying the axial-oblique slice that showed the largest section of the hippocampi along the anterior-posterior axis, approximately in superior-inferior middle of the structure, parallel with the anterior-posterior axis of the hippocampus (e.g., Figure 1.5a, slices 11/12; 1.5b, slices 11/12; 1.5c, slices 8/9). The most anterior hippocampal tissue detected is typically the alveus over the hippocampal GM. The alveus is a thin WM layer which lays upon the hippocampal head GM and appears as a bright line along the anterior boundary of the hippocampal head from the axial-oblique plane, sometimes with a CSF inlet separating the amygdala and the hippocampal head in the axial-oblique plane (e.g., Figure 1.5a, slice 13/14; 1.5b, slice 12; 1.5c, slice 11). The lateral boundary at the most anterior slices at the level of the hippocampal head sometimes includes the amygdala, otherwise it is composed of the dark CSF of the lateral ventricles against the bright WM of the alveus/fimbria forming the lateral border of the hippocampus and is easily observable from the anterior at the hippocampal head all the way to the posterior end at the hippocampal tail (e.g., Figure 1.5a, slices 9/10; 1.5d-i-ii; 1.5b, slices 8/9; 1.5e-i-ii; 1.5c, slices 9/10; 1.5f-i-ii). The most

posterior portion of the hippocampus at the level of the tail is where bright border turns medially at the trigone of the lateral ventricle (e.g., Figure 1.5a, slices 9/10; Figure 1.5b, slices 8; Figure 1.5c, slices 9). The medial boundary consists of CSF at the level of the head, and the subiculum or CSF at the level of the body and tail (Figure 1.5a, slice 10; 1.5d-i-ii; 1.5b, slice 11; 1.5e-i-ii; 1.5c, slice 7; 1.5f-i-ii). For exclusion of the subiculum, morphology (e.g., Figure 1.5d-i-ii; 1.5e-i-ii; 1.5f-i-ii) is shown to be more reliable than arbitrary landmarks (i.e., higher intra- and inter-rater reliability; Boccardi, Bocchetta, Ganzola, et al., 2015). The mean DWIs allow for visualization of morphological differences of the subiculum from the hippocampus (e.g., Figure 1.5a, slices 10; 1.5d-i-ii; 1.5b, slices 10; 1.5e-i-ii; 1.5c, slices 7; 1.5f-i-ii). The axial-oblique plane can be used to identify the subiculum medial hippocampus proper and lateral to CSF (e.g., Figure 1.5a, slices 10; 1.5d-i-ii; 1.5b, slices 10; 1.5e-i-ii; 1.5c, slices 7; 1.5f-i-ii). The coronal plane can be used to confirm subiculum location as it extends medially beyond the 2 U-shaped interlocking laminae (CA and DG) of the hippocampus (e.g., Figure 1.5e-i-ii; 1.5f-i-ii). The superior boundary at the level of the head is at the amygdala (e.g., Figure 1.5d-i) and at the body/tail the superior boundary is at CSF (e.g., Figure 1.5e-i-ii; 1.5f-i-ii) until the fimbria separates to the fornix at the tail (e.g., Figure 1.5f-i-ii). The inferior boundary consists of the WM of the parahippocampal gyrus from head to tail (e.g., Figure1.5d-i-ii).

To separate the hippocampus into the head, body, and tail, two landmarks are used, one for each the head/body border and the body/tail border. The posterior border of the head (after which the body starts) is marked by the most posterior end of the uncal apex on the axial-oblique slice (e.g., Figure 1.5a, slice 11; 1.5b, slices 10; 1.5c, slice 8; Figure 1.6) at the last slice where the hippocampus appears as a folded/double layer structure in the coronal plane (e.g., Figure 1.5d-i-ii, double fold, versus 1.5e-i-ii, single fold; Figure 1.6). The posterior border of the body is marked

by the posterior end of the inferior colliculi on the axial-oblique slice (e.g., Figure 1.5a, slice 11; 1.5b, slice 10; 1.5c, slice 8; Figure 1.6) after which the rest of the hippocampal tissue is tail.

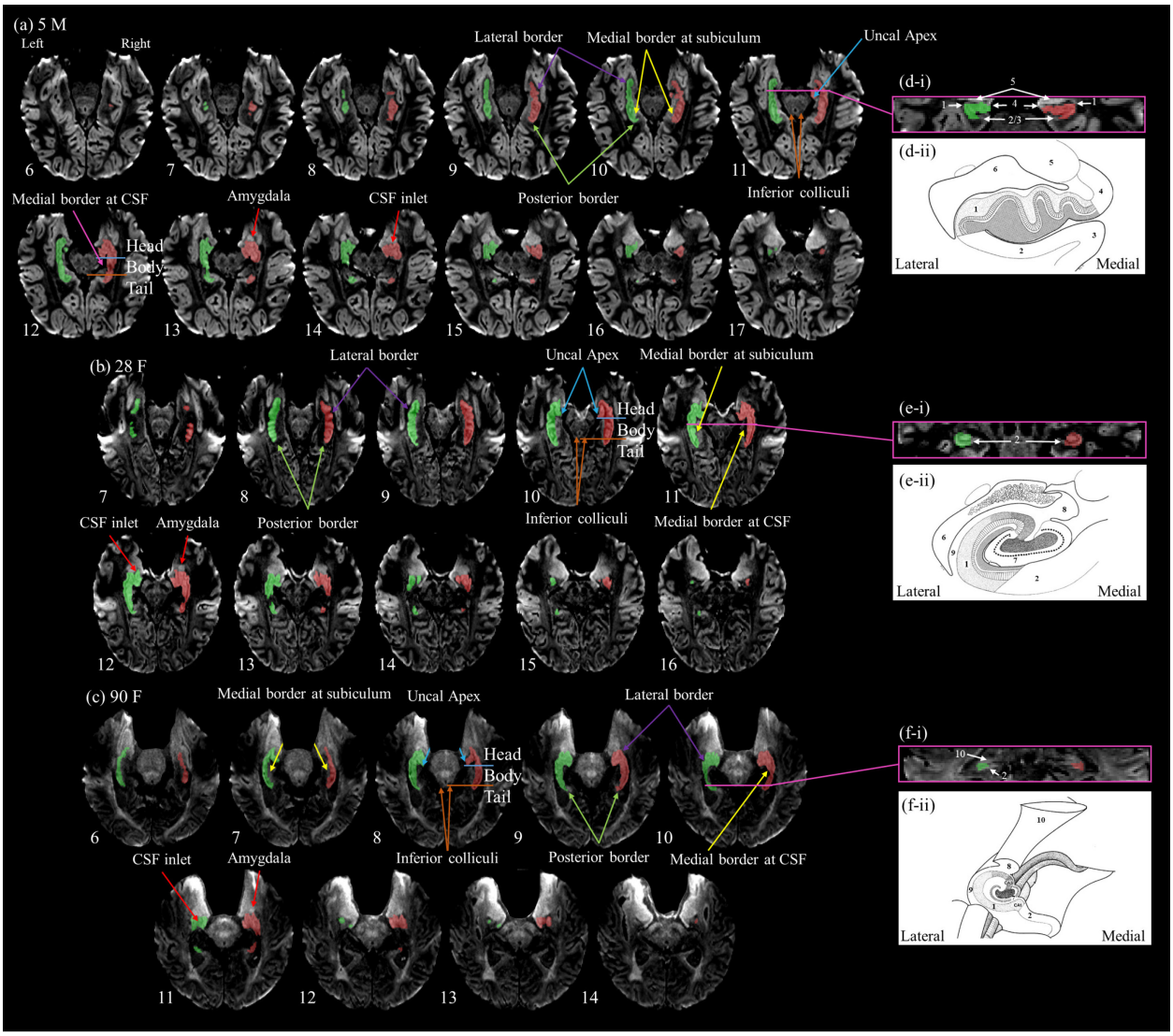

Figure 1.5: Manual hippocampal segmentation on mean DWIs. All axial-oblique slices covering the hippocampus (green, left; red, right) for two healthy volunteers, (a) 5 year old male and (b) 28 year old female, from the single-shell data (mean diffusion weighted image, DWI, based on 100 DWIs; 10 averages of 10 directions at b = 500 s/mm^2) and one healthy volunteer, (c) 90 year old male, from the multi-shell data (mean DWI based on 64 DWIs; 64 directions at b = 500 s/mm^2). Slice number increases from inferior to superior. (d) Hippocampal head, coronal slice, (d-i) from the year-old male and (d-ii) as illustrated, with (1) cornu ammonis, (2) subiculum, (3) parahippocampal gyrus, (4) subiculum in the dentate gyrus, (5) amygdala, and (6) lateral ventricle. Note medial borders at 2, 3 and 4. (e) Hippocampal body, coronal slice, (e-i) from the 28 year-old female and (e-ii) as illustrated with (1) cornu ammonis, (2) subiculum, (6) lateral ventricle, (7) dentate gyrus, (8) fimbria, (9) alveus. Note the medial borders at 2. (f) Hippocampal tail, coronal slice, (f-i) from the 90 year-old female and (f-ii) as illustrated with (1) cornu ammonis, (2) subiculum, (7) dentate gyrus, (8) fimbria, (9) alveus, (10) crus of the fornix. Note the medial border at 2 and the exclusion of 10. (d-ii, e-ii, f-ii) Reprinted/adapted by permission from Springer Nature Customer Service Centre: The human hippocampus by Henri Duvernoy, Françoise Cattin, Pierre-Yves Risold 2013.

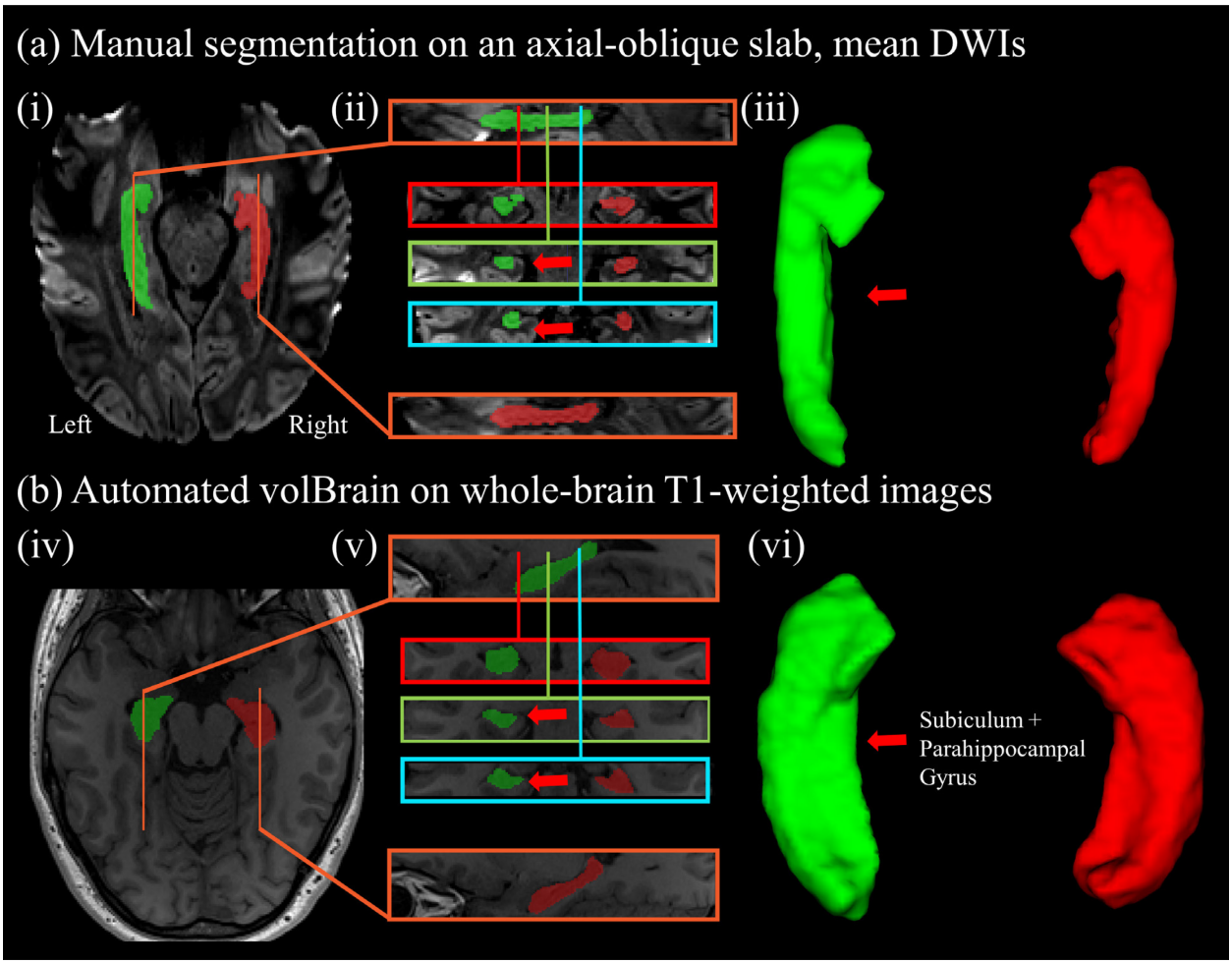

Figure 1.6: Manual hippocampal subregion segmentation and 3D reconstruction. (a) Axial-oblique slice at the longest anterior-posterior axis of the hippocampus (segmentation overlay: head, red; body, green; tail, blue). (b) Sagittal view. (c) Head, body, and tail coronal view. (d) 3D hippocampal segmentation as viewed from the superior surface. (e) 3D hippocampal segmentation as slightly rotated counter-clockwise to feature the lateral surface of the left hippocampus and the medial surface of the right hippocampus. Data is from a healthy 24 year old female.

1.4. A Brief Discussion of Manual versus Automated Hippocampus Segmentation

To characterize WM and cortical and subcortical GM volumes from conventional MRI data, automatic segmentation and volume analysis tools are useful, especially for large datasets. Two of the most ubiquitous software packages that perform automated segmentation include FreeSurfer (Fischl et al., 2002, 2004) and more recently, volBrain (Manjón & Coupé, 2016). These approaches most often rely on conventional T1-weighted MRI data, but T2-weighted data may be used as well. FreeSurfer must be downloaded and installed on the user's workstation, and its segmentation protocol relies on image intensity and a single probabilistic atlas that is used to assign a label to each voxel, and it identifies the hippocampi by utilizing known spatial patterns of subcortical structures relative to one another (Fischl et al., 2004). The single atlas-based, voxel assignment per region, method of FreeSurfer is limited by a failure to account for inter-person variability; the volBrain method is web-based (https://volbrain.upv.es/) whereby the user must simply upload their MRI data, and it aims to overcome inter-person differences in brain structure by segmentation in a multi-atlas, patch-based label fusion approach (Akudjedu et al., 2018; Manjón & Coupé, 2016). The volBrain approach identifies the hippocampus as per the European Alzheimer's Disease Consortium (EADC) and Alzheimer's Disease Neuroimaging Initiative (ADNI) Harmonized Protocol (HarP) (Boccardi, Bocchetta, Apostolova, et al., 2015; Frisoni et al., 2015; Manjón & Coupé, 2016). Overall, the volBrain pipeline is faster and more efficient than FreeSurfer (Manjón & Coupé, 2016).

Automated segmentation on T1-weighted images is shown to overestimate hippocampal volumes considerably, for example, in a sample of 104 healthy individuals aged 16-60 years, the average bilateral (left + right averaged) hippocampus volume was ~4400 mm^3 with FreeSurfer and ~4000 mm^3 with volBrain versus ~2500 mm^3 with manual tracing (Akudjedu et al., 2018). The

authors mention that their manual segmentations excluded alveus and fimbria WM but included "a portion of the subiculum" and they note the importance of the hippocampus/subiculum border which highly influences final volume. The automated approaches include the alveus, fimbria and subiculum, and the authors show that the alveus and fimbria may account for ~15-30% overestimation and the subiculum when included in the hippocampus volume accounts for ~15% of the total, but overall automated volumes are ~60-75% higher relative to manual (Akudjedu et al., 2018). The additional ~1500-1900 mm^3 of hippocampal volume identified by automated T1 segmentation relative to manual T1 segmentation suggests that automated approaches are tracing non-hippocampal tissue, likely including tissue beyond the subiculum such as the parahippocampal gyrus (medial and inferior to the subiculum) (Figure 1.5a-ii, 3) or the fimbria after it separates from the hippocampus as the crus of the fornix (Figure 1.5c-ii, 13'). For an example from the data used in this thesis, the mean DWI and T1-weighted image, along with the corresponding volBrain automated (T1) and manual (mean DWI) hippocampus segmentations are shown and both segmentations are shown (a) overlaid on both the mean DWI and T1-weighted image to allow for comparison slice-by-slice in the main manual tracing plane, axial-oblique (Figure 1.7; healthy 47 year old male) and (b) overlaid on their respective images in a single axial-oblique (mean DWI) and axial (T1-weighted) slice along with sagittal views, coronal views along the head, body, and tail, and 3D renderings (Figure 1.8; healthy 24 year-old female). For the 47 year old male, the left + right average hippocampus volume as estimated by automated segmentation on the T1-weighted image was 5375 mm^3, substantially larger than as estimated by manual tracing on the mean DWI at 3225 mm^3 (67% overestimation) (Figure 1.7), likewise for the 24 year old female (Figure 1.8; automated, 3907 mm^3; manual, 2539 mm^3; 65% overestimation). The additional volume is seen in the inferior aspect of the automated segmentation relative to the

manual (e.g., Figure 1.7, slices 4-6; Figure 1.8; likely subiculum with some parahippocampal gyrus), in the medial aspect in the middle slices (e.g., Figure 1.7, slices 8-14; Figure 1.8; likely subiculum with some parahippocampal gyrus), and in the superior-medial aspect of the most superior slices (e.g., Figure 1.7, slices 12-19; Figure 1.8; likely including segments of the fimbria that belong to the crus of the fornix after separating from the hippocampus). Chapter 5 of this thesis also provides a comparison of automated and manual techniques in the context of prenatal alcohol exposure (PAE) wherein hippocampal atrophy is one of the most commonly reported GM volume reductions (Donald et al., 2015).

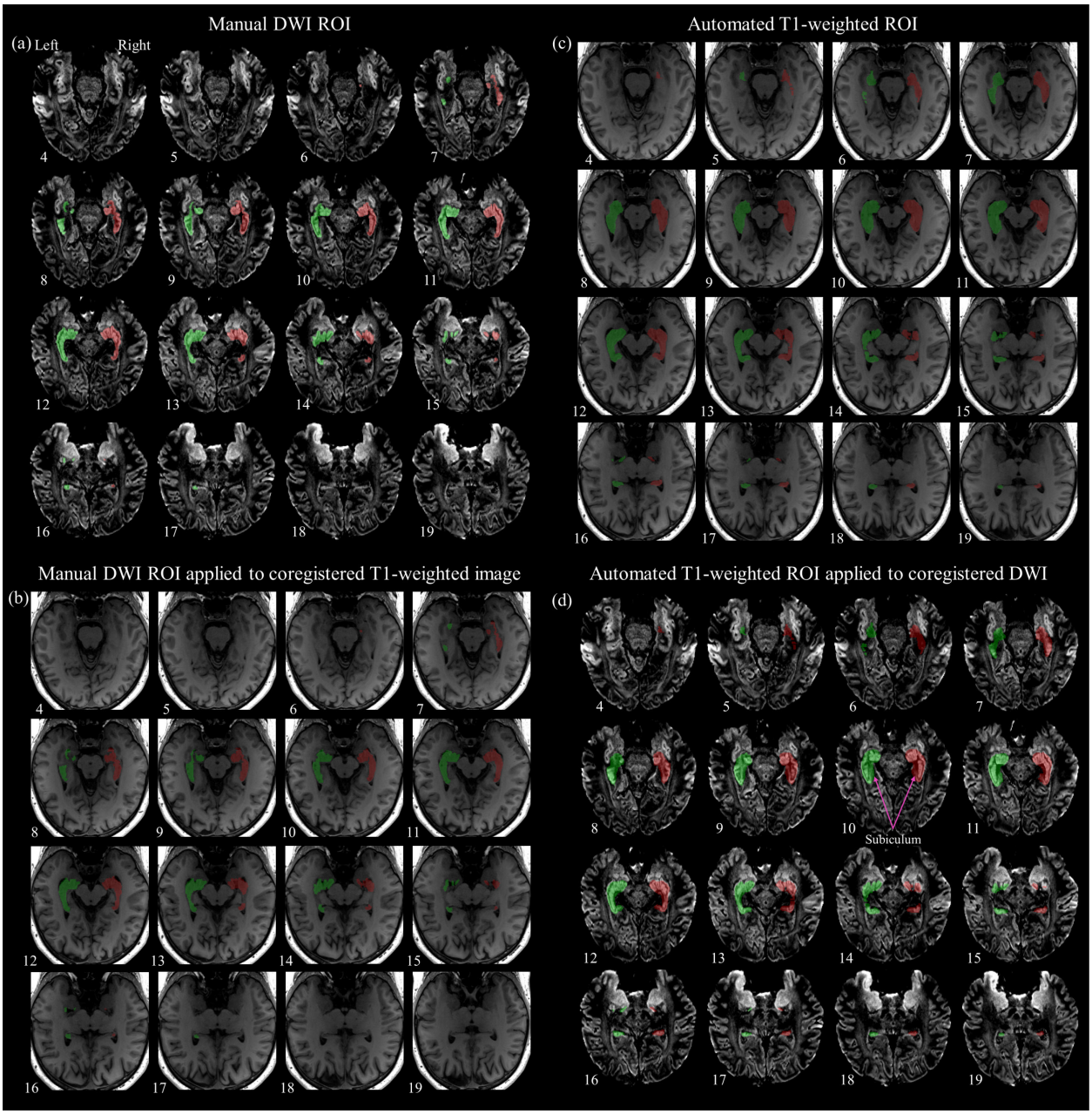

Figure 1.7: Manual hippocampal segmentation on mean DWI versus automated on T1. All axial-oblique slices covering the hippocampus for one healthy 47-year-old male. (a) Mean diffusion-weighted image (DWI) from single-shell diffusion data (100 DWIs; 10 averages, 10 directions at b500) with the bilateral hippocampal regions-of-interest (ROI) (green, left; red, right) as manually traced on the mean DWI. (b) Coregistered T1-weighted (T1w) image with the manual (DWI) ROI. (c) T1-weighted image with the automatic (T1w; volBrain) ROI. (d) T1w image with the manual (DWI) ROI. Slice number increases from inferior to superior. The additional superior, inferior, and medial tissue included in the (c, d) automatic ROIs relative to the (a, b) manual ROIs is most likely subiculum and parahippocampal tissue.

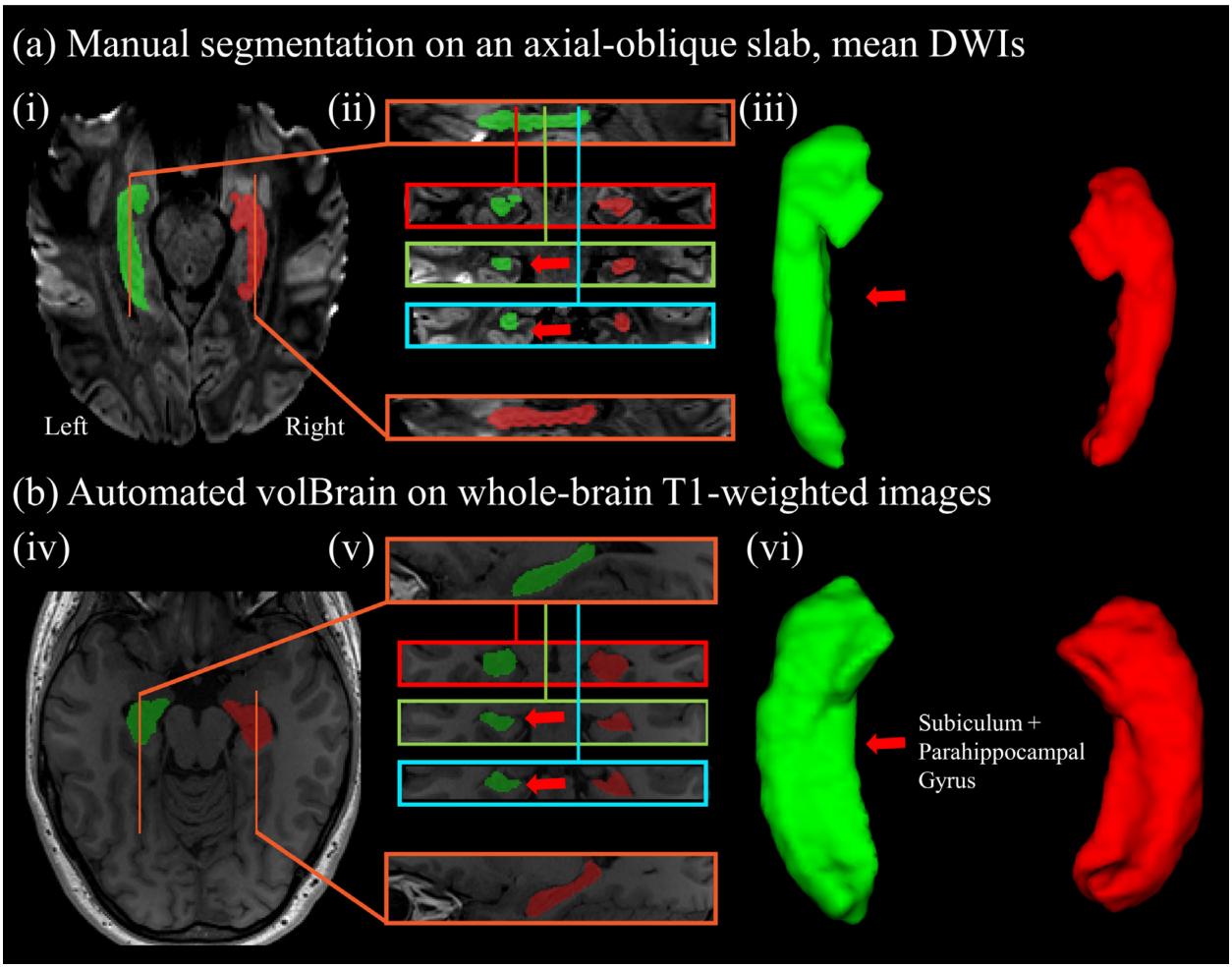

Figure 1.8: Manual hippocampal segmentation on mean DWI versus automated on T1. (a) Manual segmentation as performed on mean diffusion-weighted b500 images as acquired in a slab of 20 1 mm slices aligned to the long-axis of the hippocampus. (b) Automated segmentation as performed by volBrain on whole-brain T1-weighted images. Both images are from a healthy 24-year-old female. (a,i) Mean diffusion-weighted image (DWI), axial-oblique slice at the longest axis of the hippocampus (segmentation overlay: left, green; right; red). (b,iv) T1-weighted image, axial view, taken at the anterior hippocampus. (a,ii; b,v) Sample sagittal (orange rectangles) view and coronal views (head, red rectangle; body, green rectangle; tail, blue rectangle) of the two segmentation approaches. Note the red arrows which point to subiculum tissue that is excluded in the (a,ii) manual segmentation but included (b,v). The exclusion of non-hippocampal tissue by the (a) manual diffusion method relative to the (b) automated T1-weighted method is evident in the 3D renderings that show the extra volume in the automated segmentation (b, vi) relative to the manual segmentation (a,iii; see red arrows).

2. Magnetic Resonance Imaging

2.1. MRI, from Hydrogen Atoms to Brain Images

MRI relies on 5 essential elements to generate brain images. First, MRI is a non-invasive imaging approach that generally utilizes the magnetization properties of the nuclei of the hydrogen atom, ^{1}H, within water molecules which are most abundant in the human body. The nucleus contains a single proton. Thus, the hydrogen nucleus has a magnetic moment that is proportional to its spin angular momentum as determined by the magnetogyric ratio for hydrogen, so that the hydrogen act like a magnetic dipole. Second, MRI requires that the sample (e.g., human body) be placed in a powerful (e.g., an MRI is typically 1.5T+, whereas Earth's magnetic field is only $0.5E^{-4}$ T), uniform magnetic field (B_0). The application of this strong, static, homogenous, temporally stable external magnetic field exerts torque on the hydrogen protons and causes precession at the Larmor frequency (ω_0) which is determined by the magnetogyric ratio (γ) of a given nuclear species and varies with the strength of the magnetic field ($\omega_0 = \gamma B_0$). This magnetic field will polarize the sample to create longitudinal magnetization by causing protons to align (while undergoing precession) parallel or anti-parallel to the main magnetic field (the majority align parallel because it is a lower energy position relative to anti-parallel). Third, to make the net magnetization of the sample observable, it must be excited from its longitudinal position parallel with the main magnetic field, into the transverse plane so that the net magnetization rotates there by using a radio frequency (RF) coil which generates an RF pulse. This rotating transverse magnetization is how we measure the MR signal; it induces an electric current in a receiving RF coil as a signal called the Free Induction Decay (FID). Fourth, the measurable magnetization needs to be localized in 3D space which is accomplished by using 3 complementary sets of gradient coils to generate linearly varying magnetic fields that add/subtract to the net static magnetic field along

the x, y, and z axes (slice selection, frequency, and phase encoding), spatially localizing the signal from the hydrogen nuclear spins. Finally, the computer console is responsible for controlling all the acquisition pulse sequences and protocol parameters, then initial processing and storage of data directly from the scanner.

Longitudinal, T1 or spin-lattice relaxation describes the recovery of longitudinal magnetization as protons re-emit energy to their surrounding environment towards equilibrium. Transverse, T2 or spin-spin relaxation describes the loss of rotating transverse magnetization as proton spins lose phase coherence due to the magnetic fields generated by their neighboring spins and due to magnetic field inhomogeneities. The FID signal reduces as the transverse magnetization decays according to T2. T1 and T2 times vary by brain tissue in health and can be altered in pathological tissue. CSF is free water, and it has the longest T1 and T2 times in the brain (i.e., it appears dark on T1-weighted images and bright on T2-weighted images; Figure 2.1). GM is largely comprised of neuronal soma, unmyelinated axons, and dendrites, and it has the second longest T1 and T2 times. WM consists of tightly packed, myelinated neurons, and because myelin is lipid based and hydrophobic, there is little free water, and T1 and T2 times are shortest relative to GM and CSF. We take advantage of these relaxation property differences which form the basis for tissue contrast in MRI.

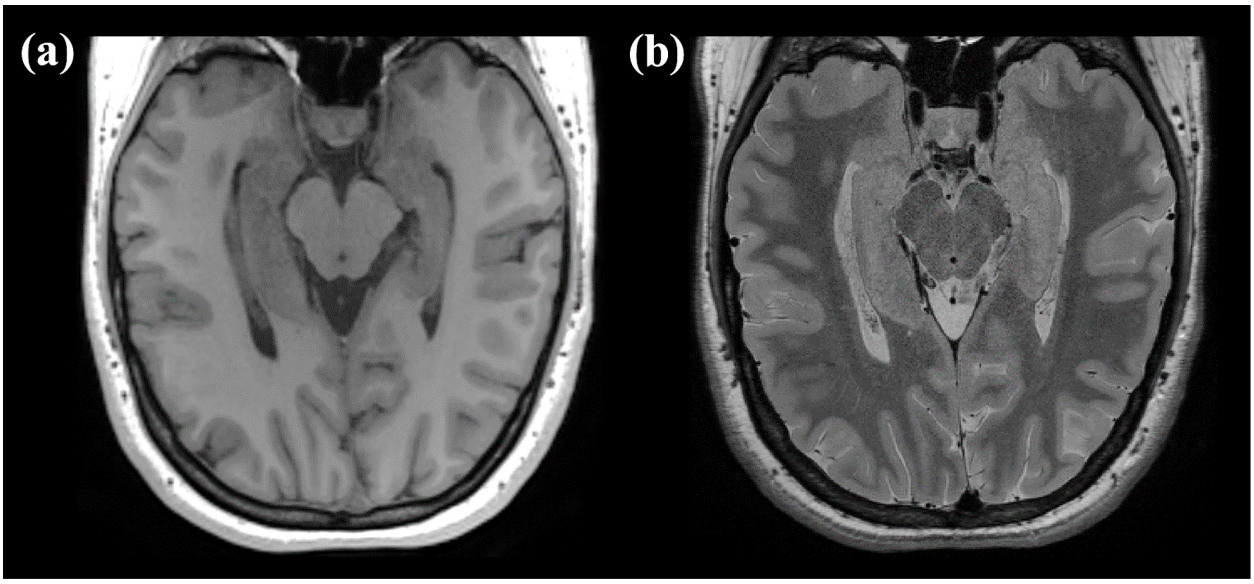

Figure 2.1: T1 and T2-weighted structural magnetic resonance images. Examples of (a) T1 and (b) T2-weighted images, axial-oblique orientation parallel to the anterior-posterior axis of the hippocampus. Data is from a healthy 24-year-old female.

2.2. Diffusion Imaging

A complementary imaging method to anatomical imaging for macrostructural characteristics including volume and shape changes is diffusion weighted imaging (DWI) which generates parameters indicative of tissue microstructure (e.g., axonal packing, myelination). This dissertation is focused on DWI in application to the healthy lifespan and development in prenatal alcohol exposure.

2.2.1. Background and Acquisition

Water molecules are in constant, random motion (called Brownian motion, as first described by Robert Brown in 1828) due to the presence of thermal energy. In 1905, Einstein described the free diffusion of water in a homogeneous medium with no boundaries, wherein water molecules will move a unidimensional distance ⟨r⟩ that is dependent on diffusion time (t) and the diffusion coefficient (D) of the medium (Einstein, 1905).

Equation 2.1 $$\langle r^2 \rangle = 2Dt$$

The microscopic structure of the brain is not homogeneous but heterogeneous with numerous barriers (e.g., cell membranes, macromolecules) and distinct compartments (i.e., intra or extracellular spaces) with which water molecules interact as they diffuse. These barriers and compartments differ between typical brain tissues (e.g., GM, WM, CSF) and are altered by various pathologies (e.g., acute stroke, tumor). Effectively, water molecules probe brain tissue structure at a micrometer scale (microstructure) on their diffusion-driven movements - a higher scale resolution than typical MRI in the millimeter scale. Dependent on the medium, diffusion can be more or less isotropic (Soares et al., 2013). Isotropic diffusion is defined as equal diffusion/displacement in all directions, whereas anisotropic diffusion varies with direction (Figure 2.2). Brain tissues show varying degrees of anisotropy (Soares et al., 2013). WM fiber tracts comprise the most anisotropic brain tissue due to the tight parallel organization of axons and their membranes which allow water molecules to diffuse fairly unrestricted in the parallel direction of the long axis of given WM tract (Beaulieu, 2002). On the other hand, CSF is the most isotropic brain tissue due to the fact that it is fluid in which water molecules diffuse unhindered in all directions equally (Soares et al., 2013) (Figure 2.2). Additionally, pathological tissue shows diffusion differences relative to healthy tissue, for instance, areas of stroke hinder diffusion. Therefore, by measuring the diffusion of water molecules in the brain, inferences can be made about the tissue in which water diffusion was measured (Figure 2.2).

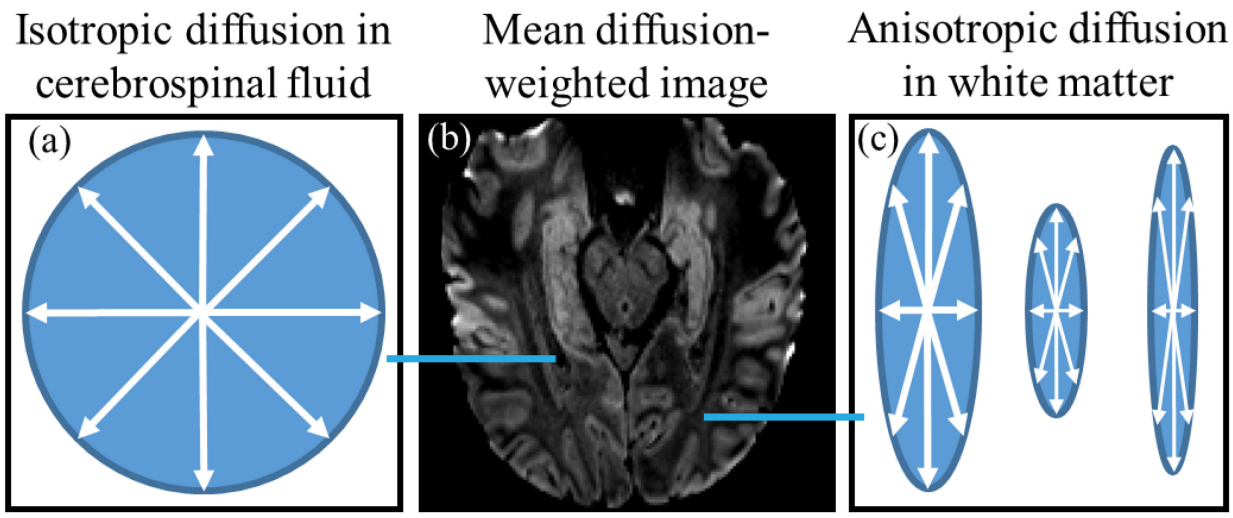

Figure 2.2: Isotropic and anisotropic diffusion in the human brain. (a) Isotropic diffusion as would be observed in the cerebrospinal fluid (CSF) of the human brain. (b) Mean diffusion-weighted image. (c) Anisotropic diffusion as would be observed within and between the axonal fiber bundles that comprise white matter (WM) tracts. Reference mean diffusion-weighted image is from a healthy 24-year-old female.

MRI can be used to measure the diffusion of water molecules in the brain by applying a pair of bipolar magnetic gradient pulses that add/subtract field strength to/from the main magnetic field so that the effective magnetic field (and the frequency of precession) which a given spin experiences will vary based on position (Figure 2.3). First, the sample is excited by using an RF pulse (typically 90°) so that all spins precess in-phase at the same frequency (Figure 2.3i). Next, the application of the first diffusion gradient pulse will add/subtract to/from the main magnetic field so that the effective magnetic field a given proton experiences and its corresponding frequency of precession will vary as a function of position (Figure 2.3ii). Following the first diffusion gradient pulse, the spins will begin to precess out of phase based on their location, which leads to an overall decrease in MRI signal (Figure 2.3iii). After a brief diffusion time (e.g., ~50 ms), the complementary rephasing diffusion gradient pulse is applied with equal strength/duration and opposite polarity than the first (Figure 2.3iv). As a result, for spins that did not diffuse during the diffusion time in between gradients, their phase difference due to the first diffusion gradient

pulse will be completely reversed and the MRI signal will increase back to where it was prior to the first diffusion gradient pulse due to being in the same location during the second diffusion gradient relative to the first (ignoring T2 relaxation) (Figure 2.3v). For spins that did diffuse during the diffusion time in between gradients, their phase difference will not be completely reversed because they will experience a different effective magnetic field due to being in a different location during the second diffusion gradient relative to the first, and their MRI signal will be lower (such as in CSF where spins are free to diffuse, Figure 2.3b) relative to spins that did not diffuse and hence undergo more rephasing with the second gradient to recover a higher MRI signal (such as in a stroke area of hindered diffusion where spins are not free to diffuse, Figure 2.3a). With the diffusion gradients turned on, diffusion-weighted source images are produced. Diffusion gradients are sensitized to diffusion in the direction in which they are applied, and the implications are discussed below.

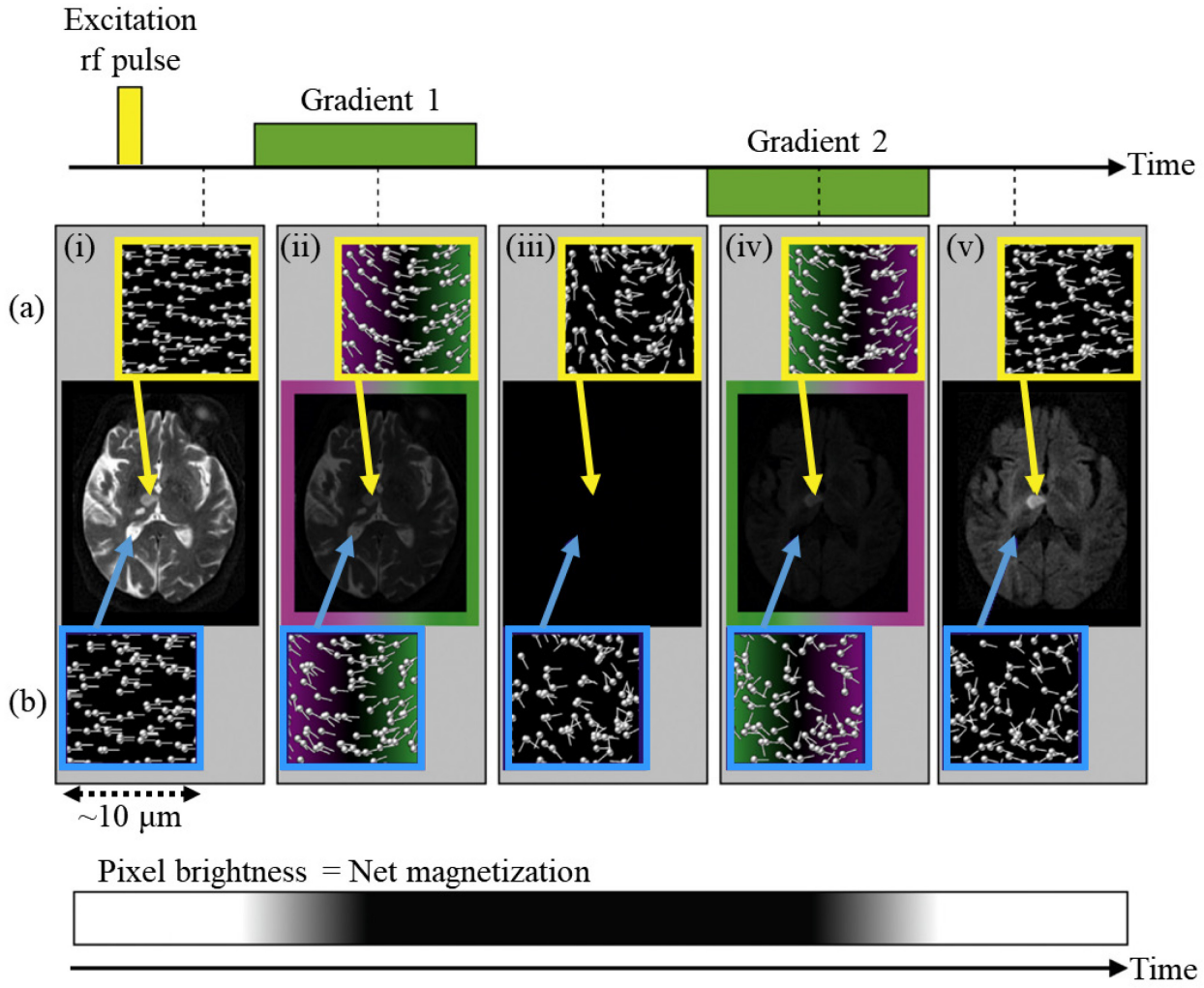

Figure 2.3: Diffusion sensitive bipolar magnetic field gradients. Spins in (a) cerebrospinal fluid (CSF) and (b) an area of stroke. (i) Spins precessing in-phase after the RF excitation pulse but before the first dephasing diffusion gradient. Pixel brightness is high because the net magnetization is high due to all spins precessing in-phase. (ii) Spins during the first dephasing gradient application begin to dephase as a function of their location (note that spin position varies along the small sample voxel here from left to right, pink to green). (iii) Spins after the first gradient have lost phase coherence and pixel brightness is down. (iv) Spins during the second (rephasing) gradient application begin to rephrase and magnetization recovery is (a) almost complete in the area of stroke because stroke restricts diffusion, but (b) incomplete due to diffusion of water in the relatively unrestricted CSF space. Consequently, at time (v) after the refocusing pulse, the (a) area of stroke appears bright because it has a higher net magnetization than (b) CSF which appears dark because it has a lower net magnetization. Reprinted/adapted by permission from Elsevier and Copyright Clearance Center: Diffusion MRI by Jim Pipe 2014.

An advantage of DWI is that the diffusion of hydrogen spins within the water molecules of the brain can be imaged using conventional MRI hardware and does not require contrast agents.

Current DWI sequences all rely on the tenets developed by Edward Stejskal and John Tanner for the pulsed gradient spin echo (PGSE) acquisition (Stejskal & Tanner, 1965) (Figure 2.4).

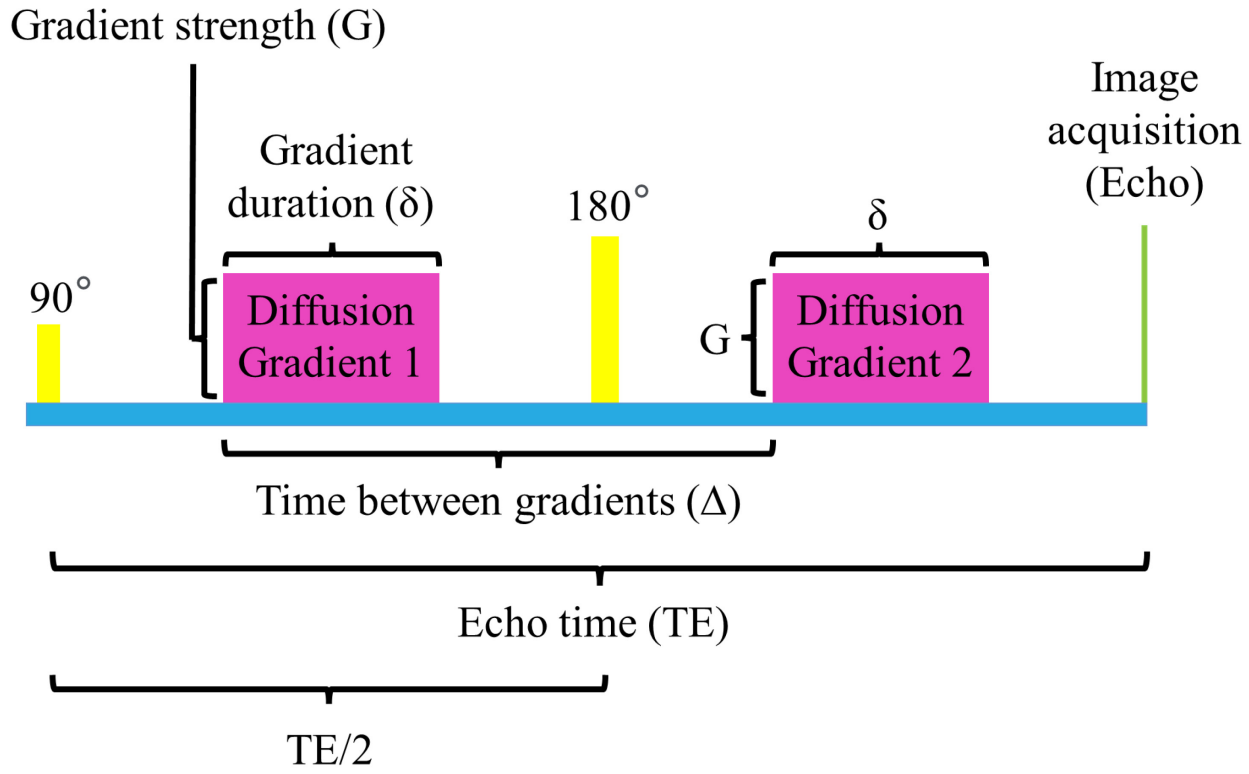

Figure 2.4: Stejskal and Tanner Pulsed Gradient Spin Echo (PGSE) technique. The pulse gradient spin echo (PGSE) technique includes a pair of diffusion sensitive gradients with gradient strength (G) and gradient duration (δ). The time between gradients (Δ) is the diffusion time. The image acquisition (echo) occurs at the echo time (TE).

The PGSE applies a pair of diffusion sensitive gradients with the same gradient strength (G) and gradient duration (δ) with a 180° refocusing pulse in between to produce a spin-echo (Figure 2.4). The 90° pulse at the beginning knocks the net magnetization of the sample into the transverse plane, then phase accumulation brought onto the nuclei of the sample by application of the first diffusion gradient is reversed by the second diffusion gradient due to the 180° pulse that flips the spins in between the diffusion gradients – applying the same essential dephasing/refocusing as discussed above so that there is signal loss from diffusing (moving) but not static nuclear spins. Essentially, the spin-echo approach is applied to refocus dephasing that

results from static field inhomogeneities and produce signal loss as T2 instead of T2* (Hahn, 1950). T2 signal loss or weighting contributes to the amazing tissue contrast between WM and GM as seen in diffusion data due to the tissue differences in T2 relaxation times (i.e., at 3T, relative T2 relaxation times have been reported as 69 ms in WM and 99 ms in GM in Stanisz et al., 2005).

This signal can be represented by Equation 2.2 in which the MR signal with diffusion gradient application (S) depends on the MRI signal with diffusion-weighting (S_0), and the magnetogyric ratio (γ) for hydrogen, gradient amplitude (G), gradient duration (δ), and the time between diffusion gradients also known as diffusion time (Δ-$\delta/3$) - which together can be represented as b value in Equation 2.2 - and the apparent diffusion coefficient (ADC). The ADC is "apparent" because the natural diffusion coefficient of water is altered by tissue microstructure restrictions.

$$\text{Equation 2.2} \quad S = S_0 e^{-\gamma^2 G^2 \delta^2 \left(\Delta - \frac{\delta}{3}\right) ADC}$$

$$\text{Equation 2.3} \quad S = S_0 e^{-bADC}$$

As equations 2.2 and 2.3 demonstrate, diffusion MRI requires acquisition of a diffusion-weighted signal (S) and a non diffusion-weighted signal (S_0) or multiple diffusion-weighted signals in order to calculate ADC of a given sample, and the degree of diffusion weighting is determined by the b value (diffusion sensitization factor) which can be increased by raising the gradient duration or strength (typical) or the diffusion time (the time between the pair of dephasing/rephasing diffusion gradients). Therefore, two major downsides of higher b values include: (a) signal drop because of greater dephasing due to higher diffusion sensitization (Figure 2.5), and (b) longer echo time (TE; the time from the middle of the RF excitation pulse to the middle of the echo) and repetition time (TR; the time between corresponding RF excitation sequences) with all else equal because

gradients need to be on for longer for the echo and the overall repetition. Due to the differences in diffusion in WM (anisotropic, parallel to axons), GM (less anisotropic than WM, with cell membrane barriers), and CSF (more isotropic than GM as free water with no barriers), the PGSE sequence produces great diffusion-weighted contrast between the three brain tissues (Figure 2.5).

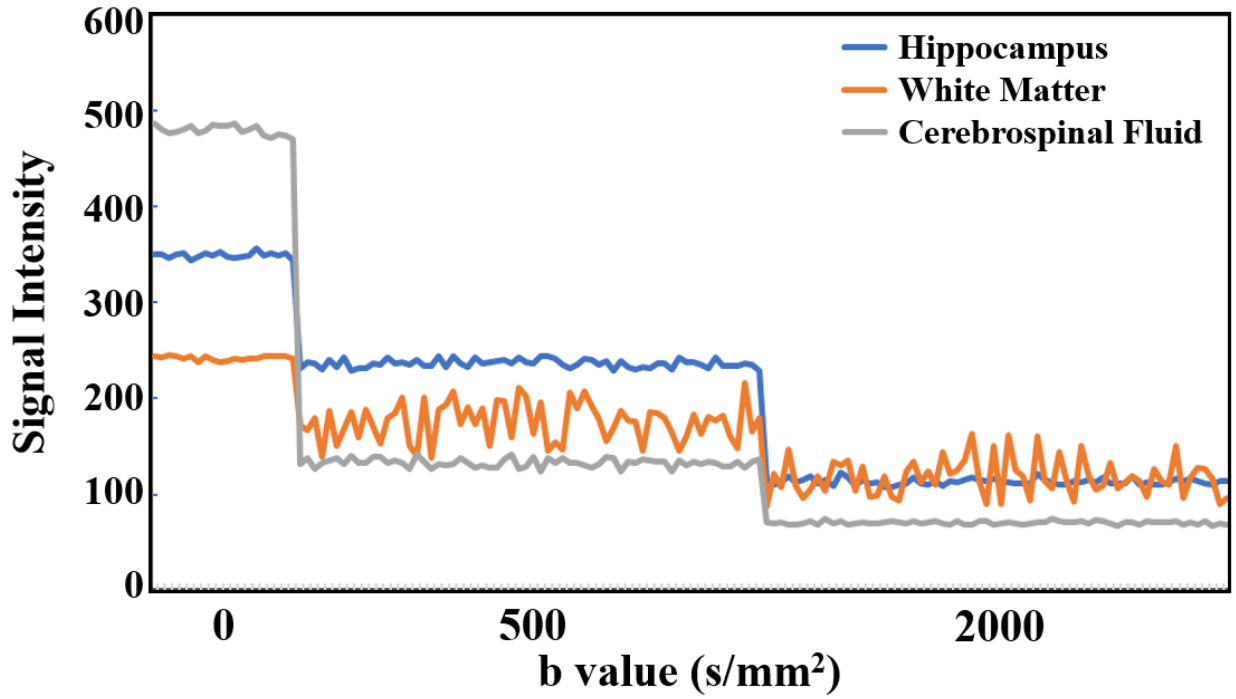

Figure 2.5: Signal Intensity Versus b Value Plot. As measured in the multi-shell diffusion protocol used in Chapter 6 with 20 b0s, 64 b500s, and 64 b2000s. From b0 to b500, signal intensity in the hippocampus drops 32%, in white matter (WM) 28%, and in cerebrospinal fluid (CSF) 72%. From b500 to b2000, signal intensity in the hippocampus drops 52%, in WM 33%, and in CSF 47%. The WM signal (orange line) fluctuates more with the gradient direction than the hippocampus (blue line) because the WM is made up of coherently oriented axon bundles that cause greater signal loss in WM when diffusion gradients are aligned parallel to their axis, whereas the hippocampus does not have such anisotropic, directional tissue, therefore the signal loss due to varying directions is not as great. Data from a healthy 31-year-old female.

Each diffusion gradient is directional in that it is sensitized to diffusion in the direction in which it is applied. In Figure 2.5, the tissue signals fluctuate with the direction of the diffusion gradient, particularly in the WM (Figure 2.5, orange line) which has more signal loss when diffusion images are acquired with gradients aligned along their axis. On the other hand, the signal

from the hippocampus (Figure 2.5, blue line) is flatter than the WM signal across multiple directions because it does not have coherent, anisotropic directionality like WM, for the different diffusion directions to align to. Moreover, the WM signal begins to level off at b2000 relative to b500 (at higher b values) due to restriction. The angular resolution of a diffusion-weighted sequence increases with an increase in the number of gradient directions, and so does the complexity of analyses that are possible. Using equation 2.3, ADC can be calculated from the slope based on the signal (S) from the image with diffusion-weighting and the signal (S_0) from the image without diffusion-weighting. To calculate ADC, a minimum of 3 sets of DWIs must be acquired with diffusion gradients applied respectively in 3 orthogonal directions, typically along the x, y and z axes in order to overcome the signal changes due to the directionality of diffusion (by cancelling them out through averaging of diffusion-weighted images acquired along the three orthogonal directions). As discussed in detail below, standard diffusion tensor imaging requires a minimum of 6 unique directions, and more complex analyses such as HARDI based CSD require at least 45 unique directions (Descoteaux, 2015). Although only a single S_0 reference is needed as provided by the b0 image, acquiring more than one reduces noise in calculations for the analyses in this thesis.

This dissertation involved the use of two high spatial resolution (1 mm isotropic voxels) diffusion MRI protocols acquired as a partial-brain slab of 20 1 mm slices oriented along the long anterior-posterior axis of the hippocampus using a 3D T1-weighted image on the scanner console (Figure 2.6) (Treit et al., 2018). Orienting the slices on both hippocampi can be challenging as the left and right hippocampus do not always align parallel with one another along their anterior-posterior axes, nor are they always in line in the superior-inferior direction. The two protocols are as follows: (a) a single-shell protocol acquired using a single unique b value of 500 s/mm^2 with

images acquired along 10 monopolar directions, 10 times each, for a total of 100 DWIs, along with 10 b0 images, and (b) a multi-shell protocol acquired using two unique b values of 500 s/mm^2 and 2000 s/mm^2 with images for each shell (each unique b value) acquired along 64 monopolar directions for a total of 128 DWIs with 64 DWIs at 500 s/mm^2 and 64 DWIs at 2000 s/mm^2, along with 20 b0 images (Figure 2.5). Both protocols acquired DWIs to b0s at a ratio of 10:1 to increase SNR in the 1 mm isotropic 20 slice slab.

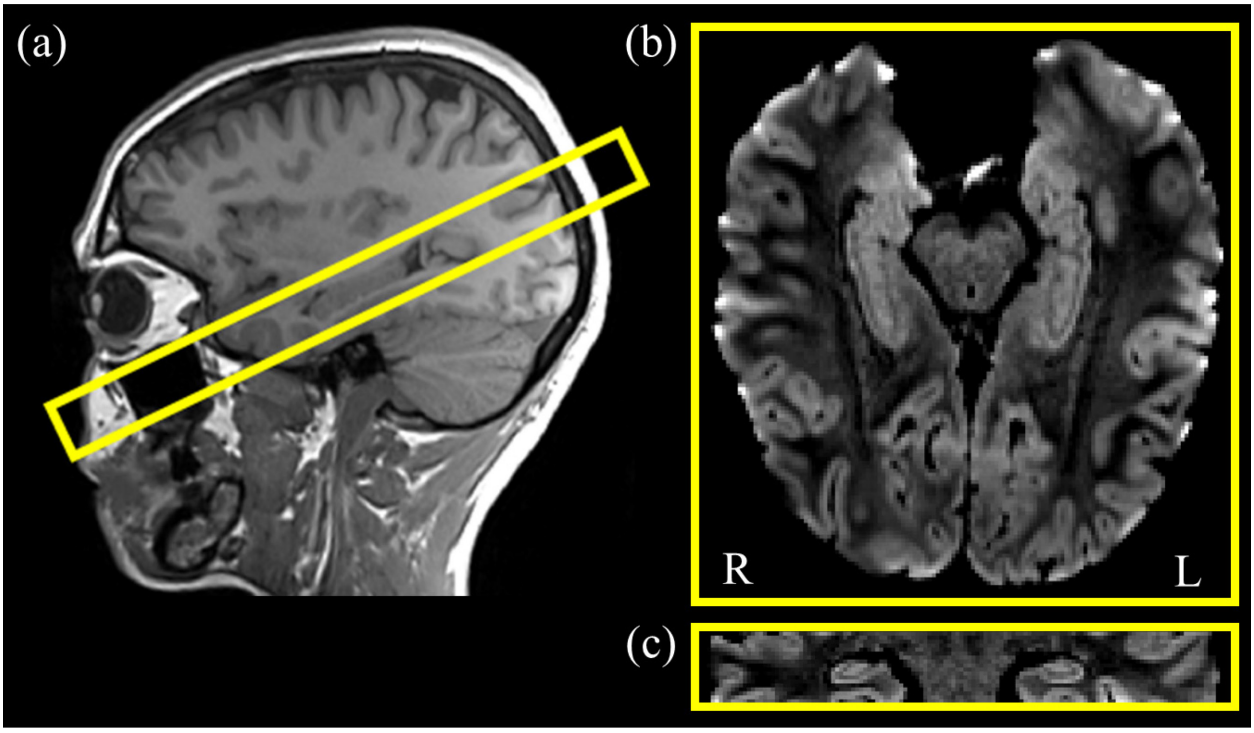

Figure 2.6: Hippocampal diffusion imaging acquisition slab. (a) T1-weighted MPRAGE, 0.85 mm isotropic spatial resolution with yellow axial-oblique slab of 20 1 mm slices aligned to the long, anterior-posterior, axis of the hippocampus. Mean diffusion weighted image (DWI) of 100 (10 averages of 10 directions) b = 500 s/mm^2 in the (b) axial-oblique and (c) coronal planes. Data is from a healthy 10 year-old male.

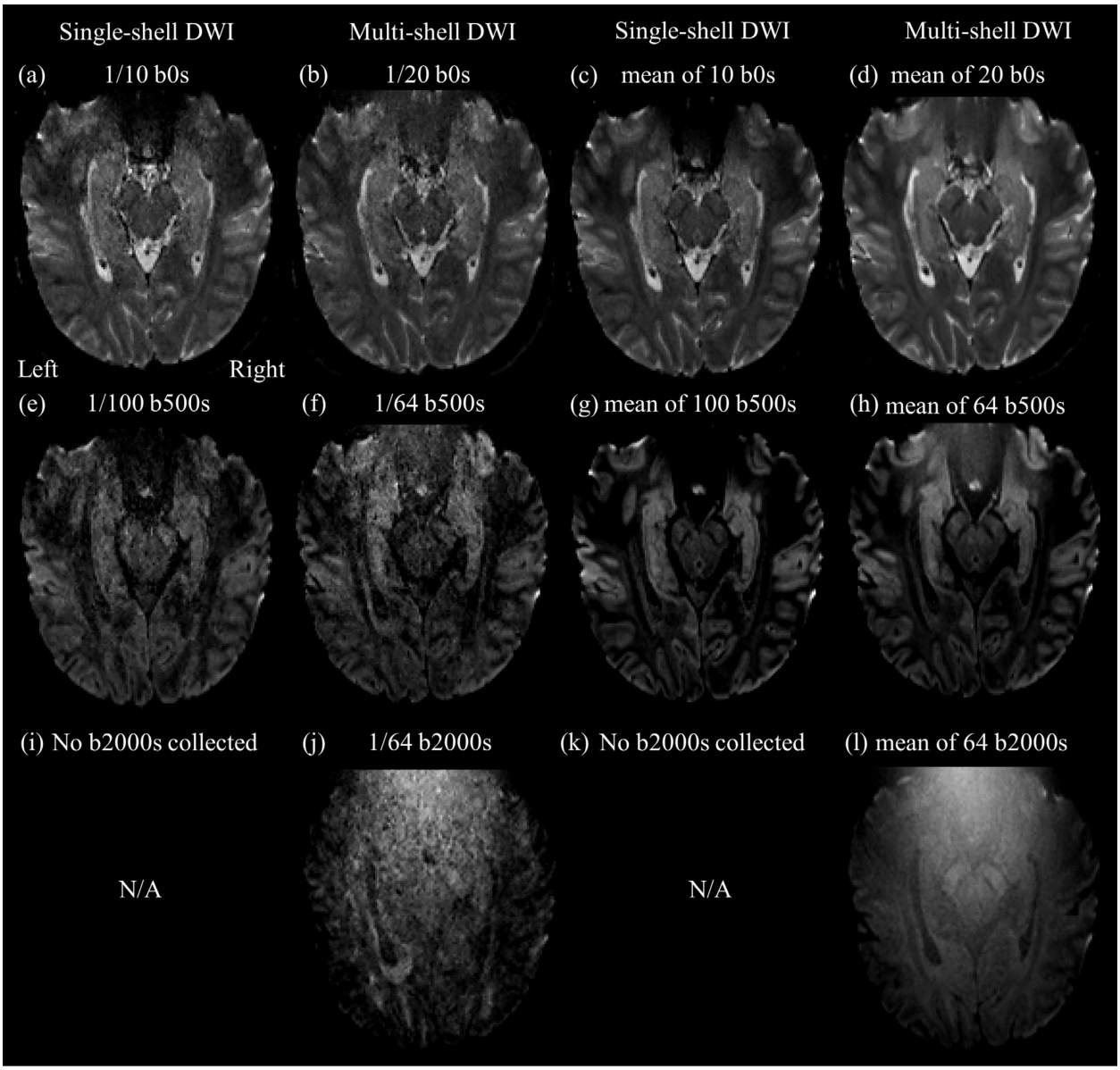

Figure 2.7: Non Diffusion-Weighted and Diffusion-Weighted Images. For the single-shell diffusion protocol used in Chapters 4 and 5, and the multi-shell diffusion protocol used in Chapter 6. (a, b) One b = 0 s/mm^2 (b0) image; (c, d) mean b0 image; (c, f) one b = 500 s/mm^2 (b500) image; (g, h) mean b500 image; (i, k) there was no b = 2000 s/mm^2 (b2000) images collected for the single shell protocol; (j) one b2000 image; (l) mean b2000. For the b500 shell in the single-shell protocol, 100 DWIs were produced by acquiring 10 averages of 10 unique diffusion gradient directions. For the b500 shell in the multi-shell protocol, 64 DWIs were produced by acquiring 64 unique diffusion gradient directions. Note the b value related signal drop in the b2000 relative to the b500. Data is from a healthy 24 year-old female.

The most popular MRI sequence for acquiring DWI data was utilized for both DWI protocols applied for this dissertation. This sequence is the single-shot spin-echo echo-planar imaging (SS-EPI) approach (Figure 2.6). The single-shot aspect of this technique is key for diffusion imaging because it is less sensitive to differences in motion-induced phase of the data and allows for rapid acquisition. Fast imaging is important when acquiring DWI to keep scan-times down in consideration of clinical feasibility, and it is especially important for acquiring data with high spatial resolution, multiple directions, and high b-values (Pipe, 2009), such as in this dissertation. Faster imaging reduces motion which can corrupt phase and information from the phase of spins forms the basis for diffusion-weighted contrast as described above, therefore the single-shot is ideal for diffusion imaging. Each slice can be acquired in well under 1 second, for instance, in the acquisition used for the first two research chapters of this thesis, each slice is acquired in ~145 milliseconds. Moreover, to reduce scan time (by reducing TE) and T2 signal decay in diffusion MRI, SS-EPI uses partial k-space coverage and fills the acquisition space by oscillating back and forth in k_x while moving along k_y (Figure 2.8). Partial Fourier imaging techniques are used to reconstruct data from as little as one-half of k-space, though due to phase errors that all image data sets contain because of issues such as B_0 inhomogeneity, eddy currents, and susceptibility effects, slightly more than 50% of k space, at least 60%, is required for image reconstruction. There are different approaches to partial Fourier imaging, and for the DWI data in this dissertation, phase partial Fourier (PPF) imaging was used in which phase-encoding steps are skipped so that only 6/8 partial k-space was utilized (Feinberg et al., 1986). PPF reduces imaging time but causes blurring with a reduction in SNR (Feinberg et al., 1986). Another time-saving technique that was applied in all DWI sequences of this dissertation is called parallel imaging which drastically reduces acquisition time by shortening the echo train length through the

reduction of the number of phase-encode steps that are acquired in k-space (Blaimer et al., 2004). In partial replacement of information otherwise derived from phase-encoding steps, parallel imaging reduces TE by utilizing spatial information from multiple RF coils. The main distinction for different types of parallel imaging approaches is whether reconstruction of the data takes place in image space (e.g., SENSitivity Encoding, SENSE) or in k-space (e.g., GeneRalized Autocalibrating Partially Parallel Acquisition, GRAPPA) (Blaimer et al., 2004). In the diffusion MRI acquisitions for this dissertation, the GRAPPA method was utilized which estimates missing spatial information from the skipped phase-encoding steps using spatial information estimated from the RF coil arrays to create the missing k-space lines, then generate a complete image (Blaimer et al., 2004). An acceleration rate of 2 (R2) was utilized for the data in this dissertation so that the phase encoding steps were twice as large ($2\Delta K_y$) as steps without the parallel imaging (ΔK_y). Like PPF, parallel imaging will also reduce SNR, therefore one must balance acceleration methods in the interest of maintaining image quality in line with sequence goals.

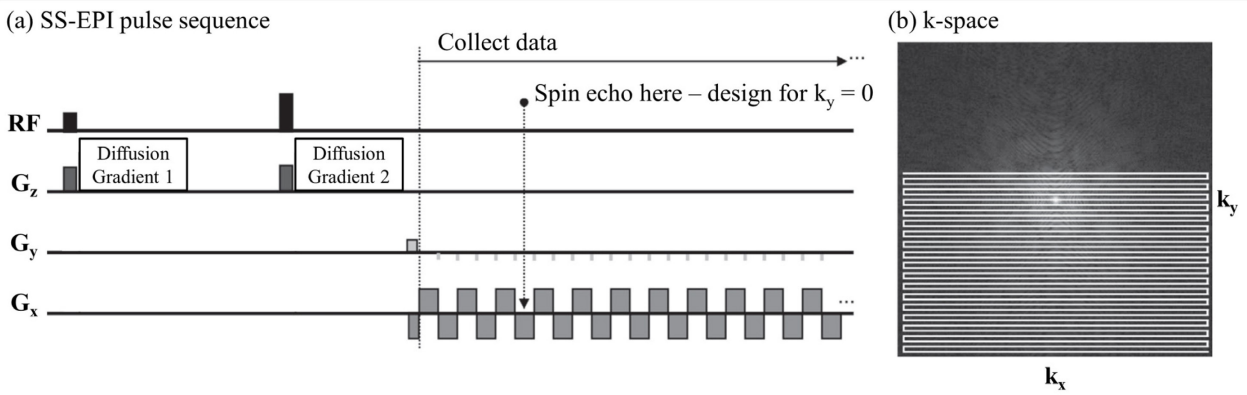

Figure 2.8: Single-shot spin-echo echo-planar imaging (SS-EPI) diffusion magnetic resonance imaging (MRI) pulse sequence. SS-EPI (a) pulse sequence and (b) k-space sampling trajectory. Reprinted/adapted by permission from Elsevier and Copyright Clearance Center: Diffusion MRI by Jim Pipe 2014.

All research chapters in this dissertation utilize 1 mm isotropic DWI data acquired as an axial-oblique slab of 20 1 mm slices that covers the hippocampus. This high spatial resolution is difficult to achieve using the SS-EPI pulse sequence, in part due to the inherent downsides of the sequence, which are discussed below, and acquisition time requirements. To arrive at 1 mm isotropic resolution, first a 1 mm slice must be selected by using a frequency-specific (slice-select gradient) RF pulse to define slice center frequency and range. To cover the 20 mm slab, a 1 mm isotropic sequence requires 20 1 mm slices whereas a 2 mm isotropic sequence would only require 10 2 mm slices. Acquisition of twice the number of slices requires double the EPI readout trains (i.e., double the total scan time). For in-plane resolution, given the same field of view (FOV), the matrix for a 1 mm isotropic acquisition must be twice as large as the matrix required for a 2 mm isotropic acquisition, effectively increasing the TE and TR by increasing the length of the EPI readout train which also increases the potential effects of SS-EPI distortions. In part to achieve the excellent image quality of hippocampal DWI in this dissertation, the use of PPF helped reduce SS-EPI artifacts and overall scan time (Treit et al., 2018, 2022). The single-shell sequence acquired 100 diffusion-weighted volumes (10 unique directions acquired 10 times each at b500) with 10 b0s and the multi-shell sequence acquired 128 total diffusion-weighted volumes (64 unique directions at b500 and at b2000) with 20 b0s. The multiple volumes/directions and high b values are costly on imaging parameters (i.e., longer TE and TR), so SS-EPI with PPF is particularly important to keep scan-times clinically feasible.

2.2.2. The Diffusion Tensor Imaging Model

The ADC as a single variable is too simple to describe the complex microstructure of the human brain which is made up of tissues of varying anisotropy with WM being the most anisotropic. The most common quantitative analysis of DWI data is based on the diffusion tensor

model which utilizes a [3 x 3] array of numbers called the diffusion tensor, D, to represent diffusion along all combinations of the principal axes (x, y, z) in an ellipsoid (Figure 2.9a). Within the array, there are six unique elements (D_{xx}, D_{yy}, D_{zz}, $D_{xy} = D_{yx}$, $D_{yz} = D_{zy}$, $D_{xz} = D_{zx}$), wherein the diagonal elements correspond to diffusion rates along the principal axes, and the off-diagonal elements correspond to diffusion as related between a given pair of principal directions. To model the 6 unique directional elements, at least 6 noncollinear directions of diffusion weighted images along with one non-diffusion weighted image must be acquired. The coordinate system that is used in the diffusion tensor model is the diffusion ellipsoid, the longest axis of which corresponds to the principal direction of the rate of diffusion within a voxel (Figure 2.9b). As a representation of diffusion rates in 3D space within the voxel, the magnitude of major and minor axes of the diffusion ellipsoid are represented by eigenvalues (λ) and the major ellipsoid direction by the primary eigenvector (Basser et al., 1994) (Figure 2.9a, b). The direction of diffusion is indicated by eigenvectors (ε) which are ultimately used in DTI tractography to virtually reconstruct WM tracts (Figure 2.9a).

DTI is used to generate quantitative diffusion maps based on the eigenvalues and eigenvectors from the diffusion ellipsoid. FA is calculated as a ratio of the anisotropic components of the ellipsoid to the entire ellipsoid so that it provides an index of the portion of the tensor that represents anisotropic diffusion (Equation 2.4). Since FA is normalized by the magnitude of the entire tensor, it is represented as a value of 0 (perfectly isotropic diffusion) to 1 (perfectly anisotropic diffusion). Thus, on an FA map of the brain, highly isotropic tissue like cerebrospinal fluid (CSF) will appear darkest and highly anisotropic tissue like WM will appear bright (Figure 2.10c). Mean diffusivity (MD) is a measure of the total mean squared displacement of molecules due to diffusion within the tensor ellipsoid (Equation 2.5). The MD values are higher due to greater

displacement in CSF, and they are relatively lower in areas with less displacement such as in WM (2.10c). Conversely, on an MD map, CSF is bright and WM is relatively darker (2.10b). MD provides indicators of neuron density and extracellular space (Soares et al., 2013). Axial diffusivity (AD) represents the diffusion coefficient parallel to the long axis of the ellipsoid (Equation 2.6). Radial diffusivity (RD) provides the degree of diffusion perpendicular to the long axis of the ellipsoid (Equation 2.7). Like MD maps, AD and RD maps show CSF as the brightest tissue while WM and GM are relatively darker (Figure 2.9c). When considered together, AD and RD metrics can provide additional information that MD maps cannot, for instance, increased RD but unchanged AD is indicative of dysmyelination in WM (Song et al., 2002), though these metrics are more difficult to interpret and not often reported for GM structures. For example, changes in AD and RD in GM structures in healthy adults have simply been interpreted as a loss of cell alignment (Kumar et al., 2013).

(Equation 2.4) $$\mathrm{FA} = \sqrt{\frac{1}{2}\frac{(\lambda_1-\lambda_2)^2+(\lambda_2-\lambda_3)^2+(\lambda_1-\lambda_3)^2}{{\lambda_1}^2+{\lambda_2}^2+{\lambda_3}^2}}$$

(Equation 2.5) $$\mathrm{MD} = \frac{\lambda_1+\lambda_2+\lambda_3}{3} = \frac{D_{xx}+D_{yy}+D_{ZZ}}{3}$$

(Equation 2.6) $$AD = \lambda_1$$

(Equation 2.7) $$RD = \frac{\lambda_2+\lambda_3}{2}$$

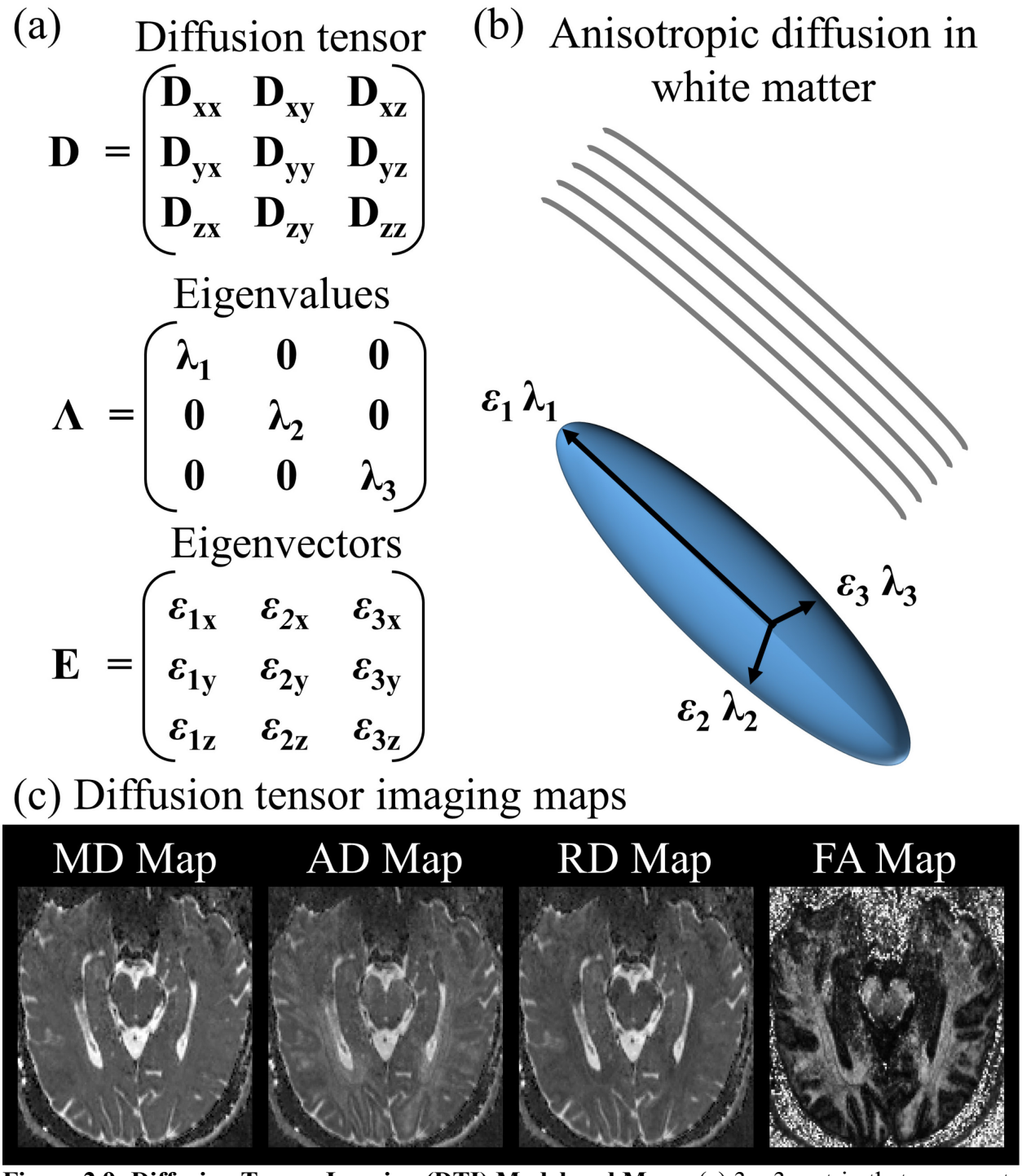

Figure 2.9: Diffusion Tensor Imaging (DTI) Model and Maps. (a) 3 x 3 matrix that represents the diffusion tensor and can be decomposed to eigenvalues and eigenvectors in order to model diffusion in human brain tissue. (b) Anisotropic diffusion in WM as modeled by the diffusion tensor wherein the eigenvector with the largest magnitude is assigned the primary number ($\varepsilon_1 \lambda_1$). (c) DTI maps including mean, axial and radial diffusivity (MD, AD, RD) and fractional anisotropy (FA). Data is from a healthy 24-year-old female.

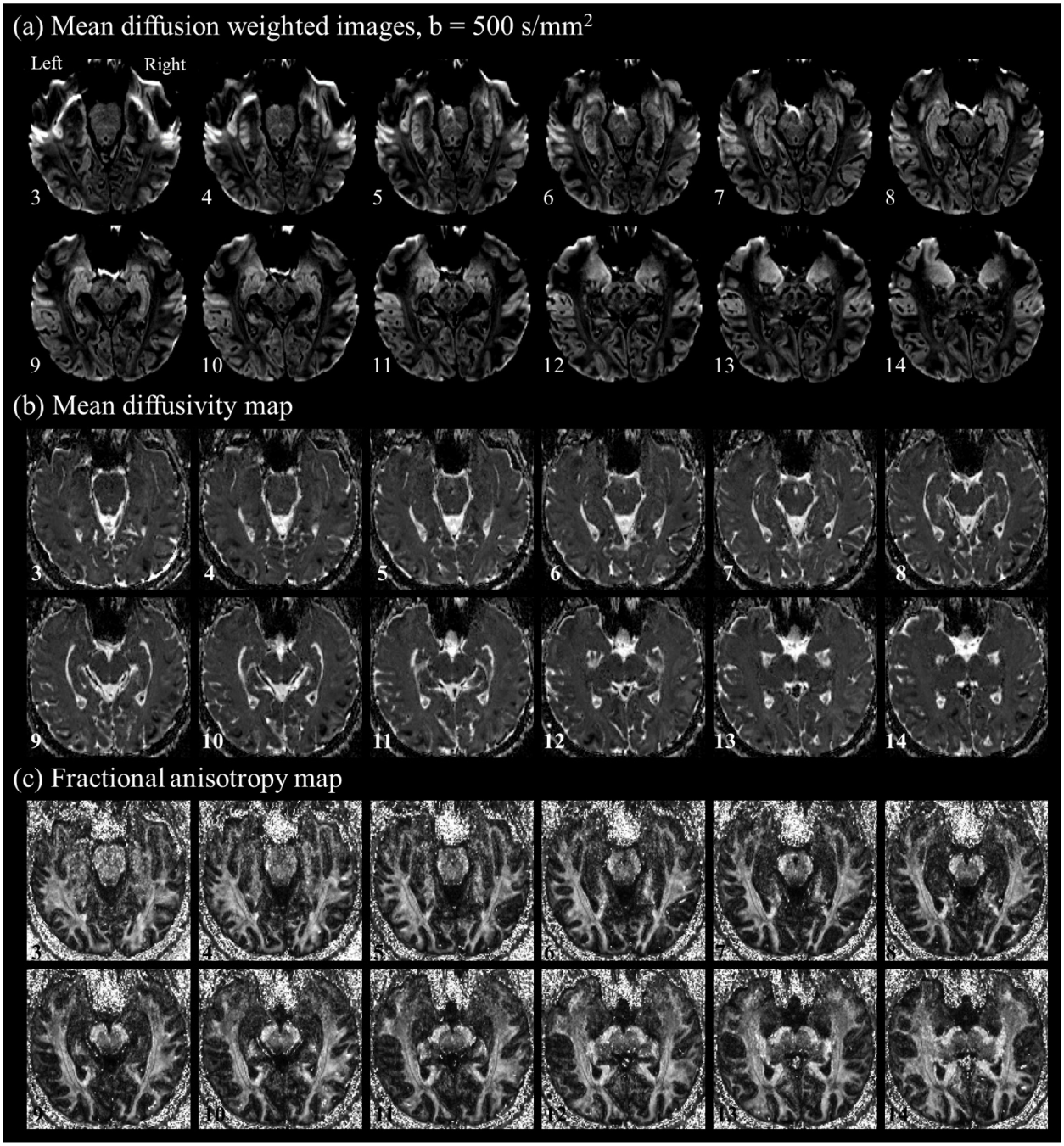

Figure 2.10: Hippocampal diffusion imaging slab slices. Twelve out of the 20 total slices acquired for this healthy volunteer (29-year-old female) provided full bilateral hippocampal coverage. (a) Mean diffusion weighted image (DWI) based on 100 b = 500 s/mm^2 images (10 averages of 10 directions). Diffusion tensor imaging (DTI) model derived (b) mean diffusivity (MD) and (c) fractional anisotropy (FA) maps.

2.2.3. SS-EPI and Diffusion Gradient Distortions

There are some downsides of this SS-EPI approach which can have a deleterious effect on image quality and quantitative metrics. They include geometric image warping due to magnetic field inhomogeneities and eddy currents, as well as signal loss from dephasing (Pipe, 2009). Magnetic field inhomogeneities cause off-resonance precession, which produces a phase change and a corresponding geometric shifting/warping. Sources of static magnetic field inhomogeneities vary but most often they happen in areas nearby tissue/air boundaries (e.g., frontal lobe tissue with air in sinuses) and metal (e.g., braces). The SS-EPI involves rapid slice acquisition that requires fast on/off switching of the image acquisition gradients, and DWI requires that diffusion gradients are maxed-out. This use of the image acquisition gradients induce small currents called eddy currents in conductive surfaces of the scanner (e.g., often in the cryostat) (Pipe, 2009). Eddy currents can persist after the gradients are turned off, and these currents create their own magnetic fields which alter that which a given spin is experiencing as prescribed by the pulse sequence, hence introducing off-resonance precession which cause warping distortions to the image (Le Bihan et al., 2006). Eddy currents are more problematic than static magnetic field inhomogeneities because they are dynamic in that they change with each diffusion gradient direction and they are not constant throughout the data readout (Pipe, 2009). Finally, signal loss occurs from dephasing of spins within a voxel during the EPI sampling trajectory. Although all spins are in-phase when the spin echo occurs, they begin to dephase as per the static magnetic field inhomogeneities (e.g., air/tissue interface, metal) within a given voxel. All these SS-EPI artifacts occur in the phase encoding direction because phase encoding occurs over a much longer time during the readout than frequency encoding (e.g., 100-1000s of milliseconds for phase encoding *versus* 10s of milliseconds for frequency encoding). Parallel imaging can reduce warping caused by static

magnetic field inhomogeneities and eddy currents as well as signal loss from dephasing by reducing phase encoding steps, hence reducing the total sampling trajectory and readout time (Pipe, 2009).

The diffusion-weighting aspect of DWI sequences also introduces artifacts to the acquired images. The diffusion gradients cause distortions in the images by inducing eddy currents and introducing gradient nonlinearities (Pipe, 2009). Eddy currents like those described above in the SS-EPI paragraph are induced by strong diffusion gradients that are often maxed out and held on for longer durations to achieve higher b values. Gradient nonlinearities occur when the diffusion gradient is not perfectly linearly varying within an image volume and/or not sharply dropping off outside the image volume. The effect is that the direction and strength of diffusion weighting will vary across the imaging volume. In addition to diffusion gradient distortions, DWI sequences are also sensitive to bulk motion in the form of head movement and cardiac pulsations (Pipe, 2009). When motion is in the direction of a given diffusion gradient application, a change in phase occurs with any affected voxel. There are three image corruption mechanisms that can occur due to motion-related phase change, they include (a) changes in Fourier-encoded phase, (b) k-space data shifting to excessive asymmetry in data sampling, (c) spin dephasing that derives from bulk motion, not related to diffusion.

In addition to the SS-EPI and diffusion gradient related distortions, diffusion MRI is sensitive to the thermal noise of a sample, and it will cause signal fluctuations that create noise in the acquired images (Perrone et al., 2015; Veraart et al., 2016). Another artifact called Gibb's ringing can affect many types of MRI and is related to the inverse Fourier transformation that is used to transform acquired MRI data from k-space to image space. The effect is more severe with faster imaging modalities (e.g., SS-EPI) and acquisition acceleration techniques (e.g., partial

Fourier imaging) such as those used in this thesis (Perrone et al., 2015). The result is signal fluctuations near regions of sharp signal differences, typically at tissue boundaries (e.g., WM-CSF), which appear as evenly sized alternating lines of bright/dark composure that decrease in intensity with increased distance from the tissue interface (Perrone et al., 2015). In diffusion MRI, this ringing is particularly evident on the b0 images near the CSF which appears bright due to its long T2. The ringing is deleterious for DTI maps, particularly MD and FA. Gibb's ringing causes increases in FA with decreases in MD and decreases in FA with increases in MD as the artificial signal intensity differences oscillate with signal overshoots and undershoots in the source data (Perrone et al., 2015).

2.2.4. DWI Data Preprocessing

Prior to DWI analyses such as DTI or CSD, data must be preprocessed to reduce distortions and mitigate errors in the qualitative images and quantitative maps. This section includes a summary of common distortions/inhomogeneities and corrections as applied in the pre-processing pipeline used for the 1 mm isotropic DWI data acquired for this dissertation. First, the DWI data was denoised using random matrix denoising technique that employs a principal components analysis to separate signal and noise and demonstrates impressive results (Figure 2.11a, b). The denoising resulted in a signal-to-noise ratio (SNR) increase in the hippocampus of 180% for the single-shell b500 DWIs (19.3 non-denoised; 54.0 denoised), 159% for the multi-shell b500 DWIs (19.9 non-denoised; 51.5 denoised), and 171.6% for the b2000 DWIs (9.9 non-denoised; 26.8 denoised) (Figure 2.11a, b). This noise reduction is especially important in high-resolution DWI which will have inherently lower signal (relative to lower spatial resolution acquisitions) due to the small size of the 1 mm isotropic voxels (Treit et al., 2018). Moreover, this denoising must be the first preprocessing step because the corrections that follow will alter the

data, potentially violating noise assumptions (e.g., via smoothing) that the denoising algorithm relies upon (Veraart et al., 2016). In the second step, Gibb's ringing artifact removal was performed using a sub-voxel shift re-interpolation approach to improve qualitative and quantitative observations, although this approach may not remove all ringing artifacts in PPF sequences such as the one used in this thesis (Kellner et al., 2016). For example, on the b0 images from data used in this thesis, the lateral ventricles are bright due to the long T2 of CSF and the medially adjacent hippocampus is darker due to the shorter T2 of GM/WM, and as a result, there are Gibb's ringing artifacts along the lateral borders of the hippocampus (Figure 2.11b shows Gibb's ringing which is reduced after the correction step in Figure 2.11c). The third step corrects for eddy current (by modelling diffusion data using a Gaussian Process that overcomes the limitations of registration based approaches which have difficulty correcting images acquired with multiple diffusion gradient directions; Andersson et al., 2012) and motion distortions (by adjusting all images to align with a reference image; all b0s with the first b0 and all DWIs with the first DWI; all DWIs with the b0s) (Figure 2.11d). The last step corrected for B1 field inhomogeneities causing a nonparametric nonuniform intensity normalization approach (Tustison et al., 2010) which further flattened out image signal in addition to the "Prescan Normalize" option that was utilized on the Siemens Prisma 3T scanner for all acquisitions (Figure 2.11e). MRtrix3 was used to run this entire processing pipeline (Tournier et al., 2019)

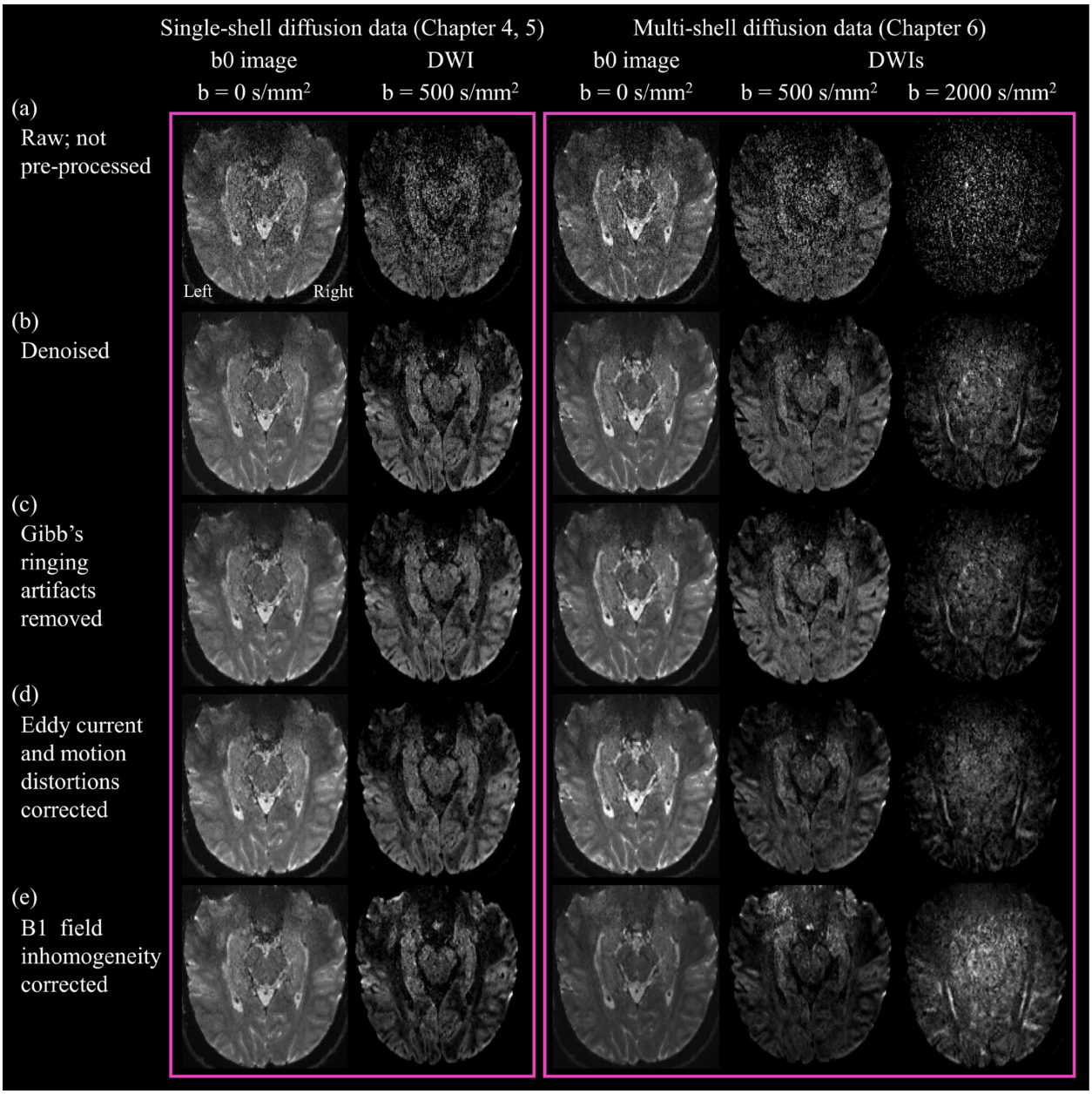

Figure 2.11: Pre-processing steps for diffusion imaging data. For the single-shell diffusion data used in Chapters 4 and 5, and the multi-shell diffusion data used in Chapter 6, each step of the pre-processing pipeline used (same for each dataset) is featured for the individual, non-averaged b0 images and the diffusion-weighted images (DWI), starting from the (a) raw, not yet pre-processed data, (b) denoised, (c) Gibb's ringing artefacts removed, (d) Eddy current and motion distortion corrected, and (e) B1 field inhomogeneity corrected. MRtrix3 was used to run this entire processing pipeline (Tournier et al., 2019).

2.2.5. Development of a Multi-shell DWI Acquisition Sequence for the Hippocampus

The above-mentioned 1 mm isotropic multi-shell DWI protocol was developed by testing different numbers of directions and b values for the low and high b value shells and analyzing resultant DTI and CSD orientations in relation to known anatomy. The purpose of this acquisition was two-fold, first and foremost was to allow for the application of CSD to perform intra-hippocampal tractography using the entire acquisition, and second to generate accurate DTI hippocampal metrics and intra-hippocampal tractography using the low b value shell. For the first shell, I chose a b value of 500 s/mm^2 to help overcome the low SNR of a 1 mm isotropic echo-planar imaging (EPI) acquisition, same as for the original single-shell acquisition which has demonstrated accurate DTI metrics at high spatial resolution (Treit et al., 2018) as applied in research Chapters 4 and 5 of this thesis. In the original protocol, 10 averages of 10 unique diffusion directions were acquired to increase SNR instead of using 100 unique diffusion directions, however, averaging was shown to have no advantage over unique directions (Treit et al., 2018). Additionally, more unique directions as opposed to averages of the same directions will increase angular resolution which was desirable for the CSD tractography goals of this protocol. Therefore, for the first shell, 100 unique directions at b = 500 s/mm^2 were acquired and this number was reduced by 10 until the mean DWI no longer allowed for clear delineation of the hippocampus and/or the quality of the DTI maps deteriorated. Below 60 directions at b500, the hippocampus structure became less clear on the mean DWI and the DTI maps became noticeably noisier (Figure 2.12). To meet requirements of angular resolution for more complex models, 64 directions at b500 was chosen (which is also a number provided as a default on the Siemens Prisma) (Figure 2.12).

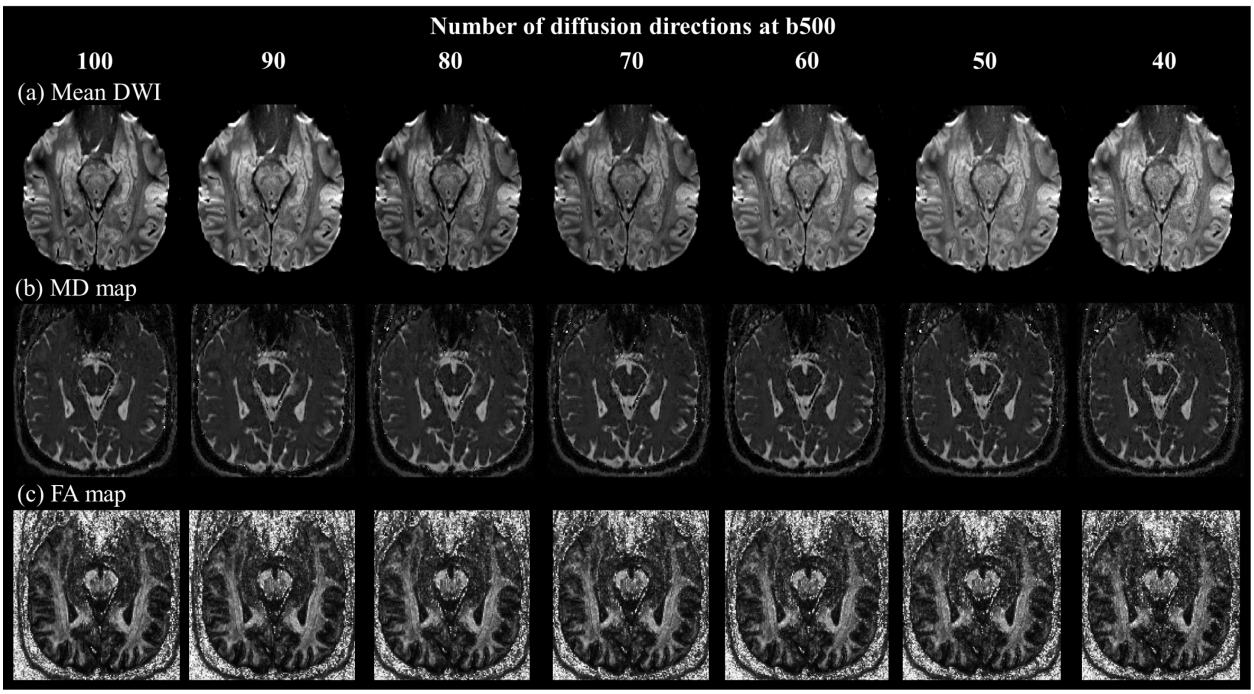

Figure 2.12: Low b value shell, diffusion-weighted test data. (a) Mean diffusion-weighted images (DWI), (b) mean diffusivity (MD) maps, and (c) fractional anisotropy (FA) maps as calculated from 100, 90, 80, 70, 60, 50, and 40 unique diffusion gradient directions at b = 500 s/mm^2. Note the reduction in clarity of the hippocampus structure (e.g., noisier, less pronounced tissue borders) in the (a) mean DWIs after 60 directions and lower, as well as the general increase in noise after 60 directions and lower in the (b, c) MD and FA maps.

For the second shell, diffusion-weighted images at a b value of 2000 s/mm^2 were acquired because that is the minimum diffusion weighting recommended to resolve crossing fibers using CSD (Tournier et al., 2008), and a 64 directions were acquired because it is also recommended to acquire more than 45 directions in order to increase SNR and angular resolution and overcome imperfections in the uniformity of diffusion-weighted gradients (Tournier et al., 2013). The authors also suggest that only very slight improvements are seen over 70 directions (Tournier et al., 2013), so I tested 64 directions at b values of ranging from 2000 to 2500 s/mm^2. I determined the final parameters for the second shell by examining the SNR of the diffusion-weighted images and running CSD tractography. In the tractography output, the presence of major WM tracts (e.g., splenium of the corpus callosum, posterior WM crossing regions) and intra-hippocampal connections in relation to known anatomy were examined and compared at b2000 and b2500

(Figure 2.13). In consideration of the very low SNR in the mean DWI at b2500 (i.e., mean DWI is much noisier at b2500 relative to b2000; Figure 2.13a, d), the less complete corpus callosum and greater noise in the CSD fODF maps at b2500 relative to b2000 (Figure 2.13b, e), and the less robust anterior-posterior green streamlines likely representing the fimbria in the hippocampus as seen in the hippocampus CSF fODFs (Figure 2.12g, i) and streamlines (2.12h, j) produced with the b2500s relative to the b2000s, 64 directions at 2000 s/mm^2 was chosen for the second shell (Figure 2.12k-m). This protocol was then acquired as part of a large population normative sample of 378 neurotypical controls (aged 5-90 years; median 31 years; 216 females, 162 males) (Treit et al., 2022). Chapter 6 comprises the first application of high spatial resolution and high angular resolution diffusion MRI to the hippocampus with CSD-based intra-hippocampal tractography in direct comparison to DTI tractography as applied in an age- and sex-matched subsample of 40 neurotypical controls (aged 5-90 years; median 31 years; 22 females, 18 males) from the aforementioned normative study (Treit et al., 2022) along with 6 healthy volunteers scanned twice.

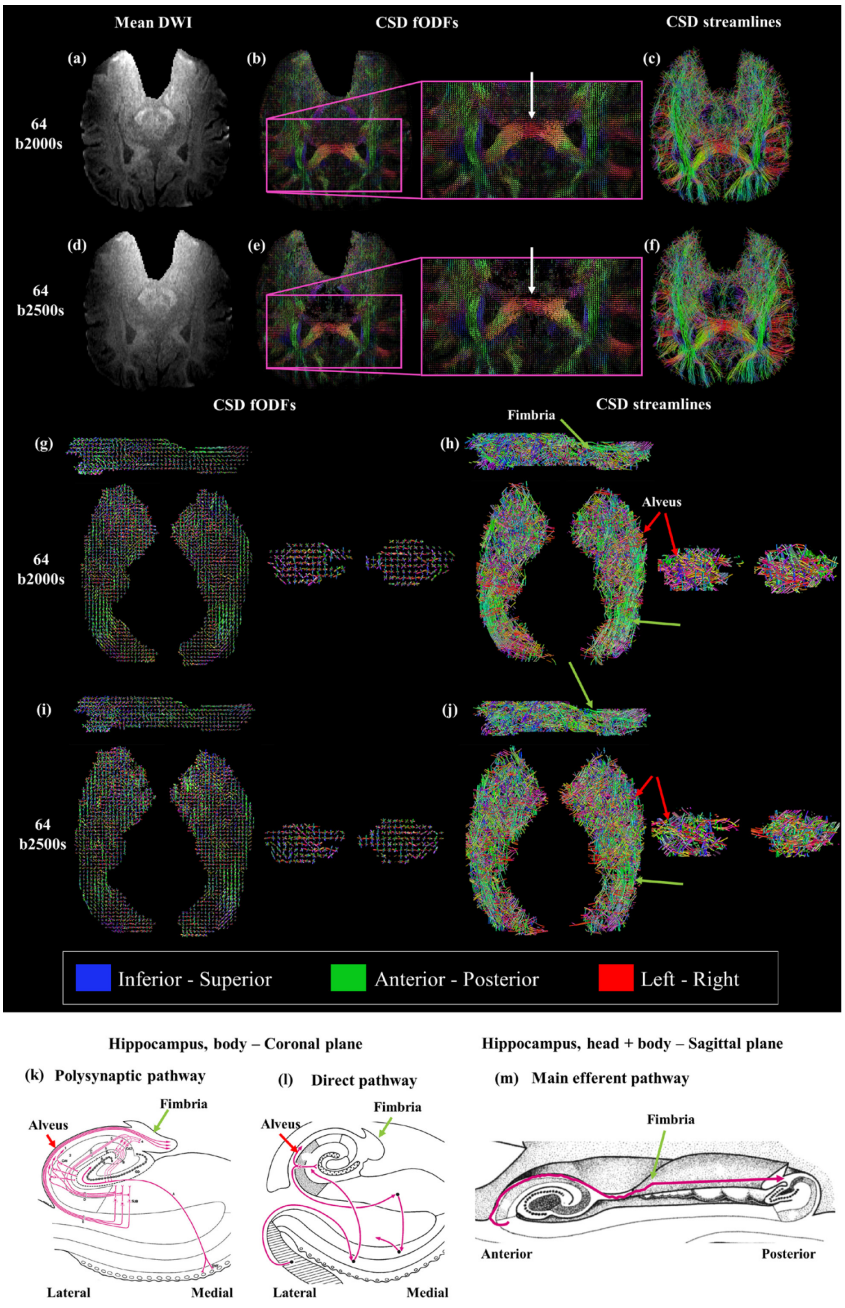

Figure 2.13: High b value shell, diffusion-weighted test data. Mean diffusion-weighted images (DWI) from 64 directions at (a) b2000 and (d) b2500, wherein the hippocampus structure is clearer and the images are less noisy at (a) b2000 than (d) b2500. Constrained spherical deconvolution fiber orientation distribution function (fODF) maps for the whole brain at (b) b2000 and (e) b2500, wherein the (b) b2000 fODF map is less noisy and features a more complete corpus callosum splenium (white arrows) than at (e) b2500; these differences are reflected in the CSD streamlines at (c) b2000 and (f) b2500. For intrahippocampal activity, the anatomically-plausible streamlines are more difficult to identify, but the fimbria (green arrows) and alveus (red arrows) appear to be more robust at (g, h) b2000 than (i, j) b2500 relative to known hippocampal pathways (k, l, m). (k, l, m) Reprinted/adapted by permission from Springer Nature Customer Service Centre: The human hippocampus by Henri Duvernoy, Françoise Cattin, Pierre-Yves Risold 2013.

2.2.6. Diffusion Tractography

DWI data is unique in its capability to enable virtual identification and quantification of WM tracts in the brain. There are two types of tractography approaches that can be applied to DTI data. Deterministic tractography assumes a single orientation at each voxel and produces a single streamline per voxel. Probabilistic tractography assumes a distribution of orientations at each voxel and produces a probability distribution of multiple streamline samples per seed voxel from a probability distribution. Deterministic tractography was applied in this thesis and discussed below.

2.2.6.1. DTI Tractography

The premier and most commonly used method to identify WM tracts is the DTI model which estimates the magnitude of diffusion anisotropy and its orientation by way of the diffusion tensor (Basser et al., 1994), which provides fiber orientation information via the primary eigenvector per voxel for streamline algorithms to follow (Basser et al., 2000; Mori et al., 1999). A seminal line propagation approach for reconstructing 3D WM streamlines is referred to as the fiber assignment by continuous tracking (FACT) algorithm (Mori et al., 1999). The deterministic FACT algorithm works so that streamline tracking starts from the center of a given voxel and continues based on the direction of the primary eigenvector to connect voxels with vectors that align with one another to assign a fiber. For any given voxel, the DTI model generates an estimate of the average fiber orientation based on the direction of the primary eigenvector or main axis of the diffusion ellipsoid. Line propagation in streamline tracking will continue to connect voxels and terminate fiber assignment based on specific, pre-set criteria which can vary based on your target tracts. The first and most important criteria is the degree of anisotropy as set by choosing an FA value that is typical of WM (e.g., FA = 0.2 as the minimum FA value to continue tracking). The

second termination criterion involves the minimum allowable turning angle between voxels (e.g., 40-70°). The third consideration involves tract length for which a minimum and maximum can be chosen. The final criterion involves the step size which should be set at ~1/10th of the voxel size to prevent overshooting curvature in a given WM tract (Tournier et al., 2012). As described in the beginning of this subsection, DTI based tractography assigns fibers based on the average fiber orientation of the entire voxel, thus it cannot resolve instances of multiple, complex fiber orientations such as crossing fibers which are observed in the large majority of human brain WM (Jeurissen et al., 2010).

2.2.6.2. CSD Tractography (A Higher Order Diffusion Analysis)

Two key limitations of the DTI model need to be considered: (a) its inability to resolve multiple fiber bundle orientations in a single voxel such as crossing and kissing fibers, and (b) the bias introduced to the directionality estimate by the presence of GM and CSF (Newman et al., 2020). To overcome these limitations, higher order diffusion analysis approaches take advantage of HARDI data. However, HARDI approaches that are parametric model based such as neurite orientation dispersion and density imaging (NODDI) rely on stringent assumptions about microstructure (e.g., the ratio of intracellular space, to extra cellular space, and CSF, per voxel) (Jeurissen et al., 2014). Moreover, parametric model based techniques can only resolve a limited number of fiber orientations and much like DTI, they do not provide an accurate representation of the actual fiber distribution in a given voxel (Jeurissen et al., 2014). Spherical deconvolution, as developed in MRtrix3 by Tournier *et al.*, 2004, is non-parametric, does not rely on a mathematical model for each tissue compartment, and only imposes a specific degree of spherical smoothness onto the fiber orientation distribution functions by spherical harmonics (SH). SHs are functions defined on the surface of a sphere, forming a complete orthonormal set, and can be used to

represent a spherical function (similar to how the Fourier series forms a complete orthonormal basis over an interval in Cartesian space). Consequently, the data fitting becomes a linear least squares problem, faster to solve than any of the non-linear models (Jeurissen et al., 2014). SD is used to directly estimate what is called the fiber orientation distribution function (fODF) from the diffusion imaging data. The fODF describes the distribution of fibers within a given voxel, and it is estimated by SD of the response function of the diffusion-weighted (DW) signal with no a priori information about the likely number of fiber populations present and with no dependence on any assumed model of diffusion (Tournier et al., 2004) (Figure 2.8). There is a marked reduction in noise sensitivity by introducing a non-negativity constraint to SD (CSD) in order to null the appearance of physically impossible negative values in the reconstructed fODF. In CSD, tissue response functions are used as the kernels by the deconvolution algorithm. Their calculation is the first step in performing CSD, and they may be calculated per tissue (WM, GM, CSF). CSD in MRtrix3 can be accomplished by estimating only a single-tissue (WM only) response function using a DWI dataset with a single diffusion-weighted shell (and a non diffusion-weighted shell) or multi-tissue (WM, GM, CSF) response functions using a DWI dataset with at least 2 unique diffusion weighted shells with different b values/diffusion weighted (and a non diffusion weighted shell) (Jeurissen et al., 2014). Recent work suggests that it is important to estimate separate response functions for all 3 tissues using a method called multi-tissue CSD (as opposed to single-tissue CSD which only estimates WM), for instance, especially in the hippocampus, where the WM and CSF response functions will be overestimated if the GM is ignored (Newman et al., 2020). For example, in a region of WM crossing fibers, DTI fails to model the 2+ fiber orientation populations that are estimated by both single-tissue and multi-tissue CSD (Figure 2.14; corresponding streamlines in Figure 2.15). Moreover, multi-tissue CSD demonstrates bright,

higher amplitude fODFs in the WM relative to single-tissue CSD which is much noisier with less well-defined tracts due to a decrease in WM signal due to the presence of spherical, isotropic, GM and CSF-like fODFs that are otherwise excluded in the multi-tissue CSD results due to the estimation of separate GM and CSF tissue responses. Like DTI, CSD can be used to calculate quantitative metrics, mainly the apparent fiber density (AFD) which provides a relative measure of the density and direction of fibers within an intra-axonal volume (Raffelt et al., 2012). Deterministic CSD tractography can be performed based on the same tenants as the FACT algorithm (Mori et al., 1999) for DTI tractography (Tournier et al., 2012) with a key difference: the algorithm follows the direction of the fODF peak orientation in CSD instead of the ellipsoid primary eigenvector orientation as in DTI. Tracking criteria works similarly for CSD tractography as in DTI (e.g., step size, curvature, tract length) with another key difference: instead of using anisotropy (FA values) as a termination threshold, an fODF peak amplitude value is used (Tournier et al., 2012). The fODF peak amplitude threshold values for CSD tractography are not as well-established as FA thresholds in DTI tractography, thus a value or series of values to be tested as part of the experiment should be chosen to minimize spurious fibers and maximize true fibers.

For as low as a 45° crossing, the minimum b-value required to resolve the fibre orientations using CSD tractography is estimated at ~2000 s/mm^2 for CSD (Tournier et al., 2008). The minimum data requirements for diffusion tractography based on the CSD technique includes a minimum 45 directions (diffusion volumes) at a minimum of b = 2000 s/mm^2 in order to achieve an SH degree of l_{max} = 8 (the highest achievable SH degree) (Tournier et al., 2012, 2013). The purpose of Chapter 6 was to contrast DTI and CSD tractography in the hippocampus which contains crossing fibers.

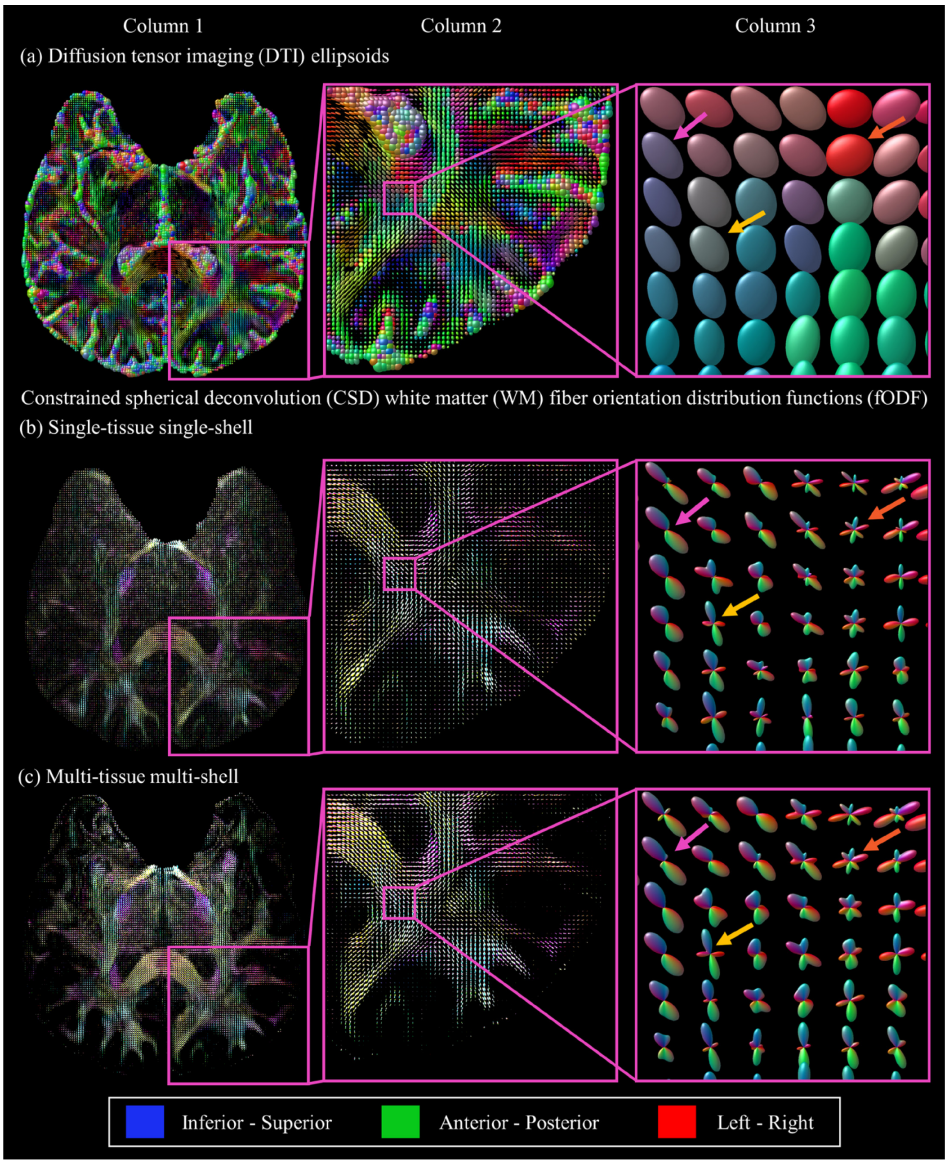

Figure 2.14: Diffusion tensor imaging (DTI) versus Single- and Multi-tissue Constrained Spherical Deconvolution (CSD) in posterior crossing white matter (WM). Posterior crossing fiber regions as modeled by (a) DTI and estimated by (b) single-tissue single-shell (64 directions at b = 2000 s/mm^2) CSD and multi-tissue multi-shell (64 directions at b = 500 s/mm^2 and 64 directions at b = 2000 s/mm^2 from an axial-oblique DWI slab of 20 1 mm slices aligned to the long-axis of the hippocampus with 1 mm isotropic voxels, displayed as (column 1) the full axial-oblique, (column 2) zoomed 4x and (column 3) zoomed 16x at 6x6 1 mm voxels wide. (Column 3) the pink, yellow and orange arrows respectively indicate voxels with a single fiber orientation (pink arrow), two fiber orientations (yellow arrow), and three fiber orientations (orange arrow), in which (a) DTI fails to model the 2+ fiber anatomically plausible orientations populations estimated by (b) single-tissue and (c) multi-tissue CSD. (Columns 1, 2) (c) multi-tissue CSD demonstrates higher amplitude fODFs in the WM relative to (b) single-tissue CSD, the WM signal of which is decreased by the presence of spherical, isotropic, grey matter (GM)- and cerebrospinal fluid (CSF)-like fODFs that are excluded in (c) multi-tissue CSD due to the estimation of separate GM and CSF tissue responses. Data is from a healthy 28-year-old female.

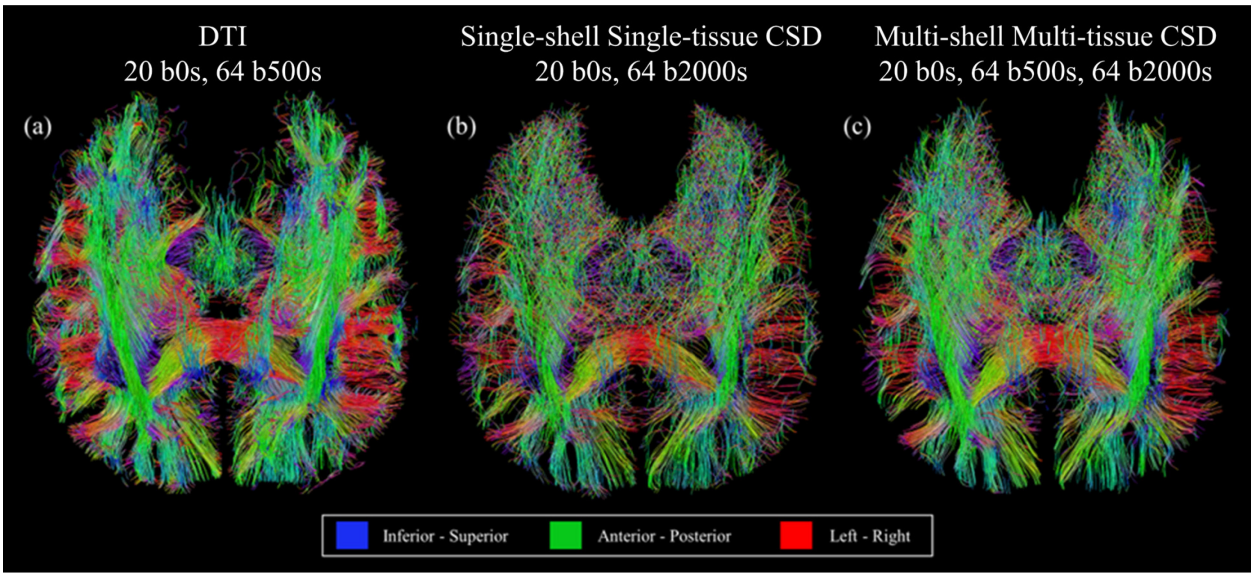

Figure 2.15: Diffusion tractography using diffusion tensor imaging (DTI) and single- and multi-shell constrained spherical deconvolution (CSD). Deterministic diffusion tractography within a 1 mm isotropic slab of 20 1 mm slices aligned along the long axis (anterior-posterior) of the hippocampus using the (a) DTI model based on single-shell DTI data collected with 100 b500s and 10 b0s, (b) CSD model based on multi-shell high angular resolution diffusion imaging (HARDI) data, using 64 b500s and 20 b0s and (c) using 64 b500s, 64 b2000s and 20 b0s. Data is from a healthy 28 year old female. The effect of adding the b500s for CSD and performing multi-tissue CSD demonstrates more anatomically plausible streamlines.

3. Prenatal Alcohol Exposure

3.1. The Effects of PAE

Prenatal alcohol exposure (PAE) is the most common preventable cause of birth defects worldwide (Lange et al., 2017; May et al., 2018; Popova et al., 2019). PAE has been extensively studied using numerous research methods from animal models to human brain imaging. Animal models have demonstrated that PAE effects vary based on pattern, timing, amount, and genetics (Petrelli et al., 2018), and include a spectrum of craniofacial malformations, altered brain development (e.g., overall atrophy with some regions more severely affected than others), and cognitive/behavioural deficits (Petrelli et al., 2018). Potential prenatal mechanisms of brain injury

as demonstrated in animal models of PAE include the disruption of neuronal differentiation (Schaffner et al., 2020), migration (Delatour et al., 2019; Miller, 1986; Skorput et al., 2015), and development (Delatour et al., 2019), and cell death (Creeley et al., 2013; Schaffner et al., 2020). There is also rodent model evidence of disruption in postnatal neurogenesis in the hippocampus on into adulthood (Gil-Mohapel et al., 2010). Similarly, human PAE demonstrates a range of cognitive (e.g., memory, executive functioning, learning), behavioural (e.g., mood/behaviour regulation, attention, impulse control), and physical effects (e.g., low birthweight, small cranial size, facial abnormalities) as described by the umbrella term Fetal Alcohol Spectrum Disorder (FASD) (Chudley et al., 2005; Mattson et al., 2019). The prevalence of FASD is approximately 4% in the general Canadian population (Flannigan et al., 2018b). Specifically, the prevalence rates for children in care (e.g., foster care) range from 4% in Alberta to 11% in Manitoba (Flannigan et al., 2018a). At the most involved end of the fetal alcohol spectrum of disorders is fetal alcohol syndrome (FAS), a diagnosis defined by a pattern of central nervous system problems, facial abnormalities, and growth issues. The other end of the spectrum is less complicated as defined by a lack of physical abnormalities but with moderate neurological symptoms; the diagnosis is called alcohol-related neurodevelopmental disorder (ARND). Although neurobehavioral symptoms vary from severe to moderate along the spectrum, they are always present, unlike physical abnormalities.

3.2. Neuroimaging in PAE

Neuroimaging has provided a valuable window into the structural and functional brain changes that may underlie the neurobehavioral symptoms observed in PAE. The consequences of PAE on the human brain were first demonstrated in an autopsy report which contrasted a brain from a healthy 6 week old infant to a relatively atrophied brain of a 6 week old who had severe

effects of PAE (as evidenced by a diagnosis of FAS) (Clarren et al., 1978). Structural MRI (i.e., T1/T2-weighted), diffusion MRI, proton magnetic resonance spectroscopy (^{1}H-MRS), and functional MRI (fMRI) studies have been applied to examine the human brain in PAE (see review of 64 studies by Donald et al., 2015; see book chapter by Treit & Beaulieu, 2018). Structural MRI is used to examine volume and shape – macrostructural changes. In children to adults with PAE, structural MRI shows several common findings as reported in the aforementioned reviews. First, individuals with FASD show reductions in total brain volume (e.g., Nardelli et el., 2011 reported -8%, and Treit et al., 2013b -11%), total WM volume (e.g., Nardelli et el., 2011 reported -9%, and Treit et al., 2013b -7%), total cortical GM volume (e.g., Nardelli et el., 2011 reported -8%, and Treit et al., 2013b -16%), and total subcortical GM volume (e.g., Nardelli et el., 2011 reported -13%, and Treit et al., 2013b -14% average reductions across the hippocampus, caudate, putamen, thalamus, amygdala and globus pallidus). Hippocampus volume reductions are the most commonly reported amongst subcortical structure volume reduction (Donald et al., 2015). Diffusion MRI in PAE has mainly focused on WM tracts and applied diffusion tractography to virtually identify and quantify WM (Lebel et al., 2008; Treit et al., 2013). Numerous DTI studies consistently demonstrate reduced FA in the corpus callosum in individuals with PAE (see two recent reviews focused on DTI studies of white matter in PAE: Ghazi Sherbaf et al., 2019; Nguyen et al., 2017). Beyond WM tracts, DTI has only been applied in one study to assess subcortical GM regions, specifically the putamen, caudate, globus pallidus, and thalamus – each of which showed diffusion parameter differences in children with PAE (Lebel et al., 2008). Another method to probe WM tracts is myelin water imaging (MWI), which has also been sparsely applied to PAE; in one recent study MWI did not reveal any PAE-control group differences as measured by the myelin water fraction of the hippocampus from childhood to adolescence (McLachlan et al., 2019). ^{1}H-

MRS studies are less numerous than the aforementioned approaches, but together they reveal altered neurochemistry in WM and GM of individuals with PAE (Donald et al., 2015). Finally, functional MRI has revealed alterations in the pattern of functional activation, most commonly during working memory tests and in the frontal lobe of individuals with PAE (Donald et al., 2015). Together, these studies suggest potential fruitful avenues for identifying structural and functional brain changes that may help advance research, diagnostic and treatment approaches in PAE.

3.3. MRI Studies of the Hippocampus in PAE

MRI studies of the human hippocampus in PAE are largely limited to macrostructural features. Early qualitative MRI research demonstrate hippocampal atrophy in children with PAE (Mattson & Riley, 1995). Whole-hippocampus volumes on T1-weighted images have demonstrated reductions that begin in the neonate period (Donald et al., 2016) and continue into childhood to adulthood. Atrophy in the hippocampus has been shown to range from 5-25% in individuals with PAE (Astley et al., 2009; Biffen et al., 2018; Coles et al., 2011; Dodge et al., 2020; Dudek et al., 2014; Gross et al., 2018; Krueger et al., 2020; McLachlan et al., 2020; Nardelli et al., 2011; Roussotte et al., 2012; Treit et al., 2013, 2017; Uban et al., 2020; Willoughby et al., 2008) (Table 3.1; there were 16 total volumetric studies of the hippocampus in PAE and/or FASD, wherein PAE indicates individuals with cognitive/behavioural deficits and confirmed PAE but without an FASD diagnosis of partial-FAS or FAS, 14 of which showed group differences between PAE/FASD and controls). Individuals with facial dysmorphology have also shown more severe hippocampal atrophy relative to people with PAE but no facial dysmorphology (Coles et al., 2011) (Table 3.1). Sex differences have also been implicated in PAE: one study that found reduced hippocampus volumes in the PAE group, also reported expected sex differences (female hippocampal volumes smaller than males) in controls, but not in PAE (McLachlan et al., 2020). In

addition, the prediction of PAE diagnosis using only brain volumes by way of multivariate models in machine learning has ranked right hippocampus volume in the top five volumetric characteristics for a male-specific model that was more accurate than a female-specific model (Little & Beaulieu, 2020). Macrostructural MRI further suggests PAE related hippocampus volume reductions may be regionally specific. One investigation reported sparring of the head or anterior hippocampus with volume reductions found only in the posterior (body and tail combined) (Dudek et al., 2014). Furthermore, regional shape abnormalities in the head and tail (but not body) have been measured in children with PAE (Joseph et al., 2014).

Reduced hippocampal volumes have also shown different relationships with cognitive deficits in PAE. For instance, smaller hippocampi in PAE have been associated with poorer spatial navigation in children (Dodge et al., 2020), impaired verbal learning and verbal and spatial recall in children and adolescents (Willoughby et al., 2008), and impaired verbal and nonverbal memory performance in adults (Coles et al., 2011). Other work has shown no relationships between hippocampal subregion volumes and episodic memory performance in PAE from 8-16 years (Roediger et al., 2021). Moreover, the relationship between hippocampal volume reductions and cognition in PAE may vary by sex, as suggested by work that found correlations between reduced hippocampal volumes and poorer visuospatial memory in females but not males with PAE (Treit et al., 2017).

As mentioned above, DTI allows for WM tract identification and the quantification of microstructure by way of diffusion maps, and it has largely been limited to WM in PAE (for recent reviews of DTI studies of white matter in PAE see (Ghazi Sherbaf et al., 2019; Nguyen et al., 2017). There is a single DTI study that examined four deep GM regions, including the caudate, globus pallidus, thalamus, and putamen, which demonstrated diffusion microstructural

abnormalities in children with PAE (Lebel et al., 2008). Although animal model finding suggest microstructural hippocampal changes, there were no diffusion MRI studies of the hippocampus in PAE prior to the published 5th chapter of this dissertation. A reasonable explanation for the lack of any diffusion MRI hippocampus studies in PAE is likely related to the challenges of imaging the hippocampus at high spatial resolution due to the limitations of how SS-EPI diffusion sequences have been applied. Most DTI studies generally use data acquired with ~8 mm^3 voxels (i.e., 2x2x2 = 8 mm^3); for instance, Lebel et al. 2008 used 8.9 mm^3 voxels. Hippocampal DTI is feasible at high spatial resolution ~8x higher than the majority of DTI studies with 1 x 1 x 1 = 1 mm^3 voxels as acquired in a 20 1 mm slice slab aligned to the long-axis (anterior-posterior) of the hippocampus (Treit et al., 2018). This acquisition only requires 5:18 minutes in scan time, thus it is applicable for use in children. Chapter 5 comprises the first published application of this high spatial resolution DTI as applied to examine group differences and relationships to memory performance in children to young adults with PAE (Solar et al., 2022).

Table 3.1: T1-weighted MRI studies of hippocampus volume in prenatal alcohol exposure.

	Age range (years)			Hippocampus Tracing	Hippocampus Volume (cm^3)			
	Controls	PAE	FASD		Controls	Sig diff	PAE	FASD
Archibald et al., 2001	7-24	10-22	8-19	Manual	2.20	no	2.10	1.80
Astley et al., 2009	12 (x̄)	12 (x̄)	13 (x̄)	Manual	3.40	>	3.00	2.90
Biffen et al., 2018	9-11	9-11	9-11	Manual	2.42	>	2.43	2.3
Coles et al., 2011	23 (x̄)	23 (x̄)	N/A	Automatic (FreeSurfer)	3.64	>	3.53* 3.34‡	N/A
Dodge et al., 2020	10 (x̄)	11 (x̄)	10 (x̄)	Automatic (FreeSurfer)	4.37	>	4.11	3.88
Dudek et al., 2014	12 (x̄)	13 (x̄)	N/A	Manual	1.69	>	1.26	N/A
Gross et al., 2018	14 (x̄)	13 (x̄)	N/A	Automatic (FreeSurfer)	4.20	>	4.00	N/A
Krueger et al., 2020	8-16	8-16	N/A	Automatic (FreeSurfer)	4.19	>	3.96	N/A
McLachlan et al., 2020	7-19	7-19	N/A	Automatic (FreeSurfer)	4.35	>	4.05	N/A
Nardelli et al., 2011	6-17	N/A	6-17	Automatic (FreeSurfer)	4.40	>	N/A	3.90
Riikonen et al., 2005	7-14	5-16	N/A	Manual	2.89	no	2.47	N/A
Roussotte et al., 2012	13 (x̄)	N/A	13 (x̄)	Automatic (FreeSurfer)	†	>	N/A	†
Treit et al., 2013	5-15	N/A	5-15	Automatic (FreeSurfer)	~4.30	>	N/A	~3.80
Treit et al., 2017	5-32	5-32	5-32	Automatic (FreeSurfer)	4.30	>	N/A	3.95
Uban et al., 2020	7-18	N/A	7-18	Automatic (FreeSurfer)	4.15	>	N/A	3.92
Willoughby et al., 2008	9-15	N/A	9-15	Manual	2.0	>	N/A	1.90

x̄ Mean age; range not provided
* PAE without dysmorphic effects
‡ PAE with dysmorphic effects
† Volumes not provided

Research

4. High-Resolution Diffusion Tensor Imaging of the Hippocampus Across the Healthy Lifespan[1]

Abstract

The human hippocampus is difficult to image given its small size, location, shape, and complex internal architecture. Structural magnetic resonance imaging (MRI) has shown age-related hippocampal volume changes that vary along the anterior-posterior axis. Diffusion tensor imaging (DTI) provides complementary measures related to microstructure, but there are few hippocampus DTI studies investigating change with age in healthy participants, and all have been limited by low spatial resolution. The current study uses high resolution 1 mm isotropic DTI of 153 healthy volunteers aged 5-74 years to investigate diffusion and volume trajectories of the hippocampus (whole, head, body, and tail) and correlations with memory. Hippocampal volume showed age related changes that differed between head (peaking at midlife), body (no changes) and tail (decreasing across the age span). Fractional anisotropy (FA) and mean, axial, and radial diffusivities (MD, AD, RD) yielded peaks or minima, respectively, at ~30-35 years in all three subregions of the hippocampus. Greater magnitude changes were observed during development than in aging. Age trajectories for both volume and DTI were similar between males and females. Correlations between tests of memory and FA and/or volume were significant in younger subjects (5-17 years), but not in 18-49 year olds or 50-74 year olds. MD was significantly correlated with memory performance in 18-49 year olds, but not in other age groups. Given the diffusion-weighted image contrast and resolution, head digitations could be examined revealing that the majority of

[1] A version of this chapter has been published. Solar K, Treit S, Beaulieu C. (2021) High resolution diffusion tensor imaging of the hippocampus across the healthy lifespan. *Hippocampus.* 31(12): 1271-1284.

subjects had 3-4 (48%) or 2 (32%) bilaterally with no effect of age. 1 mm isotropic DTI yielded high quality diffusion-weighted maps of the human hippocampus that showed regionally specific age effects and cognitive correlations along the anterior-posterior axis from 5-74 years.

4.1. Introduction

The hippocampus is challenging to image *in vivo* due to its small size, location, shape, and complex internal architecture (Duvernoy et al., 2013). Magnetic resonance imaging (MRI) studies of the healthy hippocampus have focused mainly on whole-structure volume measured on relaxation-weighted anatomical scans, and have found right-larger-than-left asymmetry (Malykhin et al., 2008; Nobis et al., 2019; Pedraza et al., 2004; Voineskos et al., 2015; Wellington et al., 2013), mixed findings for sex differences (Malykhin et al., 2017; Narvacan et al., 2017; Nobis et al., 2019; Wellington et al., 2013), and nonlinear changes with age (Malykhin et al., 2017; Narvacan et al., 2017; Walhovd et al., 2005; Yang et al., 2013).

There has also been interest in regional change along the anterior-posterior (A-P) axis, which is often coarsely segmented into the head, body, and tail (Duvernoy et al., 2013). MRI studies have shown volume/shape changes that differ along the A-P axis during development (Daugherty et al., 2017; Lin et al., 2013; Riggins et al., 2015, 2018) and aging (Chen et al., 2009; Gordon et al., 2013; Malykhin et al., 2008, 2017; Nordin et al., 2018). Head digitations visualized on MRI vary across healthy subjects (Piccirilli et al., 2020) and are reduced in Alzheimer's disease (Adler et al., 2018) and temporal lobe epilepsy (Henry et al., 2011; Oppenheim et al., 1998), but changes with typical aging have not been reported. Cognitive correlations with volume also vary along the A-P axis during development (De Master et al., 2014; Riggins et al., 2015, 2018; Schlichting et al., 2017) and aging (Chen et al., 2009; Hackert et al., 2002; Nordin et al., 2018).

Ex vivo diffusion tensor imaging (DTI) at ultra-high resolution has shown excellent depiction of internal hippocampal architecture and metrics linked to microstructure (Coras et al., 2014; Shepherd et al., 2007). *In vivo* DTI (at lower resolutions) has shown whole-hippocampus diffusion parameter differences in epilepsy (Kimiwada et al., 2006; Yokoi et al., 2019), preterm

children (Duerden et al., 2016), and Alzheimer's disease (Fellgiebel & Yakushev, 2011; Hong et al., 2013; Mak et al., 2017) relative to healthy controls. Hippocampus DTI metrics have been correlated with memory in development (Callow et al., 2020; Fjell et al., 2019), aging (Carlesimo et al., 2010; Den Heijer et al., 2012) and across the lifespan demonstrating stronger correlations in the elderly (Langnes et al., 2020). MD of the hippocampus decreases with age during development (Callow et al., 2020; Fjell et al., 2019; Mah et al., 2017), as does radial diffusivity (RD) (Mah et al., 2017), while FA increases (Fjell et al., 2019; Mah et al., 2017). The opposite pattern is observed in aging, which is associated with higher MD and lower FA (Anblagan et al., 2018; Carlesimo et al., 2010; Den Heijer et al., 2012; Pereira et al., 2014; Venkatesh et al., 2020). There is only one study that has examined hippocampal DTI (MD only) across the lifespan (4-93 years of age) reporting longitudinal decreases of anterior hippocampus MD from childhood until ~50 years, after which MD increased into the 90s, while posterior hippocampus MD did not change during childhood to adolescence, but increased at older ages (Langnes et al., 2020).

The above hippocampal DTI studies all used low spatial resolution 'whole brain' acquisitions with voxel volumes of 5-25 mm^3, with most using 2x2x2 = 8 mm^3. This prevents accurate depiction of hippocampal subregions and increases partial volume errors in diffusion quantification. The outlining of regions for diffusion measurements has thus relied on co-registration to much higher resolution anatomical imaging (e.g., T1 or T2), which leads to segmentation and co-registration errors. High resolution (1 mm^3 voxel volume) DTI of the hippocampus is feasible at 3T wherein twenty 1 mm axial-oblique slices, aligned along the long axis of the hippocampus, are acquired in 5.5 minutes (Treit et al., 2018). This protocol yields mean diffusion-weighted images (DWI) with excellent contrast and visualization of the external hippocampal surface and internal architecture, enabling direct segmentation (i.e., without co-

registration to T1/T2). This protocol has revealed subfield specific hippocampal diffusion abnormalities and correlations with verbal memory in epilepsy (Treit et al., 2019), but it has not yet been applied to study healthy neurodevelopment or aging.

The purpose of this study was to apply this 1 mm isotropic hippocampal DTI acquisition to 153 healthy volunteers aged 5 to 74 years to investigate: (i) cross-sectional trajectories of age-related change in volume and DTI metrics of the whole hippocampus, head, body and tail, (ii) cognitive correlations with hippocampus measures, and (iii) prevalence of hippocampal digitations across the lifespan.

4.2. Methods

4.2.1. Participant Demographics

Healthy volunteers (n = 153, 84 females/69 males) aged 5 to 74 years participated in this study (Figure 4.1a). Volunteers had no self-reported history of brain injury, neurological or psychiatric disorders. They were recruited through advertising and provided written informed consent prior to study participation. Both child assent and parent/guardian consent were obtained for volunteers under 18 years of age. This study was approved by the University of Alberta Human Research Ethics Board.

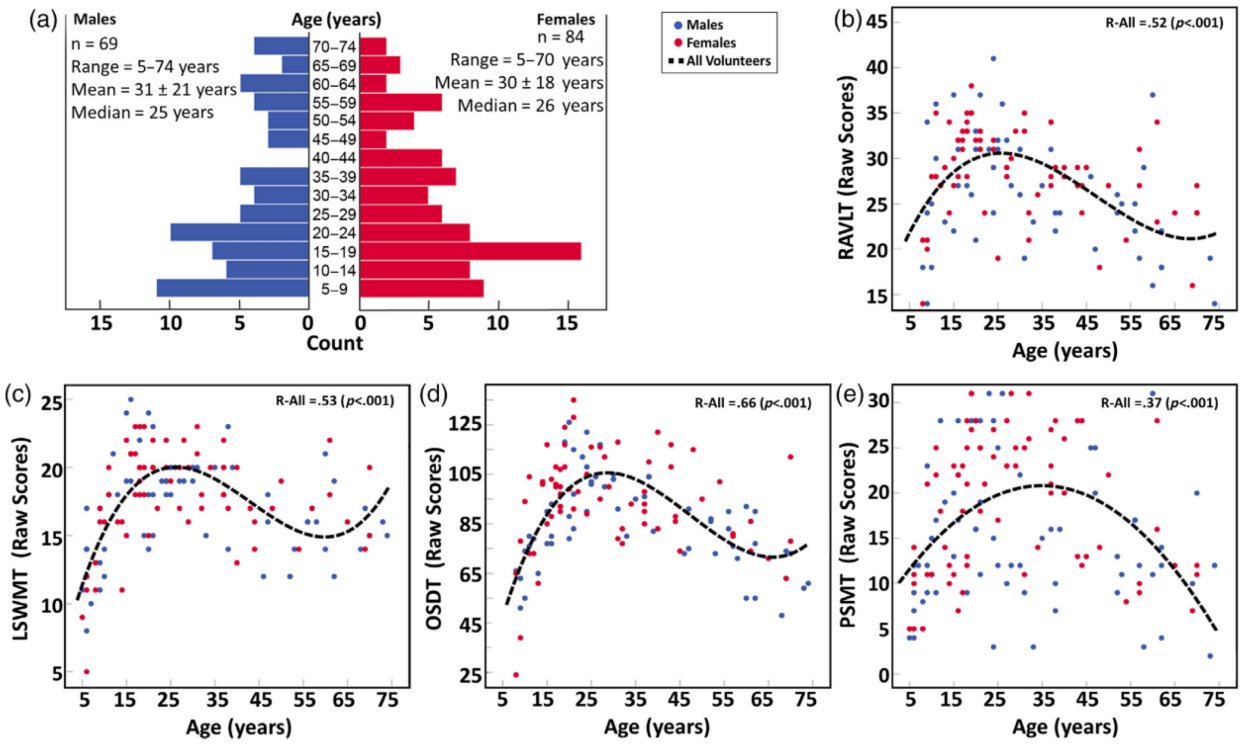

Figure 4.1: Demographics and cognitive scores. (a) Participant distribution as a function of both age and sex and (b-e) raw cognitive scores across the lifespan. (b) Rey Auditory Verbal Learning Test (RAVLT, immediate verbal recall), (c) List Sorting Working Memory Test (LSWMT, working memory) and (d) Oral Symbol Digit Test (OSDT, processing speed) all fit cubic models while (e) Picture Sequence Memory Test, (PSMT, acquisition, storage, and retrieval of novel information) fit a quadratic model. R and Benjamini–Hochberg false discovery rate (FDR-BH) corrected p values (in brackets) with a threshold of p = 0.035 are shown per plot.

4.2.2. Cognitive Assessment

The same four cognitive tests from the National Institutes of Health (NIH) Toolbox Cognitive Battery (Denboer et al. 2014) were administered to all participants to assess different aspects of memory performance: the Rey Auditory Verbal Learning Test (RAVLT) measures verbal recall; the List Sorting Working Memory Test (LSWMT) measures working memory capacity; the Oral Symbol Digit Test (OSDT) measures processing speed; and the Picture Sequence Memory Test (PSMT) provides an index of the ability to acquire, store and retrieve new information in the construct of episodic memory (Figure 4.1b-e).

4.2.3. MRI Protocol and Analysis

All MRI data was acquired using a 64-channel RF coil on the same 3T Siemens Prisma. 1 mm isotropic diffusion MRI data of the hippocampus was acquired with 20 1 mm slices, no gap, single shot 2D EPI (GRAPPA R2; 6/8 PPF; A/P phase encode), FOV 220 x 216 mm^2, matrix 220 x 216, BW 1420 Hz/px, 1x1x1 mm^3 with no interpolation, TE 72 ms, TR 2800 ms, diffusion-time 29 ms, b 500 s/mm^2 with 10 monopolar gradient directions and 10 averages (for a total of 100 diffusion weighted volumes), and 10 non diffusion weighted images in 5:18 min (Treit et al., 2018). The slices were aligned to the long axis of the hippocampus using a whole brain high resolution 3D T1-weighted MPRAGE for reference (0.85 mm isotropic; 3:39 min). Pre-scan normalize was used to minimize B1-inhomogeniety across the slice; this drastically improves visualization of the hippocampus on the b500 images with no effect on DTI parameters (Treit et al., 2018). MRtrix3 (Tournier et al., 2019) was used to process the diffusion data including denoising (Veraart et al., 2016), Gibbs-ringing (Kellner et al., 2016), eddy current and motion distortion correction, B1 field inhomogeneity correction (Tustison et al., 2010) and tensor parameter estimation to produce mean DWIs, and FA, MD, AD and RD maps (Figure 4.2).

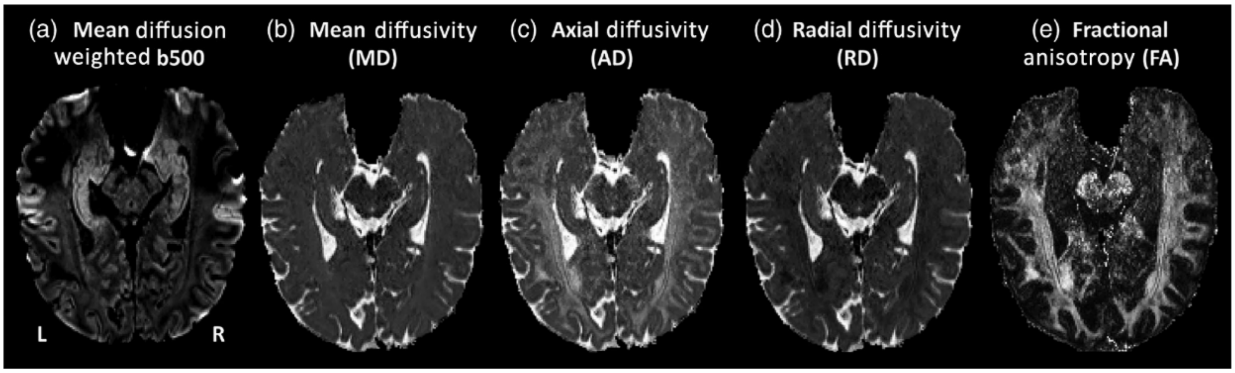

Figure 4.2: One millimeter isotropic DTI data. Example of 1 mm isotropic diffusion tensor imaging (DTI) data from a healthy 30-year-old male showing one slice of a (a) mean b500 diffusion-weighted image (DWI), and (b) mean diffusivity (MD), (c) axial diffusivity (AD), (d) radial diffusivity (RD), and (e) fractional anisotropy (FA) maps. In the mean DWI (a), the external borders and internal architecture of the hippocampus are well delineated, and the digitations of the head are clear and distinct from the adjacent amygdala.

4.2.4. Hippocampal Segmentation

Regions-of-interest (ROI) were traced manually by a single user (author KGS), blinded to participant age, on mean DWIs in the axial-oblique plane using ITK-SNAP (http://www.itksnap.org) (Yushkevich et al., 2006) to yield 3D segmentations of the whole hippocampus bilaterally. The whole hippocampus was segmented in accordance with the European Alzheimer's Disease Consortium (EADC) and Alzheimer's Disease Neuroimaging Initiative (ADNI) Harmonized Protocol (HarP) (Boccardi, Bocchetta, Apostolova, et al., 2015; Frisoni et al., 2015), wherein the procedure included the fimbria/alveus and whole tail but excluded the subiculum (Figure 4.3). Segmentations were drawn in the axial-oblique plane along the long hippocampal axis with reference to the coronal and sagittal planes, and edits were made in all planes in accordance with respective boundaries described in the EADC-ADNI HarP (Boccardi, Bocchetta, Apostolova, et al., 2015; Frisoni et al., 2015). Segmentations were then divided into head, body and tail using external landmarks which demarcate the anterior boundary of the body as the posterior end of the uncal apex, and the posterior boundary of the body as the posterior end

of the colliculi (Berron et al., 2017; Olsen et al., 2019). Volumes, FA, MD, AD, and RD were extracted from each whole hippocampus and subregion 3D ROI (Figure 4.4). Dice similarity index for intra-rater reliability of author KGS was 0.94 for the whole hippocampus ROIs, and 0.92 for the head, 0.91 for the body and 0.87 for the tail ROIs, as measured in 10% of the total sample (n = 15/153; 30 hippocampi), randomly chosen (from age bins stratified by each decade of life) according to the same age/sex distribution of the entire sample (females = 8, age range 5-74 years).

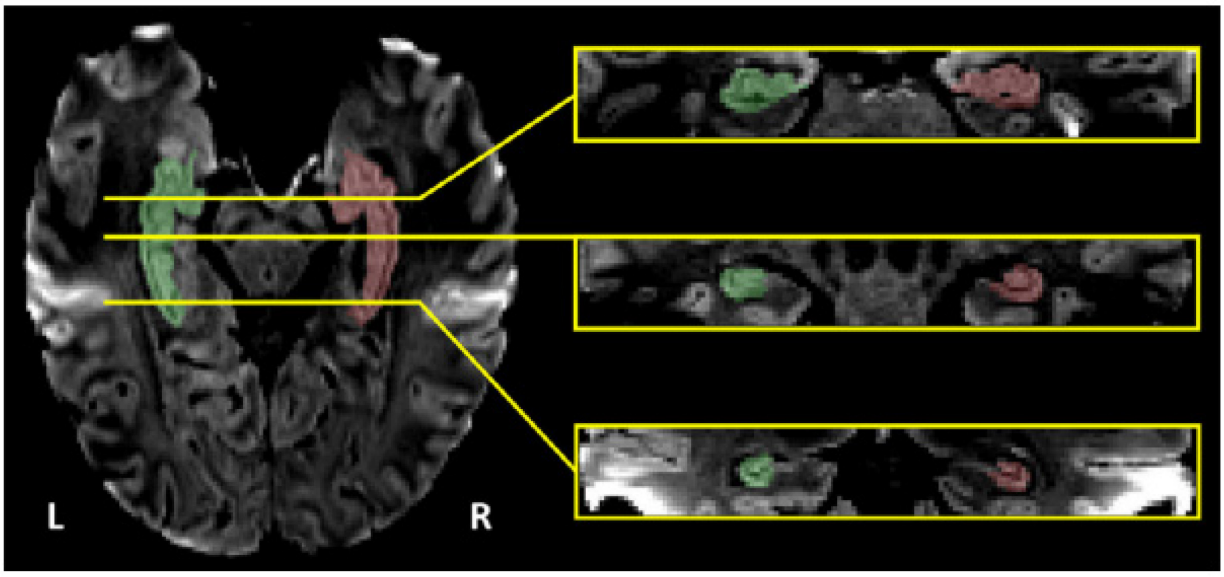

Figure 4.3: Manual hippocampus segmentation on mean DWI. Example of 1 mm isotropic diffusion tensor imaging (DTI) data and whole hippocampus segmentation from a healthy 28 year old female showing one axial-oblique slice of the mean diffusion weighted image (DWI) with three coronal slices (head, body, tail) featured along the hippocampal anterior-posterior axis, and the hippocampus segmentation overlay (green, left; red, right).

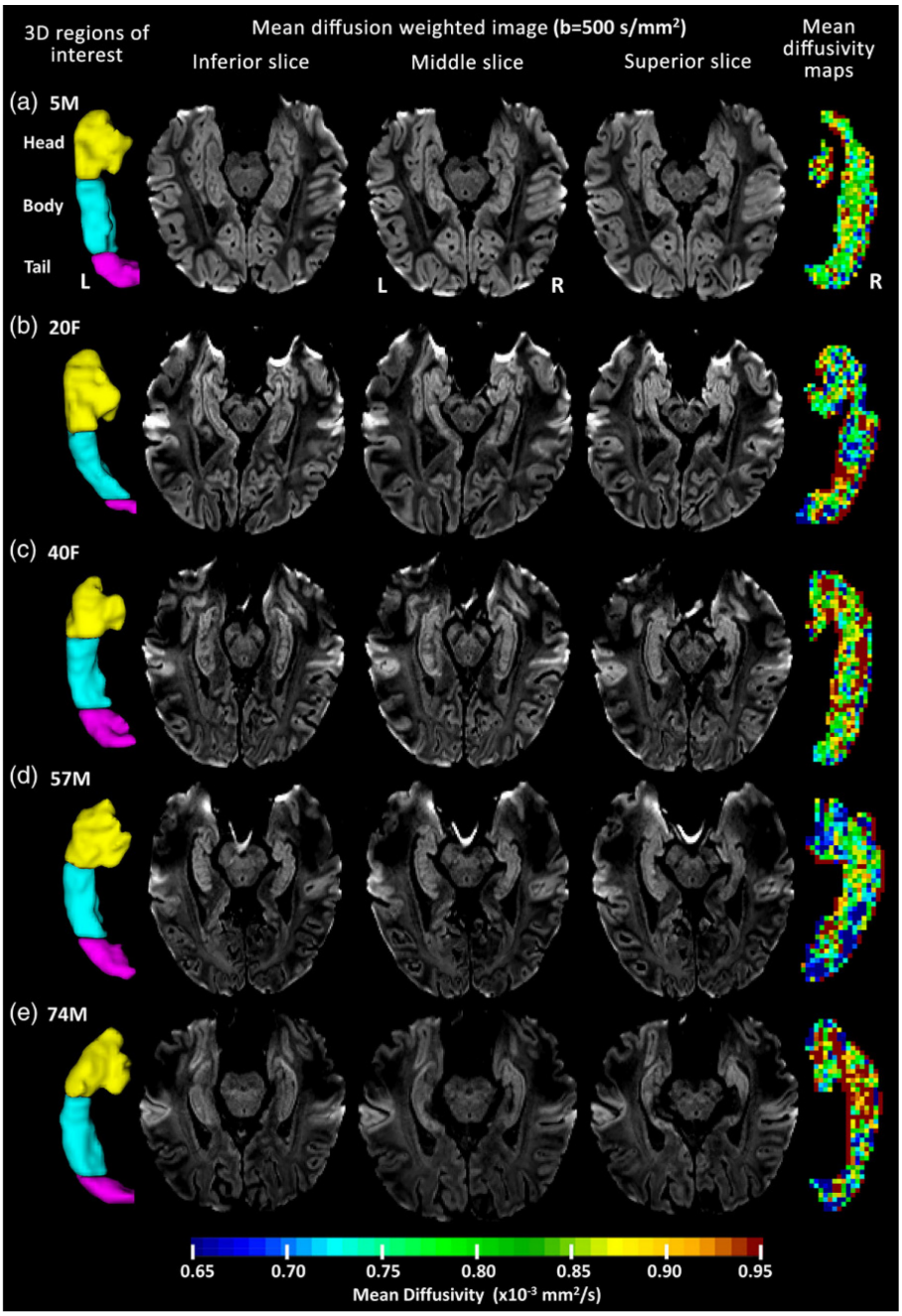

Figure 4.4: 3D segmentations, mean DWIs, and MD maps. 1 mm isotropic axial oblique mean diffusion weighted images (DWI) of three slices, manually traced head, body, and tail 3D regions-of-interest (ROIs) (left hippocampus of middle slice), and colour-coded mean diffusivity (MD) (right hippocampus of middle slice) in 5 healthy volunteers (2 females, F; 3 males, M) aged (A) 5, (B) 20, (C) 40, (D) 57, and (E) 74 years. There is marked inter-subject variability in the internal anatomy of the hippocampus (seen on the mean DWI) and in the external shape of the hippocampus (seen on the exterior ROI renderings). Also, note the digitations seen on the lateral and anterior hippocampal head in volunteers A (three), B (three), C (two) and D (three) – as opposed to volunteer E without prominent digitations. The MD maps are heterogeneous within each person, and there appears to be higher MD values at the youngest and oldest ages. Focal regions of very high MD (red) are likely cerebrospinal fluid spaces.

4.2.5. Hippocampal Digitations and Visual Evaluations

To investigate age related differences in the number of hippocampal head digitations, digitations were counted on the axial-oblique slices of the mean DWI (e.g., all mean DWI slices were examined including the slices in Figure 4.4). Hippocampi were categorized into those with three to four digitations (e.g., Figure 4.4a, b, d), two (e.g., Figure 4.4c), or one to none (e.g., Figure 4.4e), separately in each hemisphere. These three categories were plotted as a function of age to determine if the number of hippocampal digitations were related to age. Additionally, colour-coded MD maps of the hippocampus were created (Figure 4.4), which better allowed for visualization of regional MD differences.

4.2.6. Cerebrospinal Fluid (CSF) within the Hippocampus

As a marker of internal hippocampal atrophy, CSF volume within the hippocampus was calculated by applying an MD threshold of 1.5 $x10^{-3}$ mm^2/s (determined as the lower-end of the range of CSF MD values as measured in the lateral ventricles) within the whole hippocampal ROIs to produce CSF-only maps used to analyze age changes in hippocampal CSF volume, and to allow comparison with the whole structure volume.

4.2.7. Statistical Analysis

Statistical analyses were performed using SPSS version 26.0 (IBM Corp, 2019) and Prism (GraphPad, 2020), with Benjamini–Hochberg false discovery rate (FDR-BH) correction in MATLAB R2017a applied to all analyses.

4.2.7.1. Digitations

Independent samples Kruskal-Wallis tests were used to check for differences in age distribution across categories of head digitation count. These classifications were: (a) 3-4 digitations, (b) 2 digitations, and (c) 0-1 digitations.

4.2.7.2. Preliminary Analysis of Hemispheric Asymmetry and Sex Differences

Paired t-tests were used to examine hemispheric differences in volume, MD, AD, RD, and FA values. This revealed no hemispheric differences in diffusion metrics but some right-larger-than-left asymmetry in the volumes of the whole hippocampus (Right 2.37 ± 0.39 cm^3 > Left 2.22 ± 0.39 cm^3, $t(152) = -8.67$, $p < .001$) and head subregion (Right 1.16 ± 0.28 cm^3 > left 0.98 ± 0.25 cm^3, $t(152) = -12.92$, $p < .001$). However, since the primary focus was on diffusion, all left and right values were averaged prior to all remaining analysis. Likewise, independent samples t-tests were used to test for sex differences in the whole hippocampus, head, body and tail ROIs for volume and diffusion measurements, which revealed no sex differences in absolute volume or diffusion metrics. Therefore, data from males and females was combined for subsequent analyses (but separate male and female age-fits are also shown out of interest).

4.2.7.3. Curve Fitting for Age-Relationships

For each hippocampal diffusion and volume measurement, quadratic and cubic models were compared, and the best fit was chosen as the fit with the smallest AIC value and significant F test (FDR-BH corrected $p < 0.05$). This curve-fitting procedure was completed first in the entire participant pool, and then separately in males and females. Linear fits were not considered based on evidence from prior lifespan work indicating non-linear fits for DTI of white matter (WM) (Lebel et al., 2012; Slater et al., 2019), and volumetrics in the hippocampus (Langnes et al., 2020;

Malykhin et al., 2017; Narvacan et al., 2017; Walhovd et al., 2005) as well as visual evaluation of clear non-linear patterns in the raw data here.

4.2.7.4. Cognitive Correlations with Hippocampal Metrics

Age-adjusted residuals were calculated from the best-fit age regression models for volume, MD, and FA of each hippocampal ROI. The NIH Toolbox provided age standardized scores for the PSMT and LSWMT, but only raw scores for the RAVLT and OSDT. For the RAVLT and OSDT, the same curve fitting procedure described above was applied to fit raw scores with age (Figure 4.1b, d). Pearson's correlations were then tested between cognitive scores (residuals of the RAVLT and OSDT regressions, and standard scores for the PSMT and LSWMT) versus age-corrected residuals from the whole, head, body and tail volume, MD and FA regression models. Based on the age distribution of the current sample (Figure 4.1a) and age related patterns in the cognitive test raw scores (Figure 4.1b, c, d, e), this correlational analysis was completed separately within three age groups: (i) childhood to adolescence, 5 - 17 years (n = 47/153), (ii) young to middle adulthood, 18 - 49 years (n = 71/153), and (iii) middle to later adulthood, 50 - 74 years (n = 35/153). Note that AD/RD were excluded from the cognitive score correlations for simplification.

4.3. Results

4.3.1. Hippocampal Digitations and Visual Assessments

From 5-74 years, the hippocampus was well delineated on the 1 mm isotropic mean DWIs, showing marked inter-subject variability in the internal anatomy and digitations of the head, as well as in the external shape of the entire hippocampus (Figure 4.4). Overall, 48% of volunteers had 3-4 digitations bilaterally, 32% had 2 digitations bilaterally, 10% had 3-4 digitations on one

side and 2 on the other, 6% had 0-1 bilaterally, and 4% had 1 digitation on one side and 2 on the other. Overall, only 1/306 (0.3%) total hippocampi showed a count of 0 digitations. The various groupings of head digitation were evenly distributed across age and sex (data not shown). Compared to the younger ages of 5 years, the MD maps appear more elevated at middle age and then less so at older ages (Figure 4.4). Higher CSF-like MD values appeared as narrow A-P lines just inside/along the lateral or medial borders (e.g., Figure 4.4c, e) or as /pockets towards the head or tail (e.g., Figure 4.4b, c).

4.3.2. Age-related Volume and Diffusion Trajectories in the Hippocampus

Volume of the whole hippocampus best fit an inverted U-shaped quadratic model (Figure 4.5a) with a maxima at 31 years of age, at which point volume was 7% larger than at 5 years and 18% larger than at 74 years of age (Table 4.1). Likewise, the hippocampal head volume fit a quadratic model with a maxima at 37 years of age where volume was 17% larger than at 5 years, and 21% larger than at 74 years of age (Figure 4.6a; Table 4.1). The volume of the body did not change significantly with age (Figure 4.6b). The hippocampal tail volume fit a shallow quadratic model and was ~34% smaller at 74 years than 5 years (Figure 4.6c; Table 4.1). The volume of CSF within the whole hippocampus fit a quadratic model (Figure 4.5b) with a peak at 57 years of age where CSF volume was 208% higher than at 5 years, levelling off for the remainder of the lifespan (Figure 4.5b). Note that the peak CSF volume of ~32 mm^3 is only ~1% of the peak whole hippocampus volume (Table 4.1).

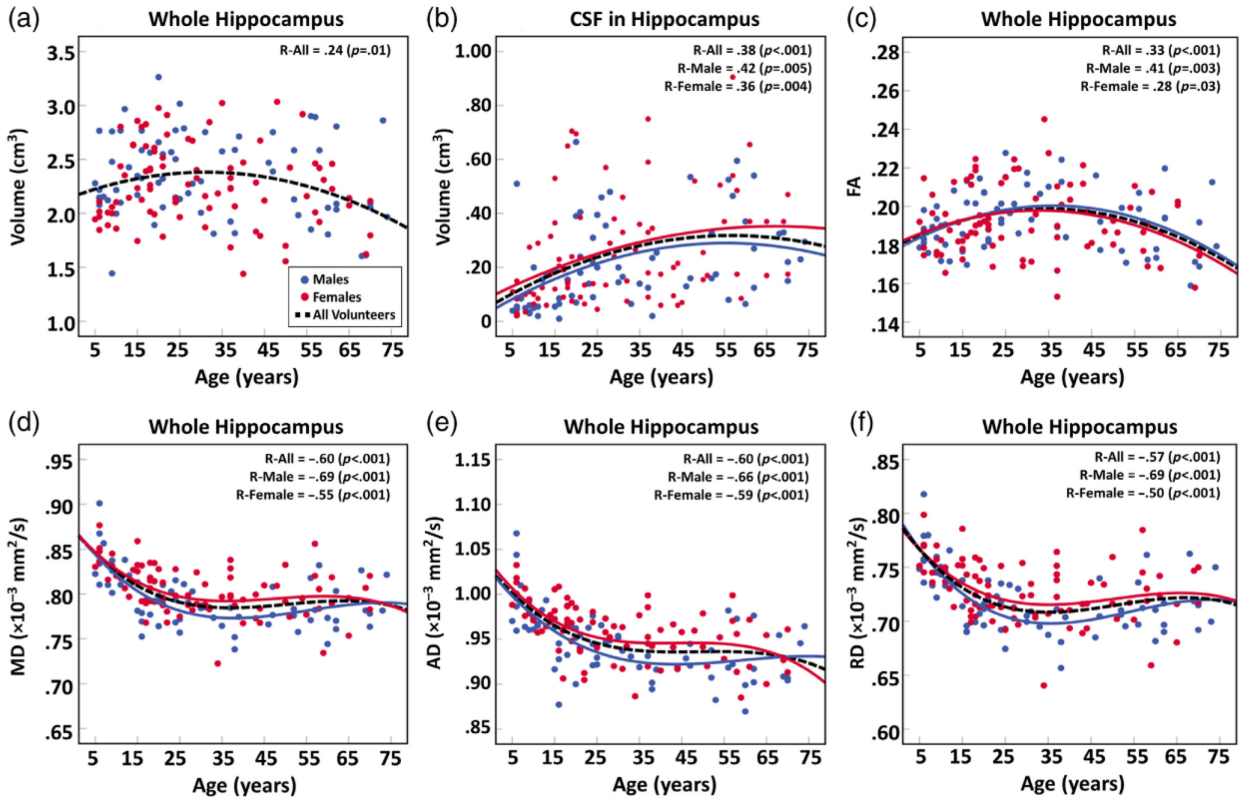

Figure 4.5: Whole-hippocampus age trajectories. Curve fitting results for age-related changes over 5-74 years in bilateral whole hippocampal metrics (average of left+right for volumes and diffusion metrics) for all 153 volunteers combined (black-dashed line), and males (blue) and females (red) fit separately. The fits were mainly quadratic or cubic with similar curves for males and females (only shown if significant). (a) Hippocampal volume was greater at mid-life than at younger or older ages, (b) while cerebral spinal fluid (CSF) volume was greatest at older ages. Relative to 5 years, (c) fractional anisotropy (FA) was larger and (d, e, f) mean, axial and radial diffusivities (MD, AD, RD) lower by middle age (~mid-30s) with subsequent plateaus and reverse changes with aging. R and Benjamini–Hochberg false discovery rate (FDR-BH) corrected p values (in brackets) with a threshold p = 0.035 are shown per plot.

Table 4.1: Hippocampus age trajectory metrics: Left/right average hippocampal volume and diffusion metrics versus age with relevant parameters for whole, head, body, and tail in all 153 volunteers aged 5-74 years.

		Best fit	Value at 5 years	Max/ min vertex values	% change from 5 years to max/min	Age (years) at max/min	Value at 74 years	% change from max/min to 74 years
Volume (L+R AVG) (mm^3)	Whole (W)	Quad	2225	2382	7.0	31	1963	-17.6
	Head (H)	Quad	977	1143	16.8	37	906	-20.7
	Body (B)	Non-sig	850				822	
	Tail (T)	Quad	424	419	-1.0	11	279	-33.6
	W - CSF	Quad	10	32	207.8	57	29	-7.7
FA	W	Quad	0.19	0.20	7.4	35	0.17	-12.4
	H	Quad	0.18	0.19	8.8	35	0.17	-13.3
	B	Quad	0.19	0.21	10.2	37	0.18	-12.3
	T	Quad	0.21	0.22	2.4	28	0.20	-9.6
MD ($x10^{-3}mm^2/s$)	W	Cubic	0.85	0.78	-7.3	38	0.78	0.2
	H	Cubic	0.84	0.77	-8.2	36	0.79	2.6
	B	Cubic	0.85	0.79	-6.7	37	0.80	0.3
	T	Cubic	0.84	0.80	-5.2	36	0.73	-4.3
AD ($x10^{-3}mm^2/s$)	W	Cubic	1.00	0.94	-6.6	45	0.93	-1.3
	H	Quad	0.98	0.91	-6.8	47	0.94	3.2
	B	Quad	1.00	0.94	-5.7	53	0.95	1.2
	T	Cubic	1.02	0.97	-5.3	31	0.91	-6.1
RD ($x10^{-3}mm^2/s$)	W	Cubic	0.77	0.71	-7.6	35	0.72	1.5
	H	Cubic	0.77	0.70	-9.0	35	0.73	3.4
	B	Quad	0.76	0.71	-6.6	44	0.74	4.1
	T	Quad	0.74	0.70	-4.8	59	0.71	0.4

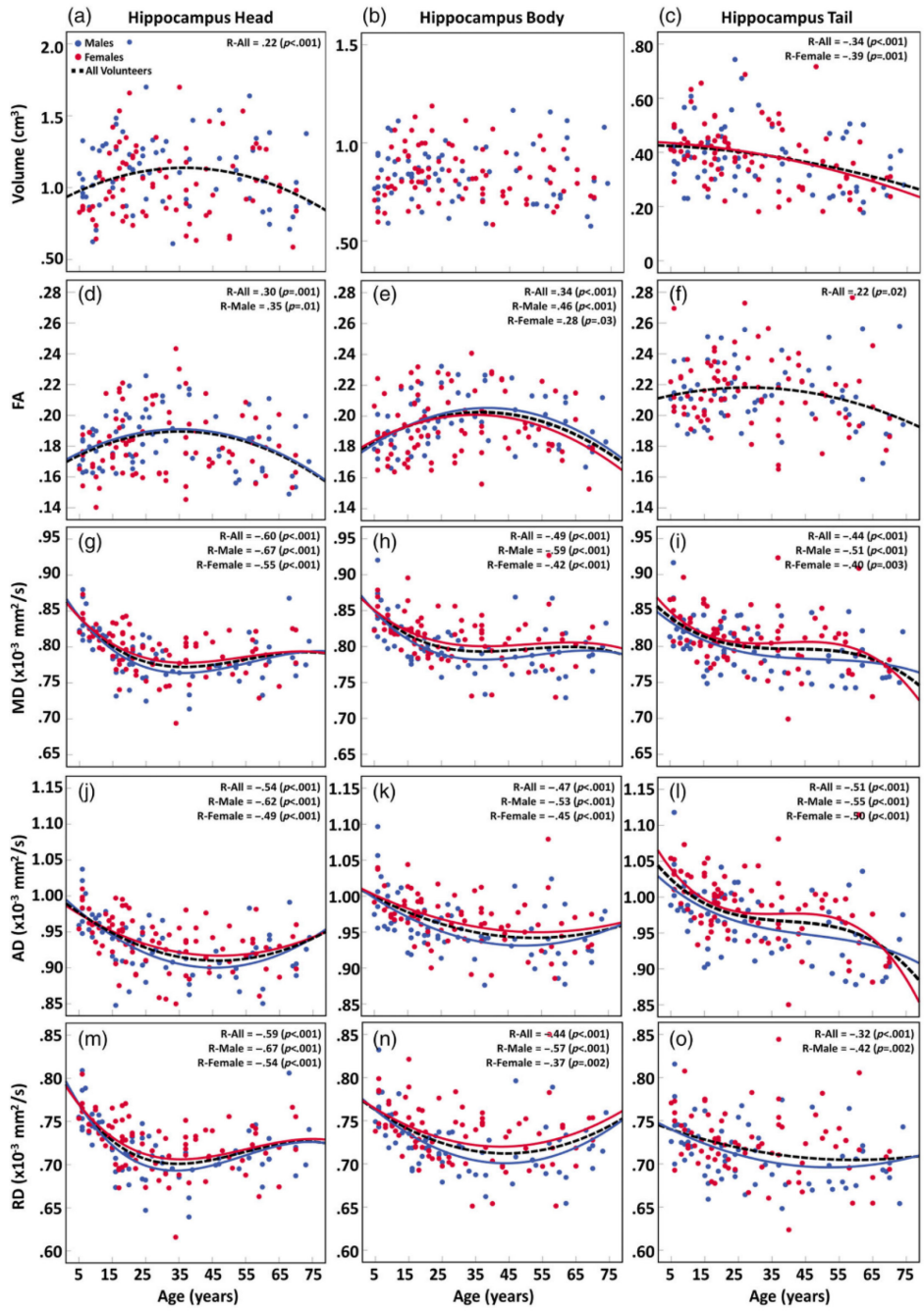

Figure 4.6: Hippocampal head, body, and tail age trajectories. Curve fitting results for age relationships over 5-74 years in bilateral average hippocampal metrics for the head (column 1), body (column 2), and tail (column 3) of all 153 volunteers combined (black-dashed line), and males (blue) and females (red) fit separately. (a-c) Volumes showed quadratic age trajectories in the head and tail but no significant fits in the body. (d-o) The head, body, and tail diffusion metrics (fractional anisotropy, FA; mean, axial and radial diffusivities, MD, AD, RD) had quadratic and cubic fits with steeper differences during neurodevelopment to middle age than from middle age to the elderly. Similar fits were observed between males and females for all metrics versus age (only shown when significant). R and Benjamini–Hochberg false discovery rate (FDR-BH) corrected p values (in brackets) with a threshold of p = 0.035 are shown per plot.

FA of the whole hippocampus best fit a quadratic model with a maxima at 35 years of age at which point FA was 7% higher than at 5 years, and 12% higher than at 74 years (Figure 4.5c; Table 4.1). Likewise, hippocampal head, body and tail FA fit inverted U-shaped models (Figure 4.6d, e, f) with the head and body showing the largest FA percent differences from 5 years to the maxima in the mid-30s (head +9%; body +10%, tail +2%) and similar percent reductions to 74 years for head (-13%) and body (-12%), but greater drops for tail (-10%; Table 4.1).

MD of the whole hippocampus best fit a cubic model with a minima at 38 years (7% lower MD than at 5 years) followed by a plateau with values at 74 years only ~1% higher than at the minima (Figure 4.5d; Table 4.1). Hippocampal head, body and tail MD also fit cubic models with similar ages of inflection, with percent changes from 5 years to the minima that were progressively smaller from head to tail (Figure 4.6g, h, i; Table 4.1). MD was 3% higher in the head and ~1% higher in the body at age 74 than at the mid-life minima, while tail MD showed a further drop of 4% in the elderly (Figure 4.6g, h, i; Table 4.1).

AD of the whole hippocampus best fit a cubic model reaching a minima at 45 years of age with 7% lower AD than at 5 years of age, and plateauing thereafter for the remainder of the lifespan (Figure 4.5e; Table 4.1). In the head and body, AD was best fit to quadratic models reaching minima in the mid-40s to early-50s, with values that were 7% lower in the head and 6% lower in the body than at age 5. AD was 3% higher in the head and 1% higher in the body at age 74 than at its mid-life minimum value (Figure 4.6j, k; Table 4.1). Hippocampal tail AD fit a cubic model which showed a 5% lower value at 31 years (relative to 5 years of age), followed by a plateau and a further 6% drop in the elderly (Figure 4.6l; Table 4.1).

RD of the whole hippocampus best fit a cubic model with a minima at 35 years (-8% lower than at 5 years, but only 2% lower than at 74 years (Figure 4.5f; Table 4.1). Hippocampal head RD fit a cubic model with a minima at 35 years (9% lower than at 5 years and 3% lower than at 74 years) (Figure 4.6m; Table 4.1). Hippocampal body and tail RD fit U-shaped models: body RD was 7% lower at its minima of 44 years than at 5 years, and 4% lower at 44 years than at 74 years, and tail RD was 5% lower to a plateau starting in the mid-30s (Figure 4.6n, o; Table 4.1).

Males and females fit the same models for each metric, with substantial overlap in the raw data (Figures 4.5-6).

4.3.3. Cognitive Performance versus Hippocampal Diffusion and Volume

Twelve correlations between (age-corrected) cognitive scores and diffusion metrics or volumes survived FDR-BH correction. Nine of 12 correlations were found in the youngest age group (Figure 4.7a). Notably, 6 of these were positive correlations between volume and RAVLT (whole – Figure 4.7b, body, tail), LSWMT (whole – Figure 4.7c, head), and OSDT (body). The other 3 correlations in the young group were negative correlations between FA (whole – Figure 4.7d, head, body) and PSMT performance. The remaining 3 correlations were found in the middle age group (18-49 years), all positive correlations between MD (whole and head) with RAVLT and/or PSMT (Figure 4.7a). There were no cognitive correlations in the older (50-74 years) group (Figure 4.7a).

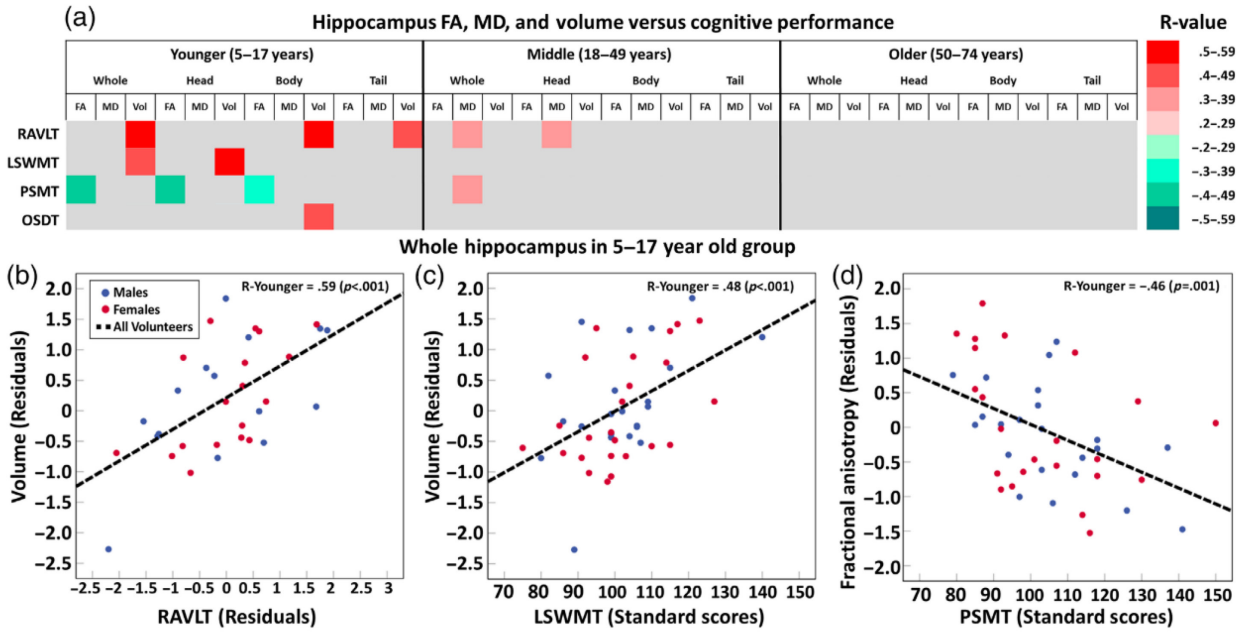

Figure 4.7: Hippocampus memory correlations. (a) Linear correlations (red – positive; green – negative; all p values shown are Benjamini–Hochberg false discovery rate (FDR-BH) corrected with threshold of p = 0.014) between age corrected residuals of hippocampus (whole, head, body, and tail) fractional anisotropy (FA), mean diffusivity (MD), and volume versus four cognitive performance scores. Nine of 12 significant correlations were found in the youngest age (5-17-year-olds) group. RAVLT, LSWMT, and OSDT scores were positively correlated with hippocampal volumes (better performance with larger volumes) whereas the PSMT was negatively correlated with FA (better performance with lower FA). The other 3/12 correlations between MD and cognitive scores in the middle age group were all positive; better performance was associated with higher MD, while no correlations were observed in the older group. (b-d) Example scatter plots are shown for significant whole hippocampus correlations all in the youngest group (5-17 years). RAVLT - Rey Auditory Verbal Learning Test for immediate verbal recall; LSWMT - List Sorting Working Memory Test for working memory performance; PSMT - Picture Sequence Memory Test for acquisition, storage, and retrieval of novel information; and OSDT - Oral Symbol Digit Test for processing speed.

4.4. Discussion

This study is the first to apply high resolution (1 mm isotropic) DTI of the hippocampus (Treit et al., 2018) to study healthy development and aging. Head, body and tail macro- (volumes) and micro-structure (via DTI parameters) showed distinct trajectories with age in this cross-sectional study of 153 healthy participants aged 5 to 74 years. Most of the subregion volume/DTI measures (11/15; Figure 4.6) reached a maximum or minimum in mid-life, with steeper changes of diffusivity metrics during development than aging. Body volume was the only measurement to

show no correlation with age. Males and females had similar relationships with age for all metrics. Diffusion metrics showed more marked changes over the lifespan than volumes. For cognition, only the younger age group had significant correlations between cognitive scores and age-adjusted volume (positive correlations) or FA (negative correlations), and only the middle age group showed significant correlations between cognitive scores and age-adjusted MD (positive correlations). No correlations between hippocampus metrics and cognitive scores were found in older subjects.

There are two primary methodological differences (relative to previously published work) that lend confidence to these results. First, the DTI protocol was designed to examine the hippocampus at 1 mm isotropic resolution, in contrast to previous work that measured diffusion in the hippocampus on image resolutions typically 8x that (2x2x2 = 8 mm^3) or worse, using protocols designed for whole brain white matter tract analysis. Few (if any) of the previous hippocampus diffusion papers show mean diffusion-weighted images or DTI parameter maps, likely given their low spatial resolution. The low spatial resolution will cause marked partial volume effects with adjacent CSF spaces (low FA, high diffusivity), which will worsen with age-related atrophy, confounding this macroscopic change with diffusion indicated measures of microstructure. Second, in this study the hippocampus was delineated with time consuming manual region-of-interest directly on the mean diffusion-weighted images, which is possible given the image quality and contrast, as opposed to using automated segmentation software to extract the hippocampus contours on 3D T1-weighted images which are then transferred to co-registered DTI images/maps to extract the diffusion values. This latter approach is problematic given known EPI distortions in diffusion acquisition that may cause poor alignment between the hippocampus on diffusion and T1 images. Additionally, it is well known that T1-based automated segmentation methods

overestimate the extent of the hippocampus considerably, e.g. ~4400 mm^3 volume in one hemisphere with FreeSurfer versus ~2500 mm^3 with manual tracing (Akudjedu et al., 2018); the latter being closer to our maximum curve fitted value of ~2400 mm^3 manually traced on DWI directly (Table 4.1, Figure 4.5a). This additional 2000 mm^3 of voxels identified by the automated T1 segmentation strongly suggests that diffusion metrics are being measured in non-hippocampal tissue in prior work. Although it has clear advantages over automated methods, manual segmentation of the hippocampus into the head/body/tail by way of external landmarks (Olsen et al., 2019) is still limited by age related changes in the positions of these landmarks. For instance, the uncal apex has been shown to move in the anterior direction from 18-87 years, a change which can effectively reduce hippocampal head volume and increase body volume (Poppenk, 2020). A continuous evaluation along the axis would be ideal, though diffusion metrics are less affected by these divisions than measures of volume.

To our knowledge, only one previous study has reported diffusion metrics (MD, but not FA, AD, or RD) along the anterior/posterior axis of the hippocampus across the lifespan of 4-93 years (Langnes et al., 2020). This longitudinal study acquired DTI with typical 2 mm isotropic resolution and used FreeSurfer based segmentation on T1-weighted images to measure diffusion on co-registered maps (see concern in previous paragraph), splitting the hippocampus into two regions – anterior (i.e., head) and posterior (i.e., body and tail combined). Both anterior and posterior regions showed small increases of volume with age from 4 to 20 years, after which volume of the anterior plateaued until ~60 years decreasing thereafter; whereas volume of the posterior hippocampus showed steeper reductions starting at ~40 years. The latter observation is mainly in agreement with our quadratic volume correlation in the tail; however, we do not observe a greater magnitude reduction of head volume with aging relative to the increase seen in childhood.

The reduction of anterior MD in development to a minimum around age 40 years agrees with our minimum age of 38 years, as well as the magnitude of MD reduction (~$0.08x10^{-3}$ mm^2/s from their Figure 4.3a versus our change of $0.07x10^{-3}$ mm^2/s reported in Table 4.1). However, their anterior MD increases from 4-93 years are far steeper than observed for the head and body MD in our Canadian cohort, though our age range is almost two decades shorter than their Norwegian cohort (74 instead of 93 years). There is greater disagreement between our two studies for MD versus age in the posterior region, which we have separated into body and tail. They report no posterior MD changes from 4 to 40 years followed by a steep increase. In our case, both the body and tail show MD decreases until middle but then levels off (i.e., does not steeply increase) for the remainder of the age-span. It is possible that the elevated MD observed by Langnes et al in the elderly is related to the hippocampal volume reductions and partial volume effects with neighboring CSF, given their low spatial resolution. Discrepancies may also relate to differences in fitting procedures since we applied nonlinear regression in a cross sectional sample, while they used a generalized additive mixed-models approach in longitudinal data. Finally, our study may have been more sensitive to age changes in development relative to aging since our sample was slightly skewed with a greater number of volunteers at younger ages (Figure 4.1a).

4.4.1. Hippocampal Macrostructure (Volume) Age Trajectories

Whole hippocampus volume measured on the 1 mm DWI fit a shallow quadratic trajectory over the ages of 5-74 years, suggesting subtle differences with age and lots of intersubject variability (e.g. individual values ranging from ~1800-3000 mm^3 per hippocampus at any given age across the lifespan; Figure 4.5a), in agreement with previous work examining whole hippocampus volumes (for example: Narvacan et al., 2017). Absolute volumes were in agreement with previous manual measures on 3D T1-weighted scans (for example: Akudjedu et al., 2018).

Hemispheric asymmetry of volumes for the whole hippocampus (right>left) are also in agreement with prior volumetric studies (for example: Nobis et al., 2019). Volumes versus age differed between head (quadratic with maximum in mid-life), body (no correlation) and tail (quadratic decrease), in line with prior T1/T2/proton density volumetric studies that showed distinct A-P trajectories of hippocampal size and shape maturation; however, specific patterns are inconsistent between studies (Daugherty et al., 2017; De Master et al., 2014; Gogtay et al., 2006; Lynch et al., 2019). In healthy aging, findings are slightly more consistent, with several reports agreeing that the macrostructure of the head is disproportionally affected (Wang et al., 2003; Wolf et al., 2015; Yang et al., 2013), while others find age related change only in the body (Malykhin et al., 2017).

Ninety percent of the volunteers in the present study had 2-4 digitations bilaterally, with no age or sex differences. Although the implications of this observation in our cohort are unclear, this finding does agree with a recent developmental study which examined healthy volunteers from 18-39 years and showed that the majority of the sample (~88%) had 2-3 digitations (Piccirilli et al., 2020). Additionally, the current analysis showed that ~10% of volunteers had a hippocampus with 0-1 digitations, but only 0.3% of total hippocampi (1/306) showed no digitations, also in agreement with recent work (Piccirilli et al., 2020). Furthermore, inter-hemispheric concordance was very high here, with zero participants having 3-4 digitations in one hemisphere and 0-1 in the other, which may help to provide a baseline for observations in pathological conditions with marked asymmetry of hippocampal macrostructure such as hippocampal sclerosis (Oppenheim et al., 1998).

4.4.2. Hippocampal Microstructure (Diffusion) Age Trajectories

Whole hippocampus MD, AD and RD were highest at the youngest ages, decreasing by 7-8% to a minimum at 35-45 years, followed by a slight increase of 1.5% by 74 years. Conversely,

FA was lowest at the youngest ages, increasing by 7% to a peak at 35 years of age, followed by a decrease of 12% at 74 years. Prior diffusion studies of the whole hippocampus likewise show lower MD/RD and higher FA in older children or young adults relative to younger children in cross-sectional (Callow et al., 2020; Mah et al., 2017) and longitudinal work (Fjell et al., 2019). The reverse pattern is evident in healthy aging in which MD is higher and FA is lower in older adults relative to younger adults in cross-sectional studies (Carlesimo et al., 2010; Den Heijer et al., 2012; Pereira et al., 2014; Venkatesh et al., 2020; Wolf et al., 2015) and longitudinal studies (Anblagan et al., 2018).

Similar DTI parameter age fits were observed for head, body, and tail as whole hippocampus here, with changes at younger ages most apparent in the head followed by the body then the tail. Greater diffusivity changes in the head may be related to a disproportionate amount of inter-subfield connections (potentially represented by pyramidal cell connections from cornu ammonis 1, CA1, to the lacunosum-molecular, part of the perforant pathway) relative to the body and tail as reported in a post-mortem diffusion MRI study (Beaujoin et al., 2018). Although our study was limited to the head, body and tail, future analyses should segment the CA/dentate gyrus (DG) subfields, this is possible at least for the body on 1 mm DWI as has been shown previously (Treit et al., 2018). Lower diffusivities with neurodevelopment may reflect decreases of extracellular space in combination with increases of neurogenesis rates (number and size of neurons), cellular barriers, dendritic branching and axonal packing (e.g., stratum granulosum, CA3 stratum pyramidale) (Coras et al., 2014; Shepherd et al., 2007). Elevations of FA during development (due to greater reductions of RD than AD) may reflect increased axonal packing as well as myelination of the intra-hippocampal connections crossing throughout the hippocampus and in specific regions like the alveus and axons leading into the fimbria (Coras et al., 2014;

Shepherd et al., 2007). FA showed greater aging effects than MD potentially reflecting demyelination given the greater increase of RD over AD (Song et al., 2002). Overall, the age trajectories of hippocampal diffusion appear distinct from those of volume, and provide additional information regarding the evolution of hippocampal microstructure across the lifespan that volume and shape analyses cannot show.

4.4.3. Hippocampal DTI Correlations to Memory Performance

Nine hippocampus-memory correlations were observed in the youngest group, 6 of which were positive correlations between volumes (2 whole, 1 head, 2 body, and 1 tail) and RAVLT, LSWMT, or OSDT. The other 3 correlations in the young group were negative correlations between FA (whole hippocampus, head and body) and PSMT. The remaining two correlations were found in the middle age group, which showed positive correlations between MD and the RAVLT or PSMT (2 whole, 1 head). The finding of larger hippocampal volumes with better memory in development is generally supported by prior volume findings (De Master et al., 2014; Fjell et al., 2019; Langnes et al., 2020), although one study has shown that smaller volumes in the head correlated with better memory (Schlichting et al., 2017). Moreover, subfield volumetrics in 4-8 year-old children revealed that smaller CA1 and larger CA2-4/DG volumes in the body were associated with better memory (Riggins et al., 2018), thus highlighting the importance of examining these subfields in future studies. Larger hippocampus volumes in relation with better memory may be explained by increased neuron count and/or size, as well as increased number of axonal and/or dendritic connections. On the other hand, prior DTI studies have typically found associations between lower MD and/or higher FA with better memory performance (Callow et al., 2020; Fjell et al., 2019; Langnes et al., 2020; Venkatesh et al., 2020) while the is opposite is found here with better performance correlating with higher MD in the middle age group and lower FA

in the young group. Also opposite to our results is a diffusion imaging study of aging (acquired with high in-plane resolution) which focused on the perforant pathway of the hippocampus, finding correlations only in older subjects which suggested that perforant path degradation is associated with poorer Rey Auditory Verbal Learning performance (Yassa et al., 2010). Although unexpected, the association of better memory with both lower FA (and higher MD) values in our study may be explained by the development of hippocampal WM crossing fibres. This notion is supported by a recent study which suggested that lower FA from 22-35 years in medial stratum radiatum/lacunosum/molecular and CA1 subfields may be due to crossing-fibre areas where the perforant pathway enters from the entorhinal cortex (Patel et al., 2020). DTI cannot disentangle crossing-fibres and calculates artificially low FA in areas where 2 or more fiber bundles overlap, therefore the development of a new fiber bundle to make a crossing area would result in lower FA values in a given region (Jones et al., 2013). In consideration of the complex internal architecture of the hippocampus, future studies should utilize diffusion reconstruction models such as constrained spherical deconvolution which can disentangle crossing and other intricate fibre bundle orientations (Jeurissen et al., 2014).

A greater number of correlations in the youngest age group relative to middle aged and older subjects is perhaps not surprising given their greater dynamic range of improvement in cognitive score, and change in hippocampal MRI metrics. Although Langnes et al. 2020 reported generally stronger correlations with older age, another adult lifespan study provides support for the current finding by showing that higher whole-hippocampus FA correlated with better episodic memory in a younger group (20-38 years) but not an older group (59-84 years) (Venkatesh et al., 2020). It is possible that age-related reductions in memory performance later in life are related to the degradation of other memory-involved cortical (e.g., entorhinal cortex) and/or subcortical gray

matter structures (e.g., anterior thalamic nucleus) or WM tracts (e.g., fornix), rather than changes in the hippocampus, as these other brain regions do not share the unique hippocampal propensity to undergo neurogenesis into late adulthood (Lee & Thuret, 2018). Another reason for the age discrepancies, related to the plasticity of the brain, may be that older adults depend less than children and adolescents on the hippocampus for these memory processes (Venkatesh et al., 2020).

4.5. Conclusions

High-resolution 1 mm isotropic DTI yielded excellent visualization and contrast within the hippocampus across 5 to 74 years in 153 healthy volunteers, enabling quantification of diffusion metrics and volume directly on the diffusion images. Hippocampal volume and FA peaked in the mid-30s with similar magnitude increases in development as decreases in aging. In contrast, MD, AD, and RD decreased to a greater extent from childhood to adulthood than the small increase observed with aging. Hippocampus correlations with specific cognitive functions were observed primarily in childhood to adolescence. Males and females appear to show similar hippocampal maturation across the lifespan in relation to age. High resolution DTI of the hippocampus in this healthy cohort will form the basis of comparison to numerous neurological or psychiatric disorders.

5. High-resolution Diffusion Tensor Imaging Identifies Hippocampal Volume Loss without Diffusion Changes in Individuals with Prenatal Alcohol Exposure[2]

Background: Magnetic resonance imaging (MRI) studies of prenatal alcohol exposure (PAE) commonly report reduced hippocampal volumes, which animal models suggest may result from microstructural changes that include cell loss and altered myelination. Diffusion tensor imaging (DTI) is sensitive to microstructural changes but has not yet been used to study the hippocampus in PAE.

Methods: Methods: Thirty-six healthy controls (19 females; 8 to 24 years) and 19 participants with PAE (8 females; 8 to 23 years) underwent high-resolution (1 mm isotropic) DTI, anatomical T1-weighted imaging, and cognitive testing. Whole-hippocampus, head, body, and tail subregions were manually segmented to yield DTI metrics (mean, axial, and radial diffusivities—MD, AD, and RD; fractional anisotropy—FA), volumes, and qualitative assessments of hippocampal morphology and digitations. Automated segmentation of T1-weighted images was used to corroborate manual whole-hippocampus volumes.

Results: Gross morphology and digitation counts were similar in both groups. Whole-hippocampus volumes were 18% smaller in the PAE than the control group on manually traced diffusion images, but automated T1-weighted image segmentations were not significantly different. Subregion segmentation on DTI revealed reduced volumes of the body and tail, but not the head. There were no significant differences in diffusion metrics between groups for any hippocampal region. Correlations between age and volume were not significant in either group, whereas negative

[2] A version of this chapter has been published. Solar K, Treit S, Beaulieu C. (2022) High-resolution diffusion tensor imaging identifies hippocampal volume loss without diffusion changes in individuals with prenatal alcohol exposure. *Alcoholism: Clinical and Experimental Research.* 46(7): 1204-1219

correlations between age and whole-hippocampus MD/AD/RD, and head/body (but not tail) MD/AD/RD were significant in both groups. There were no significant effects of sex, group by age, or group by sex for any hippocampal metric. In controls, seven positive linear correlations were found between hippocampal volume and cognition; five of these were left lateralized and included episodic and working memory, and two were right lateralized and included working memory and processing speed. In PAE, left tail MD positively correlated with executive functioning, and right head MD negatively correlated with episodic memory.

Conclusions: Reductions of hippocampal volumes and altered relationships with memory suggest disrupted hippocampal development in PAE.

5.1. Introduction

Prenatal alcohol exposure (PAE) is the most common preventable cause of birth defects worldwide (Lange et al., 2017; Popova et al., 2019). Decades of animal research have demonstrated that the effects of PAE on the brain depend on genetics, timing, amount, and pattern of alcohol exposure (Petrelli et al., 2018). Magnetic resonance imaging (MRI) studies of the brain in mouse models of PAE have shown right side hippocampal volume reductions (Parnell et al., 2009, 2014) as well as shape changes in the absence of volume changes (Parnell et al., 2013). Histological studies in rat models also reveal reduced volume, pyramidal cell density, and number in cornu ammonis (CA) 1 associated with PAE during the third trimester, reduced volume in CA3 from exposure during any trimester, and reduced pyramidal cell density and number in CA3 from exposure during the third trimester (Livy et al., 2003). More recent work in mice suggests that PAE alters oligodendrocyte generation and myelination in the hippocampus (Niedzwiedz-Massey et al., 2021). Apoptosis in the hippocampus is also observed in guinea pig models of PAE (Green et al., 2005). Moreover, PAE mouse models demonstrate poor performance on hippocampus-dependent tasks, suggesting long-term learning and memory impairments (Brady et al., 2012).

Early MRI case studies in humans reported severe atrophy of the hippocampus (qualitatively assessed) in a small number of children with heavy PAE (Mattson & Riley, 1995). Quantitative measurements of whole-hippocampus volume from T1-weighted MRI with PAE have demonstrated volume reductions in the neonate period (Donald et al., 2016) that persist into childhood to adulthood, demonstrating 5% to 25% smaller hippocampal volumes in participants with PAE than in healthy controls (Astley et al., 2009; Biffen et al., 2018, 2020; Coles et al., 2011; Dodge et al., 2020; Dudek et al., 2014; Gross et al., 2018; Krueger et al., 2020; McLachlan et al., 2020; Nardelli et al., 2011; Roussotte et al., 2012; Treit et al., 2013, 2017; Uban et al., 2020;

Willoughby et al., 2008). One study also provided evidence that the magnitude of hippocampal volume reduction is greater in individuals with PAE-related facial dysmorphology than in those with PAE but no dysmorphic facial features (Coles et al., 2011). Structural MRI further suggests that reductions of hippocampal volume in PAE may be regionally specific, with one study showing volume reductions in the posterior (body and tail combined) but not anterior hippocampus (Dudek et al., 2014). Likewise, shape abnormalities in the head and tail (but not the body) have also been reported in children with PAE (Joseph et al., 2014). One study demonstrated that expected sex differences (female hippocampal volumes smaller than males) were present in controls but absent in individuals with PAE (McLachlan et al., 2020). Moreover, machine learning of multivariate models for the prediction of PAE diagnosis based solely on brain volumes identified right hippocampus volume in the top five features for a male-specific model that was not as highly ranked in a female-specific model (Little & Beaulieu, 2020).

Smaller hippocampal volumes in PAE are also associated with poorer spatial navigation in children (Dodge et al., 2020), impaired verbal learning and verbal and spatial recall in children and adolescents (Willoughby et al., 2008), and impaired verbal and nonverbal memory performance in adults (Coles et al., 2011). However, a recent study showed no correlations between hippocampal subregion volumes and episodic memory in 8 to 16-year olds with PAE (Roediger et al., 2021), whereas another reported smaller hippocampal volumes in PAE in association with better episodic memory in 9 to 11-year olds (Biffen et al., 2018), suggesting that relationships between hippocampal volume and memory function are not straightforward. Furthermore, this relationship may differ between males and females, as suggested by one study showing correlations between reduced hippocampal volumes and poorer visuospatial memory in females but not males with PAE (Treit et al., 2017).

A complementary method to T1-weighted imaging is diffusion tensor imaging (DTI). DTI is typically used to study white matter since it enables virtual identification of major tracts that have a high degree of diffusion anisotropy and yields diffusion metrics indicative, but not specific to, tissue microstructure (e.g., axon packing/myelination) within those tracts. Thus, DTI studies in PAE have mainly been limited to white matter (for recent reviews of DTI studies of white matter in PAE see Ghazi Sherbaf et al., 2019; Nguyen et al., 2017); however, one DTI study has assessed four deep gray matter regions (putamen, caudate, globus pallidus, and thalamus) showing regional diffusion parameter differences in children with PAE (Lebel et al., 2008). Despite animal models suggesting microstructural changes, DTI of the hippocampus has not been investigated in PAE, presumably due to challenges in accurately depicting the hippocampus on the low spatial resolution acquisitions designed for whole brain (Lebel et al., 2008 DTI acquisition resolution was $1.7 \times 1.7 \times 3 = 8.9$ mm^3). A recently developed high-resolution in vivo diffusion MRI protocol (1 mm3 voxel volume; ~8× higher resolution than typical whole-brain protocols) of the hippocampus has been demonstrated to yield mean diffusion-weighted images (DWI) with exceptional definition of the external surface and internal anatomy (e.g., stratum lacunosum moleculare, SLM), allowing for regional quantification of diffusion parameters within the hippocampus (Treit et al., 2018).

The current study acquired 1 mm isotropic DTI of the hippocampus in 19 individuals with PAE (aged 8 to 23 years) and 36 healthy controls (aged 8 to 24 years). The purpose was to examine: (i) group differences (PAE vs. controls) in hippocampal volume and DTI metrics (whole, head, body, and tail) as well as a qualitative evaluation of digitations, general size and shape, and internal architecture; (ii) cross-sectional trajectories with age for hippocampus volume and diffusion metrics; and (iii) correlations between age-adjusted cognitive performance and hippocampal volume and DTI metrics.

5.2. Materials and Methods

5.2.1. Participants

The healthy control group included 36 volunteers (aged 8 to 24 years; mean 14.5 ± 4.5 years; 19 females) and the PAE group included 19 volunteers (aged 8 to 23 years; mean 14.6 ± 4.1 years; 8 females). Controls were enrolled as part of a larger normative study on brain development through advertising on campus and in local community venues (e.g., recreation centers) and were screened for self-reported history of brain injury or neurological/psychiatric disorders. Volunteers in the PAE group were recruited through advertising and word of mouth, had confirmed prenatal alcohol exposure, and had been previously assessed in one of several fetal alcohol spectrum disorder (FASD) clinics in Alberta. PAE was confirmed by the FASD clinic via chart reviews, justice system and child services documentation, and family interviews. Two participants had a diagnosis of FASD with mild facial dysmorphology, 14 had a diagnosis of FASD without sentinel facial features, and three had confirmed prenatal alcohol exposure but were not given a formal diagnosis for various reasons (e.g., the child met criteria but was too young at the time of assessment, etc.). One of the children with confirmed PAE also had documented mild facial features (as assessed by a developmental pediatrician), but assessment by the FASD clinic was not completed and therefore, a formal diagnosis was not given. None of the participants with PAE had a diagnosis of partial fetal alcohol syndrome (pFAS) or fetal alcohol syndrome (FAS). Written informed consent was obtained from all participants, and both child assent and parent/guardian consent were obtained for volunteers under the age of 18 years. This study was approved by the University of Alberta Human Research Ethics Board.

5.2.2. Cognitive Assessment

Both groups completed six tests from the National Institutes of Health Toolbox (NIHTB) Cognition Battery (http://www.healthmeasures.net/exploremeasrement-systems/nih-toolbox; Denboer *et al.*, 2014). Together, these tests assessed four distinct cognitive domains: (i) episodic memory by the Picture Sequence Memory Test (PSMT) and the Rey Auditory Verbal Learning Test (RAVLT); (ii) executive function by the Flanker Inhibitory Control and Attention Test (FICAT) and the Dimensional Change Card Sort Test (DCCST); (iii) working memory by the List Sorting Working Memory Test (LSWMT); and (iv) processing speed by the Oral Symbol Digit Test (OSDT). The NIHTB generates age-standardized scores for the PSMT, LSWMT, FICAT, and DCCST. However, the NIHTB produces only raw scores for the RAVLT and OSDT; therefore, normative data (Slotkin et al., 2012b, 2012a) were used to calculate age-standardized z scores for these two tests.

5.2.3. MRI Protocol and Image Processing

MRI data were acquired on a 3T Siemens Prisma equipped with a 64 channel RF coil. One millimeter isotropic diffusion MRI of the hippocampus was acquired with 20 1 mm slices, no gap, single-shot 2D EPI (GRAPPA R2; 6/8 PPF; A/P phase encode), FOV 220 × 216 mm^2, matrix 220 × 216, BW 1420 Hz/px, 1 × 1 × 1 mm^3 with no interpolation, TE 72 ms, TR 2800 ms, diffusion time 29 ms, b 500 s/mm^2 with 10 monopolar gradient directions and 10 averages (for a total of 100 diffusion-weighted volumes), and 10 non-diffusion-weighted images in 5:18 min (Treit et al., 2018). Prescan normalize was used to minimize B1-inhomogeneity across the slice, in turn, improving hippocampal visualization on the b500 diffusion-weighted images with no effect on DTI parameters (Treit et al., 2018). The 20 slice slab was aligned parallel to the long axis of the hippocampus on a whole-brain high-resolution 3D T1-weighted MPRAGE acquired with 208 0.85

mm sagittal slices, GRAPPA R3, FOV 250 × 250 mm^2, matrix 288 × 288, 0.87 × 0.87 × 0.85 mm^3, TE 2.37 ms, TR 1800 ms, TI 900 ms in 3:39 min.

For diffusion data processing, MRtrix3 (Tournier et al., 2019) was used to apply denoising (Veraart et al., 2016), Gibbs-ringing (Kellner et al., 2016), eddy current and motion distortion correction, B1 field inhomogeneity correction (Tustison et al., 2010), tensor parameter estimation, and to produce mean DWI, fractional anisotropy (FA), mean, axial, and radial diffusivity (MD, AD, and RD) maps (Figure 5.1).

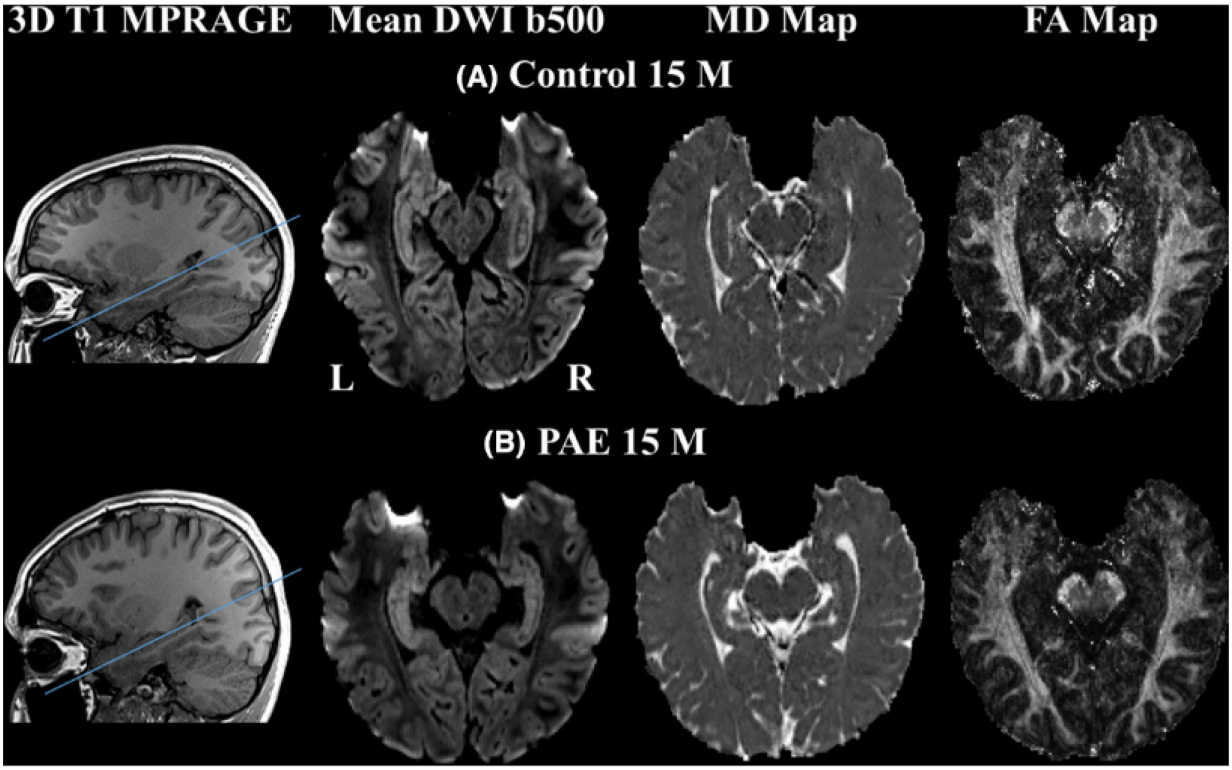

Figure 5.1: Diffusion weighted images and maps in a healthy control and in prenatal alcohol exposure. (A) Healthy control (15 year old male) and (B) an age- and sex-matched participant with prenatal alcohol exposure (PAE) showing examples of a 3D T1-weighted MPRAGE with a blue line representing the plane of acquisition for the diffusion slices featured to the right, 1 mm isotropic mean diffusion-weighted image (DWI, b = 500 s/mm2), mean diffusivity (MD), and fractional anisotropy (FA) maps. The external borders and internal architecture of the hippocampus are well defined in both groups, with the hippocampal head digitations visibly separate from the adjacent amygdala on the mean DWI. No qualitative group differences were evident in the diffusion images maps. L, left; R, right.

5.2.4. Manual Hippocampus Segmentation on Mean DWI (Whole and Subregion Volumes and Diffusivities)

Regions of interest (ROI) were manually segmented on mean DWIs by a single user (author KGS) blinded to participant age and group in ITK-SNAP (http://www.itksn ap.org) (Yushkevich et al., 2006), to yield 3D segmentation of the whole-hippocampus bilaterally which were then divided into head, body, and tail subregions. Bilateral volumes, FA, MD, AD, and RD were extracted from each whole-hippocampus and subregion 3D ROI (Figure 5.2). The segmentation procedure and intra-rater reliability (for author KGS) for segmentation of healthy controls are reported in a recent hippocampal DTI lifespan study (Solar et al., 2021). Inter-rater reliability (authors KGS and ST; bilateral segmentations of 15 healthy controls) was assessed using the Dice similarity index yielding 86% voxel overlap between raters, and an intraclass correlation coefficient of 0.96 for volume. Intra- and inter-rater reliabilities were analyzed only in the healthy controls because there was no evidence to suggest that manual segmentation methods would be influenced by group. The mean DWIs demonstrated that the hippocampi of both groups had similar gross morphology and overall shape (i.e., there were no overt structural abnormalities such as those seen in epilepsy; e.g., Treit *et al.*, 2019), internal architecture, and contrast of tissue boundaries.

5.2.5. Hippocampal Visual Evaluation and Digitation Counting

In order to evaluate qualitative differences between groups, mean DWIs and 3D ROIs of the manually traced hippocampi were visually inspected for: (i) the prevalence of digitations on the head, (ii) the presence of the SLM, (iii) the overall size and shape (e.g., narrowing along the medial– lateral axis and/or shortening along the anterior-posterior axis); and (iv) the appearance of hippocampal or parahippocampal abnormalities (e.g., hyperintensities) on the mean DWIs.

5.2.6. Automatic Hippocampus Segmentation on T1-Weighted Images (Whole Volumes)

For comparison between volumes derived from automated T1-weighted image segmentations versus manual tracing on high-resolution DTI, T1-weighted images were segmented using the automated pipeline volBrain (http://volbrain.upv.es) (Manjón & Coupé, 2016) using both the whole brain and HIPS segmentation pipelines (Romero et al., 2017). The most recent HIPS pipeline allows for segmentation with or without the subiculum (Kulaga-Yoskovitz et al., 2015) (HIPS K-Y), therefore generating a total of three automated whole-hippocampus volumes from the T1-weighted images: volBrain's whole-brain protocol (includes subiculum), HIPS K-Y pipeline with subiculum, and HIPS K-Y without subiculum.

5.2.7. Cerebrospinal Fluid (CSF) within the Hippocampus

As a marker of internal hippocampal atrophy, CSF volume within the hippocampus was calculated by applying an MD threshold of 1.5×10^{-3} mm^2/s (determined as the lower end of the range of CSF MD values as measured in the lateral ventricles) to yield the volume of voxels within the hippocampus presumed to contain primarily CSF.

5.2.8. Statistical Analysis

Statistical analyses were performed using IBM SPSS Statistics for Windows, version 28.0 (IBM Corp., Armonk, NY, USA, 2021) with Benjamini-Hochberg false discovery rate (FDR-BH) multiple comparison correction in MATLAB R2017a (MathWorks Inc., Natick, MA, USA) applied to all analyses.

5.2.8.1. Demographics and cognitive testing

Independent sample t-test was used to check for group differences in age, foster care placements, and number of psychiatric medications. Chi-squared test was used to test for group

differences in categorical variables (i.e., sex, ethnicity, living situation, and psychiatric comorbidities; Table 5.1). Analysis of covariance (ANCOVA) was used to test first for the main effects of group and sex, and second for interaction effects of the group by sex if sex or group had a significant effect on the age-standardized scores of each cognitive test.

Table 5.1: Demographic and clinical data. Controls and prenatal alcohol exposure (PAE) demographic and clinical information. Benjamini–Hochberg false discovery rate (FDR-BH) corrected threshold of $p \leq 0.02$.

	Control (n = 36)	**PAE (n = 19)**	**Group Difference Test Statistic (p)**
Age (years): mean, standard deviation, range	14.5 ± 4.5 (8–24)	14.6 ± 4.1 (8–23)	ns
Females	19 (53%)	8 (42%)	ns
Ethnicity	n = 33	n = 16	
Caucasian	20 (61%)	4 (25%)	$\chi2 = 5.47$ (p=.02)
Aboriginal	6 (18%)	7 (43%)	ns
Metis	2 (6%)	2 (13%)	ns
Other	5 (15%)	3 (19%)	ns
Living situation	n = 33	n = 17	
Biological parent(s)	30 (91%)	0 (0%)	$\chi2 = 38.64$ (p<.001)
Adopted/biological relative	0 (0%)	13 (76%)	$\chi2 = 34.10$ (p<.001)
Foster care	0 (0%)	1 (6%)	ns
Independent	3 (9%)	3 (18%)	ns
Foster care placement per person (mean, range)	0 (0-0)	1.6 (0-5)	ns
Basic needs not met at any time	0/33 (0%)	5/13 (31%)	$\chi2 = 14.10$ (p<.001)
Psychiatric co-morbidities	n = 36	n = 19	
Attention-deficit/ hyperactivity disorder	0 (0%)	9 (47%)	$\chi2 = 22.74$ (p<.001)
Reactive attachment disorder	0 (0%)	1 (5%)	ns
Anxiety	0 (0%)	3 (16%)	$\chi2 = 5.53$ (p=.02)
Other	0 (0%)	9 (47%)	$\chi2 = 22.74$ (p<.001)
Psychiatric medications	n = 36	n = 19	
Atypical antipsychotics	0 (0%)	4 (21%)	ns
Stimulants	0 (0%)	7 (37%)	t = -3.24 (p=.005)
Antidepressants	0 (0%)	1 (5%)	ns
Other	0 (0%)	11 (58%)	t = -2.35 (p<.001)

Table 5.2: Cognitive test scores. Age-standardized cognitive test scores in controls and prenatal alcohol exposure (PAE). Benjamini–Hochberg false discovery rate (FDR-BH) corrected threshold of $p \leq 0.008$.

Test		Mean ± Standard Deviation		Main Effects	
		Controls	PAE	Group F (p)	Sex F (p)
PSMT	Episodic Memory	104 ± 16 (n = 35)	101 ± 10 (n = 19)	ns	ns
RAVLT	Immediate Recall (z score)	1.15 ± 1.50 (n = 35)	-0.16 ± 1.72 (n = 19)	7.71 (*p=.008*)	ns
LSWMT	Working Memory	104 ± 13 (n = 35)	92 ± 12 (n = 19)	11.69 (*p=.001*)	ns
OSDT	Processing Speed (z score)	0.90 ± 1.60 (n = 34)	-0.10 ± 1.79 (n = 19)	ns	ns
FICAT	Attention & Executive Function	99 ± 14 (n = 35)	86 ± 11 (n = 19)	10.54 (*p=.002*)	ns
DCCST	Executive Function	107 ± 21 (n = 35)	102 ± 13 (n = 18)	ns	ns

Abbreviations: DCCST, Dimensional Change Card Sort Test; FICAT, Flanker Inhibitory Control and Attention Test; LSWMT, List Sorting Working Memory Test; OSDT, Oral Symbol Digit Test; PSMT, Picture Sequence Memory Test; RAVLT, Rey Auditory Verbal Learning Test.

Table 5.3: Hippocampal digitation counts. Control and prenatal alcohol exposure (PAE) hippocampal digitation counts.

Digitation Category	Digitation Count Left/Right	Controls Percentage	PAE Percentage
Highly Digitated	4/4	5.5	5.3
	3/4 or 4/3	5.5	0
	3/3	36.1	52.6
Moderately Digitated	2/3 or 3/2	38.9	26.3
Less Digitated	2/2	14.0	10.5
	3/1	0	5.3

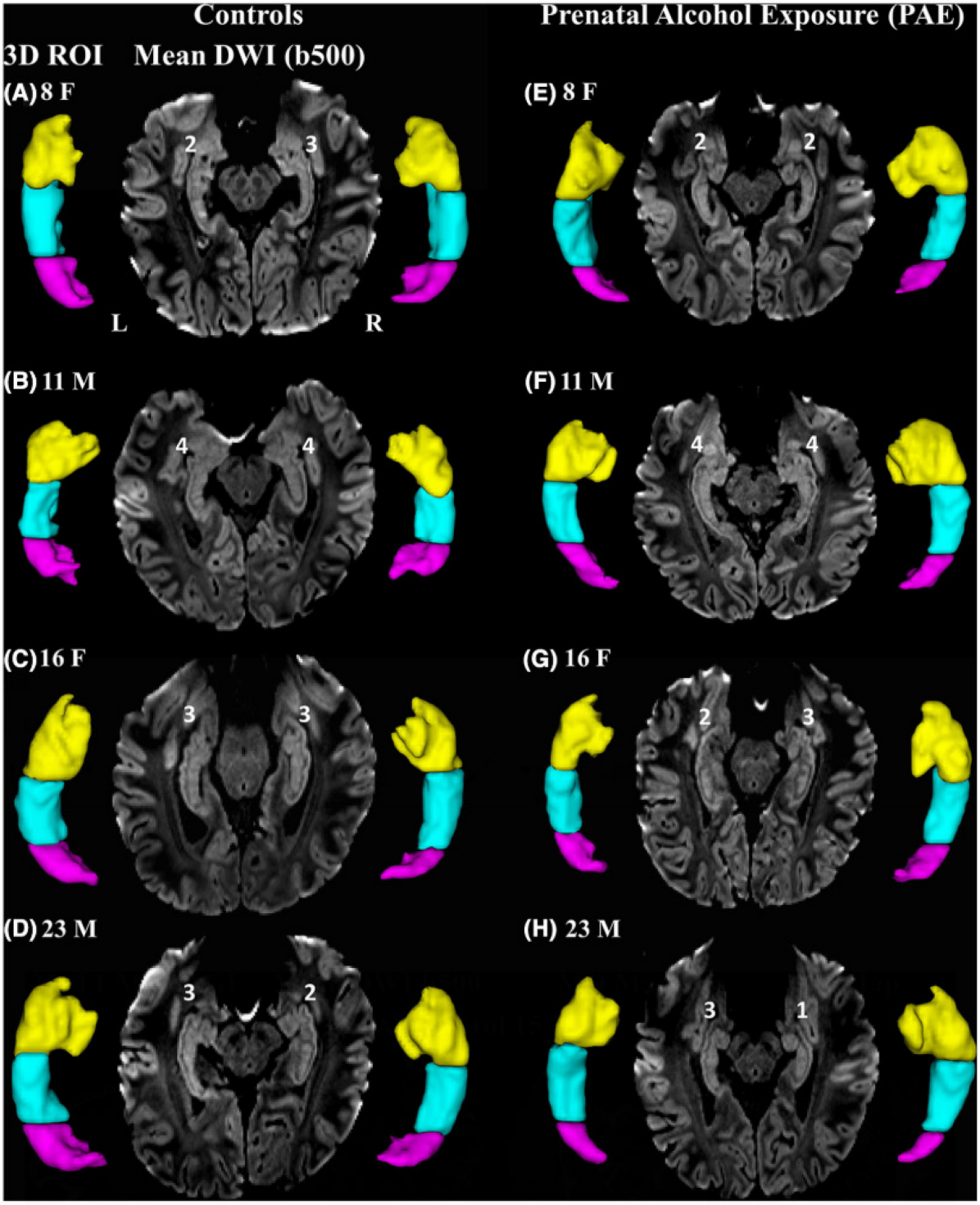

Figure 5.2: Hippocampus manual segmentations and mean diffusion-weighted images for healthy controls and individuals with prenatal alcohol exposure. Manually traced head (yellow), body (blue), and tail (pink) 3D regions of interest (ROIs) of the left (L) and right (R) hippocampus, and an axial-oblique mean diffusion-weighted image (DWI, b = 500 s/mm2) slice from the middle of the hippocampus in four pairs of age- and sex-matched control (A–D) and prenatal alcohol exposure (PAE) (E–H) participants. Digitation counts (numbers anterior to the hippocampus) are also similarly distributed among participants across the age span of both groups.

5.2.8.2. Digitations

Chi-squared test was used to test for group differences in categories of digitation counts (hemispheres combined). The categories included highly digitated (three to four digitations per side; six to eight total), moderately digitated (two digitations on one side and three on the other; five total), and less digitated (two per side, or three on one side, and one on the other; four total).

5.2.8.3. Hippocampus Volumes and DTI Metrics

Since the primary focus of this investigation was on diffusion, which showed no hemispheric differences in either group (data not shown), left and right values of all hippocampus MRI metrics were averaged for group and age analyses. A General Linear Model (GLM) was applied in two steps. First, ANCOVA with age and sex as covariates was used to test for group differences in volume, CSF volume, FA, MD, AD, and RD of the whole-hippocampus, head, body, and tail subregions (left and right averaged for all measures). Second, group by age and group by sex interaction effects were tested when at least one variable (group, sex, and age) in the interaction had a significant main effect. Next, for each hippocampal measurement that showed a main effect of age in the first ANCOVA and non-significant interaction effects in the second ANCOVA, linear regression was applied to test hippocampal age changes separately in each group.

5.2.8.4. Correlations between Cognitive Performance and Hippocampus Metrics

Given known lateralization of function in the hippocampus (Burgess et al., 2002), left and right hippocampi were assessed separately for correlations with cognitive function. Pearson's correlations between age-standardized cognitive scores and volume/MD of the right and left whole hippocampus, head, body, and tail were assessed separately in each group. If there was a significant main effect of age on hippocampal metrics as tested above, then age-adjusted residuals of

hippocampal measures were used in correlations. Note that AD and RD were excluded from the cognitive analysis to simplify analysis and reduce multiple comparisons. FA was also excluded given the lack of group and age effects.

5.3. Results

5.3.1. Demographics and Cognitive Performance

The PAE and control groups did not differ in age or sex but did significantly differ in ethnicity, living situation, comorbidities, and number of psychiatric medications (Table 5.1). Significant main effects of the group showed lower age-standardized scores in immediate recall, working memory, and attention and executive function (Table 5.2). There were no main effects of sex or group by sex interactions for any of the cognitive tests.

5.3.2. Qualitative Evaluation of High-Resolution Diffusion Images of the Hippocampus

All hippocampi in both groups were well delineated on the 1 mm isotropic mean DWIs (Figure 5.2). Both groups showed the consistent presence of the SLM, similar general shape and curvature of the whole structure, and absence of hippocampal or parahippocampal hyperintensities on the mean DWIs (Figure 5.2). The only marked qualitative difference was that the general size of the hippocampus appeared to be consistently smaller in the PAE group relative to the controls, particularly with respect to a reduced length of the long axis (anterior to posterior) rather than a narrowing of the lateral–medial axis. The distribution of hippocampal digitation counts was similar across both groups with highly, moderately, and less digitated at 47%, 39%, and 14% for controls and 58%, 26%, and 16% for PAE ($\chi 2 = 0.14$, $p = 0.93$) (Table 5.3).

5.3.3. Volumes and Diffusion Metrics from High-Resolution DTI (Left + Right Averaged)

Whole-hippocampus volumes, as measured by manual segmentation on the 1 mm DWI, were 18% smaller in the PAE group relative to controls (Figure 3A), with no significant effects of sex or group by sex interactions. Group differences of whole-hippocampus volume appear to be driven by volume reductions in the body (23% smaller in PAE) and tail (22% smaller in PAE), while the head was not significantly different between groups (Figure 3B). The volume of CSF within the whole hippocampus was not significantly different between groups (data not shown). There were no significant effects of group (Figure 3C–F), sex, or group by sex for any diffusion metric.

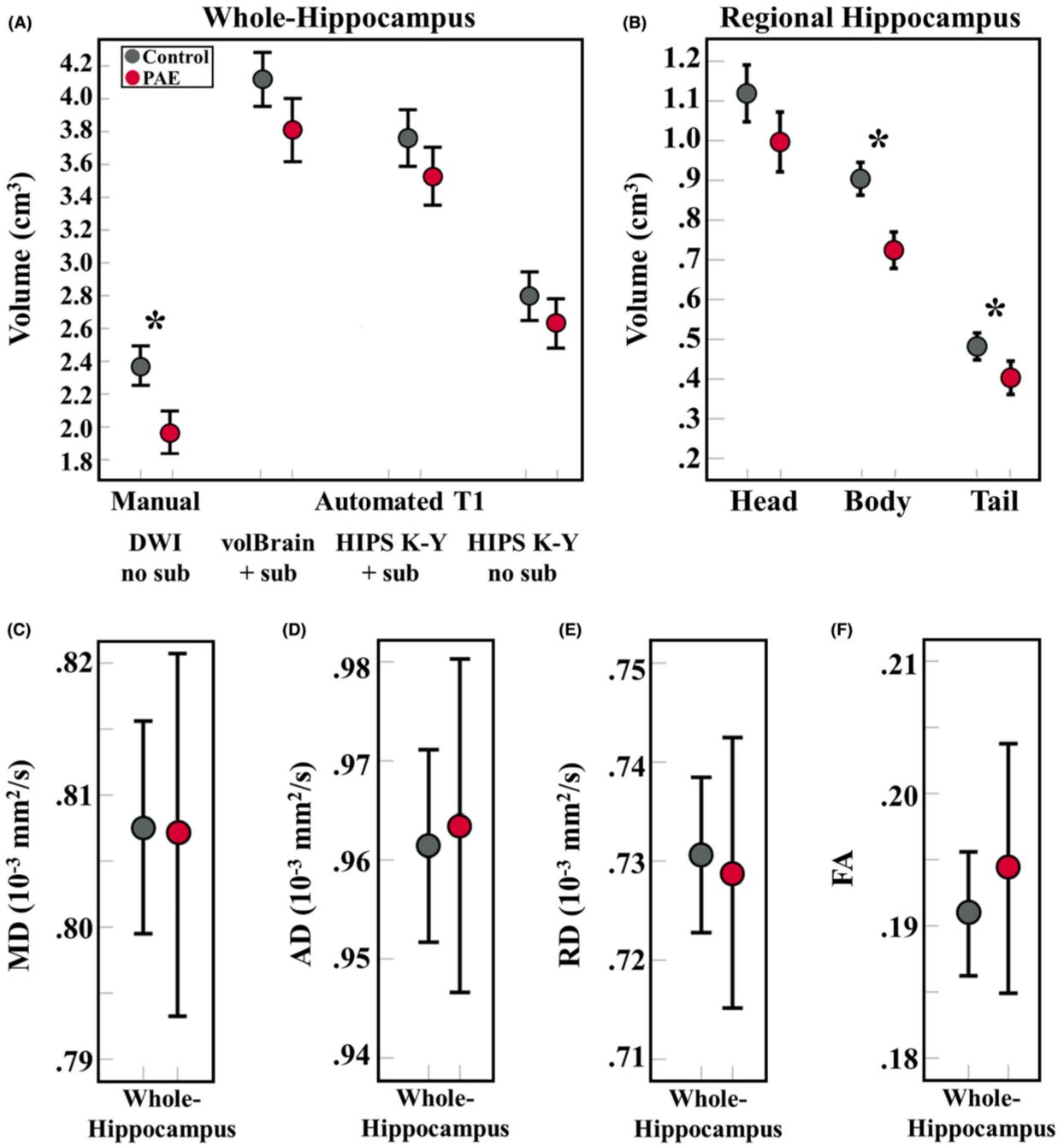

Figure 5.3: Volume and diffusion group differences. (A) Whole-hippocampus volumes (average of left and right) were significantly different between groups (with nonoverlapping 95% confidence intervals) as measured with manual tracings on 1 mm diffusion-weighted images, whereas there were no group differences for all three automated methods on T1-weighted images (controls—gray; prenatal alcohol exposure (PAE)—red). (B) On the manually traced diffusion images, the body and tail were smaller in PAE than in controls. (C–F) There were no significant group differences for any hippocampal diffusion metrics (mean, axial, radial diffusivities—MD, AD, RD; fractional anisotropy—FA). *Benjamini–Hochberg false discovery rate (FDR-BH) corrected threshold of $p \leq 0.008$.

5.3.4. Volumes from Automated Segmentation of T1 (Left + Right Averaged)

There were no effects of group, sex, or group by sex on automated T1 whole-hippocampus segmentation volumes (Figure 5.3a). There were also no effects of group, sex, or group by sex on the total brain, white or gray matter volumes as segmented on the T1-weighted images (data not shown). Pearson correlations revealed strong associations between volumes from manual segmentations on DWI versus automated methods on T1-weighted images in both groups: volBrain versus manual, control group $R = 0.76$ ($p < 0.001$), PAE group $R = 0.73$ ($p < 0.001$); HIPS K-Y with subiculum versus manual, control group $R = 0.77$ ($p < 0.001$), PAE group $R = 0.74$ ($p < 0.001$); and HIPS K-Y without subiculum versus manual, control group $R = 0.77$ ($p < 0.001$), PAE group $R = 0.78$ ($p < 0.001$) (data not shown). However, the automated T1 methods yield systematically larger volumes than the manual segmentation on DWI; nevertheless, the HIPS K-Y method without subiculum is much closer (Figure 5.3a).

5.3.5. Volume and Diffusion Changes with Age (Left + Right Averaged)

There were no main effects of age on the whole structure, head, body, or tail volumes from manual segmentation on diffusion images (Figure 5.4a), or on whole structure volumes from automated segmentation on T1-weighted MRI (data not shown), in either group. In contrast, high-resolution DTI showed negative linear correlations with age in whole-hippocampus MD, AD, and RD in both controls and PAE (Table 5.4; Figure 5.4b-d) but no age effects in whole-hippocampus FA (Figure 5.4e). Diffusivity reductions from 8 to 24 years appear to be consistently steeper in PAE relative to the control group, albeit there was no group by age (or age by sex interactions). Age-related changes of MD, AD, and RD were only significant in the head and body (but not tail) in both groups (Figure 5.5).

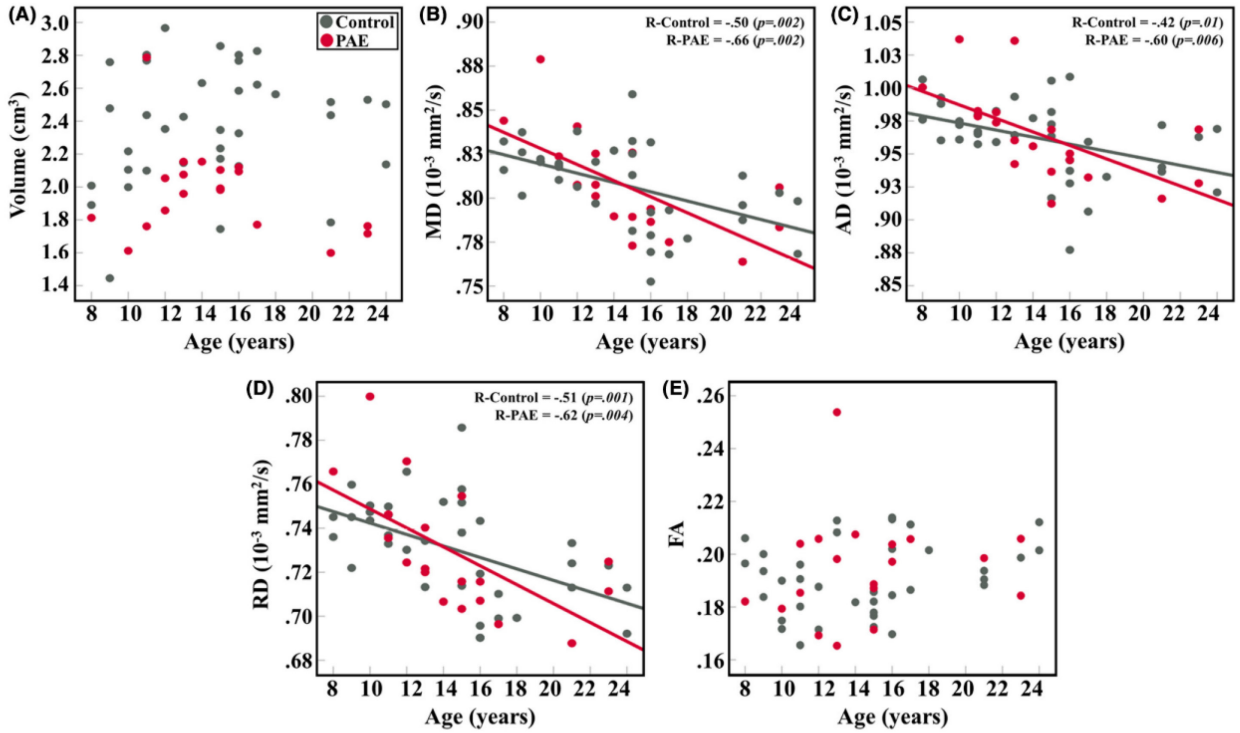

Figure 5.4: Whole-hippocampus volume and diffusion versus age. (A) Volume of the whole-hippocampus (diffusion, manually traced) was not significantly linearly correlated with age over 8 to 24 years in either group (controls—gray; prenatal alcohol exposure (PAE)—red). Negative linear correlations between age and (B) mean diffusivity (MD), (C) axial diffusivity (AD), and (D) radial diffusivity (RD) of the whole hippocampus were significant in both groups, but age effects were nonsignificant for (E) fractional anisotropy (FA). There were no significant interaction effects. Benjamini–Hochberg false discovery rate (FDR-BH) corrected threshold of $p \leq 0.03$.

Table 5.4: Hippocampus age effects. Significant age effects of diffusion metrics in the whole (W), head (H), and body (B) of the hippocampus in controls and prenatal alcohol exposure (PAE). Nonsignificant age correlations of volume, fractional anisotropy, and hippocampus tail are not shown. Benjamini–Hochberg false discovery rate (FDR-BH) corrected threshold of $p \leq 0.03$.

Left + Right Average		Control		PAE	
		Age Effect R (p)	**Units /year**	**Age Effect R (p)**	**Units /year**
Mean Diffusivity (MD) ($10^{-3}mm^2/s$)	W	-0.50 (*p=.002*)	-0.0026	-0.66 (*p=.002*)	-0.0046
	H	-0.51 (*p=.002*)	-0.0029	-0.63 (*p=.004*)	-0.0042
	B	-0.45 (*p=.006*)	-0.0026	-0.60 (*p=.007*)	-0.0052
Axial Diffusivity (AD) ($10^{-3}mm^2/s$)	W	-0.42 (*p=.01*)	-0.0027	-0.60 (*p=.006*)	-0.0051
	H	-0.39 (*p=.02*)	-0.0027	-0.50 (*p=.03*)	-0.0044
	B	-0.38 (*p=.02*)	-0.0025	-0.58 (*p=.009*)	-0.0058
Radial Diffusivity (RD) ($10^{-3}mm^2/s$)	W	-0.51 (*p=.001*)	-0.0026	-0.62 (*p=.004*)	-0.0043
	H	-0.54 (*p=.001*)	-0.0030	-0.62 (*p=.004*)	-0.0041
	B	-0.42 (*p=.008*)	-0.0027	-0.56 (*p=.01*)	-0.0049

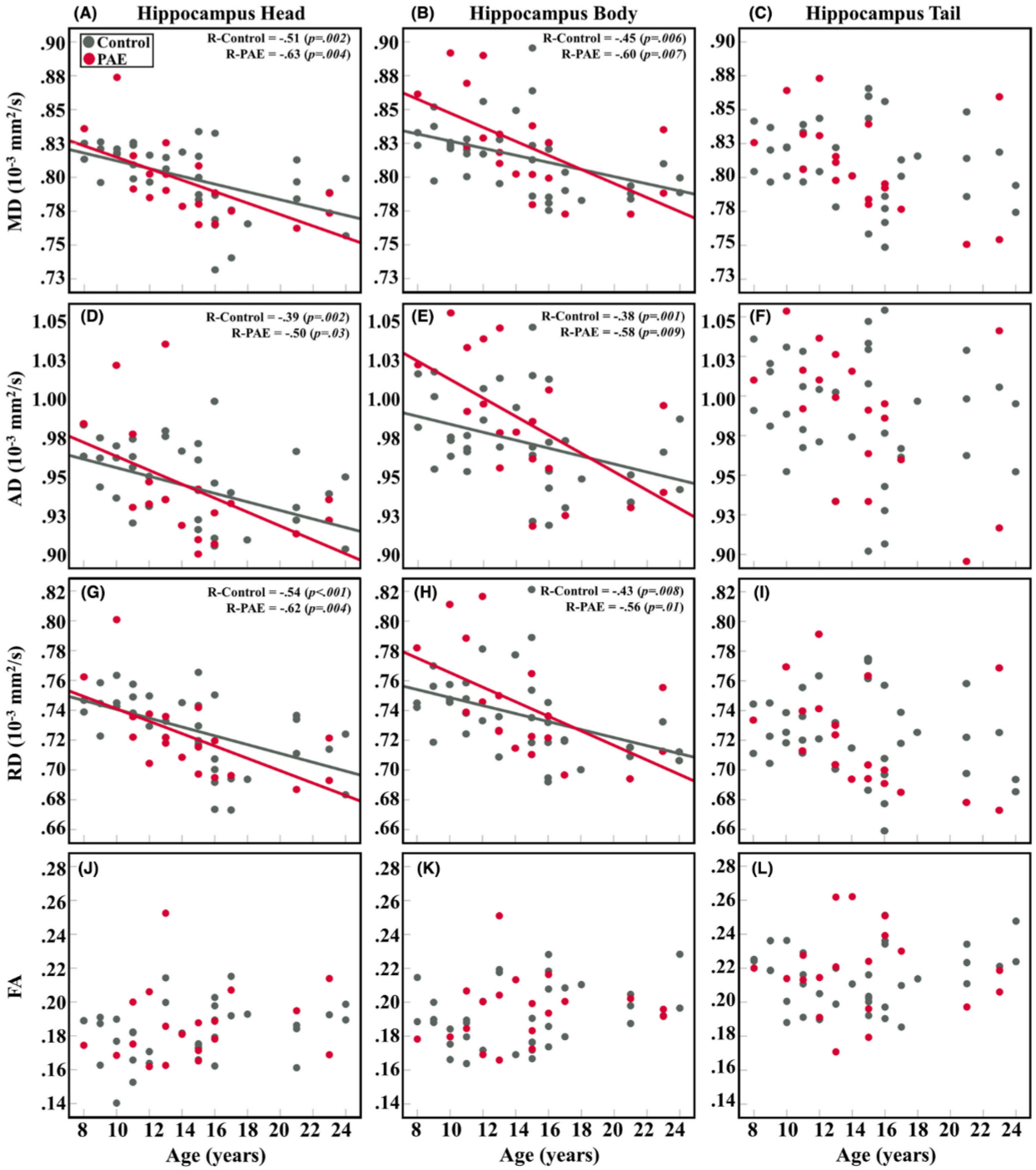

Figure 5.5: Hippocampus head, body and tail bole and diffusion versus age. Negative correlations between the hippocampal head (column 1) and body (column 2) (A, B) MD, (D, E) AD, and (G, H) RD were significant in both controls (gray) and prenatal alcohol exposure (PAE, red). The tail (column 3) showed no age correlations for (C) MD, (F) AD, and (I) RD and neither did (J, K, L) FA for either group across the head, body, and tail. There were no significant interaction effects. Benjamini–Hochberg false discovery rate (FDR-BH) corrected threshold of $p \leq 0.03$.

5.3.6. Cognitive Performance versus Hippocampal Volume and Diffusion (Left + Right Separated)

Pearson correlations revealed seven significant FDR-corrected correlations between hippocampal volume (as measured on diffusion images) and cognitive performance in the control group; five of seven of these correlations were found in the left hippocampus (Figure 5.6a). Specifically, left whole-hippocampus volume correlated with episodic memory on the RAVLT (Figure 5.6b) and PSMT and with working memory on the LSWMT in the control group (larger volume—better performance). Left and right head volume correlated with LSWMT, left tail volume correlated with PSMT, and right body volume correlated with processing speed on the OSDT in the control group (larger volume—better performance; Figure 5.6a). No significant correlations between MD and cognitive performance were found in either hemisphere in the control group. In the PAE group, there were two significant FDR-corrected correlations between hippocampal MD and cognitive performance: MD of the left tail correlated with attention and executive functioning on the FICAT (higher MD—better performance; Figure 5.6a, c), and age-adjusted residuals of MD of the right hippocampal head correlated with PSMT (higher MD—worse performance; Figure 5.6a, d).

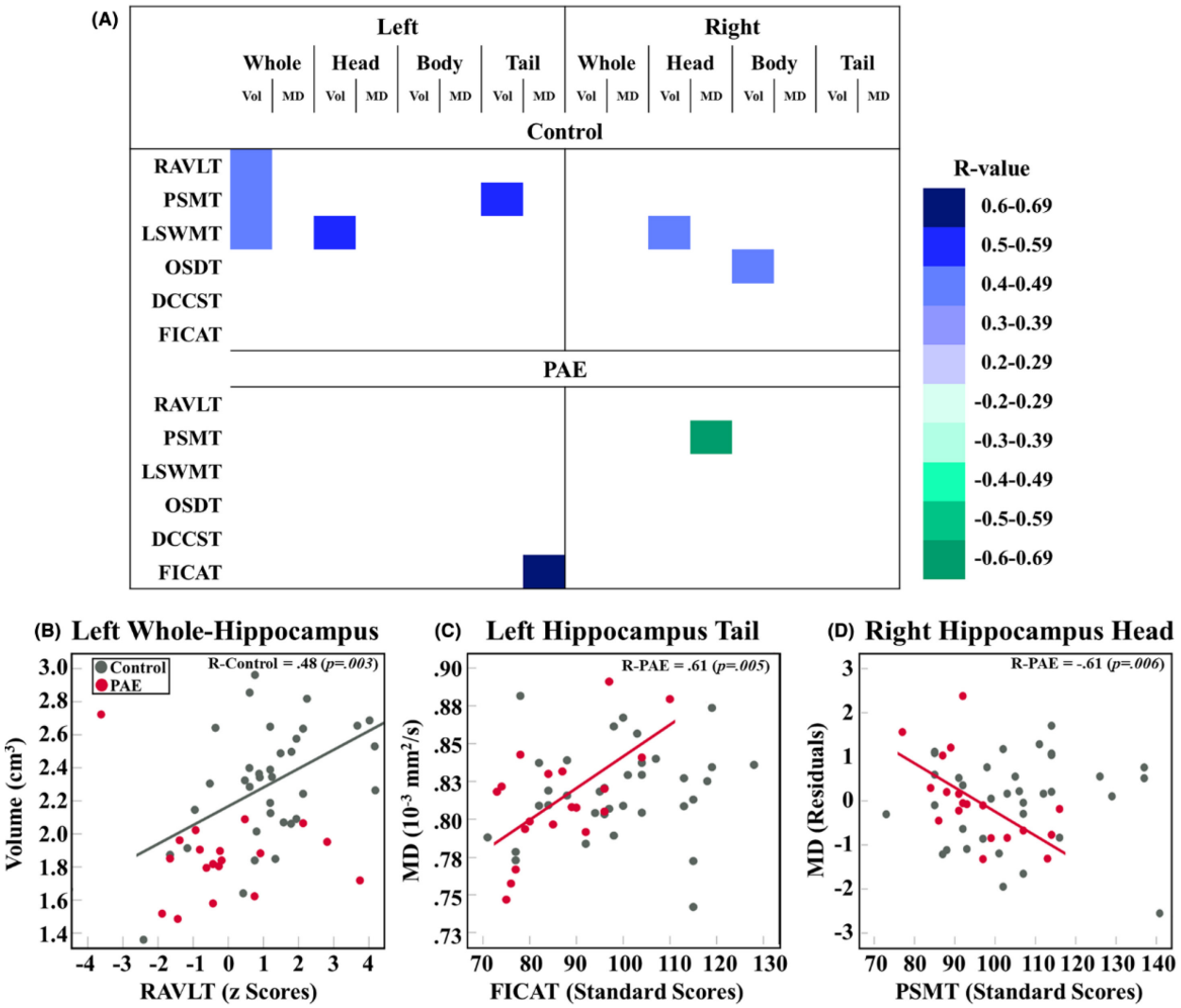

Figure 5.6: Hippocampus cognitive correlations. (A) R values from Pearson correlations (blue—Positive; green—Negative) between left and right hippocampus (whole, head, body, and tail) volume and mean diffusivity (MD) versus six cognitive performance scores in controls and PAE separately. All seven significant correlations between volumes versus cognition were found in the control group; five correlations in the left hemisphere and two in the right. These volume correlations in the control group were with (B) Rey Auditory Verbal Learning Test (RAVLT; episodic memory), Picture Sequence Memory Test (PSMT; episodic memory), List Sorting Working Memory Test (LSWMT), and Oral Symbol Digit Test (OSDT). Both significant correlations between MD versus cognition were in the prenatal alcohol exposure (PAE) group. In the PAE group, (C) left tail MD was positively correlated with the Flanker Inhibitory Control and Attention Test (FICAT), and (D) age-adjusted residuals of right hippocampus head MD were negatively correlated with the PSMT. Benjamini–Hochberg false discovery rate (FDR-BH) corrected threshold of $p \leq 0.006$.

5.4. Discussion

This high-resolution (1 mm isotropic) diffusion MRI study revealed hippocampal volume loss but no group differences in diffusion metrics in participants with PAE relative to controls. While volume did not differ with age in either group, negative correlations between age and diffusion parameters were significant in both groups, with consistently steeper slopes in the PAE group relative to the control group (albeit with nonsignificant age group interactions). Larger hippocampi were associated with better performance on episodic and working memory tasks in the control but not PAE group, suggesting altered brain-behavior relationships in the PAE group.

Animal models suggest that PAE results in apoptotic neuronal cell loss and abnormal (e.g., slower) neurogenesis in the hippocampus, leading to structure atrophy (Barnes & Walker, 1981; Berman & Hannigan, 2000; Brady et al., 2012; Gil-Mohapel et al., 2010; Klintsova et al., 2007; Marjonen et al., 2015; Morrisett et al., 1988; Olateju et al., 2018). This study demonstrates whole-hippocampus volume reductions of ~18% in the PAE group relative to controls, as measured from manual segmentation on DWIs. Volume reductions in the hippocampus have likewise been found in many previous human MRI studies, which report whole structure volume reductions of 5% to 25% in children, adolescents, and young adults with PAE (Astley et al., 2009; Biffen et al., 2018, 2020; Coles et al., 2011; Dodge et al., 2020; Dudek et al., 2014; Gross et al., 2018; Krueger et al., 2020; McLachlan et al., 2020; Nardelli et al., 2011; Roussotte et al., 2012; Treit et al., 2013, 2017; Uban et al., 2020; Willoughby et al., 2008). However, the majority of these studies (11/15; Biffen et al., 2020; Coles et al., 2011; Dodge et al., 2020; Gross et al., 2018; Krueger et al., 2020; McLachlan et al., 2020; Nardelli et al., 2011; Roussotte et al., 2012; Treit et al., 2013, 2017; Uban et al., 2020) measure hippocampal volume from automated segmentation on anatomical MRI (T1 or T2), whereas our study found no significant group differences with automated segmentation on

T1-weighted images. This may also suggest that manual segmentation on DWI is more sensitive than these automated T1 volume measures. Automated segmentation methods are known to overestimate the hippocampus volume substantially, for example, ~4400 mm3 with FreeSurfer versus ~2500 mm3 with manual tracing in the same sample (Akudjedu et al., 2018), with the former being similar to our control volBrain (T1) mean volume of 4117 mm3 (including the subiculum) and the latter being similar to our control manually traced (diffusion) mean volume of 2374 mm3 (excluding the subiculum; Figure 5.3). This suggests that the aforementioned T1 imaging studies that do report volume reductions in PAE are including non-hippocampal tissue, which may contribute to reported group differences. Nonetheless, a recent study found that both manual and automated segmentations revealed dose-dependent volume reductions of the hippocampus (greater alcohol exposure - smaller hippocampi) in a group of children with PAE aged 9 to 11 years (Biffen et al., 2020), suggesting that both methods are sensitive to PAE. However, this study and one other (which used automated segmentation) found that participants with pFAS/FAS had smaller hippocampi than those who were heavily exposed but did not receive a diagnosis of pFAS/FAS (Biffen et al., 2020; Dodge et al., 2020). As such, the lack of group differences in automated segmentation volumes may reflect that our PAE group was less severely affected than previous samples, given none here had a diagnosis of pFAS or FAS, whereas just over half of the participants with PAE (27/52) had a diagnosis of pFAS/FAS in Biffen et al. (2020). Indeed, automated T1-based segmentation did not yield significant group differences in the whole brain, gray or white matter volumes between groups here, again suggesting that our sample is less impaired than previously published samples, while also suggesting that manual tracing methods may be more sensitive to less severely affected PAE populations.

In addition to reductions in whole hippocampus volume, our study also found a bias toward greater volume reduction in posterior segments of the hippocampus (-23% in the body, -22% in the tail but non-significant in the head). This is supported by a prior anatomical MRI study finding of 30% smaller bilateral posterior hippocampus (body + tail) volumes but no significant differences in anterior (head) volume in 11 to 15 year olds with PAE (Dudek et al., 2014). Together, this work suggests that the hippocampus demonstrates regional susceptibility to PAE-related atrophy, with larger reductions more often found in posterior regions. The lack of a significant group effect on hippocampus head volume may stem from increased anatomical variability as well as increased measurement variability in the head relative to the body and tail (Figures 2 and 3b). Anatomical variability (particularly variability in shape and digitations) is well established in this region (Ding & Van Hoesen, 2015; Piccirilli et al., 2020) (for example, in the current data, see Figure 5.2 and Table 5.3). This anatomical variability, combined with its proximity to the amygdala, makes the head more challenging to trace relative to the body and tail (Figure 5.2).

Based on the evidence of reduced volume and pyramidal cell density, and apoptosis and altered myelination in the hippocampus following PAE in animal models, we hypothesized that volume reductions in the hippocampus in humans with PAE would be associated with abnormal microstructure as measured by diffusion parameters in the hippocampus. This hypothesis was not supported. Conversely, this sample demonstrates intact internal architecture (assessed visually) and microstructural properties of the hippocampus (as measured by diffusion parameters), despite significant volume reductions relative to healthy controls. Diffusivities were also negatively correlated with age in both the PAE and control groups, inferring that the smaller hippocampus is undergoing typical developmental microstructural changes during the child to young adulthood

years. Indeed, longitudinal findings from hippocampal volume and diffusion measurements across the healthy lifespan (4 to 93 years) have suggested that the neurobiological processes that underlie micro- and macrostructural changes during aging are largely unrelated (Langnes et al., 2020). In the context of PAE, this negative finding may also reflect developmental "catch up" resulting from stable postnatal environments and other factors.

Relationships between age and hippocampal volume were not significant in either group, in keeping with past literature demonstrating that only one of six studies that have examined correlations between hippocampal volume and age in PAE found any significant relationship, and only in their control group (9 to 15 year olds; Willoughby et al., 2008). The remaining five studies reported no significant effects of age on hippocampal volume in either group, with samples spanning childhood to early adulthood (Dudek et al., 2014; McLachlan et al., 2020; Nardelli et al., 2011; Treit et al., 2013, 2017). However, large sample size studies of healthy development have suggested that hippocampal volumes increase with age during childhood (Fjell et al., 2019; Solar et al., 2021). In the current study, the lack of age effects for hippocampal volume may be due to the small sample size with substantial intersubject variability (e.g., Figure 5.4a, whole hippocampus volume for 9 year old controls ranges from ~1.4 to 2.8 cm^3), as well as the limited age span.

In contrast to volumes, significant relationships between age and diffusion parameters were found in both groups, in keeping with previous cross-sectional studies on healthy development, albeit with 8 to 17× poorer spatial resolution DTI protocols ($2.2 \times 2.2 \times 3.5 = 16.9$ mm^3 - Callow et al., 2020; $2 \times 2 \times 2 = 8$ mm^3 - Fjell et al., 2019; $2.2 \times 2.2 \times 2.2 = 10.6$ mm^3 - Mah et al., 2017). The controls in the current cohort are a subset of a larger healthy lifespan study of age-related diffusivity changes during development (Solar et al., 2021). Note that the higher spatial resolution

and manual segmentation may result in lower MD values (~0.8×10^{-3} mm^2/s) since it minimizes partial volume with adjacent CSF relative to previous work showing a higher hippocampus MD (~1.0 to 1.1×10^{-3} mm^2/s - Fjell et al., 2019; absolute MD values were not given in Callow et al., 2020; Mah et al., 2017). These previous studies have interpreted the diffusivity reductions with age as reflecting increases in neurite density that further hinder water diffusion. In the current study, FA was not significantly correlated with age suggesting that "parallel" and "perpendicular" diffusivity are changing in sync, albeit these directional definitions are more ambiguous in deep gray matter tissue with limited diffusion anisotropy (low FA); this is in contrast to an earlier study that reported a positive linear correlation of FA with age in controls over 8 to 13 years albeit with a very shallow slope (Mah et al., 2017). As opposed to the head and body, the 1 mm DTI of the hippocampal tail did not show any diffusion correlations with age. Although this agrees with one past study finding no MD-age relationship in the posterior hippocampus of healthy participants (Fjell et al., 2019), our previous lifespan 1 mm DTI study in a much larger sample with a broader age range did show MD/AD/RD reductions in the tail with age, though the age-related changes at younger ages were least apparent in the tail, relative to the body and head (Solar et al., 2021). The lack of linear age correlations in the hippocampal tail may be related to our small sample size and narrow age span.

The control group performed significantly better than the PAE group on tests of verbal recall (RAVLT), working memory (LSWMT), and attention and executive function (FICAT) in keeping with previous PAE studies finding impairments in these domains (see reviews, du Plooy et al., 2016; Mattson et al., 2019) which are purported to involve the hippocampus (see reviews, Lisman et al., 2017; Rubin et al., 2014). There were seven significant correlations between hippocampal volume and cognitive scores in the control group (five in the left hemisphere and two

in the right hemisphere), and two significant correlations between hippocampal MD and cognitive scores in the PAE group (one in the left and one in the right hemisphere). Left hemisphere correlations in controls included relationships with verbal (RAVLT) and visual (PSMT) episodic memory, as well as working memory (LSWMT), in agreement with past work suggesting left lateralization of episodic (Burgess et al., 2002) and working memory (Song et al., 2002). Right hemisphere correlations involved working memory (LSWMT) and processing speed (OSDT). In the PAE group, MD (left tail) was positively correlated with attention and executive functioning performance (FICAT), and MD (right head) was negatively correlated with visual memory (PSMT) scores.

Previous studies have likewise identified different hippocampal structure-function relationships in PAE than in healthy control groups (Biffen et al., 2018; Willoughby et al., 2008). For example, larger left hippocampal volume has been associated with superior verbal memory in FASD but not controls (9 to 15 year olds; Willoughby et al., 2008). Similarly, smaller bilateral hippocampi have been associated with better episodic memory in a pFAS/FAS group but not controls (9 to 11 year olds; Biffen et al., 2018). Volume-memory correlations are also inconsistent among typical development studies, but some agree with our control findings. In control children aged 8 to 11 years, better episodic memory performance (visual and spatial tasks) was associated with a larger left hippocampal tail (in our sample from 8 to 24 years, left hippocampus tail volume positively correlated with the PSMT in controls), while the same study also showed better episodic memory with a smaller hippocampal head but larger body in 18 to 26 year olds, suggesting that these relationships differ with age (De Master et al., 2014). Another study of control 4 to 25 year olds demonstrated positive correlations between bilateral posterior (body + tail) volume and visual episodic memory performance on the Rey Complex Figure Test (RCFT) (Fjell et al., 2019); we

showed that visual episodic memory on the PSMT positively correlated with left tail volume in controls. Fjell et al. also found negative correlations between anterior hippocampus MD and visual (RCFT) and verbal memory (CVLT); we demonstrated negative correlations between age-standardized MD of the right head and PSMT in the PAE group. Together with the current findings, this work suggests that PAE-related deficits in working and episodic memory and processing speed may emerge in part due to altered hippocampal macrostructural and microstructural development (Kozareva et al., 2019). Rodent models have shown a variety of hippocampal pathologies that may contribute to memory deficits including neurogenesis impairment, cell loss (e.g., apoptosis), gamma-aminobutyric acid receptor density alterations, and oxidative stress (Brocardo et al., 2017; Gil-Mohapel et al., 2010; Nguyen et al., 2020; Soleimani et al., 2016; Toso et al., 2006). Future work using other modalities (e.g., magnetic resonance spectroscopy) may provide complementary measures to investigate hippocampal and cognitive changes in PAE.

Several limitations of this study should be noted. This study was restricted to a small sample size (n = 19) of children with confirmed PAE, and due to the retrospective nature of this study, we did not have specific details on the timing or severity of prenatal alcohol exposure. Furthermore, there are likely many differences in postnatal experiences between the healthy control and PAE groups that may also impact hippocampal development. Postnatal factors such as socioeconomic status have shown variable effects on whole-hippocampus volume in development (10 to 24 years - Ellwood-Lowe et al., 2018; 7 to 19 years - McLachlan et al., 2020; 7 to 18 years - Uban et al., 2020). Although both groups in this study reported similar annual household income, this only reflects a snapshot of their experience at the time of the study and does not account for previous households that the PAE participants have lived in. Indeed, 31% of the PAE group participants reported having experienced times in their lives when their basic needs were not met,

whereas no healthy controls answered yes to this question. Lower hippocampal volume has been reported in children experiencing poverty and may underscore the role of both pre- and postnatal experiences in abnormal hippocampal development in populations with PAE (Johnson et al., 2016). Our sample also did not include individuals diagnosed with pFAS or FAS. To make stronger inferences about hippocampal changes with age, longitudinal high-resolution DTI studies are necessary. Ethnicity differed between the control and PAE groups in this study; however, bilateral whole-hippocampus volume reductions in the current PAE group are similar to those reported in an ethnically diverse sample (Astley et al., 2009). Moreover, a machine-learning study that demonstrated discrimination of children and adolescents with FASD based on brain volume reductions, including the hippocampus, suggests that volume differences in PAE do not differ based on ethnicity (Little & Beaulieu, 2020).

5.5. Conclusion

High resolution DTI demonstrated reduced whole-hippocampus volume and no differences in hippocampal DTI metrics, indicating preserved microstructure in PAE. Age-related changes over 8 to 24 years were found for the hippocampal diffusivities, but not volume, in both PAE and controls. Correlations between larger hippocampal volumes and better cognitive scores were only found in the controls, and correlations between MD and better cognitive scores were found only in the PAE group, suggesting that PAE may alter the relationship between hippocampal structure and memory performance.

6. A Comparison of Diffusion Tractography of Intra-Hippocampal Streamlines with Constrained Spherical Deconvolution versus the Tensor Model[3]

Abstract

The human hippocampus contains numerous connections that form critical links in memory and learning pathways. Diffusion tensor imaging (DTI) tractography could identify this internal microstructure, but there have been few such tractography studies of the hippocampus, likely due to limited spatial resolution of the diffusion imaging and the complex hippocampal crossing fibers which DTI cannot disentangle. Constrained spherical deconvolution (CSD) is a diffusion model that can resolve complex fiber orientations including crossing fibers, yet it has only been applied in one prior hippocampus study which was limited by low spatial resolution and low angular resolution. Although DTI metrics of the hippocampus have been studied with age, it is not known how the intra-hippocampal connectivity changes over the lifespan. The current study uses a multi-shell diffusion acquisition with high spatial resolution (1 mm isotropic) and high angular resolution (64 directions at b = 500 s/mm^2, 64 directions at b = 2000 s/mm^2) of 40 volunteers aged 5-90 years scanned once, and six volunteers (aged 23-49 years) scanned twice to qualitatively investigate intra-hippocampal streamlines as produced using DTI (b0s, b500s) in comparison to multi-shell multi-tissue CSD (b0s, b500s, b2000s) by examining consistent patterns of directionality in relation to known intra-hippocampal pathways, changes in these patterns with age, and intra-subject replicability.

DTI ellipsoid maps and streamlines and CSD fODF maps and streamlines demonstrated consistent two patterns of anatomically plausible orientations from 5-90 years and across both

[3] A version of this chapter has not yet been published; however, it is currently in preparation for journal submission.

acquisitions of the twice-scanned volunteers. First, streamlines that radiate perpendicular to the long anterior-posterior are plausibly segments of the polysynaptic and direct pathways, extending from the dentate gyrus and through the cornu ammonis. Second, anterior-posterior bundles are likely connections forming the alveus/fimbria as those pathways exit the hippocampus from the cornu ammonis to the alveus and fimbria. CSD revealed anatomically plausible regions of crossing fibers that could not be resolved with DTI. These areas correspond to the polysynaptic and direct pathways and gross hippocampal morphology, showing the primary area of crossing fibers as the head. Additionally, both DTI and CSD streamlines show apparent age-related patterns across the anterior-posterior axis of the hippocampus wherein the younger participants (up to ~20 years of age) show more red left-right oriented streamlines relative to the rest of the age span which shows more green anterior-posterior oriented streamlines at older ages. One millimeter isotropic multi-shell high angular resolution diffusion imaging revealed consistent anatomically plausible intra-hippocampal streamlines across the lifespan of 5-90 years with intra-subject replicability using both DTI and CSD methods, and CSD extended this information by resolving anatomically plausible regions of crossing fibers that the DTI model could not resolve.

6.1. Introduction

Intra-hippocampal pathways are critical for memory and learning, but are difficult to image due to their complex organization and the overall small size, shape, and location of the hippocampus structure (Duvernoy et al., 2013). Diffusion tensor imaging (DTI) is commonly used to study white matter (WM) because it allows for virtual identification of tracts that have a high degree of diffusion anisotropy and yields diffusion metrics indicative, but not specific to, tissue microstructure (e.g., axon packing/myelination). Hippocampal region-of-interest (ROI) analyses of DTI maps have demonstrated age-effects and memory correlations in development (Callow et al., 2020; Langnes et al., 2019), aging (Carlesimo et al., 2010; Den Heijer et al., 2012), and across the lifespan (Langnes et al., 2020; Solar et al., 2021). Additionally, DTI studies have also reported altered hippocampal microstructure in neurodegenerative disorders such as temporal lobe epilepsy (TLE) (Treit et al., 2019) and Alzheimer's disease (Mak et al., 2017). However, there are few hippocampal diffusion MRI *in vivo* human studies that have performed tractography to identify intra-hippocampal connections (Meyer et al., 2017; Schlichting et al., 2021; Zeineh et al., 2012).

Ex vivo DTI tractography at ultra-high resolution has shown streamlines that correspond to specific segments of the polysynaptic intra-hippocampal pathway, including the perforant (Colon-Perez et al., 2015; Coras et al., 2014) and alveus segments (Coras et al., 2014) in healthy specimens. Additionally, altered organization of intra-hippocampal fibers relative to controls has also been observed in TLE specimens with sclerotic hippocampi (Coras et al., 2014). *In vivo* DTI tractography at lower spatial resolutions has shown sparse results in identifying intra-hippocampal streamlines (Meyer et al., 2017; Zeineh et al., 2012). An exploratory investigation of 6 healthy volunteers applied DTI tractography based on manual hippocampal subfield segmentation to identify multiple fiber segments of the polysynaptic (e.g., Schaffer collaterals from CA3 to CA1;

perforant path) and direct pathways (e.g., CA1 to subiculum) (Zeineh et al., 2012). Another DTI tractography study could not identify any anatomically plausible intra-hippocampal pathways, and only showed a bulk of streamlines which extended throughout the anterior-posterior axis of the entire hippocampus and beyond its borders (maybe including the fimbria) (Meyer et al., 2017). Both of these studies suffer from lower spatial resolution DTI acquisitions (2x2x2 = 8 mm^3 - Meyer et al., 2017; 1.7x1.7x1.7 = 4.9 mm^3 - Zeineh et al., 2012) that were not ideal for the hippocampus; further the latter study required ~1 hour of scanning time for a whole-brain acquisition which is clinically infeasible.

A key technical issue of the above DTI tractography studies of intra-hippocampal pathways is that DTI is unable to resolve regions with multiple fiber orientations such as instances of crossing or kissing fibers (Alexander et al., 2007; Jones et al., 2013; Tournier et al., 2011). However, intra-hippocampal pathways exhibit dense, complex and crossing organization within the bi-laminate structure of the hippocampus (Beaujoin et al., 2018; Colon-Perez et al., 2015; Duvernoy et al., 2013; Shepherd et al., 2007). For example, the polysynaptic and direct pathways are two key conduits in hippocampal memory processing (Duvernoy et al., 2013). A viable solution to this problem could involve the acquisition of high angular resolution diffusion imaging (HARDI) data (Soares et al., 2013) and the application of higher order diffusion models such as constrained spherical deconvolution (CSD) which allows for accurate estimation of multiple, differently oriented fiber bundles in a single voxel (Tournier et al., 2007, 2012). There is one recent study which applied a CSD approach to track intra-hippocampal connections, and related the streamline count from CA1-CA3 with exception learning performance in healthy volunteers aged 19-33 years (Schlichting et al., 2021). However, this study was also limited by low spatial resolution (2x2x2 = 8 mm^3), co-registration to higher resolution anatomical imaging (T1-weighted) for hippocampal

segmentation which can lead to segmentation and co-registration errors, and the use of a single low b value of 1000 s/mm^2, which is below the recommended minimum b value of 2000 s/mm^2 required to resolve crossing fiber orientations in CSD analyses (Tournier et al., 2008).

Diffusion tensor imaging of the hippocampus at high spatial resolution (20 axial-oblique slices with 1 mm isotropic voxels with no interslice gap) at a single low b shell of 500 s/mm^2 acquired in 6 min at 3T has shown advantages for delineation of internal architecture and measurement of DTI metrics (Solar et al., 2021, 2022; Treit et al., 2018, 2019). A multi-shell version of this protocol (2 diffusion-weighted shells, 64 directions at 2000 s/mm^2, 64 directions at 500 s/mm^2, and 20 non-DWIs) was acquired in a large development/aging cohort and shown feasible at 3T in a clinically-relevant scan time of 7:50 min (Treit et al., 2022). The protocol allows for segmentation of the hippocampus directly on the mean DWI (i.e., without co-registration to T1/T2). The single diffusion-weighted shell version of this hippocampus acquisition (10 averages of 10 directions at b = 500 s/mm^2, and 10 b0s) (Treit et al., 2018) has revealed hippocampal DTI parameter abnormalities in TLE (Treit et al., 2019), anterior-posterior subregion specific age effects across the healthy lifespan (5-74 years - Solar et al., 2021), and reduced hippocampus volumes but preserved microstructure in prenatal alcohol exposure (Solar et al., 2022). However, the multi-shell (64 directions at b500, 64 directions at b2000) iteration of this protocol (Treit et al., 2022) has not yet been applied to study intra-hippocampal connections.

The purpose of the first part of this study was to apply this high spatial (1 mm isotropic voxels) and high angular resolution (64 directions at each b500 and b2000, 128 total) multi-shell hippocampal diffusion imaging acquisition to 40 healthy volunteers aged 5 to 90 years, to investigate: (i) intra-hippocampal DTI ellipsoid maps versus CSD fiber orientation distribution functions (fODF) maps, (ii) optimal tracking parameters for intra-hippocampal DTI and CSD

tractography streamlines, and (iii) variations of intra-hippocampal DTI and CSD streamlines patterns across age. The purpose of the second part of this study was to apply DTI and CSD tractography using the optimal parameters determined in the first part to 6 healthy volunteers (ages 20-49 years) scanned at 2 different time points to investigate intra-subject repeatability of intra-hippocampal DTI and CSD tractography streamlines.

6.2. Methods

6.2.1. Participant Demographics

Healthy volunteers (n = 40, 22 females) aged 5-90 years participated in this study as part of the cross-sectional cohort (Figure 6.1). These data are an age and sex distribution matched subsample of a larger normative MRI database of 378 neurotypical participants 5-90 years (Treit et al., 2022) (Figure 6.1). Six additional healthy volunteers (3 females) aged 20 to 49 years were scanned twice, 1-71 days apart, to assess intra-subject reproducibility of the CSD findings. Volunteers had no self-reported history of brain injury, neurological or psychiatric disorders. They were recruited through advertising and provided written informed consent prior to study participation. Both child assent and parent/guardian consent were obtained for volunteers under 18 years of age. This study was approved by the University of Alberta Human Research Ethics Board.

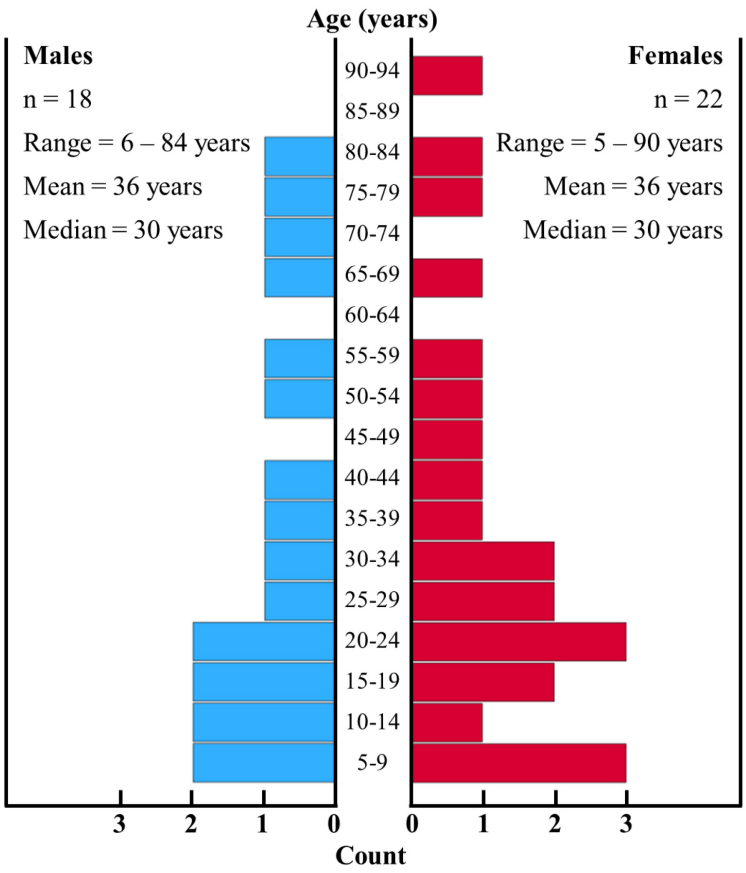

Figure 6.1: Participant distribution. Participant distribution as a function of both age and sex.

6.2.2. MRI Protocol and Processing

All MRI data were acquired using a 64-channel RF coil on a 3T Siemens Prisma. High resolution 1 mm isotropic diffusion MRI data of the hippocampus was acquired with 20 1 mm slices, no gap, single shot 2D EPI (GRAPPA R2; 6/8 PPF; A/P phase encode), FOV 220 x 216 mm^2, matrix 220 x 216, BW 1420 Hz/px, 1x1x1 mm^3 with no interpolation, TE 85 ms, TR 3100 ms, b = 500 s/mm^2 with 64 monopolar gradient directions, b = 2000 s/mm^2 with 64 monopolar gradient directions, and 20 non DWIs (b = 0 s/mm^2) in 7:50 min. The 20 slices were aligned to the anterior-posterior axis of the hippocampus using a previously acquired whole brain high-resolution 3D T1-weighted MPRAGE for reference (0.85 mm isotropic; 3:39 min). Pre-scan normalize was applied to reduce B1-inhomogeniety across the slice which considerably improves visualization of the hippocampus on the b500 DWIs with no effect on DTI parameters as calculated from the

b500 DWIs and non-DWIs (Treit et al., 2018). MRtrix3 (Tournier et al., 2019) was used to process the diffusion data including denoising (Veraart et al., 2016), Gibbs-ringing (Kellner et al., 2016), eddy current and motion distortion correction, and B1 field inhomogeneity correction (Tustison et al., 2010), and to produce mean DWIs from the b500 images and for standard tensor parameter estimation to produce fractional anisotropy (FA) and mean diffusivity (MD) maps based on the b500 images and non DWIs

6.2.3. Tractography

For both the DTI and CSD methods, whole-hippocampus 3D ROIs were used to seed streamlines randomly within the whole structure so that tractography was limited to intra-hippocampal connections. Whole-hippocampus ROIs were manually segmented on mean b500 DWIs by a single user blinded to participant age using ITK-SNAP (http://www.itksnap.org) (Yushkevich et al., 2006) to yield 3D segmentations of the whole-hippocampus bilaterally. The segmentation procedure and intra-rater reliability for segmentation of healthy participants are reported in a recent hippocampal DTI lifespan study (Solar et al., 2021), and inter-rater reliability (for author KGS and another trained user) for segmentation of healthy volunteers is reported in a recent hippocampal DTI study in prenatal alcohol exposure (Solar et al., 2022).

Tracking parameters including minimum FA (DTI), minimum fODF magnitude (CSD), and maximum turning angle (DTI, CSD), were systematically varied within the cross-sectional sample (n = 40) to evaluate their respective impact on the resultant intra-hippocampal streamlines. They were tested as follows:

- For DTI tractography, minimum FA threshold values of 0.10, 0.05, and 0.01 were tested. The MRtrix3 default and the lower end of the range typically used and recommended in tractography studies of healthy human WM bundles is 0.1 (Mukherjee et al., 2008). Lower

values of 0.05 and 0.01 were chosen because the hippocampus is a mix of GM and WM (guided by Zeineh et al., 2012).

- For CSD tractography, minimum fODF peak magnitude threshold values of 0.10, 0.05, and 0.01 were tested. The MRtrix3 default is 0.1 which is a common, recommended value for identifying regions of crossing WM in healthy human WM bundles while reducing spurious tracts using single-shell CSD (Tournier et al., 2012). However, with multi-tissue CSD as employed in this study, significantly lower fODF thresholds are possible without producing spurious tracts toward tissue boundaries (Jeurissen et al., 2014). For the same reasons (i.e., target tract size) as mentioned above for the lower DTI FA thresholds, lower fODF peak thresholds of 0.05 and 0.01 were also tested.
- For both DTI and CSD tractography, maximum turning angles of 40°, 50°, and 60° were tested as recommended by Mukherjee et al., 2008 and utilized in a prior hippocampal DTI tractography study (Zeineh et al., 2012).
- For both DTI and CSD tractography, a step size of 0.1 mm was used. This step-size is $1/10^{th}$ the voxel size of our data which is based on recommendations for tractography in crossing fiber regions and the default in MRtrix3 (Tournier et al., 2012)
- For both DTI and CSD tractography, the maximum streamline length was 10 cm. Given the average length of the hippocampus at ~4 - 4.5 cm (as measured in the current data and mentioned in Duvernoy), 10 cm should provide more than adequate coverage.
- For both DTI and CSD tractography, the minimum streamline length was 5 mm. Given the average width of the hippocampus at ~5 mm at the narrowest part of the body to ~20 mm at the widest part of the head (as measured in the current data and mentioned in Duvernoy), 5

mm should allow for detection of tracts that run the span of the body while avoiding spurious, shorter tracts.

In MRtrix3, deterministic DTI tractography was implemented using the "tckgen" streamline tractography function with the "Tensor_Det" algorithm (Basser et al., 2000) which uses the b500 DWIs and non DWIs as input.

Also in MRtrix3, a multi-shell multi-tissue CSD model was applied to our multi-shell (b500, b2000) diffusion data without the use of co-registered T1-weighted anatomical data (Jeurissen et al., 2014; Tournier et al., 2012, 2019). First, the single-fiber WM (sfWM), grey matter (GM) and cerebrospinal fluid (CSF) tissue response functions (txt files) were generated with the "dwi2response" function using "dhollander" algorithm (Dhollander et al., 2016, 2019) using all the b500 and b2000 DWIs and non-DWIs as input. Second, multi-shell multi-tissue CSD was performed (Jeurissen et al., 2014) with the "dwi2fod msmt_csd" function using the b500 and b2000 DWIs and non-DWIs in combination with the tissue response txt files (sfWM, GM, CSF) as input in order to generate 3 corresponding tissue fiber orientation distribution function (fODF) maps. Third, deterministic CSD tractography was implemented using the "tckgen" function with the "SD_STREAM" algorithm (Tournier et al., 2012) which uses the sfWM fODF map as input.

6.2.4. Qualitative Analysis of the Cross-Sectional Sample

First, tractography parameters and their effect on intra-hippocampal streamlines were compared within DTI and CSD approaches. Tractography output was qualitatively evaluated across all 40 volunteers with respect to (a) generation of streamlines that match known intra-hippocampal pathways and (b) generation of spurious streamlines that are not anatomically plausible. Tractography parameters were varied as follows: first, the FA (for DTI) and fODF (for

CSD) minimum values were respectively varied while keeping the maximum angle constant at 50°, the middle theta value in this study. Second, the turning angles were varied while holding the FA and fODF minimum values constant at the optimal respective values as determined in the prior step. Third, DTI and CSD streamlines as produced at the qualitatively determined optimal FA/fODF and turning angle thresholds, as determined the two prior steps, were (a) examined for anatomically plausible patterns and (b) compared to identify anatomically plausible crossing-fiber regions resolved with CSD but missed by DTI. Second, voxel-level DTI ellipsoid and CSD fODF maps were (a) compared for similarities and dissimilarities in patterns of directionality, (b) examined for anatomical plausible patterns of directionality, and (c) compared to identify anatomically plausible crossing-fiber regions resolved with CSD but missed by DTI. Third, DTI and CSD streamlines were examined across the age-span for directional patterns and age-related changes in those patterns.

6.2.5. Qualitative Analysis of the Twice-Scanned Sample

For the six healthy volunteers that were scanned twice, voxel-level DTI ellipsoid and CSD fODF maps and DTI and CSD streamlines were (a) examined for anatomically plausible patterns of directionality that were produced in both scans, (b) compared to one another (i.e., DTI ellipsoids versus CSD fODF maps; DTI streamlines versus CSD streamlines) to identify anatomically plausible crossing-fiber regions resolved with CSD but missed by DTI in both scans.

6.3. Results

6.3.1. Qualitative Assessment of Varying Tractography Parameters

For DTI, there are less anatomically plausible streamlines observed at the FA threshold of 0.10 than at 0.05 and 0.01 (Figure 6.2a-c) and there is no qualitative difference between 0.05 and

0.01, therefore 0.05 FA was chosen for cut-off threshold. For CSD, there are less anatomically plausible streamlines observed at the fODF thresholds of 0.10 and 0.05 than at 0.01 (Figure 6.2d-f), therefore 0.01 fODF peak magnitude was chosen for a cut-off threshold. Varying the turning-angle cut-off values generated no observable effects on the resultant streamlines for DTI nor CSD, therefore, the middle value of 50° was chosen as a cut-off threshold.

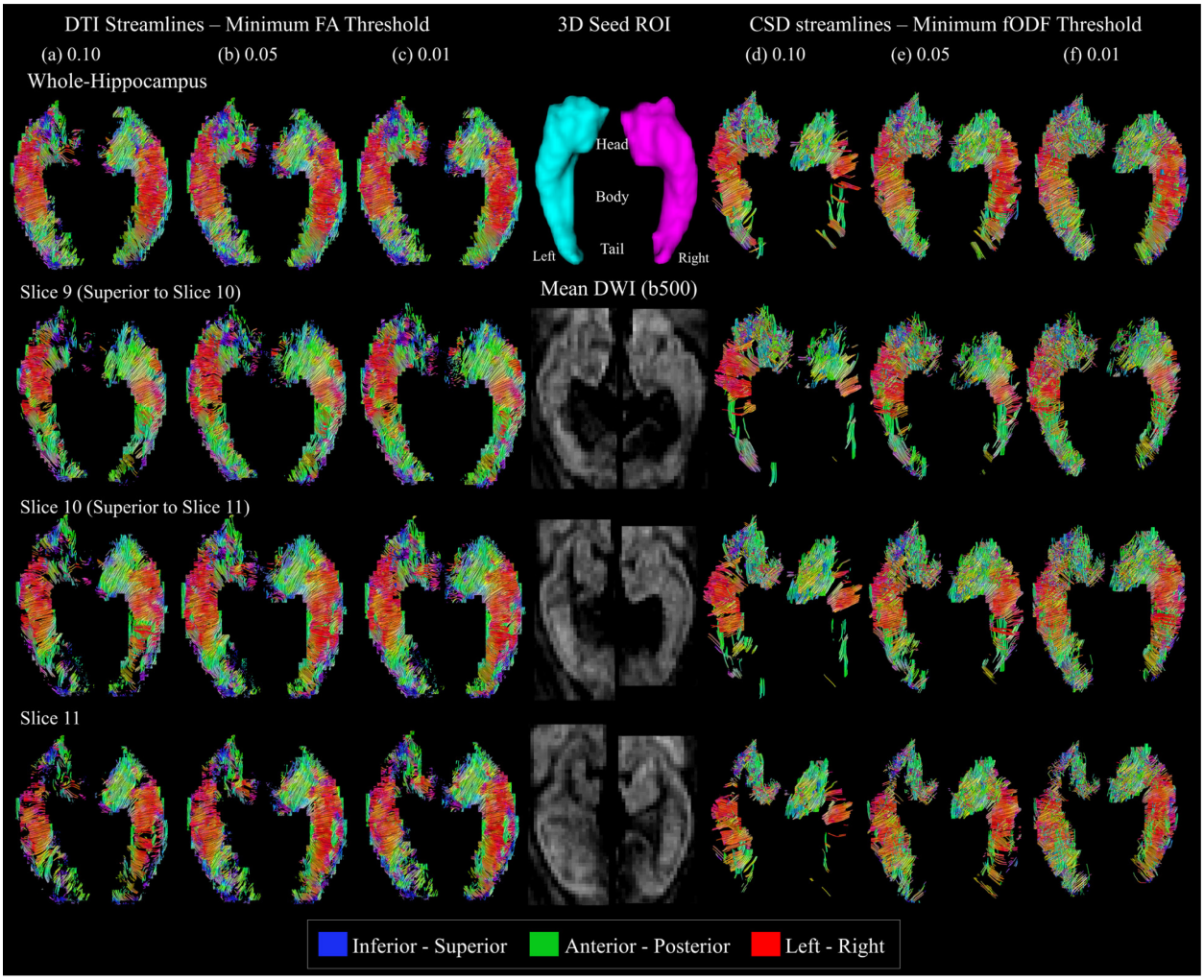

Figure 6.2: Tractography parameter testing. For 1 healthy volunteer (11 years, female): (columns 1-3) diffusion tensor imaging (DTI) streamlines in (row 1) the entire hippocampus and (rows 2-4) as confined to 3 consecutive axial-oblique slices moving inferior to superior as demonstrated in (column 4, rows 2-4) the mean diffusion-weighted images (DWI) with the turning angle threshold held constant at 50° while varying minimum fractional anisotropy (FA) thresholds at values of (a, column 1) 0.10, (b, column 2) 0.05, and (c, column 3) 0.01; (columns 5-7) constrained spherical deconvolution (CSD) streamlines in (row 1) the entire hippocampus and (rows 2-4) as confined to 3 consecutive axial-oblique slices moving anterior to posterior as

demonstrated in (column 4, rows 2-4) the mean DWIs with the turning angle threshold held constant at 50° while varying minimum fiber orientation distribution function (fODF) magnitude thresholds of (d, column 5) 0.10, (e, column 6) 0.05, and (f, column 7) 0.01.

6.3.2. Qualitative Analysis of Cross-Sectional DTI Ellipsoids/Streamlines versus CSD fODFs/Streamlines

From 5-90 years, the hippocampus was well delineated on the 1 mm isotropic mean DWIs, showing marked intersubject variability in the internal anatomy and the external shape of the entire hippocampus (Figures 6.3, 6.4, column 2). There were two distinct patterns of directionality observable across all participants in both the DTI ellipsoid and CSD fODF maps. First, in the bilateral hippocampal body, there are red left-right ellipsoids that correspond to fODFs with red left-right major peaks which radiate perpendicular to the long-axis of the hippocampus in a pattern that spreads to the head and tail, showing red left-right (in the body) that transition to green anterior-posterior orientations (in the tail) (Figures 6.3, 6.4, columns 1, 3). Second, there are green anterior-posterior orientations present throughout the head, body, and tail (Figures 6.3, 6.4, columns 1, 3). Also, there are instances of crossing fibers indicated by fODF glyphs with 2-3 peaks, and on a voxel-level basis, the head appears to show more fODF glyphs with 2+ peaks than only a single peak, and the body and tail show a mix of glyphs with 1-3 peaks (Figures 6.3, 6.4, columns 1, 3).

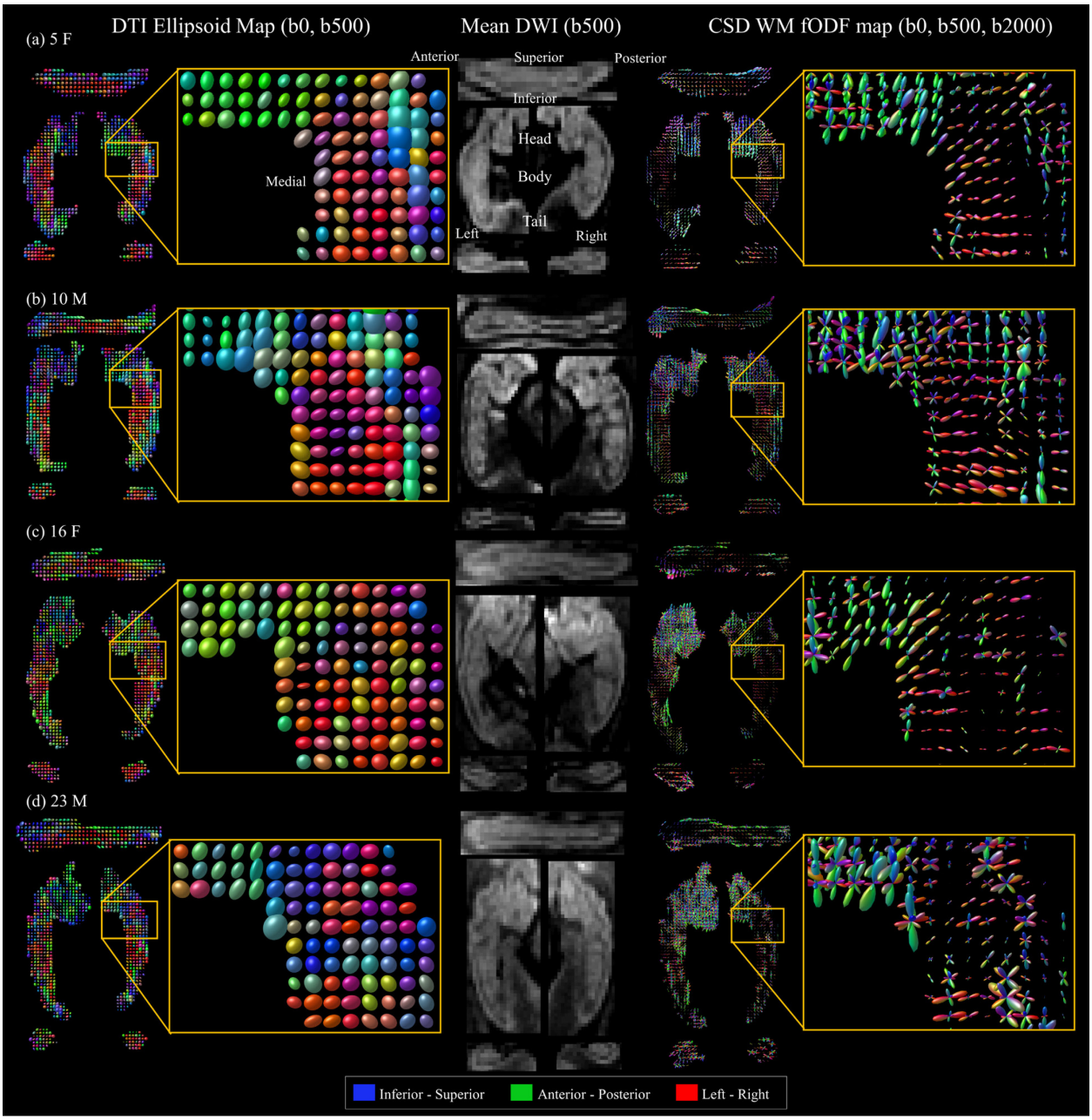

Figure 6.3: DTI ellipsoids versus CSD fODFs. For 4 healthy volunteers (2 females, F; 2 males, M) aged (a) 5, (b) 10, (c) 16, and (d) 23 years. (column 1): Diffusion tensor imaging (DTI) ellipsoid maps (from 10 non diffusion-weighted images and 64 DWIs at b = 500 s/mm^2) with zoomed-in section (yellow box) at the hippocampal head/body interface. (column 2) Mean DWIs (from 64 DWIs at b = 500 s/mm^2). (column 3) Constrained spherical deconvolution (CSD) single fiber white matter (sfWM) fiber orientation distribution function (fODF) maps (from 20 non DWIs, and 64 DWIs at b = 500 s/mm^2 and 64 directions at b = 2000 s/mm^2). Unlike the DTI ellipsoids which only provide a single fiber orientation per voxel, the CSD fODF maps reveal multiple voxels with multiple fiber orientations across the anterior-posterior axis of the hippocampi in all volunteers, especially in the head as demonstrated by the zoomed-in yellow boxes.

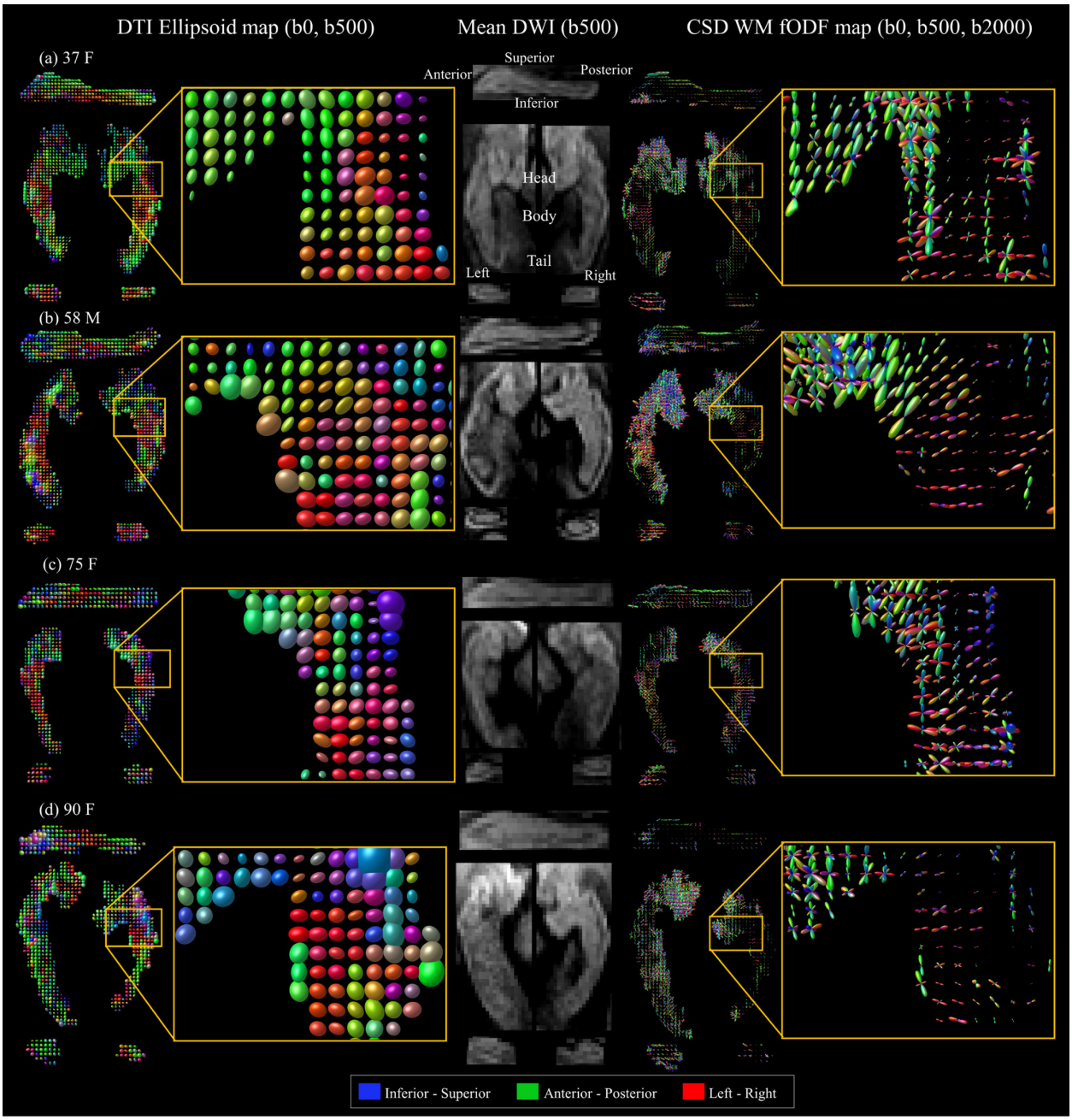

Figure 6.4: DTI ellipsoids versus CSD fODFs. For 4 healthy volunteers (3 females, F; 1 males, M) aged (a) 37, (b) 58, (c) 75, and (d) 90 years: (column 1) Diffusion tensor imaging (DTI) ellipsoid maps (from 10 non diffusion-weighted images and 64 DWIs at b = 500 s/mm^2) with zoomed-in section (yellow box) at the hippocampal head/body interface. (column 2) Mean DWIs (from 64 DWIs at b = 500 s/mm^2). (column 3) Constrained spherical deconvolution (CSD) single fiber white matter (sfWM) fiber orientation distribution function (fODF) maps (from 20 non DWIs, and 64 DWIs at b = 500 s/mm^2 and 64 directions at b = 2000 s/mm^2). Unlike the DTI ellipsoids which only provide a single fiber orientation per voxel, the CSD fODF maps reveal multiple voxels with multiple fiber orientations across the anterior-posterior axis of the hippocampi in all volunteers, especially in the head as demonstrated by the zoomed-in yellow boxes.

The same two distinct patterns are also observable across all volunteers in both the DTI and CSD streamlines. First, red left-right streamlines that extend through the majority of the hippocampal body as they radiate perpendicular to the anterior-posterior axis towards the head and tail as they transition into an orange-yellow then green anterior-posterior orientation as they curve into the head and tail (Figures 6.5, 6.6, columns 1, 3, note the red streamlines in the sagittal, axial-oblique, and coronal planes). Also, a part of this pattern includes blue anterior-posterior streamlines along select areas of the perimeter of the hippocampus from the radial pattern. Second, green anterior-posterior streamlines that extend the length of the anterior-posterior axis (Figures 6.5, 6.6, columns 1, 2, note the green arrows on the sagittal slices and the same green tracts along the axial-oblique slices). CSD tractography revealed instances of crossing fibers throughout the hippocampus with the primary area being the head with the most voxels appearing to contain crossing fibers (Figures 6.5, 6.6, column 3) as also demonstrated in the fODF maps (Figure 6.3, 6.4, columns 3).

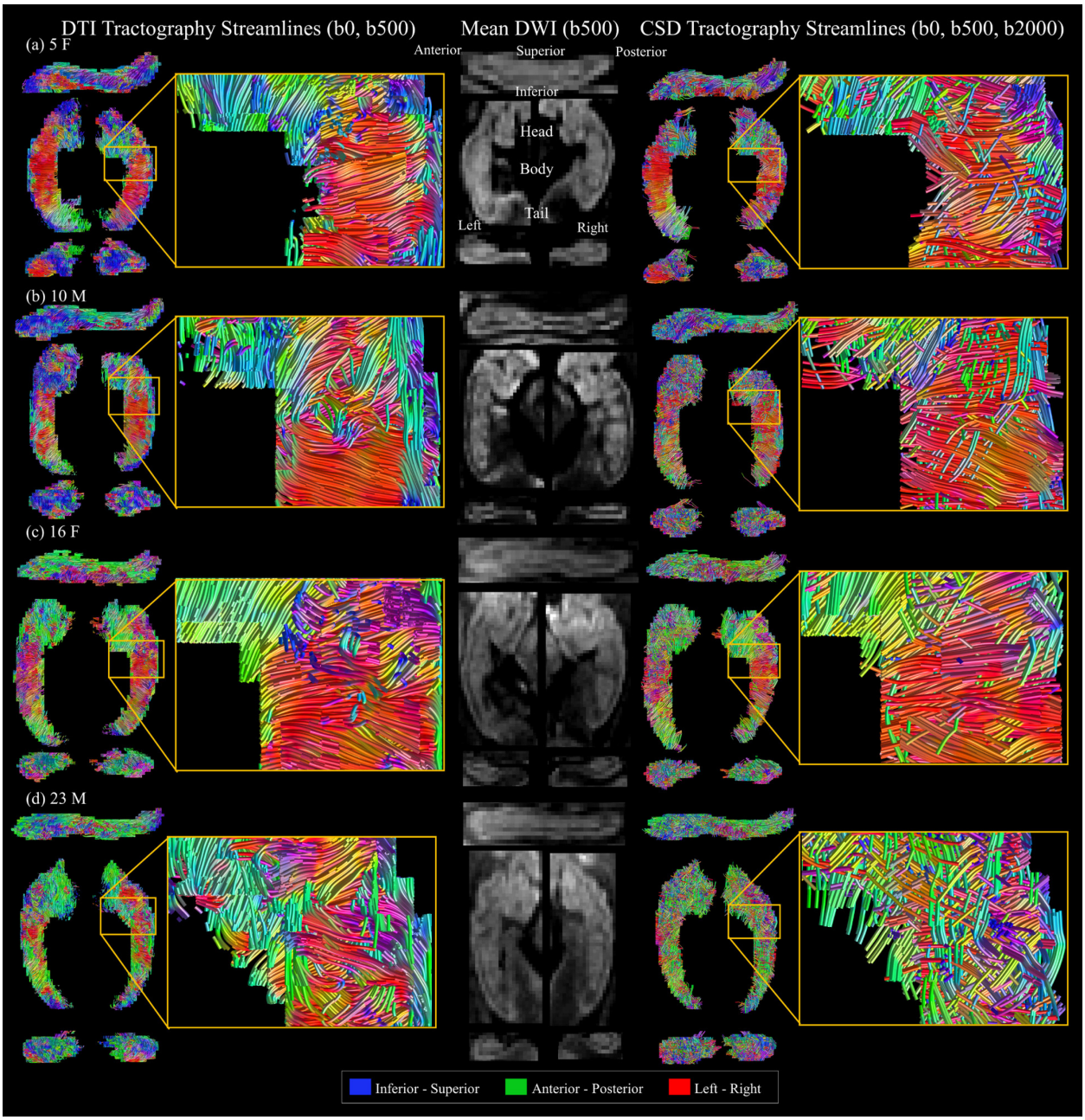

Figure 6.5: DTI versus CSD streamlines. For 4 healthy volunteers (2 females, F; 2 males, M) aged (a) 5, (b) 10, (c) 16, and (d) 23 years (same participants as Figure 6.3). (column 1) Diffusion tensor imaging (DTI) streamlines with zoomed-in section (yellow box) at the hippocampal head/body interface. (column 2) Mean diffusion-weighted images (DWI). (column 3) Constrained spherical deconvolution (CSD) streamlines with zoomed-in section (yellow box) at the hippocampal head/body interface. Both the DTI and CSD streamlines present a radial pattern of streamlines that run perpendicular to the anterior-posterior hippocampal axis, appearing red (left-right) in the body, and turning orange to yellow to green (anterior-posterior) as they turn with the head, perpendicular to the long-axis of the U-shaped interlocking laminae of the hippocampus. Green (anterior-posterior) streamlines run along the length of the hippocampal long axis. Blue (superior-inferior) streamlines run along the head and tail regions. CSD streamlines demonstrate anatomically plausible regions of crossing fibers that DTI cannot resolve.

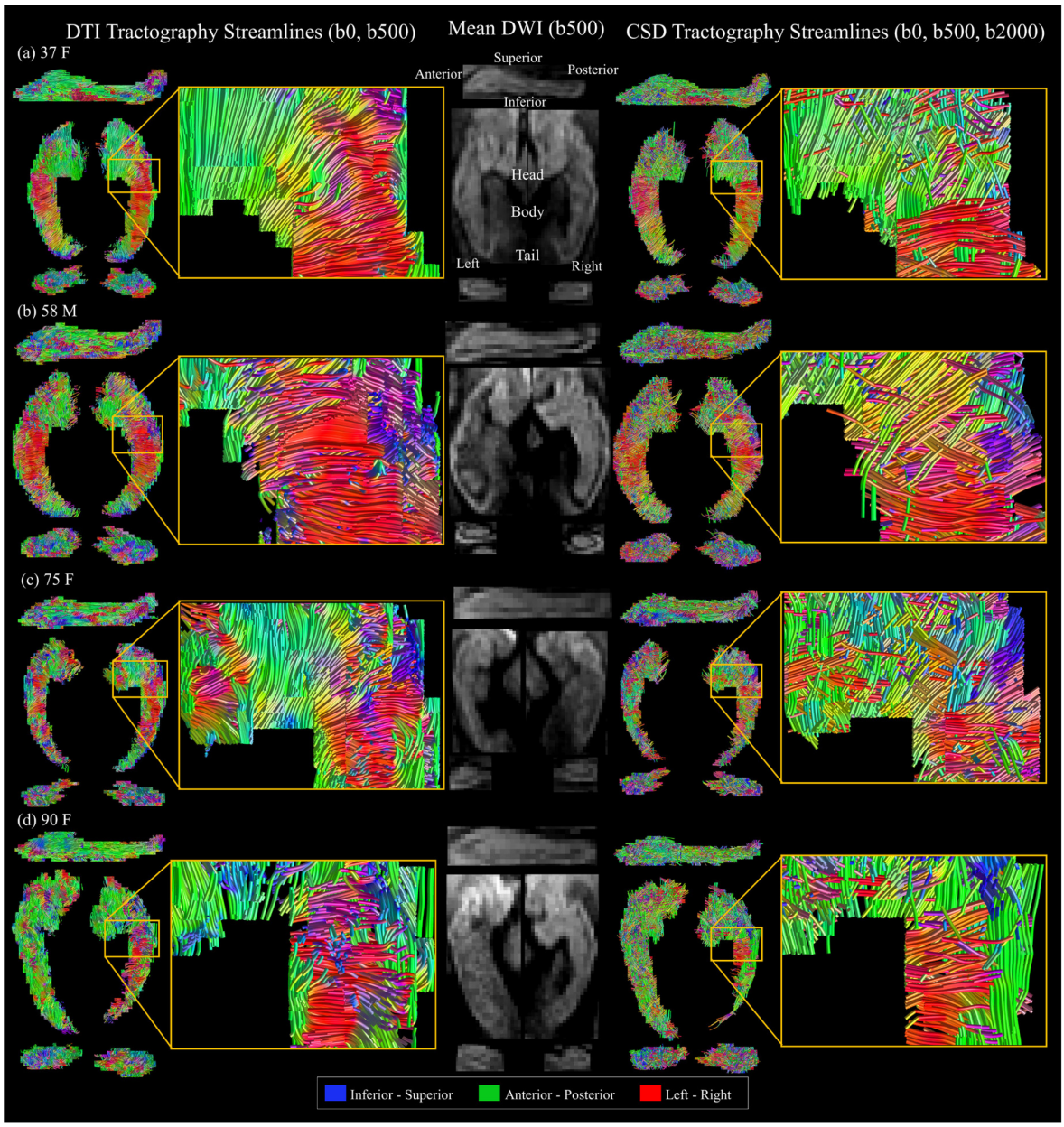

Figure 6.6: DTI versus CSD streamlines. For 4 healthy volunteers (3 females, F; 1 male, M) aged (a) 37, (b) 58, (c) 75, and (d) 90 years (same participants as Figure 6.4). (column 1) Diffusion tensor imaging (DTI) streamlines with zoomed-in section (yellow box) at the hippocampal head/body interface. (column 2) Mean diffusion-weighted images (DWI). (column 3) Constrained spherical deconvolution (CSD) streamlines with zoomed-in section (yellow box) at the hippocampal head/body interface. Both the DTI and CSD streamlines present a radial pattern of streamlines that run perpendicular to the anterior-posterior hippocampal axis, appearing red (left-right) in the body and turning orange to yellow to green (anterior-posterior) as they turn with the head, perpendicular to the long-axis of the U-shaped interlocking laminae of the hippocampus. Green (anterior-posterior) streamlines run along the length of the hippocampal long axis. Blue (superior-inferior) streamlines run along the head and tail regions. CSD streamlines demonstrate anatomically plausible regions of crossing fibers that DTI cannot resolve.

6.3.3 Interpretation of Directionality Patterns in DTI Ellipsoids/Streamlines and CSD fODFs/Streamlines

These patterns correspond to known intra-hippocampal pathways. First, the patterns observed perpendicular (i.e., red left-right patterns in the body, radiating to the head and tail) (Figures 6.3-6.6, columns 1, 3) to the long-axis of the hippocampus plausibly correspond to segments (e.g., Shaffer collaterals, mossy fibers, pyramidal neurons, alveus) of the polysynaptic and direct pathways (Figure 6.7) which run perpendicular to the long anterior-posterior axis of the hippocampus and turn along the lateral and medial borders in blue superior-inferior orientations. Second, the directionality patterns of green anterior-posterior running along the superior surface of the hippocampus (Figures 6.3-6.6, columns 1, 3, sagittal plane) and along the anterior-posterior axis in the axial-oblique plan plausibly correspond to segments of the polysynaptic and direct pathways which exit the hippocampus via the main efferent pathway of the hippocampus: the alveus then the fimbria (Figure 6.7) which involves turning to the superior-inferior (blue) then anterior-posterior (green) direction. The alveus and fimbria run along the superior surface and partly along the superior-lateral surface (alveus only) and superior-medial surface (fimbria only) of the hippocampus (Figure 6.7) (Duvernoy et al., 2013).

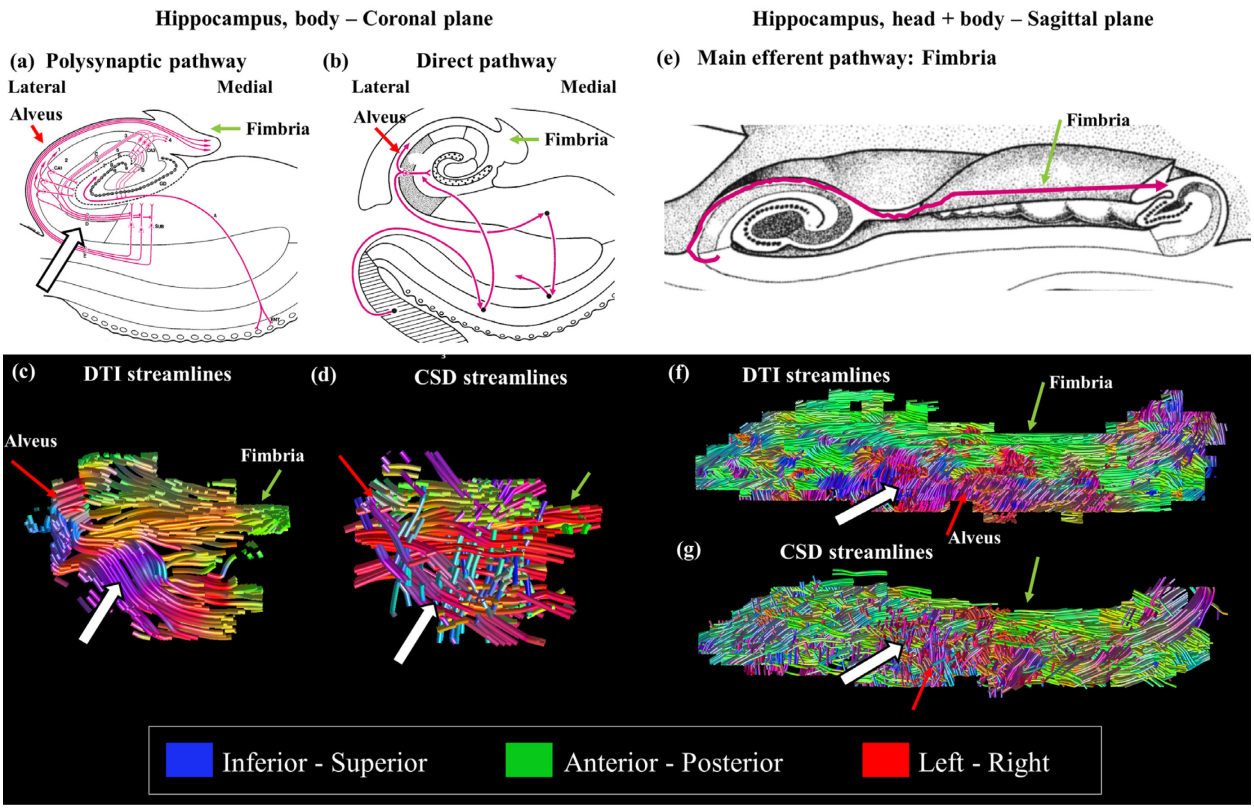

Figure 6.7: Known intra-hippocampal pathways. Structural connections of the (a) polysynaptic and (b) direct intra-hippocampal pathways as observed in a coronal slice of the hippocampus body, and of the main efferent pathway of the hippocampus, the fimbria, as observed in a sagittal slice of the hippocampus head and body. (c, f) Diffusion tensor imaging (DTI) and (d, g) constrained spherical deconvolution (CSD) streamlines from a 16 year-old healthy female. There are anatomically-plausible streamlines that may represent the alveus (red arrows) and fimbria (green arrows) as observed in the coronal and sagittal sections of the (c, f) DTI and (d, g) CSD streamlines. Also, there are anatomically-plausible streamlines at the white arrows indicated in the (a) polysynaptic pathway at segment "D" which may be represented in the (c, f) DTI and (d, g) CSD streamlines; this white arrow on the (f, g) sagittal slices indicates the position across the anterior-posterior axis featured in (c, d) the coronal slices. 1, alveus; 2, stratum pyramidale; 3, Shaffer collaterals; 4, pyramidal neuron axons. CA, cornu ammonis. GD, dentate gyrus. (a, b, e) Reprinted/adapted by permission from Springer Nature Customer Service Centre: The human hippocampus by Henri Duvernoy, Françoise Cattin, Pierre-Yves Risold 2013.

6.3.4. Qualitative Analysis of Intra-Subject Replicability of DTI Ellipsoids/Streamlines and CSD fODFs/Streamlines

Across both scans of the 6 twice-scanned participants, the same two distinct patterns in directionality were observed as described above in the cross-sectional cohort. The repeat scans for each participant showed similar patterns between one another. Example data from the first and

second acquisition is shown in detail for 1 of 6 participants (20-year-old-female; Figure 6.8) for which both DTI and CSD replicate similar patterns of red left-right orientations in the body that run perpendicular to the anterior-posterior long axis and continue into the head and tail, as well as green anterior-posterior orientations that run along the anterior-posterior long axis, with the majority appearing on the superior surface (e.g., sagittal slices shown in Figure 6.8). In the CSD streamlines, similar patterns of anatomically plausible fiber crossings are observed (e.g., red left-right streamlines crossing over green anterior-posterior streamlines in the body and tail of the right hippocampus in the 20-year-old female participant; Figure 6.8, e *versus* j).

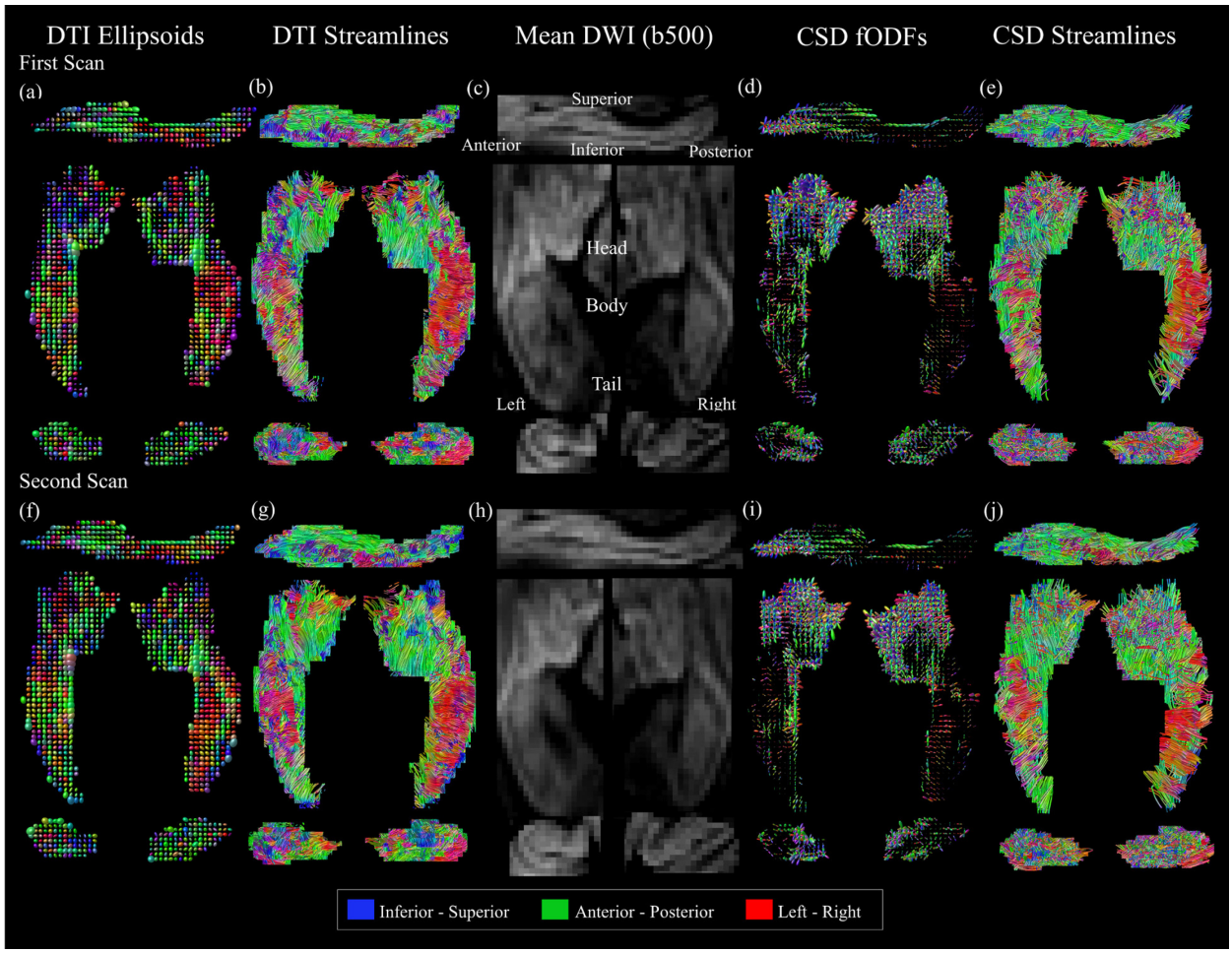

Figure 6.8: DTI and CSD in twice-scanned participants: For 1 of 6 healthy volunteers scanned twice (20 years, female), one day apart, in the (a-e, row 1) first and (f-j, row 2) second scans, there are similar and reproducible patterns of directionality observed across the anterior-posterior hippocampal axis in the sagittal, axial-oblique, and coronal planes in the (column 1, a, f) diffusion tensor imaging (DTI) ellipsoids, (column 2, b, g) DTI streamlines, (column 4, d, i) constrained spherical deconvolution (CSD), and (column 5, e, j) CSD streamlines.

6.3.5. Qualitative Assessment of Age-Related Changes in DTI and CSD Streamlines

Across the cross-sectional sample of 40 participants aged 5-90 years there are observable age-related changes in both the DTI and CSD streamlines (Figures 6.9, 6.10). First, in the childhood to young adulthood age range (Figures 6.9, 6.10, ages 5-23 years) relative to the remainder of the age range from middle to older adulthood (Figures 6.9, 6.10, ages 24-90 years), there appears to be a greater amount of blue superior-inferior streamlines in the head and red left-right orientations in the head and body. Second, in the age range from middle to older adulthood

(Figures 6.9, 6.10, ages 24-90 years) relative to childhood to young adulthood age range (Figures 6.9, 6.10, ages 5-23 years), there appears to be a greater amount of green anterior-posterior streamlines across the head, body, and tail. It does not appear that the amount of observable crossing fiber regions changes with age in the CSD streamlines, however, they do change in correspondence with the two age-related patterns (Figure 6.10).

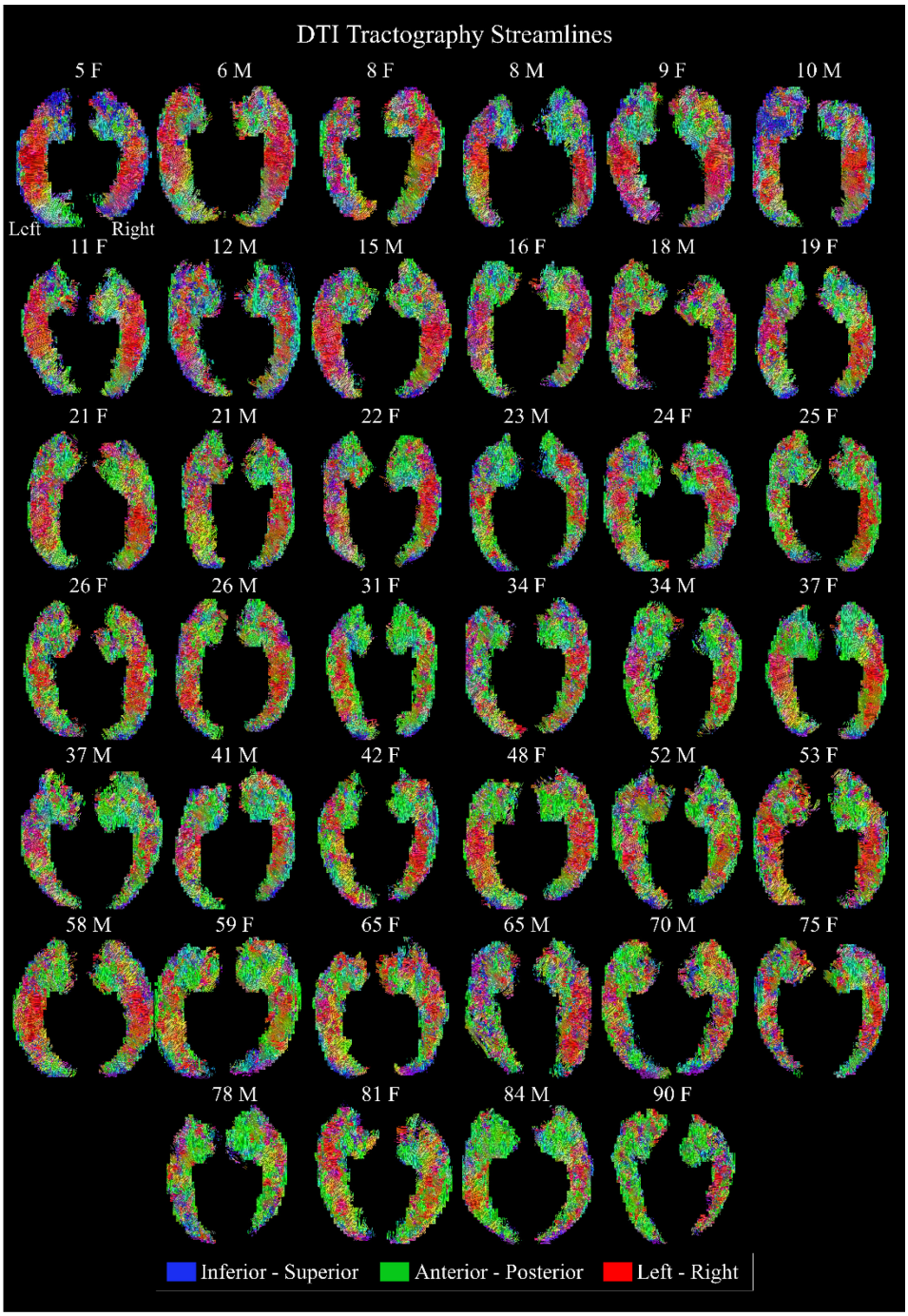

Figure 6.9: Age-sorted DTI streamlines. Diffusion tensor imaging (DTI) intra-hippocampal streamlines for all 40 healthy volunteers in order of increasing age (22 females, 18 males; 5-90 years). There are red (left-right) streamlines that radiate perpendicular to anterior-posterior hippocampal axis and are most apparent in the body; these red streamlines are also most prominent in children and adolescents (~5-18 years) relative to the rest of the age span. The same age range also shows more prominent blue (superior-inferior) streamlines in the head and tail relative to the rest of the age span. There are green (anterior-posterior) streamlines throughout the anterior-posterior hippocampal axis and they appear to be more prominent in young to older adulthood (~21-90 years) relative to adolescents (~5-18 years). Hippocampi are scaled in size to one another.

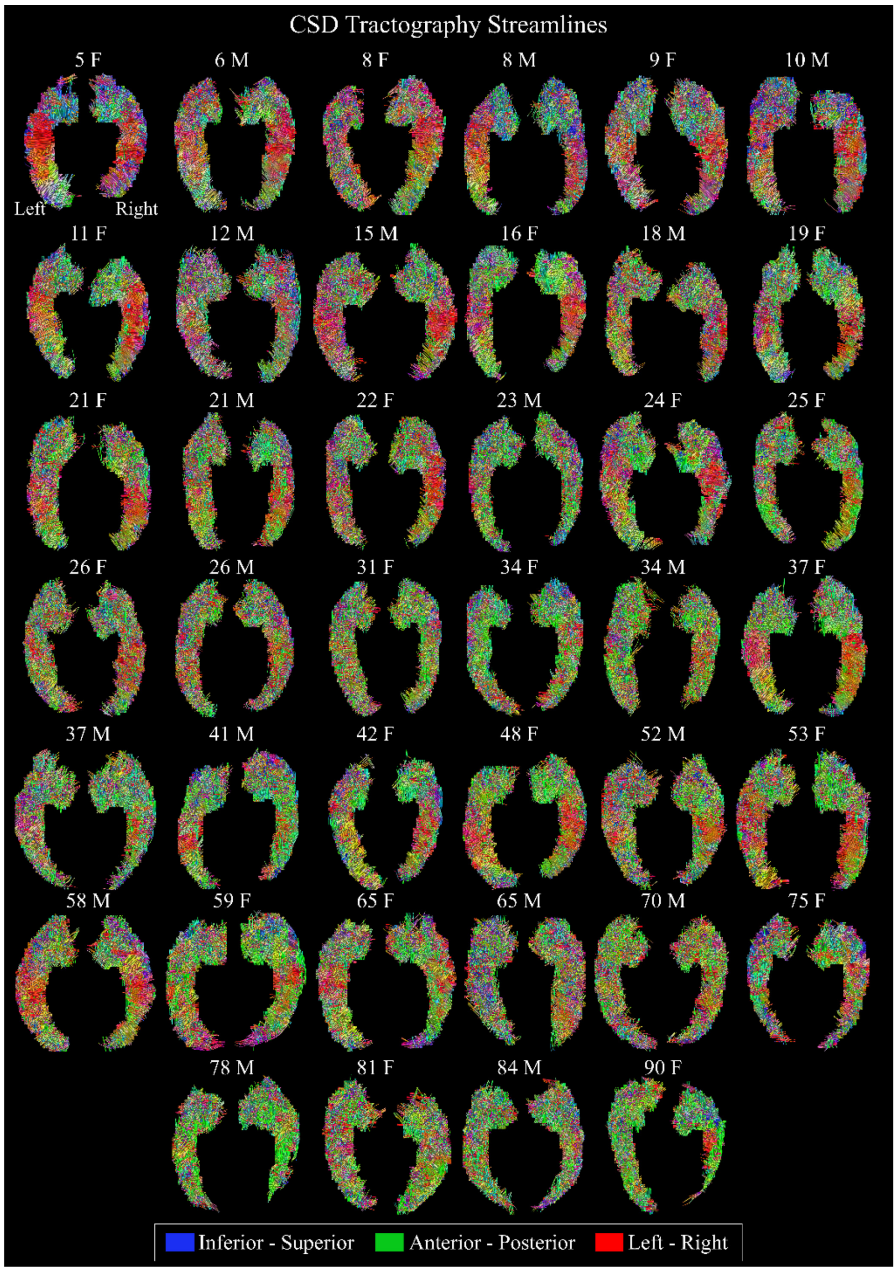

Figure 6.10: Age-sorted CSD streamlines. Constrained spherical deconvolution (CSD) intra-hippocampal streamlines for all 40 healthy volunteers in order of increasing age (22 females, 18 males; 5-90 years). There are red (left-right) streamlines that radiate perpendicular to anterior-posterior hippocampal axis and are most apparent in the body; these red streamlines are also most prominent in children and adolescents (~5-18 years) relative to the rest of the age span. The same age range also shows more prominent blue (superior-inferior) streamlines in the head and tail relative to the rest of the age span. There are green (anterior-posterior) streamlines throughout the anterior-posterior hippocampal axis and they appear to be more prominent in young to older adulthood (~21-90 years) relative to adolescents (~5-18 years). In line with these patterns, CSD also reveals consistent regions of crossing fibers such as the red left-right orientations in the body crossing with green anterior-posterior orientations. Hippocampi are scaled in size to one another.

6.4. Discussion

Our study demonstrates the feasibility of intrahippocampal DTI and CSD tractography at high spatial resolution (1 mm isotropic voxels) and high angular resolution (2 diffusion-weighted shells at 64 directions each, b values = 500, 2000 s/mm^2) as acquired in under 8 minutes at 3T. Our study shows anatomically plausible intra-hippocampal tracts as revealed by this multi-shell diffusion acquisition using both the standard DTI model and a multi-shell multi-tissue CSD approach across a cross-sectional cohort of 40 healthy volunteers aged 5-90 years, with intra-subject replicability demonstrated across six twice-scanned volunteers aged 20-49 years and scanned 1-71 days apart. The DTI ellipsoid maps and streamlines and the CSD fODF maps and streamlines each show reproducibility of fiber orientations across the cross-sectional lifespan cohort. First, a grouping of red left-right orientations across the width of the body with blue superior-inferior orientations along the lateral and medial borders in the body and radiating away toward the head and tail (turning to green anterior-posterior radiations as they follow a pattern perpendicular to the long anterior-posterior axis of the hippocampus) that likely correspond to connections in the polysynaptic (e.g., pyramidal neurons, Schaffer collaterals) and direct (e.g., pyramidal neurons) pathway as they project from the dentate gyrus and through the cornu ammonis toward the alveus and fimbria (the main efferent connection of the hippocampus). Second, green anterior posterior orientations across the anterior-posterior axis from the hippocampal head to the tail are present across most volunteers, likely corresponding to axons projecting from the polysynaptic and direct pathways along the surface, wherein the lateral surface above CA1 contains the alveus and towards the medial edge, medial to CA3/4 with the interlocking dentate gyrus, contains the fimbria. Third, there are blue inferior-superior oriented streamlines that are likely continuations of the red left-right oriented streamlines in these pathways as they wrap within

the hippocampus and project toward the alveus and fimbria from CA1 and the DG (Figure 6.7). Beyond the single-fiber orientation constrain of the DTI model, the CSD approach resolved regions of anatomically plausible regions of crossing fibers that correspond to the two directionality patterns identified above and the gross morphology of the hippocampus in which the head consisted primarily of voxel-level crossing fibers with a relatively even mix of single fiber and crossing fiber voxels in the body and tail.

Our study has two key methodological differences relative to previously published in vivo intra-hippocampal tractography examinations that provide confidence to the findings. First, the diffusion imaging protocol was designed to acquire the hippocampus with high spatial resolution at 1 mm isotropic with no gap, compared to prior work which acquired voxels ~3-8x the size (1.4x1.4x1.4 = 2.7 mm^3 voxels – Zeineh et al., 2012; 2x2x2 = 8 mm^3 voxels – Meyer et al., 2017; 2x2x2 = 8 mm^3 voxels – Schlichting et al., 2021). Lower spatial resolution increases partial volume effects with adjacent CSF spaces, an effect that increases with age-related atrophy, in turn confounding both DTI and CSD based modelling of fiber orientations. Additionally, larger voxels are more likely than smaller voxels to comprise of more than one fiber orientation (Mukherjee et al., 2008), thus further limiting DTI tractography as the tensor approach can only model a single fiber orientation per voxel. Few of these studies provide visual examples of the tracts that they measured, likely due to the low spatial resolution of the data. For instance, Meyer et al. show a single example with limited information (e.g., no directional legend; only coloured to indicate left and right hemispheres) in two volunteers (one patient and one control, no age mentioned; Figure 2 in Meyer et al., 2017), Schlichting et al. also provide only a single example with little detail (i.e., no age indicated, no directional legend for the featured tracts; Figure 2 in Schlichting et al., 2021), and Zeineh et al. shows single examples of each pathway but with little information (i.e., no

directional legend; Figures 5-6 in Zeineh et al., 2021). Second, the multi-shell diffusion imaging protocol was also created to image the hippocampus with high angular resolution by acquiring two diffusion weighted shells, one at a high b value of 2000 s/mm^2 with 64 directions and another at a lower b value of 500 s/mm^2 with 64 directions. Low angular resolution typically limits analyses to the tensor model and does not allow for more advanced analyses such as CSD which unlike DTI can disentangle multiple fiber orientations within a given voxel. All (Meyer et al., 2017; Zeineh et al., 2012) but one (Schlichting et al., 2017) in vivo intra-hippocampal tractography studies have applied the DTI model, and as a result they were unable to disentangle more complex fiber orientations such as crossing fibers which have been suggested by ex vivo imaging (Colon-Perez et al., 2015; Coras et al., 2014; Shepherd et al., 2007).

To our knowledge, the only other study which has examined intra-hippocampal connectivity using an advanced diffusion model beyond DTI, also CSD, applied a single diffusion-weighted shell approach at a b value of 1000 s/mm^2 (Schlichting et al., 2021). Although they did acquire this single shell with 64 directions (adequate angular resolution), the b value is well below the minimum suggested high b value of at least 2000 s/mm^2 required to resolve crossing fiber orientations using CSD (Tournier et al., 2008). Furthermore, their study was also limited by low spatial resolution (8 mm^3 voxel size) which likely increased partial volume effects that could have confounded the directionality of the results due to CSF (isotropic) influence. Moreover, such low spatial resolution is not adequate to tract intra-hippocampal pathways within a structure that is on average ~4 cm long and 0.5-2 cm wide (Duvernoy et al., 2013).

The crossing fiber regions observed in the present study were omnipresent as a primary feature of the head of the hippocampus across the age span, although the head did appear to have more complex crossings (less green streamlines) at younger ages relative to older ages. This

finding was expected given the gross anatomy of the hippocampus, in which the two interlocking U-shaped laminae, the cornu ammonis and dentate gyrus, run anterior-posterior from the tail straight upwards into the body then toward the head where they make a ~180° turn to form the head which is on average ~twice the width of the body (i.e., for the average hippocampus, the head is ~2 cm wide and the body is approximately 1 cm wide). This structural morphology dictates that the polysynaptic and direct pathways which connect in a left-right and superior-inferior circular pattern parallel to the coronal plane curve with the 180° anterior-posterior turn, resulting in an inverted u-shaped coil of streamlines crossing with alveus and fimbria streamlines projecting from those pathways. Although both DTI and CSD streamlines demonstrated directionality patterns that plausibly follow these pathways, there are instances where the crossing fibers resolved by CSD and ignored by DTI may have allowed for a more anatomically-plausible sets of streamlines such as in Figure 6.3d (23-year-old male) in which the CSD streamlines in the hippocampal head demonstrate a clear radial n-shaped coil pattern in the turn from the body to head, with crossing fibers. There appears to be a qualitative age-effect wherein this n-shaped pattern running perpendicular to the 180° turn of the hippocampal body to head is more evident in older ages after adolescence (i.e., 23+ years, Figure 6.10). This finding may reflect age-related changes in the fibers in the polysynaptic and direct pathways increase with age, and is partially supported by our recent high spatial resolution DTI lifespan study of 153 healthy volunteers aged 5-74 years that showed non-linear age trajectories of FA with peak FA reached at 35 years (Solar et al., 2021).

One *ex vivo* stereological study of aging in the hippocampus reported regionally specific neuron loss of 31% in the dentate gyrus across 32 left hippocampi specimens from individuals (all males) whom were aged 18-85 years at the time of death (West, 1993). Axons from the DG project in a left-right orientation to CA3 and they synapse with pyramidal neuron dendrites as part of the

polysynaptic pathway (Figure 6.7). An age-related reduction of these connections from the DG due to neuron loss in the DG may result in the age-related reduction of the red left-right streamlines observed in the DTI and CSD streamlines (Figure 6.9, 6.10). The axons of the DG in the polysynaptic also project slightly in the inferior-superior direction on their way to CA3, which may explain the blue streamlines that are also more prominent at younger ages and disappear at older ages in this study (Figure 6.9, 6.10).

Several limitations of our study should be noted. First, our study was limited to a small cross-sectional sample size of only 40 cross-sectional healthy volunteers as stretched across a wide age span of 5-90 years. Future work can apply this approach to the entire normative database (the "AB300" as described in Treit et al., 2022) and utilize the automated mean DWI whole-hippocampus segmentation approach developed for with this data as recently developed and published in co-authorship with our colleagues in the Computing Science department (Efird et al., 2021). Moreover, although 6 twice-scanned healthy volunteers were analyzed, there are 19 more to be examined from the "Travelling Phantom" pool of volunteers that were scanned twice on our 3T Siemens Prisma as part of the AB300 normative database project (Treit et al., 2022). Second, the analysis was restricted to the whole-hippocampus structure, therefore excluding any assessment of whether there are anatomically plausible connections that extend from the subiculum to the dentate gyrus, and from the cornu ammonis and alveus out of the fimbria towards the fornix, as would be expected in completing the circuits to which the intra-hippocampal segments of the polysynaptic and direct pathways project. Third, the multi-tissue CSD approach that was utilized allowed us to assume that all GM and CSF tissue influences were removed and that our fODF maps and streamlines represented single fiber white patter tissue (Jeurissen et al., 2014). If the multi-tissue separation was not performed accurately, then the CSD approach may

have tracked through non-WM regions of the hippocampus, which is a mix of grey and white matter tissue. It would be useful to examine discrete fiber populations such as the alveus segment of the polysynaptic pathway. Subfield identification and segmentation would be useful in more precise intra-tractography and selective/exclusive ROIs. Finally, quantitative comparisons such as DTI *versus* CSD and males *versus* females within the whole hippocampus (e.g., proportion of voxels in the whole hippocampus with 1, 2, or 3 distinct fiber populations) and specific to discrete fiber populations (e.g., FA or MD from DTI, apparent fiber density from CSD).

7. Summary & Conclusions

The research presented in this dissertation adds to the growing body of knowledge in the field of diffusion MRI as it applies to the memory and learning center of the human brain, the hippocampus, in both the healthy lifespan and development in PAE. One millimeter isotropic DTI revealed nonlinear hippocampal volume and diffusion age trajectories and cognitive correlations that varied with age across the typical lifespan. This high spatial resolution DTI was also sensitive to hippocampal atrophy in children to young adults with PAE, wherein automated T1 segmentation approaches did not show any group differences. Interestingly, there were no PAE group differences in any hippocampal DTI metrics. Cognitive performance also correlated differently to hippocampal metrics in PAE relative to the healthy controls, suggesting that hippocampal-dependent cognitive processes are disrupted in PAE. One millimeter isotropic diffusion imaging also produced anatomically plausible intra-hippocampal orientations/streamlines with both the standard DTI model and a multi-shell multi-tissue CSD approach in a qualitative lifespan pilot study. These findings were realized by applying high spatial resolution and high angular resolution diffusion MRI acquisitions to the hippocampus.

7.1. The Hippocampus in Healthy Individuals

High spatial resolution 1 mm isotropic DTI demonstrated utility in allowing for visualization, manual segmentation, and quantification (FA, MD, AD, RD, volume) of the hippocampus across 5-74 years (n = 153) in Chapter 4. Manual hippocampal segmentation direction on 1 mm isotropic mean DWIs lends confidence to these results relative to prior studies that were limited by low resolution diffusion imaging and T1-weighted imaging with automated segmentation approaches that tend to overestimate the hippocampus. The volume and FA of the hippocampus peaked in the mid-30s with similar magnitudes of change in development and aging,

whereas MD, AD and RD showed greater magnitude changes in development toward their minima than in aging. Another notable finding in this chapter was that the life period of childhood to adolescence showed the most cognitive correlations with hippocampus metrics, relative to middle and older adulthood, suggesting that in younger ages, these memory processes rely more on the hippocampus than at middle to older ages, or that the memory performance degradation observed in middle to older adulthood is related to changes in other memory related structures and not the hippocampus. Moreover, better cognitive performance was correlated with lower FA and higher MD, a finding which may be due to these memory processes relying on the development of intra-hippocampal connections fibers that cross throughout the structure. These findings form a basis for comparison to PAE in Chapter 5, and to numerous other neurological or psychiatric disorders. Also, the indication of crossing fiber development with memory ability informed the value of pursuing higher order diffusion analyses, mainly CSD, to resolve crossing fiber pathways with diffusion tractography in Chapter 6.

7.2. The Hippocampus in Individuals with PAE

Chapter 5 reports the first study to apply diffusion MRI to study the hippocampus in PAE. Although hippocampal volumes were smaller in the PAE group on manual DWI segmentations, there were no group differences in hippocampal diffusion metrics, and both groups underwent similar age-related changes in diffusion metrics. Moreover, there were no individuals in the PAE group with severe FASD diagnoses like FAS. This evidence is the first to suggest that in individuals with PAE, the smaller hippocampus is seemingly undergoing typical microstructural development. This study is also the first to demonstrate greater sensitivity to hippocampal atrophy in PAE using manual mean DWI segmentations relative to automated T1 segmentations. This

Chapter highlights the potential value of high-resolution diffusion imaging in identifying hippocampal atrophy.

7.3. Tractography in the Hippocampus

As a qualitative pilot study, Chapter 6 included the examination of a subsample (n = 40) from a larger normative database (n = 378) of healthy participants with an age span of 5-90 years to compare diffusion tractography of intra-hippocampal pathways as derived from the standard tensor model versus multi-shell multi-tissue CSD using data acquired with an advanced version of the 1 mm isotropic DTI acquisition applied in Chapters 4 and 5. Chapter 6 demonstrates the first application of high spatial resolution DTI and CSD to reveal patterns of anatomically plausible intra-hippocampal directionality and streamlines across the lifespan with intra-subject replicability. Moreover, there are potential changes with age that can be identified by directional eigenvalues in DTI, fODFs in CSD, and streamlines derived from DTI and CSD; these changes may be related to improvements and declines in cognitive performance with age and pathology.

7.4. Limitations

Although the axial-oblique slab used for both diffusion MRI acquisitions utilized in this thesis were convenient for tracing the hippocampus, it would be valuable to have the entire brain acquired with 1 mm isotropic diffusion MRI for the tractography in Chapter 6 in order to explore the subcortical and cortical connections of the hippocampus. The axial-oblique slab also precludes most (if not all) automated diffusion MRI masking approaches and requires manual masking of the brain within the slab. The masking problem is likely due to most approaches working on the assumption of a standard full brain image input.

The main limitation of the lifespan study in Chapter 4 was that volume and diffusion measurements were restricted to the whole-hippocampus, head, body, and tail, while specific subfields, known to have different microstructural composition, were not considered. Chapter 4 was also limited as a cross-sectional study.

The PAE study in Chapter 5 was also limited to the whole-hippocampus, head, body, and tail regions for volume and diffusion measurements. Also, the PAE analysis had a small sample size of only 19 individuals with PAE. Moreover, as a retrospective investigation, we could not make conclusions about the pattern, timing, or amount of PAE. Also, the healthy control and PAE groups likely had many differences in postnatal experiences that could have impacted hippocampal development. Furthermore, there were no individuals with PAE who had a severe FASD diagnosis (e.g., pFAS or FAS). Finally, the PAE study was also limited to cross-sectional analyses.

The intra-hippocampal diffusion tractography study of Chapter 6 was limited as a qualitative pilot study with no quantitative measurements and with a sample size of n = 40 which should be considered small as stretched across the wide age span of 5-90 years. Additionally, the analysis was restricted to the whole-hippocampus structure with no isolation of specific pathways and the exclusion of examining the extensions of the intra-hippocampal pathways as they enter/exit the hippocampus from the rest of the brain.

7.5. Future Directions

In consideration of all 3 diffusion MRI research chapters in this dissertation, future diffusion ROI and tractography investigations should both segment CA and DG hippocampal subfields. The importance of subfield analysis is highlighted by a volumetric study that showed smaller CA1 and larger CA2-4+DG volumes in the body in association with better memory

performance (Riggins et al., 2018). Also relevant to all the research presented here, to make stronger inferences about age-related changes in the hippocampus, both typical lifespan and PAE group comparisons require longitudinal diffusion MRI studies. For PAE, it would be useful to examine groups with more severe diagnoses and break the analysis up into subgroups of varying severity of PAE-related outcomes or FASD diagnoses. Also, a more in-depth analysis of previous households and experiences may be especially important in PAE investigations because most demographics, such as the annual household income variable collected, only provide a snapshot of a given volunteer's current situation and does not consider their past. Hippocampal CSD tractography must be expanded upon by the use of subfield ROIs and the isolation and quantification of specific intra-hippocampal pathways, such as the polysynaptic and direct pathways, in relation to both age and cognitive performance, as well as by exploring beyond the restrictive slab and into the whole-brain so that the subcortical and cortical projections of the aforementioned hippocampal pathways may also be identified and quantified.

The hippocampus has unique cellular properties as the only brain region to undergo continued neurogenesis into late adulthood, and it contains memory and learning pathways that change with normal aging and in pathologies including Alzheimer's disease. Currently, the worldwide number of older individuals (aged 65 years or greater) is predicted to overtake the younger population over the next three decades (He et al., 2016). Therefore, diffusion MRI of the hippocampus is an important avenue to continue in understanding the hippocampus in health and disorder. Due to the small size, location, and shape of the hippocampus, and its complex internal architecture including tightly packed, crossing, and complex intra-hippocampal memory connections (e.g., polysynaptic pathway), diffusion MRI of the hippocampus may be improved by acquiring sub-millimetric resolution data, however issues of lower SNR and longer scan time must

be carefully considered. For these same reasons, future diffusion-weighted hippocampal imaging will also benefit from a multi-shell, high b value, high angular resolution, and high spatial resolution approach to run higher order analyses including CSD and tractography to further elucidate healthy and pathological microstructural changes within the entire structure, its subregions, and its structural connections (including intra-hippocampal connections and its connections to the rest of the brain). Finally, it is important to create these hippocampal sequences with a clinically feasible scanning time and a simple-to-implement (on the scanner) protocol so that data may be easily collected across the vast variety of patient populations with confirmed or suspected hippocampal involvement.

References

Adler, D. H., Wisse, L. E. M., Ittyerah, R., Pluta, J. B., Ding, S. L., Xie, L., Wang, J., Kadivar, S., Robinson, J. L., Schuck, T., Trojanowski, J. Q., Grossman, M., Detre, J. A., Elliott, M. A., Toledo, J. B., Liu, W., Pickup, S., Miller, M. I., Das, S. R., … Yushkevich, P. A. (2018). Characterizing the human hippocampus in aging and Alzheimer's disease using a computational atlas derived from ex vivo MRI and histology. *Proceedings of the National Academy of Sciences of the United States of America*, *115*(16), 4252–4257. https://doi.org/10.1073/pnas.1801093115

Akudjedu, T. N., Nabulsi, L., Makelyte, M., Scanlon, C., Hehir, S., Casey, H., Ambati, S., Kenney, J., O'Donoghue, S., McDermott, E., Kilmartin, L., Dockery, P., McDonald, C., Hallahan, B., & Cannon, D. M. (2018). A comparative study of segmentation techniques for the quantification of brain subcortical volume. *Brain Imaging and Behavior*, *12*(6), 1678–1695. https://doi.org/10.1007/s11682-018-9835-y

Alexander, A. L., Lee, J. E., Lazar, M., & Field, A. S. (2007). Diffusion tensor imaging of the brain. *Neurotherapeutics : The Journal of the American Society for Experimental NeuroTherapeutics*, *4*(3), 316–329. https://doi.org/10.1016/j.nurt.2007.05.011

Anblagan, D., Valdés Hernández, M. C., Ritchie, S. J., Aribisala, B. S., Royle, N. A., Hamilton, I. F., Cox, S. R., Gow, A. J., Pattie, A., Corley, J., Starr, J. M., Muñoz Maniega, S., Bastin, M. E., Deary, I. J., & Wardlaw, J. M. (2018). Coupled changes in hippocampal structure and cognitive ability in later life. *Brain and Behavior*, *8*(2), 1–13. https://doi.org/10.1002/brb3.838

Andersson, J. L. R., Junquian, X., Yacoub, E., Auerbach, E., Moeller, S., & Ugurbil, K. (2012). A comprehensive Gausssian Process framework for correcting distortions and movements in diffusion images. *Proc. Intl. Soc. Mag. Reson. Med.*, *20*, 2426.

Astley, S. J., Aylward, E. H., Olson, H. C., Kerns, K., Brooks, A., Coggins, T. E., Davies, J., Dorn, S., Gendler, B., Jirikowic, T., Kraegel, P., Maravilla, K., & Richards, T. (2009). Magnetic resonance imaging outcomes from a comprehensive magnetic resonance study of children with fetal alcohol spectrum disorders. *Alcoholism: Clinical and Experimental Research*, *33*(10), 1671–1689. https://doi.org/10.1111/j.1530-0277.2009.01004.x

Baddeley, A., Jarrold, C., & Vargha-Khadem, F. (2011). Working memory and the hippocampus. *Journal of Cognitive Neuroscience*, *23*(12), 3855–3861. https://doi.org/10.1162/jocn_a_00066

Barnes, D. E., & Walker, D. W. (1981). Prenatal ethanol exposure permanently reduces the number of pyramidal neurons in rat hippocampus. *Developmental Brain Research*, *1*(3), 333–340. https://doi.org/10.1016/0165-3806(81)90071-7

Basser, P. J., Mattiello, J., & LeBihan, D. (1994). MR diffusion tensor spectroscopy and imaging. *Biophysical Journal*, *66*(1), 259–267. https://doi.org/10.1016/S0006-3495(94)80775-1

Basser, P. J., Pajevic, S., Pierpaoli, C., Duda, J., & Aldroubi, A. (2000). In Vivo Fiber Tractography Using DT-MRI Data. *Magnetic Resonance in Medicine*, *44*, 625–632.

https://doi.org/10.1002/1522-2594

Beaujoin, J., Palomero-Gallagher, N., Boumezbeur, F., Axer, M., Bernard, J., Poupon, F., Schmitz, D., Mangin, J.-F., & Poupon, C. (2018). Post-mortem inference of the human hippocampal connectivity and microstructure using ultra-high field diffusion MRI at 11.7 T. *Brain Structure and Function*, *223*, 2157–2179. https://doi.org/10.1007/s00429-018-1617-1

Beaulieu, C. (2002). The basis of anisotropic water diffusion in the nervous system - A technical review. *NMR in Biomedicine*, *15*(7–8), 435–455. https://doi.org/10.1002/nbm.782

Berman, R. F., & Hannigan, J. H. (2000). Effects of prenatal alcohol exposure on the hippocampus: Spatial behavior, electrophysiology, and neuroanatomy. *Hippocampus*, *10*(1), 94–110. https://doi.org/10.1002/(SICI)1098-1063(2000)10:1<94::AID-HIPO11>3.0.CO;2-T

Berron, D., Vieweg, P., Hochkeppler, A., Pluta, J. B., Ding, S. L., Maass, A., Luther, A., Xie, L., Das, S. R., Wolk, D. A., Wolbers, T., Yushkevich, P. A., Düzel, E., & Wisse, L. E. M. (2017). A protocol for manual segmentation of medial temporal lobe subregions in 7 Tesla MRI. *NeuroImage: Clinical*, *15*, 466–482. https://doi.org/10.1016/j.nicl.2017.05.022

Biffen, S. C., Warton, C. M. R., Dodge, N. C., Molteno, C. D., Jacobson, J. L., Jacobson, S. W., & Meintjes, E. M. (2020). Validity of automated FreeSurfer segmentation compared to manual tracing in detecting prenatal alcohol exposure-related subcortical and corpus callosal alterations in 9- to 11-year-old children. *NeuroImage: Clinical*, *28*, 102368. https://doi.org/10.1016/J.NICL.2020.102368

Biffen, S. C., Warton, C. M. R., Lindinger, N. M., Randall, S. R., Lewis, C. E., Molteno, C. D., Jacobson, J. L., Jacobson, S. W., & Meintjes, E. M. (2018). Reductions in corpus callosum volume partially mediate effects of prenatal alcohol exposure on IQ. *Frontiers in Neuroanatomy*, *11*, 132. https://doi.org/10.3389/fnana.2017.00132

Boccardi, M., Bocchetta, M., Apostolova, L. G., Barnes, J., Bartzokis, G., Corbetta, G., Decarli, C., Detoledo-Morrell, L., Firbank, M., Ganzola, R., Gerritsen, L., Henneman, W., Killiany, R. J., Malykhin, N., Pasqualetti, P., Pruessner, J. C., Redolfi, A., Robitaille, N., Soininen, H., … Frisoni, G. B. (2015). Delphi definition of the EADC-ADNI harmonized protocol for hippocampal segmentation on magnetic resonance. *Alzheimer's and Dementia*, *11*(2), 126–138. https://doi.org/10.1016/j.jalz.2014.02.009

Boccardi, M., Bocchetta, M., Ganzola, R., Robitaille, N., Redolfi, A., Duchesne, S., Jack, C. R., Frisoni, G. B., Bartzokis, G., Csernansky, J. G., De Leon, M. J., Detoledo-Morrell, L., Killiany, R. J., Lehericy, S., Malykhin, N., Pantel, J., Pruessner, J. C., Soininen, H., & Watson, C. (2015). Operationalizing protocol differences for EADC-ADNI manual hippocampal segmentation. *Alzheimer's and Dementia*, *11*(2), 184–194. https://doi.org/10.1016/j.jalz.2013.03.001

Brady, M. L., Allan, A. M., & Caldwell, K. K. (2012). A limited access mouse model of prenatal alcohol exposure that produces long-lasting deficits in hippocampal-dependent learning and memory. *Alcoholism: Clinical and Experimental Research*, *36*(3), 457–466. https://doi.org/10.1111/j.1530-0277.2011.01644.x

Brocardo, P. S., Gil-Mohapel, J., Wortman, R., Noonan, A., McGinnis, E., Patten, A. R., & Christie, B. R. (2017). The effects of ethanol exposure during distinct periods of brain development on oxidative stress in the adult rat brain. *Alcoholism: Clinical and Experimental Research*, *41*(1), 26–37. https://doi.org/10.1111/acer.13266

Burgess, N., Maguire, E. A., & O'Keefe, J. (2002). The human hippocampus and spatial and episodic memory. *Neuron*, *35*(4), 625–641. https://doi.org/10.1016/S0896-6273(02)00830-9

Calamante, F. (2019). The seven deadly sins of measuring brain structural connectivity using diffusion MRI streamlines fibre-tracking. *Diagnostics*, *9*(3). https://doi.org/10.3390/diagnostics9030115

Callow, D. D., Canada, K. L., & Riggins, T. (2020). Microstructural integrity of the hippocampus during childhood: Relations with age and source memory. *Frontiers in Psychology*, *11*, 1–9. https://doi.org/10.3389/fpsyg.2020.568953

Carlesimo, G. A., Cherubini, A., Caltagirone, C., & Spalletta, G. (2010). Hippocampal mean diffusivity and memory in healthy elderly individuals. *Neurology*, *74*(3), 194–200. https://doi.org/10.1212/WNL.0b013e3181cb3e39

Chen, K. H. M., Chuah, L. Y. M., Sim, S. K. Y., & Chee, M. W. L. (2009). Hippocampal region-specific contributions to memory performance in normal elderly. *Brain and Cognition*, *72*, 400–407. https://doi.org/10.1016/j.bandc.2009.11.007

Chudley, A. E., Conry, J., Cook, J. L., Loock, C., Rosales, T., & LeBlanc, N. (2005). Fetal alcohol spectrum disorder: Canadian guidelines for diagnosis. *Cmaj*, *172*(5 SUPPL.). https://doi.org/10.1503/cmaj.1040302

Clarren, S. K., Alvord, E. C., Sumi, S. M., Streissguth, A. P., & Smith, D. W. (1978). Brain malformations related to prenatal exposure to ethanol. *The Journal of Pediatrics*, *92*(1), 64–67. https://doi.org/10.1016/S0022-3476(78)80072-9

Coles, C. D., Goldstein, F. C., Lynch, M. E., Chen, X., Kable, J. A., Johnson, K. C., & Hu, X. (2011). Memory and brain volume in adults prenatally exposed to alcohol. *Brain and Cognition*, *75*(1), 67–77. https://doi.org/10.1016/j.bandc.2010.08.013

Colon-Perez, L. M., King, M., Parekh, M., Boutzoukas, A., Carmona, E., Couret, M., Klassen, R., Mareci, T. H., & Carney, P. R. (2015). High-field magnetic resonance imaging of the human temporal lobe. *NeuroImage: Clinical*, *9*, 58–68. https://doi.org/10.1016/j.nicl.2015.07.005

Coras, R., Milesi, G., Zucca, I., Mastropietro, A., Scotti, A., Figini, M., Mühlebner, A., Hess, A., Graf, W., Tringali, G., Blümcke, I., Villani, F., Didato, G., Frassoni, C., Spreafico, R., & Garbelli, R. (2014). 7T MRI features in control human hippocampus and hippocampal sclerosis: An ex vivo study with histologic correlations. *Epilepsia*, *55*(12), 2003–2016. https://doi.org/10.1111/epi.12828

Creeley, C. E., Dikranian, K. T., Johnson, S. A., Farber, N. B., & Olney, J. W. (2013). *Alcohol-induced apoptosis of oligodendrocytes in the fetal macaque brain*. https://doi.org/10.1186/2051-5960-1-23

Daugherty, A. M., Flinn, R., & Ofen, N. (2017). Hippocampal CA3-dentate gyrus volume uniquely linked to improvement in associative memory from childhood to adulthood. *NeuroImage*, *153*, 75–85. https://doi.org/10.1016/j.neuroimage.2017.03.047

De Master, D., Pathman, T., Lee, J. K., & Ghetti, S. (2014). Structural development of the hippocampus and episodic memory: Developmental differences along the anterior/posterior axis. *Cerebral Cortex*, *24*(11), 3036–3045. https://doi.org/10.1093/cercor/bht160

Delatour, L. C., Yeh, P. W., & Yeh, H. H. (2019). Ethanol Exposure In Utero Disrupts Radial Migration and Pyramidal Cell Development in the Somatosensory Cortex. *Cerebral Cortex*, *29*, 2125–2139. https://doi.org/10.1093/cercor/bhy094

Den Heijer, T., der Lijn, F. van, Vernooij, M. W., de Groot, M., Koudstaal, P. J., der Lugt, A. van, Krestin, G. P., Hofman, A., Niessen, W. J., & Breteler, M. M. B. (2012). Structural and diffusion MRI measures of the hippocampus and memory performance. *NeuroImage*, *63*(4), 1782–1789. https://doi.org/10.1016/j.neuroimage.2012.08.067

Denboer, J. W., Nicholls, C., Corte, C., & Chestnut, K. (2014). National Institutes of Health Toolbox Cognition Battery. *Archives of Clinical Neuropsychology*, *29*(7), 692–694. https://doi.org/10.1093/arclin/acu033

Descoteaux, M. (2015). High Angular Resolution Diffusion Imaging (HARDI). *Wiley Encyclopedia of Electrical and Electronics Engineering*, 1–25. https://doi.org/10.1002/047134608x.w8258

Dhollander, T., Mito, R., Raffelt, D., & Connelly, A. (2019). Improved white matter response function estimation for 3-tissue constrained spherical deconvolution. *Proc. Intl. Soc. Mag. Reson. Med*, *May 11-16*, 555. https://www.researchgate.net/publication/331165168_Improved_white_matter_response_function_estimation_for_3-tissue_constrained_spherical_deconvolution

Dhollander, T., Raffelt, D., & Connelly, A. (2016). Unsupervised 3-tissue response function estimation from single-shell or multi-shell diffusion MR data without a co-registered T1 image. *ISMRM Workshop on Breaking the Barriers of Diffusion MRI*, *35*(September), 5. https://www.researchgate.net/publication/307863133_Unsupervised_3-tissue_response_function_estimation_from_single-shell_or_multi-shell_diffusion_MR_data_without_a_co-registered_T1_image

Ding, S. L., & Van Hoesen, G. W. (2015). Organization and detailed parcellation of human hippocampal head and body regions based on a combined analysis of Cyto- and chemoarchitecture. *Journal of Comparative Neurology*, *523*(15), 2233–2253. https://doi.org/10.1002/cne.23786

Dodge, N. C., Thomas, K. G. F., Meintjes, E. M., Molteno, C. D., Jacobson, J. L., & Jacobson, S. W. (2020). Reduced hippocampal volumes partially mediate effects of prenatal alcohol exposure on spatial navigation on a virtual water maze task in children. *Alcoholism: Clinical and Experimental Research*, *44*(4), 844–855. https://doi.org/10.1111/acer.14310

Donald, K. A., Eastman, E., Howells, F. M., Adnams, C., Riley, E. P., Woods, R. P., Narr, K. L.,

& Stein, D. J. (2015). Neuroimaging effects of prenatal alcohol exposure on the developing human brain: A magnetic resonance imaging review. *Acta Neuropsychiatrica*, *27*(5), 251–269. https://doi.org/10.1017/neu.2015.12

Donald, K. A., Fouche, J. P., Roos, A., Koen, N., Howells, F. M., Riley, E. P., Woods, R. P., Zar, H. J., Narr, K. L., & Stein, D. J. (2016). Alcohol exposure in utero is associated with decreased gray matter volume in neonates. *Metabolic Brain Disease*, *31*(1), 81–91. https://doi.org/10.1007/s11011-015-9771-0

du Plooy, C. P., Malcolm-Smith, S., Adnams, C. M., Stein, D. J., & Donald, K. A. (2016). The effects of prenatal alcohol exposure on episodic memory functioning: A systematic review. *Archives of Clinical Neuropsychology*, *31*, 710–726. https://doi.org/10.1093/arclin/acw067

Dudek, J., Skocic, J., Sheard, E., & Rovet, J. (2014). Hippocampal abnormalities in youth with alcohol-related neurodevelopmental disorder. *Journal of the International Neuropsychological Society*, *20*(2), 181–191. https://doi.org/10.1017/S1355617713001343

Duerden, E. G., Guo, T., Dodbiba, L., Chakravarty, M. M., Chau, V., Poskitt, K. J., Synnes, A., Grunau, R. E., & Miller, S. P. (2016). Midazolam dose correlates with abnormal hippocampal growth and neurodevelopmental outcome in preterm infants. *Annals of Neurology*, *79*(4), 548–559. https://doi.org/10.1002/ana.24601

Duvernoy, H. M., Cattin, F., Risold, P. Y., Vannson, J. L., & Gaudron, M. (2013). The human hippocampus: Functional anatomy, vascularization and serial sections with MRI, fourth edition. In *The Human Hippocampus: Functional Anatomy, Vascularization and Serial Sections with MRI, Fourth Edition* (4th ed.). Springer Berlin Heidelberg. https://doi.org/10.1007/978-3-642-33603-4

Efird, C., Neumann, S., Solar, K. G., Beaulieu, C., & Cobzas, D. (2021). Hippocampus segmentation on high resolution diffusion MRI. *Proceedings - International Symposium on Biomedical Imaging*, *2021-April*, 1369–1372. https://doi.org/10.1109/ISBI48211.2021.9434094

Ellwood-Lowe, M. E., Humphreys, K. L., Ordaz, S. J., Camacho, M. C., Sacchet, M. D., & Gotlib, I. H. (2018). Time-varying effects of income on hippocampal volume trajectories in adolescent girls. *Developmental Cognitive Neuroscience*, *30*, 41. https://doi.org/10.1016/J.DCN.2017.12.005

Feinberg, D. A., Hale, J. D., Watts, J. C., Kaufman, L., & Mark, A. (1986). Halving MR imaging time by conjugation: Demonstration at 3.5 kG. *Radiology*, *161*(2), 527–531. https://doi.org/10.1148/radiology.161.2.3763926

Fellgiebel, A., & Yakushev, I. (2011). Diffusion tensor imaging of the hippocampus in MCI and early Alzheimers Disease. *Journal of Alzheimer's Disease*, *26*, 257–262. https://doi.org/10.3233/JAD-2011-0001

Fischl, B., Salat, D. H., Busa, E., Albert, M., Dieterich, M., Haselgrove, C., Van Der Kouwe, A., Killiany, R., Kennedy, D., Klaveness, S., Montillo, A., Makris, N., Rosen, B., & Dale, A. M. (2002). Whole brain segmentation: Automated labeling of neuroanatomical structures in the

human brain. *Neuron*, *33*(3), 341–355. https://doi.org/10.1016/S0896-6273(02)00569-X

Fischl, B., Van Der Kouwe, A., Destrieux, C., Halgren, E., Ségonne, F., Salat, D. H., Busa, E., Seidman, L. J., Goldstein, J., Kennedy, D., Caviness, V., Makris, N., Rosen, B., & Dale, A. M. (2004). Automatically parcellating the human cerebral cortex. *Cerebral Cortex*, *14*(1), 11–22. https://doi.org/10.1093/cercor/bhg087

Fjell, A. M., Sneve, M. H., Sederevicius, D., Sørensen, Ø., Krogsrud, S. K., Mowinckel, A. M., & Walhovd, K. B. (2019). Volumetric and microstructural regional changes of the hippocampus underlying development of recall performance after extended retention intervals. *Developmental Cognitive Neuroscience*, *40*, 1–12. https://doi.org/10.1016/j.dcn.2019.100723

Flannigan, K., Unsworth, K., & Harding, K. (2018a). FASD Prevalence in Special Populations. *Canada FASD Research Network*, 1–4. https://canfasd.ca/wp-content/uploads/sites/35/2018/08/Prevalence-2-Issue-Paper-FINAL.pdf

Flannigan, K., Unsworth, K., & Harding, K. (2018b). The Prevalence of Fetal Alcohol Spectrum Disorder. *Canada FASD Research Network*, *July*, 1–4.

Frisoni, G. B., Jack, C. R., Bocchetta, M., Bauer, C., Frederiksen, K. S., Liu, Y., Preboske, G., Swihart, T., Blair, M., Cavedo, E., Grothe, M. J., Lanfredi, M., Martinez, O., Nishikawa, M., Portegies, M., Stoub, T., Ward, C., Apostolova, L. G., Ganzola, R., … Boccardi, M. (2015). The EADC-ADNI harmonized protocol for manual hippocampal segmentation on magnetic resonance: Evidence of validity. *Alzheimer's and Dementia*, *11*(2), 111–125. https://doi.org/10.1016/j.jalz.2014.05.1756

Ghazi Sherbaf, F., Aarabi, M. H., Hosein Yazdi, M., & Haghshomar, M. (2019). White matter microstructure in fetal alcohol spectrum disorders: A systematic review of diffusion tensor imaging studies. *Human Brain Mapping*, *40*(3), 1017–1036. https://doi.org/10.1002/hbm.24409

Gil-Mohapel, J., Boehme, F., Kainer, L., & Christie, B. R. (2010). *Hippocampal cell loss and neurogenesis after fetal alcohol exposure: Insights from different rodent models*. https://doi.org/10.1016/j.brainresrev.2010.04.011

Gogtay, N., Nugent, T. F., Herman, D. H., Ordonez, A., Greenstein, D., Hayashi, K. M., Clasen, L., Toga, A. W., Giedd, J. N., Rapoport, J. L., & Thompson, P. M. (2006). Dynamic mapping of normal human hippocampal development. *Hippocampus*, *16*(8), 664–672. https://doi.org/10.1002/hipo.20193

Gordon, B. A., Blazey, T., Benzinger, T. L. S., & Head, D. (2013). Effects of aging and Alzheimer's disease along the longitudinal axis of the hippocampus. *Journal of Alzheimer's Disease*, *37*(1), 41–50. https://doi.org/10.3233/JAD-130011

Green, C. R., Kobus, S. M., Ji, Y., Bennett, B. M., Reynolds, J. N., & Brien, J. F. (2005). Chronic prenatal ethanol exposure increases apoptosis in the hippocampus of the term fetal guinea pig. *Neurotoxicology and Teratology*, *27*(6), 871–881. https://doi.org/10.1016/j.ntt.2005.07.006

Gross, L. A., Moore, E. M., Wozniak, J. R., Coles, C. D., Kable, J. A., Sowell, E. R., Jones, K. L., Riley, E. P., & Mattson, S. N. (2018). Neural correlates of verbal memory in youth with heavy prenatal alcohol exposure. In *Brain Imaging and Behavior* (Vol. 12, Issue 3). https://doi.org/10.1007/s11682-017-9739-2

Hackert, V. H., Den Heijer, T., Oudkerk, M., Koudstaal, P. J., Hofman, A., & Breteler, M. M. B. (2002). Hippocampal head size associated with verbal memory performance in nondemented elderly. *NeuroImage*, *17*(3), 1365–1372. https://doi.org/10.1006/nimg.2002.1248

Hahn, E. L. (1950). Spin echoes. *Physical Review*, *80*(4), 580–594. https://doi.org/10.1103/PhysRev.80.580

He, W., Goodkind, D., & Kowal, P. (2016). An aging world : 2015 international population reports. *Aging*, *March*, 165. https://doi.org/10.13140/RG.2.1.1088.9362

Henry, T. R., Chupin, M., Lehéricy, S., Strupp, J. P., Sikora, M. A., Sha, Z. Y., Uğurbil, K., & Pierre-François, V. de M. (2011). Hippocampal sclerosis in temporal lobe epilepsy: Findings at 7 T. *Radiology*, *261*(1), 199–209. https://doi.org/10.1148/radiol.11101651/-/DC1

Hong, Y. J., Yoon, B., Lim, S. C., Shim, Y. S., Kim, J. Y., Ahn, K. J., Han, I. W., & Yang, D. W. (2013). Microstructural changes in the hippocampus and posterior cingulate in mild cognitive impairment and Alzheimer's disease: A diffusion tensor imaging study. *Neurological Sciences*, *34*(7), 1215–1221. https://doi.org/10.1007/s10072-012-1225-4

Jäkel, S., & Dimou, L. (2017). Glial cells and their function in the adult brain: A journey through the history of their ablation. *Frontiers in Cellular Neuroscience*, *11*(February), 1–17. https://doi.org/10.3389/fncel.2017.00024

Jeurissen, B., Tournier, J. D., Dhollander, T., Connelly, A., & Sijbers, J. (2014). Multi-tissue constrained spherical deconvolution for improved analysis of multi-shell diffusion MRI data. *NeuroImage*, *103*, 411–426. https://doi.org/10.1016/j.neuroimage.2014.07.061

Johnson, S. B., Riis, J. L., & Noble, K. G. (2016). State of the art review: Poverty and the developing brain. *Pediatrics*, *137*(4). https://doi.org/10.1542/peds.2015-3075

Jones, D. K., Knösche, T. R., & Turner, R. (2013). White matter integrity, fiber count, and other fallacies: The do's and don'ts of diffusion MRI. *NeuroImage*, *73*, 239–254. https://doi.org/10.1016/j.neuroimage.2012.06.081

Joseph, J., Warton, C., Jacobson, S. W., Jacobson, J. L., Molteno, C. D., Eicher, A., Marais, P., Phillips, O. R., Narr, K. L., & Meintjes, E. M. (2014). Three-dimensional surface deformation-based shape analysis of hippocampus and caudate nucleus in children with fetal alcohol spectrum disorders. *Human Brain Mapping*, *35*(2), 659–672. https://doi.org/10.1002/hbm.22209

Kellner, E., Dhital, B., Kiselev, V. G., & Reisert, M. (2016). Gibbs-ringing artifact removal based on local subvoxel-shifts. *Magnetic Resonance in Medicine*, *76*(5), 1574–1581. https://doi.org/10.1002/mrm.26054

Kimiwada, T., Juhasz, C., Makki, M., Muzik, O., Chugani, D. C., Asano, E., & Chugani, H. T.

(2006). Hippocampal and thalamic diffusion abnormalities in children with temporal lobe epilepsy. *Epilepsia*, *47*(1), 167–175. https://doi.org/10.1111/j.1528-1167.2006.00383.x

Klintsova, A. Y., Helfer, J. L., Calizo, L. H., Dong, W. K., Goodlett, C. R., & Greenough, W. T. (2007). Persistent Impairment of Hippocampal Neurogenesis in Young Adult Rats Following Early Postnatal Alcohol Exposure. *Alcoholism: Clinical and Experimental Research*, *31*(12), 2073–2082. https://doi.org/10.1111/J.1530-0277.2007.00528.X

Kozareva, D. A., Cryan, J. F., & Nolan, Y. M. (2019). Born this way: Hippocampal neurogenesis across the lifespan. *Aging Cell*, *18*(5), 1–18. https://doi.org/10.1111/acel.13007

Krueger, A. M., Roediger, D. J., Mueller, B. A., Boys, C. A., Hendrickson, T. J., Schumacher, M. J., Mattson, S. N., Jones, K. L., Riley, E. P., Lim, K. O., & Wozniak, J. R. (2020). Para-limbic structural abnormalities are associated with internalizing symptoms in children with prenatal alcohol exposure. *Alcoholism: Clinical and Experimental Research*, *44*(8), 1598–1608. https://doi.org/10.1111/acer.14390

Kulaga-Yoskovitz, J., Bernhardt, B. C., Hong, S.-J., Mansi, T., Liang, K. E., van der Kouwe, A. J. W., Smallwood, J., Bernasconi, A., & Bernasconi, N. (2015). Multi-contrast submillimetric 3 Tesla hippocampal subfield segmentation protocol and dataset. *Scientific Data*, *2*, 1–9. https://doi.org/10.1038/SDATA.2015.59

Kumar, R., Chavez, A. S., Macey, P. M., Woo, M. A., & Harper, R. M. (2013). Brain axial and radial diffusivity changes with age and gender in healthy adults. *Brain Research*, *1512*(4), 22–36. https://doi.org/10.1016/j.brainres.2013.03.028

Lange, S., Probst, C., Gmel, G., Rehm, J., Burd, L., & Popova, S. (2017). Global prevalence of fetal alcohol spectrum disorder among children and youth: A systematic review and meta-analysis. *JAMA Pediatrics*, *171*(10), 948–956. https://doi.org/10.1001/JAMAPEDIATRICS.2017.1919

Langnes, E., Sneve, M. H., Sederevicius, D., Amlien, I. K., Walhovd, K. B., & Fjell, A. M. (2020). Anterior and posterior hippocampus macro- and microstructure across the lifespan in relation to memory—A longitudinal study. *Hippocampus*, *30*(7), 678–692. https://doi.org/10.1002/hipo.23189

Langnes, E., Vidal-Piñeiro, D., Sneve, M. H., Amlien, I. K., Walhovd, K. B., & Fjell, A. M. (2019). Development and Decline of the Hippocampal Long-Axis Specialization and Differentiation During Encoding and Retrieval of Episodic Memories. *Cerebral Cortex*, *29*(8), 3398–3414. https://doi.org/10.1093/cercor/bhy209

Le Bihan, D., Poupon, C., Amadon, A., & Lethimonnier, F. (2006). Artifacts and pitfalls in diffusion MRI. *Journal of Magnetic Resonance Imaging*, *24*(3), 478–488. https://doi.org/10.1002/jmri.20683

Lebel, C., Gee, M., Camicioli, R., Wieler, M., Martin, W., & Beaulieu, C. (2012). Diffusion tensor imaging of white matter tract evolution over the lifespan. *NeuroImage*, *60*(1), 340–352. https://doi.org/10.1016/j.neuroimage.2011.11.094

Lebel, C., Rasmussen, C., Wyper, K., Walker, L., Andrew, G., Yager, J., & Beaulieu, C. (2008). Brain diffusion abnormalities in children with fetal alcohol spectrum disorder. *Alcoholism: Clinical and Experimental Research*, *32*(10), 1732–1740. https://doi.org/10.1111/j.1530-0277.2008.00750.x

Lebel, C., Treit, S., & Beaulieu, C. (2019). A review of diffusion MRI of typical white matter development from early childhood to young adulthood. *NMR in Biomedicine*, *32*(4), 1–23. https://doi.org/10.1002/nbm.3778

Lee, H., & Thuret, S. (2018). Adult human hippocampal neurogenesis: Controversy and evidence. *Trends in Molecular Medicine*, *24*(6), 521–522. https://doi.org/10.1016/j.molmed.2018.04.002

Lin, M., Fwu, P. T., Buss, C., Davis, E. P., Head, K., Muftuler, L. T., Sandman, C. A., & Su, M. Y. (2013). Developmental changes in hippocampal shape among preadolescent children. *International Journal of Developmental Neuroscience*, *31*(7), 473–481. https://doi.org/10.1016/j.ijdevneu.2013.06.001

Lisman, J., Buzsáki, G., Eichenbaum, H., Nadel, L., Rangananth, C., & Redish, A. D. (2017). Viewpoints: how the hippocampus contributes to memory, navigation and cognition. *Nature Neuroscience*, *20*(11), 1434–1447. https://doi.org/10.1038/nn.4661

Little, G., & Beaulieu, C. (2020). Multivariate models of brain volume for identification of children and adolescents with fetal alcohol spectrum disorder. *Human Brain Mapping*, *41*(5), 1181–1194. https://doi.org/10.1002/hbm.24867

Livy, D. J., Miller, E. K., Maier, S. E., & West, J. R. (2003). Fetal alcohol exposure and temporal vulnerability: Effects of binge-like alcohol exposure on the developing rat hippocampus. *Neurotoxicology and Teratology*, *25*(4), 447–458. https://doi.org/10.1016/S0892-0362(03)00030-8

Lynch, K. M., Shi, Y., Toga, A. W., & Clark, K. A. (2019). Hippocampal shape maturation in childhood and adolescence. *Cerebral Cortex*, *29*(9), 3651–3665. https://doi.org/10.1093/cercor/bhy244

Mah, A., Geeraert, B., & Lebel, C. (2017). Detailing neuroanatomical development in late childhood and early adolescence using NODDI. *PLoS ONE*, *12*(8), 1–16. https://doi.org/10.1371/journal.pone.0182340

Mak, E., Gabel, S., Su, L., Williams, G. B., Arnold, R., Passamonti, L., Vazquez Rodríguez, P., Surendranathan, A., Bevan-Jones, W. R., Rowe, J. B., & O'Brien, J. T. (2017). Multi-modal MRI investigation of volumetric and microstructural changes in the hippocampus and its subfields in mild cognitive impairment, Alzheimer's disease, and dementia with Lewy bodies. *International Psychogeriatrics*, *29*(04), 545–555. https://doi.org/10.1017/S1041610216002143

Malykhin, N. V., Bouchard, T. P., Camicioli, R., & Coupland, N. J. (2008). Aging hippocampus and amygdala. *NeuroReport*, *19*(5), 543–547. https://doi.org/10.1097/WNR.0b013e3282f8b18c

Malykhin, N. V., Huang, Y., Hrybouski, S., & Olsen, F. (2017). Differential vulnerability of hippocampal subfields and anteroposterior hippocampal subregions in healthy cognitive aging. *Neurobiology of Aging*, *59*, 121–134. https://doi.org/10.1016/j.neurobiolaging.2017.08.001

Manjón, J. V., & Coupé, P. (2016). Volbrain: An online MRI brain volumetry system. *Frontiers in Neuroinformatics*, *10*(JUL), 1–14. https://doi.org/10.3389/fninf.2016.00030

Marjonen, H., Sierra, A., Nyman, A., Rogojin, V., Gröhn, O., Linden, A. M., Hautaniemi, S., & Kaminen-Ahola, N. (2015). Early maternal alcohol consumption alters hippocampal DNA methylation, gene expression and volume in a mouse model. *PLoS ONE*, *10*(5), 1–20. https://doi.org/10.1371/journal.pone.0124931

Mattson, S. N., Bernes, G. A., & Doyle, L. R. (2019). Fetal Alcohol Spectrum Disorders: A Review of the Neurobehavioral Deficits Associated With Prenatal Alcohol Exposure. *Alcoholism: Clinical and Experimental Research*, *43*(6), 1046–1062. https://doi.org/10.1111/acer.14040

Mattson, S. N., & Riley, E. P. (1995). Prenatal exposure to alcohol: What the images reveal. *Alcohol Health and Research World*, *19*(4), 273–278. /pmc/articles/PMC6875740/

May, P. A., Chambers, C. D., Kalberg, W. O., Zellner, J., Feldman, H., Buckley, D., Kopald, D., Hasken, J. M., Xu, R., Honerkamp-Smith, G., Taras, H., Manning, M. A., Robinson, L. K., Adam, M. P., Abdul-Rahman, O., Vaux, K., Jewett, T., Elliott, A. J., Kable, J. A., … Hoyme, H. E. (2018). Prevalence of fetal alcohol spectrum disorders in 4 US communities. *JAMA*, *319*(5), 474–482. https://doi.org/10.1001/JAMA.2017.21896

McLachlan, K., Zhou, D., Little, G., Rasmussen, C., Pei, J., Andrew, G., Reynolds, J. N., & Beaulieu, C. (2020). Current socioeconomic status correlates with brain volumes in healthy children and adolescents but not in children with prenatal alcohol exposure. *Frontiers in Human Neuroscience*, *14*(June), 1–12. https://doi.org/10.3389/fnhum.2020.00223

Meyer, M., Scala, G., Edde, M., Dilharreguy, B., Radat, F., Allard, M., & Chanraud, S. (2017). Brain structural investigation and hippocampal tractography in medication overuse headache: A native space analysis. *Behavioral and Brain Functions*, *13*(1), 1–9. https://doi.org/10.1186/s12993-017-0124-5

Miller, M. W. (1986). Effects of Alcohol on the Generation and Migration of Cerebral Cortical Neurons. *Science*, *233*(4770), 1308–1311. https://doi.org/10.1126/SCIENCE.3749878

Mori, S., Crain, B. J., Chacko, V. P., & Van Zijl, P. C. M. (1999). Three-dimensional tracking of axonal projections in the brain by magnetic resonance imaging. *Annals of Neurology*, *45*(2), 265–269. https://doi.org/https://doi.org/10.1002/1531-8249(199902)45:2<265::AID-ANA21>3.0.CO;2-3

Morrisett, R. A., Martin, D., Wilson, W. A., Savage, D. D., & Swartzwelder, H. S. (1988). Prenatal exposure to ethanol decreases the sensitivity of the adult rat hippocampus to N-methyl-D-aspartate. *Alcohol*, *5*(July), 121–124. https://doi.org/10.1016/0741-8329(89)90013-X

Mukherjee, P., Chung, S. W., Berman, J. I., Hess, C. P., & Henry, R. G. (2008). Diffusion Tensor

MR Imaging and Fiber Tractography: Technical Considerations. *AJNR: American Journal of Neuroradiology*, *29*(5), 843. https://doi.org/10.3174/AJNR.A1052

Nardelli, A., Lebel, C., Rasmussen, C., Andrew, G., & Beaulieu, C. (2011). Extensive deep gray matter volume reductions in children and adolescents with fetal alcohol spectrum disorders. *Alcoholism: Clinical and Experimental Research*, *35*(8), 1404–1417. https://doi.org/10.1111/j.1530-0277.2011.01476.x

Narvacan, K., Treit, S., Camicioli, R., Martin, W., & Beaulieu, C. (2017). Evolution of deep gray matter volume across the human lifespan. *Human Brain Mapping*, *38*(8), 3771–3790. https://doi.org/10.1002/hbm.23604

Newman, B. T., Dhollander, T., Reynier, K. A., Panzer, M. B., & Druzgal, T. J. (2020). Test–retest reliability and long-term stability of three-tissue constrained spherical deconvolution methods for analyzing diffusion MRI data. *Magnetic Resonance in Medicine*, *84*(4), 2161–2173. https://doi.org/10.1002/mrm.28242

Nguyen, V. T., Bhalla, R., Cowin, G., Stimson, D. H. R., Song, X., Chong, S., Jackson, A., Trigg, W. J., Tieng, Q. M., Mardon, K., Galloway, G. J., & Kurniawan, N. D. (2020). GABAa receptor density alterations revealed in a mouse model of early moderate prenatal ethanol exposure using [18F]AH114726. *Nuclear Medicine and Biology*, *88–89*, 44–51. https://doi.org/10.1016/j.nucmedbio.2020.07.005

Nguyen, V. T., Chong, S., Tieng, Q. M., Mardon, K., Galloway, G. J., & Kurniawan, N. D. (2017). Radiological studies of fetal alcohol spectrum disorders in humans and animal models: An updated comprehensive review. *Magnetic Resonance Imaging*, *43*, 10–26. https://doi.org/10.1016/j.mri.2017.06.012

Niedzwiedz-Massey, V. M., Douglas, J. C., Rafferty, T., Wight, P. A., Kane, C. J. M., & Drew, P. D. (2021). Ethanol modulation of hippocampal neuroinflammation, myelination, and neurodevelopment in a postnatal mouse model of fetal alcohol spectrum disorders. *Neurotoxicology and Teratology*, *87*, 1–14. https://doi.org/10.1016/j.ntt.2021.107015

Nobis, L., Manohar, S. G., Smith, S. M., Alfaro-Almagro, F., Jenkinson, M., Mackay, C. E., & Husain, M. (2019). Hippocampal volume across age: Nomograms derived from over 19,700 people in UK Biobank. *NeuroImage: Clinical*, *23*, 1–13. https://doi.org/10.1016/j.nicl.2019.101904

Nordin, K., Persson, J., Stening, E., Herlitz, A., Larsson, E. M., & Söderlund, H. (2018). Structural whole-brain covariance of the anterior and posterior hippocampus: Associations with age and memory. *Hippocampus*, *28*(2), 151–163. https://doi.org/10.1002/hipo.22817

O'mara, S. (2005). The subiculum: what it does, what it might do, and what neuroanatomy has yet to tell us. In *J. Anat* (Vol. 207).

Olateju, O. I., Spocter, M. A., Patzke, N., Ihunwo, A. O., & Manger, P. R. (2018). Hippocampal neurogenesis in the C57BL/6J mice at early adulthood following prenatal alcohol exposure. *Metabolic Brain Disease*, *33*(2), 397–410. https://doi.org/10.1007/s11011-017-0156-4

Olsen, R. K., Carr, V. A., Daugherty, A. M., La Joie, R., Amaral, R. S. C., Amunts, K., Augustinack, J. C., Bakker, A., Bender, A. R., Berron, D., Boccardi, M., Bocchetta, M., Burggren, A. C., Chakravarty, M. M., Chételat, G., de Flores, R., DeKraker, J., Ding, S. L., Geerlings, M. I., … Wisse, L. E. M. (2019). Progress update from the hippocampal subfields group. *Alzheimer's and Dementia: Diagnosis, Assessment and Disease Monitoring*, *11*, 439–449. https://doi.org/10.1016/j.dadm.2019.04.001

Oppenheim, C., Dormont, D., Biondi, A., Lehéricy, S., Hasboun, D., Clémenceau, S., Baulac, M., & Marsault, C. (1998). Loss of digitations of the hippocampal head on high-resolution fast spin-echo MR: A sign of mesial temporal sclerosis. *American Journal of Neuroradiology*, *19*(3), 457–463.

Parnell, S. E., Holloway, H. E., Baker, L. K., Styner, M. A., & Sulik, K. K. (2014). Dysmorphogenic effects of first trimester-equivalent ethanol exposure in mice: A magnetic resonance microscopy-based study. *Alcoholism: Clinical and Experimental Research*, *38*(7), 2008–2014. https://doi.org/10.1111/acer.12464

Parnell, S. E., Holloway, H. T., O'Leary-Moore, S. K., Dehart, D. B., Paniaqua, B., Oguz, I., Budin, F., Styner, M. A., Johnson, G. A., & Sulik, K. K. (2013). Magnetic resonance microscopy-based analyses of the neuroanatomical effects of gestational day 9 ethanol exposure in mice. *Neurotoxicology and Teratology*, *39*, 77–83. https://doi.org/10.1016/j.ntt.2013.07.009

Parnell, S. E., O'Leary-Moore, S. K., Godin, E. A., Dehart, D. B., Johnson, B. W., Allan Johnson, G., Styner, M. A., & Sulik, K. K. (2009). Magnetic resonance microscopy defines ethanol-induced brain abnormalities in prenatal mice: Effects of acute insult on gestational day 8. *Alcoholism: Clinical and Experimental Research*, *33*(6), 1001–1011. https://doi.org/10.1111/j.1530-0277.2009.00921.x

Patel, R., Steele, C. J., Chen, A. G. X., Patel, S., Devenyi, G. A., Germann, J., Tardif, C. L., & Chakravarty, M. M. (2020). Investigating microstructural variation in the human hippocampus using non-negative matrix factorization. *NeuroImage*, *207*, 116348. https://doi.org/10.1016/j.neuroimage.2019.116348

Pedraza, O., Bowers, D., & Gilmore, R. (2004). Asymmetry of the hippocampus and amygdala in MRI volumetric measurements of normal adults. *Journal of the International Neuropsychological Society*, *10*(5), 664–678. https://doi.org/10.1017/S1355617704105080

Pereira, J. B., Valls-Pedret, C., Ros, E., Palacios, E., Falcón, C., Bargalló, N., Bartrés-Faz, D., Wahlund, L.-O., Westman, E., & Junque, C. (2014). Regional vulnerability of hippocampal subfields to aging measured by structural and diffusion MRI. *Hippocampus*, *24*(4), 403–414. https://doi.org/10.1002/hipo.22234

Perrone, D., Aelterman, J., Pižurica, A., Jeurissen, B., Philips, W., & Leemans, A. (2015). The effect of Gibbs ringing artifacts on measures derived from diffusion MRI. *NeuroImage*, *120*, 441–455. https://doi.org/https://doi.org/10.1016/j.neuroimage.2015.06.068

Petrelli, B., Weinberg, J., & Hicks, G. G. (2018). Effects of prenatal alcohol exposure (PAE): Insights into FASD using mouse models of PAE. *Biochemistry and Cell Biology*, *96*(2), 131–

147. https://doi.org/10.1139/bcb-2017-0280

Piccirilli, E., Gentile, L., Mattei, P. A., Maruotti, V., Briganti, C., Panara, V., & Caulo, M. (2020). MRI-based classification of the anatomical variants of the hippocampal head. *Neuroradiology*, *62*(9), 1105–1110. https://doi.org/10.1007/s00234-020-02430-y

Pipe, J. (2009). Pulse sequences for diffusion-weighted MRI. In *Diffusion MRI*. Elsevier Inc. https://doi.org/10.1016/B978-0-12-374709-9.00002-X

Popova, S., Lange, S., Poznyak, V., Chudley, A. E., Shield, K. D., Reynolds, J. N., Murray, M., & Rehm, J. (2019). Population-based prevalence of fetal alcohol spectrum disorder in Canada. *BMC Public Health*, *19*(1), 1–12. https://doi.org/10.1186/S12889-019-7213-3/

Poppenk, J. (2020). Uncal apex position varies with normal aging. *Hippocampus*, *30*(7), 724–732. https://doi.org/10.1002/hipo.23196

Postle, B. R. (2016). The hippocampus, memory, and consciousness. In *The Neurology of Conciousness* (pp. 349–363). Elsevier. https://doi.org/10.1016/B978-0-12-800948-2.00021-2

Raffelt, D., Tournier, J.-D., Rose, S., Ridgway, G. R., Henderson, R., Crozier, S., Salvado, O., & Connelly, A. (2012). Apparent Fibre Density: A novel measure for the analysis of diffusion-weighted magnetic resonance images. *NeuroImage*, *59*, 3976–3994. https://doi.org/10.1016/j.neuroimage.2011.10.045

Riggins, T., Blankenship, S. L., Mulligan, E., Rice, K., & Redcay, E. (2015). Developmental differences in relations between episodic memory and hippocampal subregion volume during early childhood. *Child Development*, *86*(6), 1710–1718. https://doi.org/10.1111/cdev.12445

Riggins, T., Geng, F., Botdorf, M., Canada, K., Cox, L., & Hancock, G. R. (2018). Protracted hippocampal development is associated with age-related improvements in memory during early childhood. *NeuroImage*, *174*, 127–137. https://doi.org/10.1016/j.neuroimage.2018.03.009

Roediger, D. J., Krueger, A. M., de Water, E., Mueller, B. A., Boys, C. A., Hendrickson, T. J., Schumacher, M. J., Mattson, S. N., Jones, K. L., Lim, K. O., & Wozniak, J. R. (2021). Hippocampal subfield abnormalities and memory functioning in children with fetal alcohol Spectrum disorders. *Neurotoxicology and Teratology*, *83*, 1–8. https://doi.org/10.1016/j.ntt.2020.106944

Roussotte, F. F., Sulik, K. K., Mattson, S. N., Riley, E. P., Jones, K. L., Adnams, C. M., May, P. A., O'Connor, M. J., Narr, K. L., & Sowell, E. R. (2012). Regional brain volume reductions relate to facial dysmorphology and neurocognitive function in fetal alcohol spectrum disorders. *Human Brain Mapping*, *33*(4), 920–937. https://doi.org/10.1002/hbm.21260

Rubin, R. D., Watson, P. D., Duff, M. C., & Cohen, N. J. (2014). The role of the hippocampus in flexible cognition and social behavior. *Frontiers in Human Neuroscience*, *8*(SEP), 1–15. https://doi.org/10.3389/fnhum.2014.00742

Schaffner, S. L., Lussier, A. A., Baker, J. A., Goldowitz, D., Hamre, K. M., Kobor, M. S., Ghezzi,

A., Rico Lei Zhao, P., & Kobor msk, M. S. (2020). Neonatal Alcohol Exposure in Mice Induces Select Differentiation- and Apoptosis-Related Chromatin Changes Both Independent of and Dependent on Sex. *Article*, *11*, 1. https://doi.org/10.3389/fgene.2020.00035

Schlichting, M. L., Guarino, K. F., Schapiro, A. C., Turk-Browne, N. B., & Preston, A. R. (2017). Hippocampal structure predicts statistical learning and associative inference abilities during development. *Journal of Cognitive Neuroscience*, *29*(1), 37–51. https://doi.org/10.1162/jocn_a_01028

Schlichting, M. L., Gumus, M., Zhu, T., & Mack, M. L. (2021). The structure of hippocampal circuitry relates to rapid category learning in humans. *Hippocampus*, *31*(11), 1179–1190. https://doi.org/10.1002/hipo.23382

Shepherd, T. M., Özarslan, E., Yachnis, A. T., King, M. A., & Blackband, S. J. (2007). Diffusion tensor microscopy indicates the cytoarchitectural basis for diffusion anisotropy in the human hippocampus. *American Journal of Neuroradiology*, *28*(5), 958–964.

Skorput, A. G. J., Gupta, V. P., Yeh, P. W. L., & Yeh, H. H. (2015). *Neurobiology of Disease Persistent Interneuronopathy in the Prefrontal Cortex of Young Adult Offspring Exposed to Ethanol In Utero*. https://doi.org/10.1523/JNEUROSCI.1462-15.2015

Slater, D. A., Melie-Garcia, L., Preisig, M., Kherif, F., Lutti, A., & Draganski, B. (2019). Evolution of white matter tract microstructure across the life span. *Human Brain Mapping*, *40*(7), 2252–2268. https://doi.org/10.1002/hbm.24522

Slotkin, J., Kallen, M., Griffith, J., Magasi, S., Salsman, J., Nowinski, C., & Gershon, R. (2012a). *NIH Toolbox Technical Manual, Cognition, Episodic Memory, NIH Toolbox Auditory Verbal Learning Test (Rey)*. National Institutes of Health and Northwestern University.

Slotkin, J., Kallen, M., Griffith, J., Magasi, S., Salsman, J., Nowinski, C., & Gershon, R. (2012b). *NIH Toolbox Technical Manual, Cognition, Processing Speed, NIH Toolbox Oral Symbol Digit Test (Supplemental Measure)*. National Institutes of Health and Northwestern University.

Soares, J. M., Marques, P., Alves, V., & Sousa, N. (2013). A hitchhiker's guide to diffusion tensor imaging. *Frontiers in Neuroscience*, *7*(31), 1–14. https://doi.org/10.3389/fnins.2013.00031

Solar, K. G., Treit, S., & Beaulieu, C. (2021). High resolution diffusion tensor imaging of the hippocampus across the healthy lifespan. *Hippocampus*, *n/a*(n/a). https://doi.org/https://doi.org/10.1002/hipo.23388

Solar, K. G., Treit, S., & Beaulieu, C. (2022). High-resolution diffusion tensor imaging identifies hippocampal volume loss without diffusion changes in individuals with prenatal alcohol exposure. *Alcoholism: Clinical and Experimental Research*, *46*(7), 1204–1219. https://doi.org/10.1111/acer.14857

Soleimani, E., Goudarzi, I., Abrari, K., & Lashkarbolouki, T. (2016). The combined effects of developmental lead and ethanol exposure on hippocampus dependent spatial learning and memory in rats: Role of oxidative stress. *Food and Chemical Toxicology*, *96*, 263–272.

https://doi.org/10.1016/j.fct.2016.07.009

Song, S. K., Sun, S. W., Ramsbottom, M. J., Chang, C., Russell, J., & Cross, A. H. (2002). Dysmyelination revealed through MRI as increased radial (but unchanged axial) diffusion of water. *NeuroImage*, *17*(3), 1429–1436. https://doi.org/10.1006/nimg.2002.1267

Squire, L. R., & Wixted, J. T. (2011). The Cognitive Neuroscience of Human Memory Since H.M. *Annual Review of Neuroscience*, *34*, 259. https://doi.org/10.1146/ANNUREV-NEURO-061010-113720

Stanisz, G. J., Odrobina, E. E., Pun, J., Escaravage, M., Graham, S. J., Bronskill, M. J., & Henkelman, R. M. (2005). T1, T2 relaxation and magnetization transfer in tissue at 3T. *Magnetic Resonance in Medicine*, *54*(3), 507–512. https://doi.org/10.1002/mrm.20605

Stejskal, E. O., & Tanner, J. E. (1965). Spin diffusion measurements: Spin echoes in the presence of a time-dependent field gradient. *The Journal of Chemical Physics*, *42*(1), 288–292. https://doi.org/10.1063/1.1695690

Toso, L., Roberson, R., Woodard, J., Abebe, D., & Spong, C. Y. (2006). Prenatal alcohol exposure alters GABA Aα5 expression: A mechanism of alcohol-induced learning dysfunction. *American Journal of Obstetrics and Gynecology*, *195*(2), 522–527. https://doi.org/10.1016/j.ajog.2006.01.098

Tournier, J. D., Calamante, F., & Connelly, A. (2007). Robust determination of the fibre orientation distribution in diffusion MRI: Non-negativity constrained super-resolved spherical deconvolution. *NeuroImage*, *35*(4), 1459–1472. https://doi.org/10.1016/j.neuroimage.2007.02.016

Tournier, J. D., Calamante, F., & Connelly, A. (2012). MRtrix: Diffusion tractography in crossing fiber regions. *International Journal of Imaging Systems and Technology*, *22*(1), 53–66. https://doi.org/10.1002/ima.22005

Tournier, J. D., Calamante, F., & Connelly, A. (2013). Determination of the appropriate b value and number of gradient directions for high-angular-resolution diffusion-weighted imaging. *NMR in Biomedicine*, *26*(12), 1775–1786. https://doi.org/10.1002/nbm.3017

Tournier, J. D., Calamante, F., Gadian, D. G., & Connelly, A. (2004). Direct estimation of the fiber orientation density function from diffusion-weighted MRI data using spherical deconvolution. *NeuroImage*, *23*(3), 1176–1185. https://doi.org/10.1016/j.neuroimage.2004.07.037

Tournier, J. D., Mori, S., & Leemans, A. (2011). Diffusion tensor imaging and beyond. *Magnetic Resonance in Medicine*, *65*(6), 1532–1556. https://doi.org/10.1002/mrm.22924

Tournier, J. D., Smith, R., Raffelt, D., Tabbara, R., Dhollander, T., Pietsch, M., Christiaens, D., Jeurissen, B., Yeh, C. H., & Connelly, A. (2019). MRtrix3: A fast, flexible and open software framework for medical image processing and visualisation. *NeuroImage*, *202*(January), 116137. https://doi.org/10.1016/j.neuroimage.2019.116137

Tournier, J. D., Yeh, C. H., Calamante, F., Cho, K. H., Connelly, A., & Lin, C. P. (2008). Resolving

crossing fibres using constrained spherical deconvolution: Validation using diffusion-weighted imaging phantom data. *NeuroImage*, *42*(2), 617–625. https://doi.org/10.1016/j.neuroimage.2008.05.002

Treit, S., & Beaulieu, C. (2018). *Imaging Brain Structure in FASD* (pp. 77–93). Springer, Cham. https://doi.org/10.1007/978-3-319-71755-5_6

Treit, S., Chen, Z., Zhou, D., Baugh, L., Rasmussen, C., Andrew, G., Pei, J., & Beaulieu, C. (2017). Sexual dimorphism of volume reduction but not cognitive deficit in fetal alcohol spectrum disorders: A combined diffusion tensor imaging, cortical thickness and brain volume study. *NeuroImage: Clinical*, *15*, 284–297. https://doi.org/10.1016/j.nicl.2017.05.006

Treit, S., Lebel, C., Baugh, L., Rasmussen, C., Andrew, G., & Beaulieu, C. (2013). Longitudinal MRI reveals altered trajectory of brain development during childhood and adolescence in fetal alcohol spectrum disorders. *Journal of Neuroscience*, *33*(24), 10098–10109. https://doi.org/10.1523/JNEUROSCI.5004-12.2013

Treit, S., Little, G., Steve, T., Nowacki, T., Schmitt, L., Wheatley, B. M., Beaulieu, C., & Gross, D. W. (2019). Regional hippocampal diffusion abnormalities associated with subfield-specific pathology in temporal lobe epilepsy. *Epilepsia Open*, *4*(4), 544–554. https://doi.org/10.1002/epi4.12357

Treit, S., Rickard, J., Stolz, E., Solar, K., Seres, P., Emery, D., & Beaulieu, C. (2022). A Normative Brain MRI Database of Neurotypical Participants from 5-90 Years of Age. *Canadian Journal of Neurological Sciences*, 1–5. https://doi.org/10.1017/cjn.2021.513

Treit, S., Steve, T., Gross, D. W., & Beaulieu, C. (2018). High resolution in-vivo diffusion imaging of the human hippocampus. *NeuroImage*, *182*, 479–487. https://doi.org/10.1016/j.neuroimage.2018.01.034

Tustison, N. J., Avants, B. B., Cook, P. A., Zheng, Y., Egan, A., Yushkevich, P. A., & Gee, J. C. (2010). N4ITK: Improved N3 bias correction. *IEEE Transactions on Medical Imaging*, *29*(6), 1310–1320. https://doi.org/10.1109/TMI.2010.2046908

Uban, K. A., Kan, E., Wozniak, J. R., Mattson, S. N., Coles, C. D., & Sowell, E. R. (2020). The relationship between socioeconomic status and brain volume in children and adolescents with prenatal alcohol exposure. *Frontiers in Human Neuroscience*, *14*, 1–11. https://doi.org/10.3389/fnhum.2020.00085

Venkatesh, A., Stark, S. M., Stark, C. E. L., & Bennett, I. J. (2020). Age- and memory- related differences in hippocampal gray matter integrity are better captured by NODDI compared to single-tensor diffusion imaging. *Neurobiology of Aging*, *96*, 12–21. https://doi.org/10.1016/j.neurobiolaging.2020.08.004

Veraart, J., Novikov, D. S., Christiaens, D., Ades-aron, B., Sijbers, J., & Fieremans, E. (2016). Denoising of diffusion MRI using random matrix theory. *NeuroImage*, *142*, 394–406. https://doi.org/10.1016/j.neuroimage.2016.08.016

Voineskos, A. N., Winterburn, J. L., Felsky, D., Pipitone, J., Rajji, T. K., Mulsant, B. H., &

Chakravarty, M. M. (2015). Hippocampal (subfield) volume and shape in relation to cognitive performance across the adult lifespan. *Human Brain Mapping*, *36*(8), 3020–3037. https://doi.org/10.1002/hbm.22825

von Bartheld, C. S., Bahney, J., & Herculano-Houzel, S. (2016). The search for true numbers of neurons and glial cells in the human brain: A review of 150 years of cell counting. *Journal of Comparative Neurology*, *524*(18), 3865–3895. https://doi.org/10.1002/cne.24040

Walhovd, K. B., Fjell, A. M., Reinvang, I., Lundervold, A., Dale, A. M., Eilertsen, D. E., Quinn, B. T., Salat, D., Makris, N., & Fischl, B. (2005). Effects of age on volumes of cortex, white matter and subcortical structures. *Neurobiology of Aging*, *26*(9), 1261–1270. https://doi.org/10.1016/j.neurobiolaging.2005.05.020

Wang, L., Swank, J. S., Glick, I. E., Gado, M. H., Miller, M. I., Morris, J. C., & Csernansky, J. G. (2003). Changes in hippocampal volume and shape across time distinguish dementia of the Alzheimer type from healthy aging. *NeuroImage*, *20*(2), 667–682. https://doi.org/10.1016/S1053-8119(03)00361-6

Wellington, R. L., Bilder, R. M., Napolitano, B., & Szeszko, P. R. (2013). Effects of age on prefrontal subregions and hippocampal volumes in young and middle-aged healthy humans. *Human Brain Mapping*, *34*(9), 2129–2140. https://doi.org/10.1002/hbm.22054

West, M. J. (1993). Regionally specific loss of neurons in the aging human hippocampus. *Neurobiology of Aging*, *14*(4), 287–293. https://doi.org/10.1016/0197-4580(93)90113-P

Willoughby, K. A., Sheard, E. D., Nash, K., & Rovet, J. (2008). Effects of prenatal alcohol exposure on hippocampal volume, verbal learning, and verbal and spatial recall in late childhood. *Journal of the International Neuropsychological Society*, *14*(6), 1022–1033. https://doi.org/10.1017/S1355617708081368

Wolf, D., Fischer, F. U., de Flores, R., Chételat, G., & Fellgiebel, A. (2015). Differential associations of age with volume and microstructure of hippocampal subfields in healthy older adults. *Human Brain Mapping*, *36*(10), 3819–3831. https://doi.org/10.1002/hbm.22880

Yang, X., Goh, A., Chen, S. H. A., & Qiu, A. (2013). Evolution of hippocampal shapes across the human lifespan. *Human Brain Mapping*, *34*(11), 3075–3085. https://doi.org/10.1002/hbm.22125

Yassa, M. A., Mattfeld, A. T., Stark, S. M., & Stark, C. E. L. (2011). Age-related memory deficits linked to circuit-specific disruptions in the hippocampus. *Proceedings of the National Academy of Sciences of the United States of America*, *108*(21), 8873–8878. https://doi.org/10.1073/pnas.1101567108

Yassa, M. A., Muftuler, L. T., & Stark, C. E. L. (2010). Ultrahigh-resolution microstructural diffusion tensor imaging reveals perforant path degradation in aged humans in vivo. *Proceedings of the National Academy of Sciences of the United States of America*, *107*(28), 12687–12691. https://doi.org/10.1073/pnas.1002113107

Yokoi, S., Kidokoro, H., Yamamoto, H., Ohno, A., Nakata, T., Kubota, T., Tsuji, T., Morishita,

M., Kawabe, T., Naiki, M., Maruyama, K., Itomi, K., Kato, T., Ito, K., & Natsume, J. (2019). Hippocampal diffusion abnormality after febrile status epilepticus is related to subsequent epilepsy. *Epilepsia*, *60*(7), 1306–1316. https://doi.org/10.1111/epi.16059

Yushkevich, P. A., Piven, J., Hazlett, H. C., Smith, R. G., Ho, S., Gee, J. C., & Gerig, G. (2006). User-guided 3D active contour segmentation of anatomical structures: Significantly improved efficiency and reliability. *NeuroImage*, *31*(3), 1116–1128. https://doi.org/10.1016/j.neuroimage.2006.01.015

Zeineh, M. M., Holdsworth, S., Skare, S., Atlas, S. W., & Bammer, R. (2012). Ultra-high resolution diffusion tensor imaging of the microscopic pathways of the medial temporal lobe. *NeuroImage*, *62*(3), 2065–2082. https://doi.org/10.1016/J.NEUROIMAGE.2012.05.065

Zhang, F., Daducci, A., He, Y., Schiavi, S., Seguin, C., Smith, R. E., Yeh, C. H., Zhao, T., & O'Donnell, L. J. (2022). Quantitative mapping of the brain's structural connectivity using diffusion MRI tractography: A review. *NeuroImage*, *249*(December 2021). https://doi.org/10.1016/j.neuroimage.2021.118870

Appendix A: General Processing and CSD and DTI Analysis Pipelines in MRtrix3

General processing pipeline (make sure to perform visual quality checks at each step):

1. In the MRtrix3 command line console, set the following:

   data_path='/main_folder/'

   output_folder='/processed_folder/'

2. Convert dicom, raw images to .mif files:

   for_each $data_path/*.dcm : mrconvert IN $data_path/$output_folder/PRE.mif

3. DWI Denoising using dwidenoise:

   for_each $data_path/$output_folder/*.mif : dwidenoise IN

   $data_path/$output_folder/PRE_DN.mif

4. DWI Gibbs ringing correction using mrdegibbs:

   for_each $data_path/$output_folder/*_DN.mif : mrdegibbs IN

   $data_path/$output_folder/PRE_G.mif

5. DWI distortion correction using dwifslpreproc (need to specify an option that indicates the phase encoding scheme, and in most cases, like in this data, use the -rpe_header option which pulls the information from the image header):

   for_each $data_path/$output_folder/*_DN_G* : dwipreproc -rpe_header IN

   $data_path/$output_folder/PRE_preproc.mif

6. DWI B1 field inhomogeneity correction using biasscorr and the -ants option:

   for_each $data_path/$output_folder/*_DN_G_preproc* : dwibiascorrect IN

   $data_path/$output_folder/PRE_biascorr.mif -ants

7. Mean DWI creation based on the b500s with dwiextract and mrmath

   a. To create a mean DWI with the b500s, first run dwiextract to create a file with only the b500s and no b0s:

for_each $data_path/$output_folder/*_DN_G_preproc_biascorr* : dwiextract IN $data_path/$output_folder/PRE_b500s.mif -shells 500

b. Next, run mrmath to produce a mean 3D image from a 4D image series:

for_each $data_path/$output_folder/*_DN_G_preproc_biascorr_b500s* : mrmath mean IN $data_path/$output_folder/PRE_meanDWI.mif -axis 3

DTI pipeline:

1. First, if using multi-shell DWI such as the AB300 data with two b values, b500 and b2000, dwiextract is needed to create a file with all the b0s and b500s but without the b2000s as those are not required nor accurate for calculating DTI metrics:

   for_each $data_path/$output_folder/*_DN_G_preproc_biascorr.mif : dwiextract IN -shell 0,500 $data_path/$output_folder/PRE_b0b500.mif
2. Tensor creation using dwi2tensor:

   for_each $data_path/$output_folder/*_DN_G_preproc_biascorr_b0b500.mif : dwi2tensor IN $data_path/$output_folder/PRE_tensor.mif
3. FA map creation using tensor2metric -fa”

   for_each $data_path/$output_folder/*_tensor.mif : tensor2metric IN -fa $data_path/$output_folder/PRE_FAmap.mif
4. MD map creation using tensor2metric -adc:

   for_each $data_path/$output_folder/*_tensor.mif : tensor2metric IN -adc $data_path/$output_folder/PRE_MDmap.mif
5. AD map creation using tensor2metric -ad:

   for_each $data_path/$output_folder/*_tensor.mif : tensor2metric IN -ad $data_path/$output_folder/PRE_ADmap.mif

6. RD map creation using tensor2metric -rd:

   for_each $data_path/$output_folder/*_tensor.mif : tensor2metric IN -rd $data_path/$output_folder/PRE_RDmap.mif

7. Use mrconvert to convert maps to nii

   for_each $data_path/$output_folder/*_tensor_*map.mif : mrconvert IN $data_path/$output_folder/PRE.nii

8. To perform deterministic DTI tractography within the hippocampus, use tckgen with the -algorithm tensor_det, and the -minlength 10, -cutoff 0.05, and -angle 50:

   for_each $data_path/$output_folder/*_DN_G_preproc_biascorr_b0b500.mif : tckgen IN $data_path/$output_folder/PRE_DTI_tensordet_tracts.mif -algorithm tensor_det -minlength 10 -cutoff 0.05 -angle 50 -seed_image $data_path/$output_folder/PRE_whole_hippocampus_ROI.mif

9. To visualize the colour coded eigenvector map or streamlines from the DTI analysis, type into the console “mrview” and open the mean DWI, then overlay the tensor file (/*_tensor_*map.mif) to visualize the eigenvectors, and overlay the tck file to visualize the corresponding streamlines.

CSD tractography:

1. With the multi-shell AB300 data, first generate multi tissue response function text files using dwi2response with the dhollander option:

   for_each $data_path/$output_folder/*_DN_G_preproc_biascorr_b0b500b2000.mif : dwi2response dhollander IN $data_path/$output_folder/PRE_CSD_dhollander_sfwm.txt $data_path/$output_folder/PRE_CSD_dhollander_gm.txt $data_path/$output_folder/PRE_CSD_dhollander_csf.txt

2. Using the response function files as kernels, run multi shell multi tissue CSD using dwi2fod msmt_csd with the whole hippocampus ROI as a mask to produce intra-hippocampal fODF maps (check the *_sfwm.mif fODF map for anatomically-plausible directionality):

   for_each $data_path/$output_folder/*_sfwm.txt $data_path/$output_folder/*_gm.txt $data_path/$output_folder/*_csf.txt : dwi2response dhollander IN $data_path/$output_folder/PRE_CSD_dhollander_fODF_sfwm.mif $data_path/$output_folder/PRE_CSD_dhollander_fODF_gm.mif $data_path/$output_folder/PRE_CSD_dhollander_fODF_csf.mif

3. To perform deterministic CSD tractography within the hippocampus, use tckgen with the -algorithm sd_stream, and the -minlength 10, -cutoff 0.05, and -angle 50:

   for_each $data_path/$output_folder_dhollander_fODF_sfwm.mif : tckgen IN $data_path/$output_folder/PRE_CSD_dhollander_fODF_sfwm_sdstream_tracts.mif -algorithm sd_stream -minlength 10 -cutoff 0.05 -angle 50 -seed_image $data_path/$output_folder/PRE_whole_hippocampus_ROI.mif

10. To visualize the colour coded fODF map or streamlines from the CSD analysis, type into the console “mrview” and open the mean DWI, then overlay the fODF file (/*_sfwm.mif) to visualize the eigenvectors, and overlay the tck file to visualize the corresponding streamlines.